Condition Monitoring

Of

Electric Motors

---

by

Sam Yiu Sum Ho, B.E. (Hons)

Submitted in fulfilment of the requirements for the degree of

Doctor of Philosophy

University of Tasmania

October 1999

Statement of Originality

This thesis contains no material which has been accepted for a degree or diploma by the University or any other institution, except by way of background information duly acknowledged in the thesis, and to the best of my knowledge and brief on material previously published or written by another person except where due acknowledgment is made in the text of the thesis.

Sam Yiu Sum Ho.

Authority of Access

This thesis may be made available for loan and limited copying in accordance with the Copyright Act 1968.

Sam Yiu Sum Ho.

Abstract

The aim of condition monitoring is to recognise the development of evolving motor faults at an early stage, so that the motor can be scheduled for repair or replacement before catastrophic failure occurs. Often in a modern industrial plant, the cost of an unscheduled shutdown of the process is very much greater than the cost of the motor itself.

This thesis concentrates on the detection of stator and rotor defects in squirrel cage induction motors. Very little work has been done on the detection of these faults when the motor is supplied at variable frequency. Hardware and software approaches have previously been attempted but with limited success. An alternative method put forward here is to compute the instantaneous input power of the motor from the two line-to-line voltages and two line currents. In order to do this, specialised hardware has been developed, including a study of the suitability of different types of current transducers.

The effects of open circuit and short circuit armature coils, and poor commutation of DC motors have been examined. Because the conventional current transformer cannot be used for DC, and the electrical noise inside the control cubicle of a thyristor-controlled DC motor prevents successful operation of a Hall Effect clip-on ammeter, an air core clip-on "Rogowski" coil was designed to monitor fault-related frequencies in armature and field current. In order to study the effect of open-circuit or short-circuit coil, steady-state models for the DC motor were developed using inductively coupled coils theory. Individual field and armature coils can be modelled, and the effect of faulty armature coils on the amplitude of frequency components that are introduced into armature and field current, can be predicted.

To summarise, the main achievements described in this thesis are as follows:

Voltage, current, and power monitoring of the induction motor

- Design of fully shielded, linear phase shift, clip-on current transducer for power monitoring (It was initially designed by Mr Langman and modified by the author).

- Design of a voltage and current monitoring hardware system for induction motors with assistance from the technical support group in the Electrical Engineering Department of the University of Tasmania.

- Theory and implementation of using input motor power for the overall check of induction motors.

- Use of spectrum analysis of current or power signal to attempt to detect bearing faults.

- Use of the instantaneous input power signal to detect stator and rotor defect of the motor with variable frequency supply.

Current monitoring of the DC motor

- Frequency spectrum analysis of armature and field current waveforms of DC motors.

- Investigation of the effect of incorrect interpole strength, open-circuit and short-circuit armature coils on the armature and field currents.

- Numerical modelling of DC motor with open-circuit armature coil for steady-state conditions.

- Numerical modelling of DC motor with short-circuit armature coil for steady-state conditions.

Acknowledgments

I would like to express my sincere appreciation to my supervisor Mr. Richard Langman for his guidance and support in conducting this research. I would also like to acknowledge Dr. John Arneaud (now with the Hydro Electric Commission Tasmania) for initially supervising my Masters degree which led into this condition monitoring work.

I am also grateful to the following people and for their permission to take measurements around their factories.

Mr. Mark Hoggins, Mr. Merv Bentley, and Mr. Woody Brown from ANM, Boyer;

Mr. Chris Bitt from APPM, Burnie;

Mr. John Frankling from Comalco, Bell Bay;

Mr. Mike Jorgensen from North Forest Products Triabunna;

Mr. Graeme Vertigan and Mr. Robert Bell from Pasminco EZ Pty. Ltd.

My thanks must go to all academic staff in the Department of Electrical Engineering and Computer Science at the University of Tasmania, in particular Mr. Peter Watt, Mr. John Brodie, Professor Thong Nguyen, Dr. Zhihong Man, Mr. Bob Wherrett, Dr. David Lewis, Dr. Michael Negnevitsky and especially the departmental secretary, Mrs. Judy Bonsey, for their kind assistance and friendship.

Thanks also go to all technical staff in the Department for their friendship and help, in particular Mr. Glenn Mayhew for help with electronic design work and solving electromagnetic interference problems; Mr. Steven Avery, Mr. Bernard Chenery and Mr. Glenn Bak for the design and fabrication of various devices and Mr. Russell Twining for his help with computing.

Many thanks must go to my fellow students, Andrew Innes, Mike O'Day, John McCulloch, Richard Andrew, Jason Pieloor, Mac Stoksik and Quang Ha. In particular I would like to thank Alan Liew, Bonnie Law, Mei Fei and his family for their friendship and valuable advice.

I would like to thank Margaret Eldridge for proof reading my thesis.

I would like to thank my parents, my brother and his family for the many years in which they have supported and encouraged me.

Finally, I would like to thank my loving wife Wendy Ng Suet Wan, my sons Jacky Kam Man and Michael Hei Man for their patience, support and love during these years that I have neglected them.

Contents

Symbols

List of symbols

f_1	=	supply frequency, Hz
f_{rt},	=	rotor speed frequency, Hz
f_r	=	rotor speed frequency, Hz
f_{bf}	=	bearing defect frequency in stator current, Hz
f_{bdf}	=	bearing defect frequency in vibration signal, Hz
f_L	=	frequency of load torque variation, Hz
f_{cb}	=	commutator bar frequency, number of commutator bars times speed frequency, Hz
f_{slot}	=	slot frequency, number of slots times speed frequency, Hz
pp	=	number of pole-pairs
S	=	number of stator slots
R	=	number of rotor slots
ω_1	=	angular supply frequency, radians/second
ω_r	=	rotational speed, radians/second
s	=	per unit slip
t	=	time variable, second
τ, b	=	time-shift variable, second
a	=	scale variable
θ	=	space variable, radian
ω	=	frequency variable, radians/second
M	=	magnetomotive force, Ampere-turns
B	=	flux density, Teslas
P, Λ	=	specific permeance, Webers/Ampere-turn meter^2
m, k, n	=	integer 1,2, 3, ...
N_{bp}	=	number of brush pairs

M	=	mutual inductance between field and armature coil, Henrys
m	=	mutual inductance between armature coils, Henrys
Φ	=	magnetic flux, Webers
i, i	=	current variable, Amperes
L, *L*	=	self inductance, Henrys
λ	=	flux linkage, Weber-turns
G	=	length, meters
L	=	inductance matrix
i	=	current matrix
v	=	voltage matrix
R	=	resistance matrix
λ	=	flux linkage matrix

Subscripts

θs	=	stator space harmonic
θr	=	rotor space harmonic
ωs	=	stator time harmonic
ωr	=	rotor space harmonic
s, st	=	stator
r, rt	=	rotor
se	=	static eccentricity
de	=	dynamic eccentricity
sa	=	saturation
l	=	leakage component of self flux
m	=	magnetising component of self flux
p	=	positive brush
n	=	negative brush
C, c	=	armature coil
f, ff	=	field winding

Preface

This project originated in 1989 with a local zinc company, Pasminco EZ Ltd., which was having problems with some critical induction motors. Each 415V, 330A motor was driving a large cooling tower fan via 11:1 reduction gearbox. If one of these fans became inoperative during the summer months, the entire plant would be shut down, costing around one million dollars per day in lost production. The motors are in an awkward position high above the ground, requiring a large crane to be brought on site in order for replacement. One of these motors showed overheating and excessive vibration. Although supply currents were well below the rating of the motor, over-temperature had caused motor protection to trip out, indicating either a faulty motor or unusual operating conditions. Due to lack of local commercial expertise, the company invited the University, whereupon Peter Watt, Richard Langman and Dr. David Lewis began an investigation and took some initial stator current spectra. Additional frequencies, which correspond to a modulation of the stator current at double slip-frequency, were present in the second set of measurements taken 13 months apart. These suggested a damaged rotor bar. Shortly after the second measurements were taken, the motor failed and was taken out of service. As the company was not interested in the failure mechanism of the motor, and had replaced it immediately, we did not have opportunity to check it.

Two years later, this project was continued as a Ph.D. topic by Andrew Innes. He wrote the software for data capture and spectrum analysis and developed the corresponding hardware. He then examined the implications that variable speed drives have for the detection of rotor damage. Very little previous work had been done on fault detection in motors controlled by such drives. Hardware and software approaches to achieve synchronous sampling were attempted, but with limited success.

In 1996, the author continued this project, although by now the industries were not financially and technically involved. After some on site measurements on motors

supplied at variable frequency, it was firstly discovered that the clip-on Hall effect ammeters are prone to electrostatic and electromagnetic interference from the drives, even though two of the ammeters had been specially shielded. A commercial precision split core current transformer was tried instead. However it was rather too bulky to clip over a motor cable and still fit in between neighbouring cables. Instead, split core current transformers were designed, that had a more suitable phase and frequency response, and importantly that would fit in between the supply cables in the motor control cubicle.

Secondly, an alternative method for stator and rotor defect detection in induction motors was proposed by the author. It is to compute and analyse the instantaneous input power of the motor from the two line-to-line voltages and two line currents. It also relied on the specially designed current transformers. An on-line monitoring system was developed and routine tests have been carried out in industry.

During the routine test in industry, the maintenance engineers asked if any condition monitoring techniques were available for DC machines, and this led to a detailed investigation of the problems associated with DC machines such as brush sparking and armature coil defects (open- or short-circuit turns). A new mathematical model was developed that could include the effect of an individual open-circuit or short-circuit armature coil.

Supporting Publications

[1] Sam Y. S. Ho, G. Mayhew, J. Arneaud, "The slip measurement of induction machines.", AUPEC'94, Vol. 2, pp238-243.

[2] Sam Y. S. Ho, R. A. Langman, "On-line estimation of induction motor speed using current and voltage measurement.", AUPEC'95, Vol. 3, pp357-363.

[3] Sam Y. S. Ho, R. A. Langman, "Rotor speed estimation of induction machines by monitoring the stator voltages and currents.", EEcon95

[4] Sam Y. S. Ho, R. A. Langman, "Accurate speed and slip measurement of induction motors.", Journal of Electrical and Electronics Engineering, Australia, Vol. 16, No.1, March 1996.

[5] Sam Y. S. Ho, R. A. Langman, " On-line condition monitoring of induction motors using voltage and current measurement.", AUPEC'96, Vol. 2, pp429-435.

[6] Andrew G. Innes, Sam Y. S. Ho, " Numerical modeling of an induction motor with a broken rotor bar.", AUPEC'96, Vol. 1, pp61-67.

[7] Sam Y. S. Ho, R. A. Langman, " Condition monitoring of induction motors.", Maintenance Journal, Vol. 10, No.3, July / August 1997, pp10-14.

[8] Sam Y. S. Ho, R. A. Langman, "Stator current frequency analysis for the condition motoring of induction motors. Part I : fixed supply frequency." Journal of Electrical and Electronics Engineering, Australia, Vol. 17, No. 1, March, 1997, pp43-56.

[9] Sam Y. S. Ho, R. A. Langman, "Stator current frequency analysis for the condition motoring of induction motors. Part II: variable supply frequency.", Journal of Electrical and Electronics Engineering, Australia, Vol. 17, No. 1, March, 1997, pp57-70.

[10] Sam Y. S. Ho, R. A. Langman, "Condition monitoring of electric motors by analysis of current waveform.", 11th International Congress and Exhibition on Condition Monitoring and Diagnostic Engineering Management, Launceston, Tasmania, Proceeding Vol. 2, December 1998, pp381-390.

[11] Sam Y. S. Ho, "The mathematical model of a DC motor" AUPEC'98 Hobart, Tasmania, Proceeding Vol. 2, Sept. 27-30, 1998, pp 389-394.

Chapter 1

Introduction

1.1 Induction Motors and DC Motors

The three-phase induction motor is used in a wide variety of industrial applications, often in critical production processes, because it is simple, rugged, low priced and easy to maintain. However, failure of the motor does occasionally occur, and will usually cause lost production in which, a high cost may be involved. Hence, it is important to recognise the state of motor faults as early as possible in order to take remedial action.

Traditionally, the induction motor is used for fixed speed application. In recent years, variable frequency AC drives have become very reliable and are widely used and have taken over many of the applications of DC motors. Therefore, the early recognition of motor faults must take into account the variable frequency drive. Although DC motor is expensive to build and to maintain, its important features include adjustable motor speed over very wide ranges, constant torque, rapid acceleration or deceleration, and responsiveness to feedback signals, making DC motors still valuable in a few industry applications. Also just because these days AC drives can in principle replace DC drives, does not mean that all DC drives will

immediately be replaced. So, this thesis examines condition monitoring of DC motors as well as the induction motor.

1.2 Plant Maintenance and Condition Monitoring

The problem of sudden failure of an electric motor has become more significant and challenging. Any failure is likely to have a number of possible causes, and may give rise to several early indications of its presence. The time taken for the fault to worsen to the stage where the motor fails will depend on many circumstances. A detailed account of failure mechanisms for electrical machines, and their early indications, is in the book of Tavner and Penman [1].

There are three methods of maintaining plant [2]:

- breakdown maintenance,
- regular preventive maintenance, and
- condition-based maintenance.

Breakdown maintenance is the simplest form of maintenance. The plant operates until a part breaks and the part is then replaced. It has the advantage of using a component to the end of its useful life. However, it can be very expensive in terms of the loss of the product from the unexpected downtime. It may also be dangerous.

The second alternative is to stop the plant at regular intervals for maintenance. It is probably the method most commonly used in industry. The choice of a regular maintenance interval is guided by two factors: maximisation of the component utility to minimise the waste, and minimisation of unexpected failures. The compromise between these two factors can be established by experience, but system failures still cannot be avoided.

The third alternative is condition-based maintenance, in which the condition of the plant is monitored to detect any deterioration in performance. The relevant part replacement is then scheduled, based on the estimation of the remaining life of the part. This maintenance method achieves maximum component utility and unscheduled outage is minimised. However, in order to provide knowledge of plant condition to estimate the rate at which deterioration is occurring, suitable parameters

must be selected to be monitored. Such a measurement system may require expensive instrumentation and a high level of expertise to interpret and analyse the data, and may require a costly initial capital investment in equipment, training, and experience.

Condition monitoring is well suited where [3]:

- a safety risk is likely to arise from the breakdown of the plant,
- high loss of production would be caused by the breakdown of machinery, machines are not easy to access, or are mobile and rarely return to base,
- operators cannot be expected to detect faults in expensive plant whose failure results in serious damage,
- plant is new in design and may have some residual development problems.

Motors are often used in critical positions in a plant, but they are still relatively cheap compared to the plant. Any unexpected failure of these machines will incur high-loss production cost that can justify a condition monitoring program.

1.3 Faults of Induction Motors and Their Detection

Possible induction motor faults are bearing faults, stator faults and rotor faults. The result of the survey [26] showed that bearing faults accounted for the majority of the failures, as much as 51.07%. Faults on stator windings and on rotor bars/rotor rings accounted to 15.76% and 4.7%, respectively. So together these three add to more than 70% of all faults that have led to a failure.

Bearings

The principal tools for condition monitoring of rolling-element bearing are temperature and vibration measurements Touch thermocouple or infrared thermography can be used to plot bearing temperature trends [2]. Vibration monitoring may be performed with hand-held detector/analysers connected to vibration transducers [4]. The periodic analysis of lubricant samples taken from the scavenge line ahead of the filter in a circulating oil system or from a static sump can provide valuable information on the bearing and lubricant condition [5] (This is only possible with sleeve bearings on very large motors).

Stator faults

Stator faults refer to insulation defects of the stator windings. Most large high voltage induction motors rated at 2.3kV and have stators with multi-turn coils. Partial discharge activity on the insulation can result in short-circuit turns, grounding fault or phase-to-phase faults [6]. Evolving stator winding faults can be identified by partial discharge testing. A recent and novel approach to this problem by Cash et al [140] uses an analysis of the three-phase line to neutral voltages of the motor. It is every effective, but requires a star-connected winding with the neutral accessible; most motors have delta-connected windings.

Early indication of winding failures of low voltage squirrel-cage induction motors can be given by an increase in winding vibration [7-8], magnetic flux analysis [7-9], monitoring negative sequence components [10], and unbalance of stator current [11].

An increasing number of low voltage motors use pulse-width modulated (PWM) drives for variable speed. High-switching-frequency steep-front pulses can be generated from such drives, which in conjunction with the line reflection, and inductive effect, may induce significant overvoltages and numerous harmonics inside the motor, and accelerate the insulation ageing [12].

Rotor faults

Rotor faults includes:

- open-circuit and short-circuit winding turns on a wound rotor motor,
- broken rotor bar and end ring for cage motor,
- static rotor eccentricity, and
- dynamic rotor eccentricity.

Rotor eccentricity can occur as static or dynamic and is usually present in even a new motor. The radial motion between the rotor and stator due to eccentricity causes variations of air gap length.

During starting, the centrifugal and magnetic forces on the cage rotor bars are high. When these combine with forces due to thermal expansion, they cause rotor bars to move slightly in the slots. This may cause fatigue cracking and result in a high-

resistance joint between the rotor bars and end rings.

Rotor faults are much more difficult to detect than bearing or stator faults because it is impossible to attach transducers directly to the rotor. Indirect measurement techniques are required. These faults can produce distinctive frequencies of the motor housing vibration, magnetic flux, and stator current, and may be detected by examining their frequency spectrum [13-21].

These fault-related frequencies should still be present when the induction motor is supplied at variable frequency, but their detection is much more complicated.

1.4 Maintenance and Condition Monitoring of the DC Motor

DC motors can have similar mechanical problems as AC motors, but the commutation process provides an extra problem: excessive sparking. This causes destructive blackening, pitting, and wear of both commutator and brushes. This results in the increase of brush-commutator contact resistance and a build up of conducting carbon dust between commutator segments. It further reduces the commutation ability of the DC motor. Severe failure to commutate can cause 'ring fire', that is arcing over the entire commutator periphery.

Excessive sparking can be due to poor commutation or an armature defect such as an open-circuit or short-circuit armature coil. A modern on-line monitoring technique is not available commercially for DC motors. So visual inspections of sparking and off-line inspection of the commutator surface conditions are still used [28], and probably are the only methods available in industry to assess DC motor condition.

1.5 Contribution of the Thesis

This thesis first examines electrical monitoring techniques to detect stator and rotor defects in an induction motor when it is supplied at variable frequency. Hardware and software methods to detect broken rotor bars have previously been attempted but with limited success [22]. An alternative method put forward here to compute the instantaneous input power of the induction motor from the two line-to-line voltages and two line currents. Examination of the frequencies present in the instantaneous

power can detect inter-turn short-circuits of stator winding, and broken rotor bars. In order to do this, specialised hardware has been developed, including clip-on current transformers.

Secondly, this thesis examines the effects of open-circuit and short-circuit armature coils, and poor commutation of DC motors. Because the conventional current transformer cannot be used for DC, and the electrical noise inside the control cubicle of a thyristor-controlled DC motor prevents successful operation of a Hall Effect clip-on ammeter, an air-core clip-on "Rogowski" coil was used instead to monitor fault-related frequencies in armature and field current. This was specifically designed for this job.

Thirdly, in order to study the effect of open-circuit and short-circuit armature coils, steady-state models for the DC motor were developed using inductively-coupled coil theory. Individual field, armature and faulty coils can be modelled, and the effect of faulty armature coil on the frequency components that are introduced into armature and field current can be predicted.

1.6 Organisation of the Thesis

Chapter 2 of this thesis gives a fairly detailed review of on-line condition monitoring techniques for induction motors. It includes the detection of rolling-element bearing faults, stator insulation defects and rotor faults.

Chapter 3 summarises the theoretical air gap flux distribution for an induction motor and the previous approaches of the work done on the detection of rotor damage with variable frequency drives. The difficulties of broken rotor detection with variable supply frequency are discussed.

Chapter 4 introduces a new method to detect the stator and rotor faults in which the instantaneous input power is computed from the two line-to-line voltages and two line currents. Theory is given, and an on-line monitoring system is described. Experimental results show that the frequency spectrum of the power signal provides much useful information in detecting fault frequency components, in variable speed drives.

Chapter 5 gives experimental results and examines the effect of incorrect interpole strength and armature defects, such as open- and short-circuit armature coils, on the armature and field currents of DC motors. In particular, the practical difficulties of current monitoring of DC motors are described.

Chapter 6 develops mathematical models for the DC motor under steady state operation in which each armature coil is modelled individually. In this way, both open-circuit and short-circuit armature coils can be realistically simulated and their effect on the armature and field current can be predicted.

Chapter 7 of this thesis provides a conclusion of the work that has been done and gives some suggestions for future work on the topic.

Chapter 2

Condition Monitoring Techniques for the Induction Motor

2.1 Introduction

Developments in motor monitoring techniques have progressed rapidly in the past decade. Some of the techniques are available commercially. This chapter gives a review of electrical monitoring techniques of induction motors. Vibration monitoring will be described in some detail because, although it is not an electrical parameter, there is a section later in this chapter that attempts to detect such faults by an electrical technique.

In order to select the appropriate parameters for condition monitoring, it is necessary to know the manner of motor failure. Faults that occur in induction motors may be divided into four main groups: bearing faults, stator faults, rotor faults, and others, such as shaft coupling, external devices, brush-gear and slip ring faults [23-27].

2.2 Motor Bearing Faults

Rolling-element bearings are normally used in the NEMA frame sizes of induction motors [28]. They have two rings, an inner and outer, between which a set of balls or rollers rotates in the raceways. The service life of a rolling-element bearing is determined by material fatigue and wearing of the running surfaces. Premature bearing failures can be caused by a large number of factors; the most common are fatigue, wear, plastic deformation, corrosion, brinelling, poor lubrication, faulty installation, and incorrect design [29-32]. Quite often there can be overlap between factors, or a bearing may start to fail in one particular mode that then leads on to other failure modes. When a small fissure appears at the surface of the raceway, continued use causes the affected area to expand rapidly, contaminating the lubrication and causing localised overloading over the entire circumference of the raceway. Rough running and failure of the bearing will eventually result.

Mechanical vibration is generated by the defective rolling-element. There are characteristic frequencies, which are related concisely to the bearing dimensions and the rotational speed of the machine. Vibration analysis is universally used to monitor these frequencies and hence to give warning of bearing deteriorations. It is very effective.

A paper by Filbert [33] described the routine detection of faults in the bearings of a universal motor for a washing machine by spectrum analysis of current. My interest in bearing problems was started by Scheon [34], who suggested that the stator current of induction motors could contain frequencies related to the vibrational frequencies. His experimental results illustrated that the frequency components in the stator current may be used to identify a bearing fault if it is severe enough. Because of these two cases where bearing faults are detected by looking at the spectrum of the motor current, the next subsections analyse the rolling-element bearing frequencies in some detail.

2.2.1 Bearing Fault Detection Using Machine Vibration Spectrum

Vibration analysis has been widely used for bearing fault detection and diagnosis. There are a number of transducer types existing for measuring vibration, including velocity transducers, accelerometers, microphones, and lasers. Smith [35] used lasers and microphones for non-contacting vibration measurement. The surface velocity of the machine is measured by the laser using the Doppler shifting principle. Surface acceleration can be derived electronically by differentiation of the velocity signal.

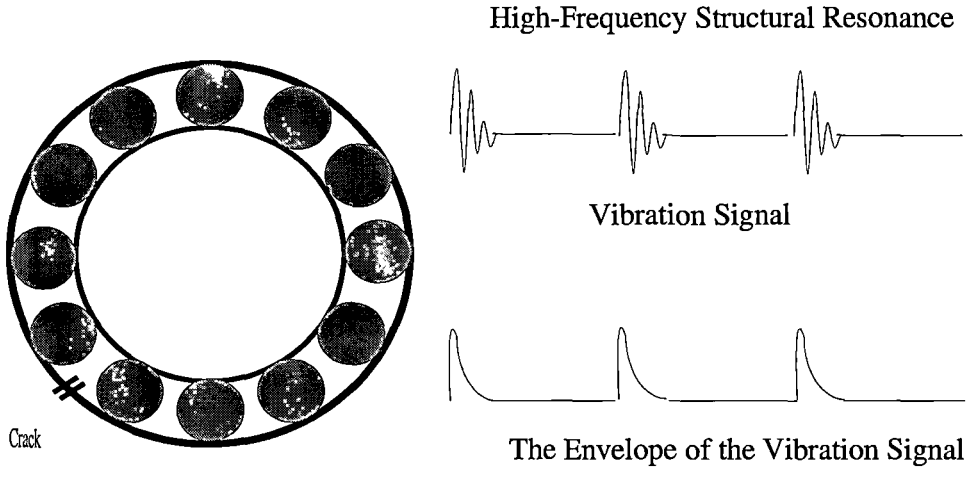

Figure 2.1: The outer race defect and the envelope analysis of vibration signal

The measurement of machine casing acceleration is the most common method of bearing fault detection [36]. An accelerometer is attached to or near the bearing housing. This will allow the bearing vibration to transmit readily through the structure to the transducer. When localised bearing faults occur, such as a crack in one of the races shown in figure 2.1, sharp impacts will excite structural resonance at its natural frequency. A high frequency damped oscillation occurs in the measured vibration signal at each impact. This gives rise to a series of very short "pings" which occur at the rate of the balls passing the defect. The resulting waveform is actually an amplitude-modulated waveform, ie the oscillating frequency is amplitude modulated by the pings. Spectrum analysis of this signal will give a component at the oscillating frequency of the race and there will be sidebands around it, spaced apart by the Ball Pass Frequency Outer. It is one of the characteristic bearing defect frequencies that

are based on bearing dimensions. These frequencies are summarised in table 2.1, where D is the pitch circle diameter of the bearing, d is the ball diameter, α is the contact angle of the rolling-element on the races, Z is the number of rolling elements, and f_{rt} is the shaft speed frequency. In practice, early detection of these frequencies in a machine vibration spectrum is very difficult. The oscillating frequency is too high (often 5kHz to 10kHz) to pick up reliably and the sidebands are usually marked by the background noise level.

Bearing Element	Frequency Equations
Inner race defect : Ball Pass Frequency Inner	$f_{bpfi} = \frac{-Zf_{rt}\left(1+\frac{d}{D}\cos\alpha\right)}{2}$
Outer race defect : Ball Pass Frequency Outer	$f_{bpo} = \frac{-Zf_{rt}\left(1-\frac{d}{D}\cos\alpha\right)}{2}$
Defective Roller : Cage Rotational frequency	$f_c = \frac{f_{rt}\left(1-\frac{d}{D}\cos\alpha\right)}{2}$
Ball Spin Frequency	$f_{bsf} = \frac{-f_{rt}D\left(1-\left(\frac{d}{D}\cos\alpha\right)^2\right)}{2d}$

Table 2.1: Summary of the general bearing defect frequency equations

Envelope analysis or Demodulated technique is one of the prominent signal processing techniques for early detection of rolling element bearing faults [37]. This technique enables the high frequency oscillation of the bearing race to be separated from the rest of the characteristic bearing defect frequencies. The vibration signal obtained from the accelerometer is passed through a high pass filter with a corner frequency of 2kHz. This filter removes all the low frequency components due to rotation, and effectively isolates the modulated natural frequencies. This waveform is then demodulated to obtain the envelope. Figure 2.1 illustrates the outer race defect and the Envelope analysis of the vibration signal. Spectrum analysis of the resultant signal will produce a prominent fundamental component and its harmonics at the Ball Pass Frequency Outer. The bearing type must be known to specify the bearing fault frequencies. Most commercial monitoring systems have a library of bearing

numbers for reference that allows very accurate diagnosis.

2.2.2 Spectrum Analysis of Stator Current for Bearing Damage Detection

Schoen et al. [34] have investigated the feasibility of detecting bearing faults using spectrum analysis of stator current of an induction motor. Any mechanical displacement resulting from the damaged bearing causes the air gap of the motor to vary in a manner that can be described by rotor eccentricity. Hence, these variations generate stator current at predictable frequencies, f_{bf}, related to the vibrational and electrical supply frequency. Let f_{bdf} be the characteristic bearing defect frequency summarised in table 2.1,

$$f_{bf} = \left| f_1 \pm \mathrm{m} f_{bdf} \right| \tag{2.1}$$

where f_1 is the supply frequency and m = 1, 2, 3, ...

As an example, bearing fault frequencies were detected during tests in industry. Vibration monitoring is carried out by maintenance engineers in ANM Boyer. Figure 2.2 shows a vibration spectrum of a three-phase, 415V, 350HP, 1478rpm, induction motor (No. 15-1853 in ANM, Boyer) coupled via a gearbox to a vacuum pump. The bearings that associate with the system are MRJ4.5EM (motor bearings), SKF22218 (bearings of gearbox), and TMK 67700 (bearings of the pump shaft). "E" highlights where the Ball Pass Frequency Outer (BPFO, outer race defect frequency of the specified bearing by the commercial monitoring systems) and its harmonics of the motor bearings (158.8Hz and its multiples) should be.

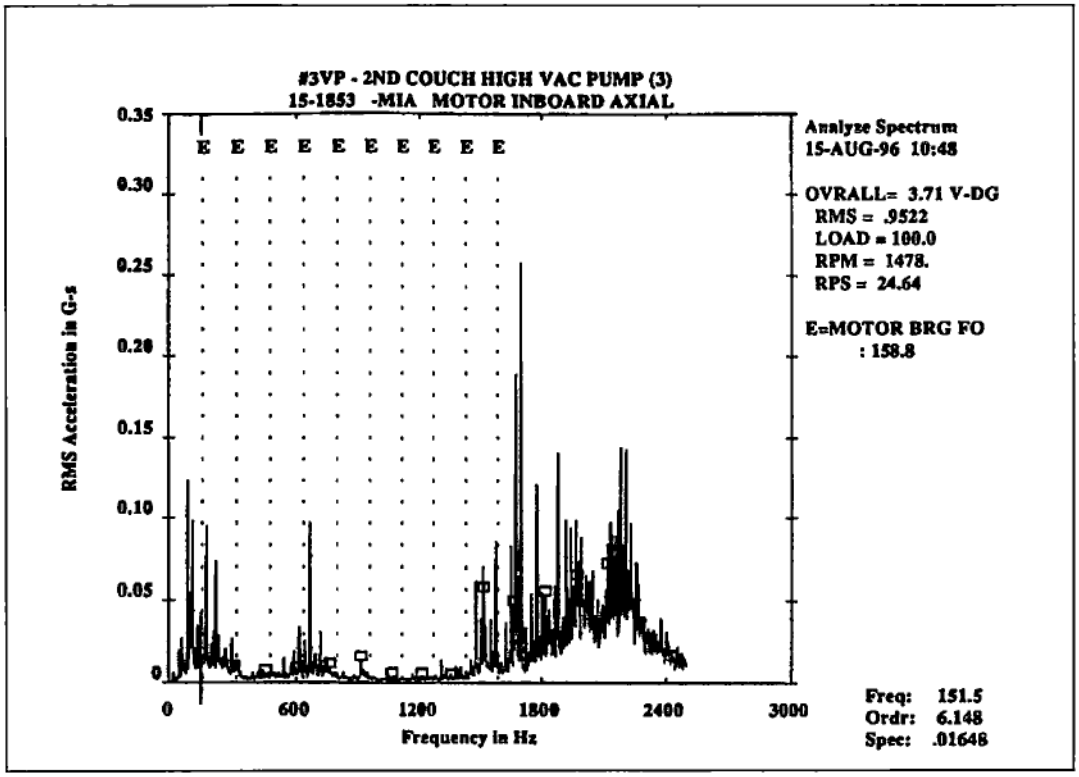

Figure 2.2: Vibration spectrum of motor 15-1853

The defect frequencies are not significant at this measurement. It only shows a few running speed harmonics and a low level noise floor at low frequency range. Significant vibration energy can be found around the 2kHz range. The prominent component at about 1600Hz is due to the rotor slots.

The vibration signal was passed through a 2kHz high-pass filter and demodulation was carried. Figure 2.3 shows the corresponding frequency spectrum of the demodulated signal. It shows the actual BPFO of the motor bearings at 151.4Hz (well above the reference noise floor) and its second harmonic as well. Running-speed-related harmonics are also indicated in the demodulated spectrum.

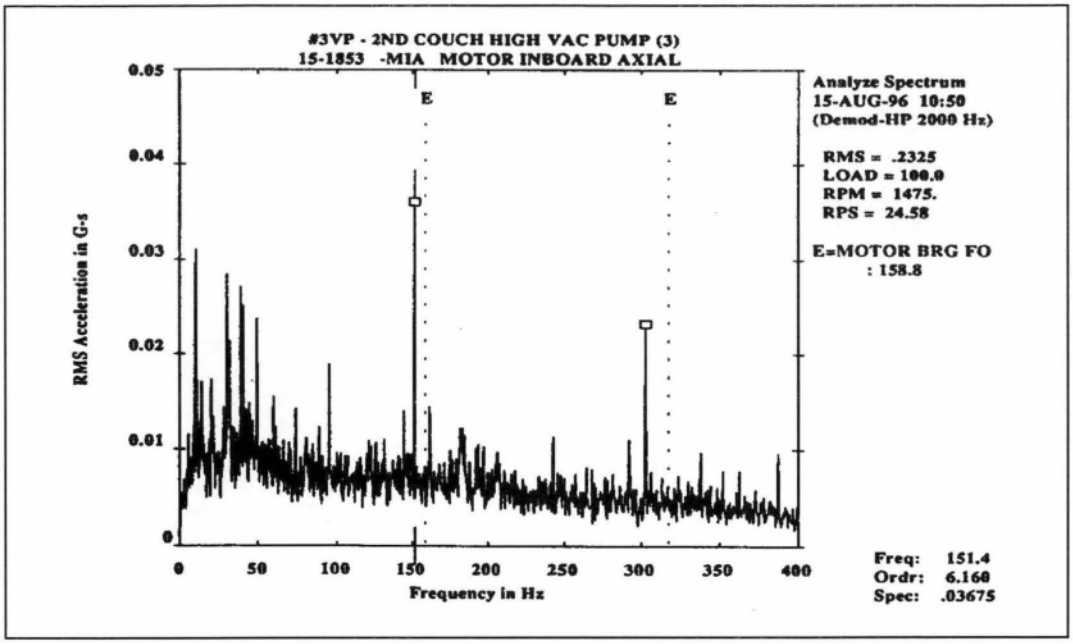

Figure 2.3: Demodulated spectrum of the vibration signal of motor 15-1853

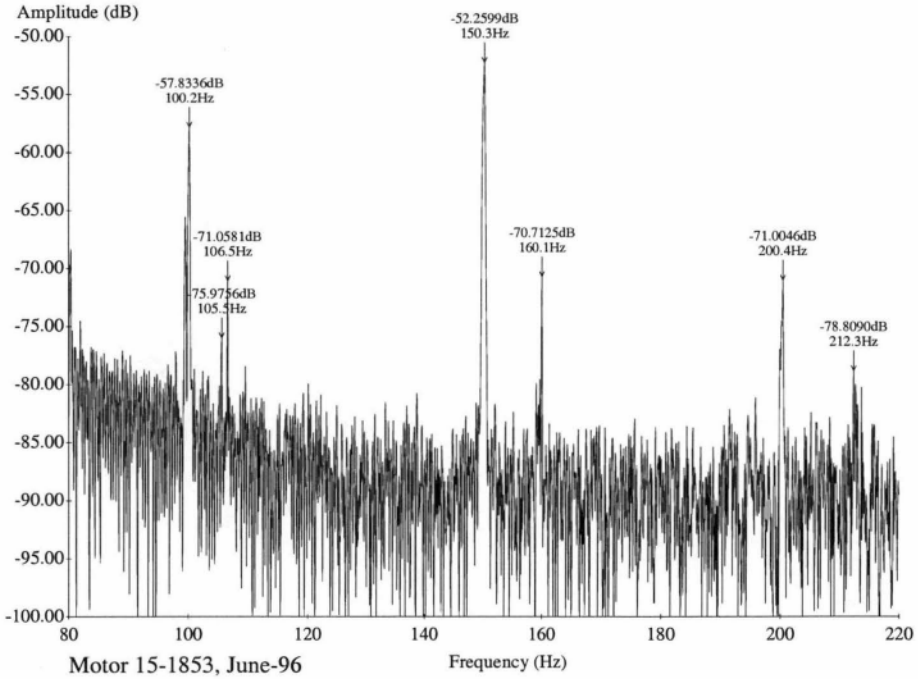

Figure 2.4: The spectrum of the stator current of motor 15-1853

From Schoen's analysis, in this case, the frequency components in stator current spectrum corresponding to the BPFO in the vibration signal is at $|151.4 \pm 50|$ Hz, ie

201.4Hz and 101.4Hz. The corresponding stator current was monitored with the clip-on ammeter. The waveform was sampled at 5kHz and 65536 data were captured. Figure 2.4 shows the spectrum of the stator current. Significant time harmonics can be found at 100.2Hz, 150.3Hz and 200.4Hz. We could not detect any frequency components related to BPFO.

For the experiment conducted by Schoen, the outer race defect was simulated by drilling a hole through the outer race of the shaft-end bearing of the tested motor. The sharpness of the impact so produced is much higher than would occur in a "normal defect". In practice, at the early stage of the defect, before the localised damage on the race surface occurs, the sharpness of the impact is much lower. The amplitude of the defect frequency is very small in the original vibrational spectrum. The mechanical displacement caused by the outer race defect is not significant and neither is the air gap variation. The amplitude of the frequency components related to the vibrational characteristic frequency is well below the noise level of the stator current spectrum.

2.3 Stator Insulation Defects

The condition of the insulation system is a function of thermal, electrical, environmental and mechanical factors plus the type of duty of which the motor is subjected. In normal service, turn insulation failure can be precipitated by voltage surge-related puncture, partial discharge deterioration, and long-term degradation [6]. However, it is possible for partial discharge deterioration alone to cause winding failure.

Most large high voltage induction motors have multi-turn coil stators. The insulation system for such a coil consists of the groundwall insulation and the strand and turn insulation. If voids occur within the insulation due to manufacturing defects, or due to the capacitive voltage division effect, some voltage will be placed across these air pockets. If the voltage is high enough, the electric stress will be higher than the breakdown strength of air and a spark will occur in the air pocket. The spark is

stopped by the solid groundwall insulation, but repeated sparking will gradually erode a hole in the insulation. This process is called partial discharging [38].

At rated voltage, partial discharge activity internal to the insulation adjacent to conductor or in the bulk of the groundwall will become serious if the strands of the conductor become loose. Partial discharge activity on the outside of the groundwall insulation in the slot area can lead to high intensity slot discharge, which can rapidly erode the groundwall of stator insulation [39-41].

The integrity of high-voltage motor stator windings is checked partly on the basis of a partial discharge test with the motor shut down. It requires a lengthy testing outage, and therefore may be inconvenient to perform frequently [28]. An improvement is reported by Sedding et al. [42], who developed an on-line partial discharge test system that can be performed by non-specialised maintenance personnel.

For low voltage motors on mains frequency supplies, the partial discharge effect is insignificant. Increase in winding vibration and negative-sequence components of voltage and current can give an indication of stator defects [1,10].

Natarajan studied the winding insulation failure of a three-phase induction motor by sensing the residual stator current [11]. To do this, the three-phase conductors are passed through a current transformer and a current will flow in the current transformer secondary.

The use of insulated-gate bipolar transistors (IGBT) in variable frequency drives allows the drives to produce high frequency (close to 20kHz), steep-front voltage pulses (2500V/μsec [42]). Such a fast-rise time surge lead to complex propagation processes in the stator windings. The effect of this on the insulation is the major concern. For example, Persson et al. [43] simulated the PWM inverter voltage amplitudes and rise times. Possible problems with long motor cables and short rise times were discussed. High-frequency radiation [44] and inductive effect [45] has also been considered.

The overall effect is that the insulation of the stator winding is subjected to increased

dielectric stress. The key point is that the original motor design for operation on sinewave 50Hz (or 60Hz) will have significantly reduced dielectric life [46-47]. The higher voltage from PWM supplies could result in partial discharge [42].

In general, stator winding defects rapidly become complete failure of the insulation, and are immediately detected by motor protection circuitry.

2.4 Rotor Eccentricity

There are two types of rotor eccentricity: static and dynamic. Static eccentricity is where the rotor is displaced from the stator bore centre but is still turning upon its own axis. The air-gap length varies only with position around the bore and is independent of movement. Dynamic eccentricity is where the rotor is turning upon the stator bore centre but not on its own centre. The air-gap length varies with both position and rotor movement [51]. The either type of rotor eccentricity may be caused by incorrect bearing position during assembly, worn bearings, bent rotor shaft, or misalignment between the rotor and mechanical load [50, 56]. Eccentricity causes a force on the rotor that tries to pull the rotor even further from the stator bore centre. In the case of static eccentricity, this is a steady pull in one direction, while dynamic eccentricity produces an unbalanced magnetic pull (UMP) on the rotor, and rotates at motor speed. Both cause the stator harmful vibration and further increases bearing wear. It is also feasible for a rotor-to-stator rub to occur with severe damage to the core, stator insulation and even breaking of rotor cage bars and end rings [51-54].

Stray flux and axial flux can be used to monitor these defects. Any distortion in the air gap flux due to these defects will change the flux pattern [7-9]. Verma and Natarajan [58] studied the changes in the air gap field as a function of static eccentricity using a search coil in the stator core. Ellison and Yang [57] verified from tests that slot harmonics in the acoustic noise spectra were functions of static eccentricity.

Spectrum analysis of line current can be used to detect air-gap eccentricity in three-phase induction motors [13-15,17,20,48-49]. Thomson [50] has reported that even

purely mechanical problems in induction motor drives may be detected by monitoring the low-frequency sideband components of the line current. Boyle et al. [56] showed that dynamic air gap eccentricity and misalignment between the motor and mechanical load can induce distinctive frequencies in the current.

Dorrell et al. [55] developed a model to determine the unbalanced magnetic pull (UMP) produced in induction motors with an eccentric rotor. The model used the conformal transformation technique coupled to a winding impedance approach. He showed that the static UMP reduces significantly by using parallel paths in the stator windings. The influence of rotor skew on the UMP with dynamic rotor eccentricity was considered [53]. They also investigated the combined effect of static and dynamic eccentricity on induction motors [57]. A theoretical analysis was given to show that both static and dynamic eccentricity is present as sideband components on the supply frequency in current. The degree of static and dynamic eccentricity and the motor load have large influence on the amplitude of these sideband components [52].

2.5 Open and Short-circuit winding turns of Wound Rotor Motors

Wound rotor motors can have defects in brazed joints and slip-ring connections. Overheating of the rotor can also be caused by current unbalance in the external resistors connected to the slip-rings. The problem is difficult to detect because the rotor currents are at very low (slip) frequency. Ellison et al. [61] used an air-core wound around the cables to the external resistors from the slip-rings to measure the residual rotor current. Kamerbeek [62] used a search coil fixed to the stator to detect rotor defects, but had difficulty fitting a sensor on industrial motors.

2.6 Broken Rotor Bar Detection of Cage Rotor Motors

The last type of rotor-related fault, which only occurs in cage rotor motors, is a broken rotor bar. The centrifugal and magnetic forces on the rotor bars are very high during starting. When they combine with the forces due to thermal expansion, rotor

bars may move slightly in the slots. This may cause cracking to occur between the rotor bars and end rings, resulting in a high resistance joint. The heating caused by this can result in further damage to the bars and end rings as well as to the laminations.

Early indications of the broken rotor bar are pulsations in the motor speed. Gaydon [64] has shown that the double slip-frequency variation in rotor speed caused by broken rotor bars can be detected by a shaft-coupled speed transducer [65]. Other techniques such as vibration monitoring [14], single-phase power monitoring [66], electromagnetic torque monitoring [67-68], rotor temperature monitoring [69] and model-based parameter estimation [70-72], have been used.

There has been considerable research on stator current monitoring for early detection of broken rotor bars [13-21, 33]. Most relies on the fact that a broken rotor bar produces unbalanced impedance in the rotor. This results in a disturbance in the air gap flux pattern, which in turn is linked into stator flux and current, and produces additional frequency components in the stator current. Hargis et al. [73] have shown that the double slip-frequency modulation of the stator current due to broken rotor bars can be detected using spectrum analysis. Figure 2.5 shows a typical stator current spectrum with upper and lower sideband [65].

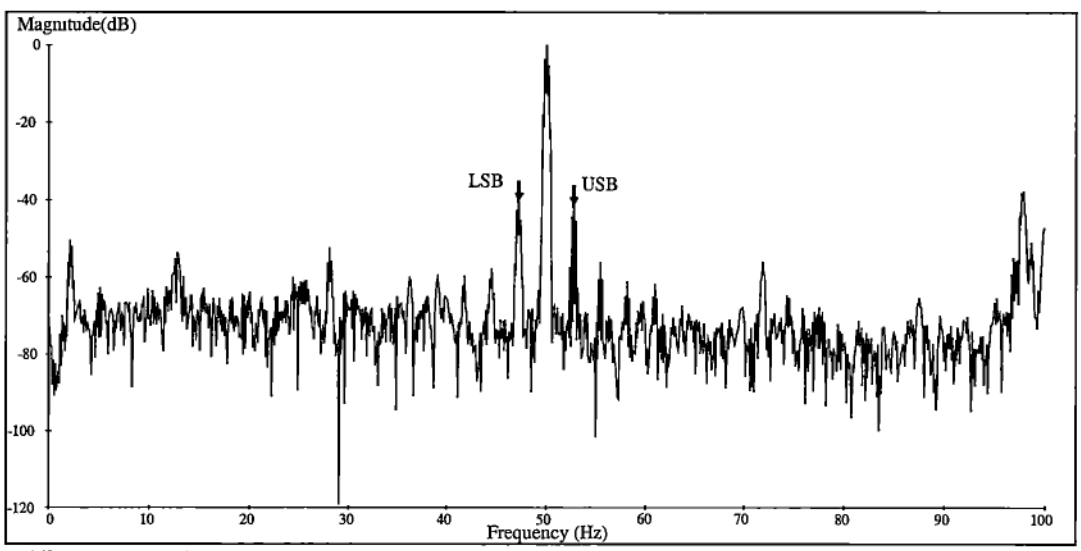

Figure 2.5: Typical stator current spectrum showing upper sidebands and lowers sidebands [65]

Hargis and Gaydon [73] were the first predict the number of broken rotor bars theoretically from the current spectrum and detail basic motor design. Thomson [16] studies this experimentally and found that the case histories from industry suggested that analysis from [73] underestimates the number of broken rotor bars.

Kliman et al. [76] developed a computer-based instrument to detect these. The diagnosis is based on an analysis by Deleroi [77]. This instrument is sensitive enough to detect the presence of a single broken, or even cracked, bar while the motor is running at full load. Chapter 4 discusses these in more details.

Elkasabgy et al. [74] did a finite element model of the flux pattern in a motor with a damaged rotor bar. The model predicted the resulting torque. They also tried several methods of detecting the rotor damage, on a real motor including measurement and analysis of voltage induced in internal stator tooth tip search coil, and an external search coil placed against the motor frame, measurement and analysis of stator current and shaft torque.

Tavner et al. [75] developed a portable Induction Motor Current Analyser (IMCA) to monitor the stator current. The input probe of the analyser can be clipped directly onto the supply cable of the motor. The signal from the probe is digitised and a spectral analysis is carried out over a narrow band close to the supply frequency using a digital heterodyne and Fast Fourier Transform. The spectrum is then searched for the additional frequencies. The interpretation of the result is shown on a display that can also give warnings. The process is fully automatic.

Different motor theoretical models allow rotor faults to be modelled, and to quantify the amplitude of the fault related frequency components in the stator current. Vas et al. [89] established a transient model in the rotor reference frame with rotor asymmetry. He concluded that the information on broken rotor bars obtained from current during a transient test is restricted. The detection of spectrum line in the steady state current is more effective. Paterson et al. [90] developed a finite element model based on a test rig to allow rotor faults to be modelled. The predicted amplitude of the double slip-frequency sideband components is two to three times

higher than the measurement although speed ripple and the non-linear characteristic of the core material were accounted. Fiser [91] presented a d-q model in rotor reference frame with higher space harmonics and rotor defects taken into account. The influence of rotor cage defects on torque and current at different slip is simulated, but no conclusion on the amplitude of the rotor fault-related frequencies in current were made. Manolas [92] developed a magnetically coupling coil model for transient and steady state operation. Only simulation result of motor speed and torque in transient operation was present.

2.7 Condition Monitoring of Induction Motors with Variable Supply Frequency (Stator and Rotor Faults)

The popularity of adjustable speed AC drives in industrial applications is increasing rapidly and it is obvious that our research should explore these. Thomson [93] was the first to give an overview of the detection of broken rotor bar with variable speed drives. Cardoso and Saraiva [94] used an image pattern recognition method to identify the faults in a current source inverter-fed induction motor. They calculated the two-phase Park's vector of the supply voltage, current and flux and displayed the locus of these vectors on an oscilloscope. They showed that the stator winding inter-turn short-circuits and open-circuit wound rotor fault could be detected through the changes in the patterns displayed. They did not apply the method on cage rotor motors.

Thian [96] published a Ph.D. thesis on methods of condition monitoring of variable frequency induction motors. He analysed the interactions of the fault frequencies and the extra supply harmonics caused by the variable drive. The use of sequence components as a monitoring tool of electrical drives was developed. He also considered monitoring of current, vibration and axial flux for the detection of stator and rotor faults and concluded that different types of faults have different degrees of influence upon these parameters.

Innes [22] examined the detection of a rotor bar defect in an induction motor

controlled by a variable speed drive, when the drive output frequency varies. He used synchronous sampling hardware, and several-advanced signal processing techniques to detect the fault-related frequencies in the stator current. He also developed a mathematical model of the induction motor based on coupled-coil theory. PWM voltage waveforms were applied and stator current and its spectrum were calculated. The effects of broken rotor bars were included.

Chapter 3

Stator Current Frequency Analysis for the Induction Motor

3.1 Introduction – frequencies that could be present in the motor current

The current-based condition monitoring system of the induction motor is popular because of its relatively simple implementation [16-17,74-76]. Current can be measured from the motor control cabinet by clamping a current transformer or Hall effect transducer around the motor supply cable. There is no need to directly access the motor.

There are many other frequency components that may be present in the stator current spectrum. It is important to know as much as possible about the motor and the driven load to determine precisely which is important to indicate the condition of the motor or the driving mechanism. This chapter presents the formulae to predict the extra frequencies of an induction motor current [48,76-77] due to air gap variations and rotor defects. The theoretical predictions of broken rotor bar number [16,73,76-77] are verified by experimental results from a laboratory motor with deliberately

damaged rotors. The remained of section 3.1 describes how many of these frequencies are produced. Later sections of the chapter give the associated theory.

The waveform of the stator current contains a fundamental frequency of 50Hz (f_s) plus integer multiples of 50Hz. These components are always present in the supply. However, the motor often adds other frequencies. Any variation in load torque can also affect the current. If the mechanical system is linear, the torque developed by the induction motor contains all the frequency components (f_L) of the load torque. Bearings, belts or chains, coupling, and gears may cause this torque oscillation. In most cases, the amplitude is low. However, any detectable amplitude will cause the stator current to be modulated by f_L and thus contain components at $f_s \pm mf_L$, where m is an integer.

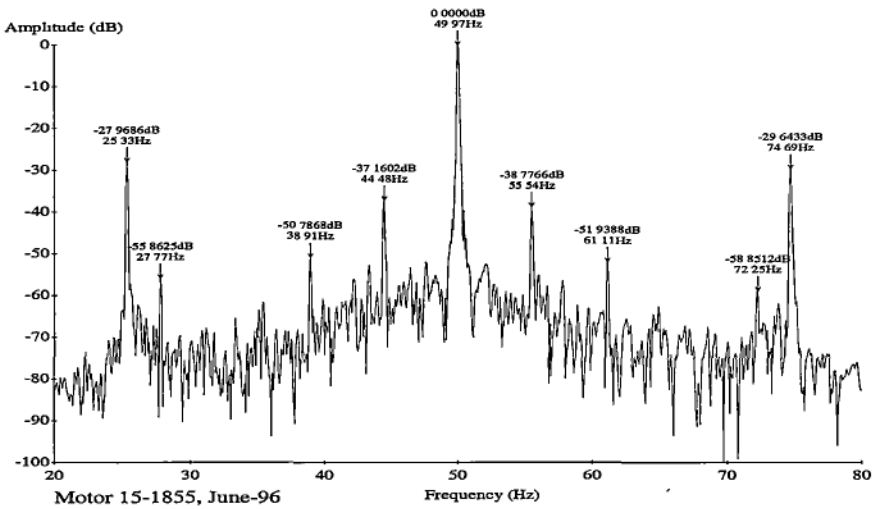

Figure 3.1 Current spectrum of a 350HP motor

For example, figure 3.1 shows the stator current spectrum of a 350HP, 415V, 1475 rpm motor (No. 15-1855 in ANM Boyer) driving a pump load through a 27:120 tooth gear box. The zero dB frequency is the fundamental 50Hz component. The rotational or speed frequency of the motor is 24.58Hz. Slight variations in the torque of the pump show up as multiples of the pump speed frequency $f_L = 24.58 \times (27 \div 120) = 5.53\text{Hz}$. These reflect back into the motor, and oscillate its torque at 5.53Hz. The expected sidebands of the fundamental supply current are summarised in table 3.1. All predicted frequencies except $f_s \pm 3f_L$ are visible. The

large magnitudes at 25.33Hz and 74.69Hz are the result of rotor eccentricity.

$f_s \pm f_L$	$f_s \pm 2f_L$	$f_s \pm 3f_L$	$f_s \pm 4f_L$
44.47 Hz	38.94 Hz	33.41 Hz	27.88 Hz
55.53 Hz	61.06 Hz	66.59 Hz	72.12 Hz

Table 3.1: The sidebands of the fundamental supply current of motor 15-1855

The magnetomotive force (MMF) produced by the current flowing in the stator and rotor windings consists of a series of space and time harmonics. Variations of the machine's air gap are caused by factors such as stator and rotor slots, and by radial motion between the rotor and stator due to rotor eccentricity. These show up as corresponding variations in the air gap flux and hence affect the stator current [48,97].

Rotor defects may be detected by the presence of particular frequency components in the spectrum of the stator current. For example, a broken rotor bar causes unbalanced impedance in the rotor circuit and results in a disturbance in the air gap flux pattern, which then causes additional frequency components in the stator current.

Fault-related frequencies should still be present in the stator current waveform of induction motors supplied with variable frequency; however, their detection is more complicated because the supply frequency is no longer constant. Essentially, it is a problem of dealing with a "non-stationary" signal. "Non-stationary" implies that the fundamental frequency varies during the sampling period. Not much research has apparently been done on condition monitoring of motors supplied with variable frequency. As the use of variable speed drives is increasing, it would seem pertinent to explore the subject. Sections 3.6 to 3.8 give a summary of previous approaches to the problem associated with variable supply frequency and the distorted voltage and current waveforms associated with commercial power electronic devices.

3.2 Variations of Air Gap

Variations of the motor air gap are caused by rotor and stator slots, and by radial motion between the rotor and stator due to rotor eccentricity. These show up as

corresponding variations in the magnetic flux in the motor, which in turn reflect back to the stator current. Cameron [48] has given an analysis based on calculation of the magnetic flux variations frequencies in the air gap from the product of permeance and MMF. His results for the extra frequencies are

$$f_{ag} = \left\{ (n_{rt} R \pm n_{de}) \frac{(1-s)}{pp} \pm 2n_{sa} \pm n_{\omega s} \right\} f_s \tag{3.1}$$

where f_s is the supply frequency in Hz, s is the per unit slip, pp is the number of pole-pairs, R is the rotor slot number; n_{rt}, n_{de}, n_{sa} and $n_{\omega s}$ are integers. The subscript rt denotes the rotor slot, de denotes the dynamic rotor eccentricity, sa denotes the saturation and ωs denotes the stator time harmonics.

Obviously equation (3.1) produces many additions and subtractions of frequencies. It is important to note that the layout of the stator winding, and its distribution factors and coil span factors, will have a very significant effect on which frequencies will actually appear in the current. Also, these harmonics are often present in the stator current in even a "good" motor. They are typically of amplitude less than 1% of the fundamental but can be detected reliably and accurately. A change in their amplitudes relative to the fundamental obviously indicates a change inside the motor.

3.3 Prediction of Broken Rotor Bars

Analysis from previous research work [13,73] has shown that the stator current variation due to rotor defects produced sidebands at $\pm 2sf_s$ around the fundamental supply current frequency f_s. Hargis and Gaydon [73] first tried to quantify the number of broken rotor bars by the following equation:

$$R_s \approx \frac{\sin(\alpha)}{2pp(2\pi - \alpha)} \tag{3.2}$$

where $\alpha = \frac{2\pi npp}{\mathrm{N}}$ for n contiguous broken rotor bars and with $n << \mathrm{N}$

R_s is the ratio of the amplitude of the lower sideband at $(1-2sf_s)$ to the amplitude

of the fundamental frequency f_s, pp is the number of pole-pairs of the stator windings, and N is the number of rotor bars.

The dB version of equation (3.2) can be determined as [16,98]

$$n = \frac{2N}{10^{\frac{R_{dB}}{20}} + 2pp} \tag{3.3}$$

where R_{dB} is the dB difference between f_s component and the lower sideband component at $(1-2s)f_s$.

Thomson [16,18] used equation (3.3) to check for one broken bar. He verified experimentally that equation (3.3) underestimates the number of broken rotor bars by 40 % lower than the actual number. He considered the effect of varying motor load on the prediction of broken rotor bar number and also verified that the double slip-frequency sideband around the slot harmonics can indicate rotor fault.

Kliman et al. [76] examined the frequency spectrum of the line current and based their diagnosis on predictions from an analysis by Deleroi et al. [77]. Their analytical expression for the frequencies that are present in the air gap flux is

$$f_{bb} = \{n_{\theta r}(1-s) \pm n_{\omega r} s\} f_s \tag{3.4}$$

where $n_{\theta r}$ is the order of the rotor space harmonics and $n_{\omega r}$ is the order of rotor time harmonics (both are integers). They pointed out that it is possible to use the $(1-2s)f_s$ component as a criterion of rotor health. A computer-based instrument was developed. It performs two basic functions, signal processing and implementing the decision algorithm, to convey the status of the rotor cage to the operator. Two different sets of decision rules are implemented in the decision algorithm:

(1) The trending decision algorithm

The instrument is set up to compare two tests run on the same motor at different time. The decision rules are:

- If the change of $(1-2s)f_s$ is less than 20 dB, the tested motor is declared to be in as good condition as it was at the time of the previous test.

- If the change of $(1-2s)f_s$ is larger than 20 dB, than the $(1+2s)f_s$, $(1\pm 2ns)f_s$ and the double slip-frequency sidebands around higher time harmonics are examined. Any of them have changed significently, a 'broken bar' is declared.

(2) The single test algorithm

This algorithm allows one to determine the presence of broken bars from a single test. The criterions are:

- If $(1-2s)f_s$ < -60dB (relative to 50Hz), the tested motor probably has no rotor fault.

- If $(1-2s)f_s$ > –54dB, there is probably a cracked rotor bar.

- If $(1-2s)f_s$ > -50dB, there is probably a broken rotor bar.

The relative amplitude of double slip-frequency sidebands centred on higher time harmonics is also examined (equation (3.4)). If these have increased by at least 10dB, relative to the value when the motor was known to be in good condition, then it is more certain that there is rotor damage. The authors made no attempt to estimate the number of broken rotor bars.

3.4 The Effect of Broken Rotor Bar on Frequency Harmonics caused by Rotor Eccentricity and Slot Harmonics

The analysis is based on Penman's paper [9], in which a master table was established for all extra frequency components induced in the stator current due to different unsymmetrical fault types.

The classical theory predicts that the variation of the air gap flux density caused by rotor eccentricity can be expressed in the stator reference frame [98] as

$$B_s(\theta_s, t) = B_1 \cos\left[\left(\frac{1-s}{pp}+1\right)\omega_s t - pp\theta_s\right] + B_2 \cos\left[\left(\frac{1-s}{pp}-1\right)\omega_s t + pp\theta_s\right] \quad (3.5)$$

where θ_s is an angle between the stator datum and an arbitrary point on rotor and $f_r=(1-s)f_s/pp$ is the speed frequency. These $(f_s \pm f_r)$ components create an air gap disturbance whose frequencies may be the same as with the broken bar. For example, the $(f_s \pm f_r)$ components of a 4.5kW, six-pole three-phase induction motor operating at 0.04 per unit slip, will be "submerged" with $(1 \pm 8s)f_s$ components.

Let θ_r be an angular separation between an arbitrary point on rotor, with respect to the rotor datum, where

$$\theta_r = \theta_s - \frac{1-s}{pp}\omega_s t \quad (3.6)$$

Equation (3.5) can be transferred to the rotor reference frame by substituting equation (3.6) into (3.5) to give

$$B_r(\theta_r, t) = B_1 \cos\left[\left(\frac{1-s}{pp}+s\right)\omega_s t - pp\theta_r\right] + B_2 \cos\left[\left(\frac{1-s}{pp}-s\right)\omega_s t + pp\theta r\right] \quad (3.7)$$

Asymmetry on the rotor introduces components in the air gap flux density that can be expressed as

$$B_r(\theta_r, t) = \frac{1}{2}\left\{\begin{array}{l} B_1 \cos\left[\left(\frac{1-s}{pp}+s\right)\omega_s t \mp pp\theta_r\right] + \\ B_2 \cos\left[\left(\frac{1-s}{pp}-s\right)\omega_s t \pm pp\theta r\right] \end{array}\right\} \quad (3.8)$$

Transfers equation (3.8) back to the stator reference frame by substituting (3.6) into (3.8) gives,

$$B_s(\theta_s,t)=\frac{1}{2}\left\{\begin{array}{l} B_1\cos\left[\left(\frac{1-s}{pp}+1\right)\omega_s t-pp\theta_s\right]+ \\ B_1\cos\left[\left(\frac{1-s}{pp}-1+2s\right)\omega_s t+pp\theta_s\right]+ \\ B_2\cos\left[\left(\frac{1-s}{pp}-1\right)\omega_s t+pp\theta_s\right]+ \\ B_2\cos\left[\left(\frac{1-s}{pp}-1-2s\right)\omega_s t+pp\theta_s\right] \end{array}\right\} \tag{3.9}$$

If the time harmonics are taken into account, in general the extra frequencies of the air gap flux density are given as

$$f_{be}=\left\{n_{\theta s}\frac{1-s}{pp}\pm n\omega s\pm 2n_{be}s\right\}f_s \tag{3.10}$$

where n_{be} is positive integer and $n_{\omega s}$ is the order of the time harmonics.

Table 3.2 illustrates the extra frequency components that are caused by the effect of broken rotor bar on the $(f_s \pm f_r)$ with the third and fifth time harmonics taken into account.

The analysis is equally applicable to the slot harmonics. In general, a corresponding set of extra harmonics could therefore be expressed as

$$f_{bs}=\left\{\frac{R(1-s)}{pp}\pm n_{\omega s}\pm 2n_{be}s\right\}f_s \tag{3.11}$$

where R is number of rotor slots.

n_{be}	Frequency factor
1	$[(1-s)/\ pp]+1$
	$[(1-s)/\ pp]+1+2s$
	$[(1-s)/\ pp]-1$
	$[(1-s)/\ pp]+1-2s$
3	$[(1-s)/\ pp]-1+2s$
	$[(1-s)/\ pp]+1+2s$
	$[(1-s)/\ pp]+1-4s$
	$[(1-s)/\ pp]-1-2s$
5	$[(1-s)/\ pp]-1+6s$
	$[(1-s)/\ pp]+1+4s$
	$[(1-s)/\ pp]+1-6s$
	$[(1-s)/\ pp]-1-4s$

Table 3.2: The effect of broken bar on $(f_s \pm f_r)$ components

3.5 Test Results of a 4-pole 7.5kW Laboratory Motor with Mains Supply and Zero, One, or Two Broken Rotor Bars

In order to monitor one phase of the stator current, a Hall effect clip-on ammeter was used (Appendix A4.1). The voltage from the ammeter (proportional to the current, and of sensitivity 1mV per ampere) was amplified and filtered to remove high frequencies that may be aliased when sampling. The output of the filter was sampled at 5kHz, digitised with a 12 bit ADC (Appendix A5). 65536 samples are captured for each measurement and result stored in a portable computer.

Motor speed was initially estimated by assuming that slip is proportional to power, and that power is proportional to current as long as the motor is at more than 50 % full load. (The rating plate gives speed at rated load). The estimated speed and the rotor slot number were used to establish the frequency range in which to search for the rotor slot harmonics. Slip and speed of the motor were then recalculated much more accurately and finally the double slip frequency components could be located confidently.

The motor under test was a three phase 7.5kW Pope motor with 32 rotor slots (Appendix A1.1). It had a good rotor and two deliberately damaged rotors. One of the

damaged rotors had one bar cut through at the end ring and the other had two adjacent cut rotor bars. It was mechanically loaded by a DC generator and resistor combination. Experimental tests were conducted at 0.0273 per unit slip with the good rotor, 0.0297 per unit slip with the one cut bar rotor, and 0.0292 per unit slip with the two cut bars rotor.

The frequency spectra shown in figures 3.2, 3.4, 3.6, and 3.8 show the double slip-frequency sideband components around the supply frequency, third, fifth, and slot harmonics with the good rotor. The double slip-frequency sideband components $(1\pm 2s)f_s$ and $f_s \pm f_r$ sidebands exist at 47.23Hz with –52.9dB and 52.72Hz with –54.8dB; and 25.63Hz and 74.31Hz with –66.86dB and –65.96dB. The third harmonic and its $\pm 2nsf_s$ sidebands are very small amplitude compared to the fifth harmonic, as would be expected for a delta-connected motor, shown in figures 3.4 and 3.6. Figure 3.8 shows the fundamental slot harmonic and its $\pm 2sf_s$ sideband components at 827.6Hz, 824.9Hz and 830.3Hz respectively.

Figures 3.3, 3.5, 3.7, and 3.9 show the current spectra of the same motor but with the one cut bar rotor. The $(1\pm 2s)f_s$ components have the largest amplitude, as shown in figure 3.3 at 47.00Hz and 52.9Hz with –47.3dB and –45.2dB (increased by 5 and 10 dB respectively) while the $(1\pm 16s)f_s$ sideband components (at 26.17Hz and 73.78Hz) do not change significantly. The change of the amplitude of the upper sideband component is less than the lower sideband. The upper sideband results from the third harmonic of the supply and speed oscillations [131], which may cause the less change in amplitude of the upper sideband component with rotor fault.

Another interesting result at the supply frequency range is the $\pm 2nsf_s$ sidebands around the $f_s \pm f_r$ components, shown in figures 3.10 and 3.11. Significant peak can be found at 28.69Hz $(f_s - f_r - 2sf_s)$, 71.26Hz $(f_s + f_r - 2sf_s)$, and 77.21Hz $(f_s + f_r + 2sf_s)$. It can be noticed that these components are located closely to the $\pm 14sf_s$ and $\pm 16sf_s$ sideband components. When the motor is operating at 0.0303 per unit slip, the $(f_s + f_r + 2sf_s)$ will merge to $(1+14s)f_s$, the $(f_s - f_r - 2sf_s)$ will merge to $(1-14s)f_s$, and $f_s \pm f_r$ will merge to $(1\pm 16s)f_s$, and so on.

The $\pm 2nsf_s$ sideband components centre on slot harmonics, third, and fifth harmonics with about 10dB increase in the relative amplitude when the motor has the 'one cut rotor'.

When the motor had two cut rotor bars, the pattern of the current spectrum was the same as for on broken rotor bar, but with higher relative amplitudes of the multiple of double slip-frequency components (another 10dB higher). The $(1\pm 2s)f_s$ components have the largest amplitude with -33.8dB (lower sideband) and -34.1dB (upper sideband) respectively. There are also relatively low increases in relative amplitude of the sidebands centred on 150Hz. The relative amplitude of the fault-related components are in tables 3.3 to 3.7 for all three different rotors.

Frequency Factor	Rotor with no cut at s=0.0273		Rotor with one cut at s=0.0297		Rotor with Two Cuts at s=0.0292	
	Hz	dB	Hz	dB	Hz	dB
1-16s	28.03	-51.48	26.22	-53.40	26.66	-54.87
1-14s	30.77	-	29.20	-63.34	29.58	-63.83
1-12s	33.52	-	32.17	-63.46	32.50	-57.61
1-10s	36.27	-	35.14	-59.55	35.41	-60.18
1-8s	39.01	-	38.11	-58.50	38.33	-54.68
1-6s	41.76	-	41.08	-61.51	41.25	-57.44
1-4s	44.51	-	44.06	-51.67	44.17	-47.96
1-2s	47.25	-52.88	47.03	-47.30	47.08	-33.49
1+2s	52.75	-54.76	52.97	-45.20	52.92	-32.57
1+4s	55.49	-	55.94	-64.88	55.83	-49.00
1+6s	58.24	-	58.92	-65.32	58.75	-55.39
1+8s	60.99	-	61.89	-66.35	61.67	-64.76
1+10s	63.73	-	64.86	-73.09	64.59	-67.76
1+12s	66.48	-	67.83	-71.57	67.50	-72.44
1+14s	69.23	-	70.80	-68.85	70.42	-68.69
1+16s	71.97	-56.48	73.78	-59.05	73.34	-60.59

Table 3.3: The $\pm 2nsf_s$ sidebands on the supply frequency

Frequency Factor	Rotor with no cut at s=0.0273		Rotor with one cut at s=0.0297		Rotor with Two Cuts at s=0.0292	
	Hz	dB	Hz	dB	Hz	dB
1-6s-(1-s)/pp	17.45	-	16.83	-	16.98	-75.32
1-4s-(1-s)/pp	20.19	-	19.80	-	19.89	-
1-2s-(1-s)/pp	22.94	-	22.77	-80.10	22.81	-71.83
1-(1-s)/pp	25.69	-66.86	25.74	-62.19	25.73	-63.66
1+2s-(1-s)/pp	28.43	-	28.72	-78.14	28.65	-75.77
1+4s-(1-s)/pp	31.18	-	31.69	-	31.56	-76.52
1+6s-(1-s)/pp	33.93	-	34.66	-	34.48	-76.56
1-6s+(1-s)/pp	66.07	-	65.34	-83.23	65.52	-72.09
1-4s+(1-s)/pp	68.82	-	68.31	-82.85	68.44	-
1-2s+(1-s)/pp	71.57	-	71.29	-68.65	71.35	-58.94
1+(1-s)/pp	74.31	-65.96	74.26	-60.41	74.27	-60.85
1+2s+(1-s)/pp	77.06	-	77.23	-78.58	77.19	-67.95
1+4s+(1-s)/pp	79.81	-	80.20	-	80.11	-76.77
1+6s+(1-s)/pp	82.55	-	83.17	-	83.02	-73.02

Table 3.4: The $\pm 2nsf_s$ sidebands on the $f_s \pm f_r$ components

Frequency Factor	Rotor with no cut at s=0.0273		Rotor with one cut at s=0.0297		Rotor with Two Cuts at s=0.0292	
	Hz	dB	Hz	dB	Hz	dB
3-6s	141.81	-	141.09	-	141.24	-73.13
3-4s	144.54	-	144.06	-71.07	144.16	-63.03
3-2s	147.27	-	147.03	-	147.08	-64.98
3+2s	152.73	-	152.97	-79.42	152.92	-
3+4s	155.46	-	155.94	-	155.84	-
3+6s	158.19	-	158.91	-	158.76	-

Table 3.5: The $\pm 2nsf_s$ sidebands on the third harmonic

Frequency Factor	Rotor with no cut at s=0.0273		Rotor with one cut at s=0.0297		Rotor with Two Cuts at s=0.0292	
	Hz	dB	Hz	dB	Hz	dB
5-6s	241.76	-79.04	241.08	-70.16	241.25	-62.37
5-4s	244.51	-72.01	244.06	-50.55	244.17	-45.42
5-2s	247.25	-68.82	247.03	-53.33	247.08	-49.49
5+2s	252.75	-81.00	252.97	-70.25	252.92	-69.51
5+4s	255.49	-	255.94	-79.45	255.83	-76.35
5+6s	258.24	-	258.92	-85.28	258.75	-73.30

Table 3.6: The $\pm 2nsf_s$ sidebands on the fifth harmonic

Frequency Factor	Rotor with no cut at s=0.0273		Rotor with one cut at s=0.0297		Rotor with Two Cuts at s=0.0292	
	Hz	dB	Hz	dB	Hz	dB
3-2s-R(1-s)/pp	625.28	-81.90	623.25	-72.12	623.74	-64.64
3-R(1-s)/pp	627.70	-62.03	625.70	-61.14	626.50	-58.90
3+2s-R(1-s)/pp	630.77	-77.69	629.20	-62.30	629.58	-56.10
3+4s-R(1-s)/pp	633.52	-	631.60	-70.20	632.50	-71.97
1-2s-R(1-s)/pp	725.28	-85.20	723.25	-78.01	723.74	-57.71
1-R(1-s)/pp	727.60	-53.00	725.60	-51.62	726.50	-46.43
1+2s-R(1-s)/pp	730.77	-80.07	729.20	-67.51	729.58	-53.41
1+4s-R(1-s)/pp	733.52	-	732.18	-	732.50	-70.29
1-4s+R(1-s)/pp	822.70	-	820.03	-	820.70	-61.41
1-2s+R(1-s)/pp	825.28	-67.70	823.25	-57.81	823.74	-44.64
1+R(1-s)/pp	827.60	-34.90	825.50	-33.70	826.60	-32.52
1+2s+R(1-s)/pp	830.77	-64.41	829.20	-59.78	829.58	-44.57
1+4s+R(1-s)/pp	833.52	-	832.18	-	837.50	-63.22
3-4s+R(1-s)/pp	922.53	-	919.50	-73.52	920.70	-64.18
3-2s+R(1-s)/pp	925.28	-76.90	929.20	-70.52	929.58	-55.24
3+R(1-s)/pp	927.50	-48.20	925.40	-45.77	926.60	-43.57
3+2s+R(1-s)/pp	930.77	-83.40	923.25	-63.07	923.74	-56.88

Table 3.7: The $\pm 2nsf_s$ sidebands on the slot harmonics

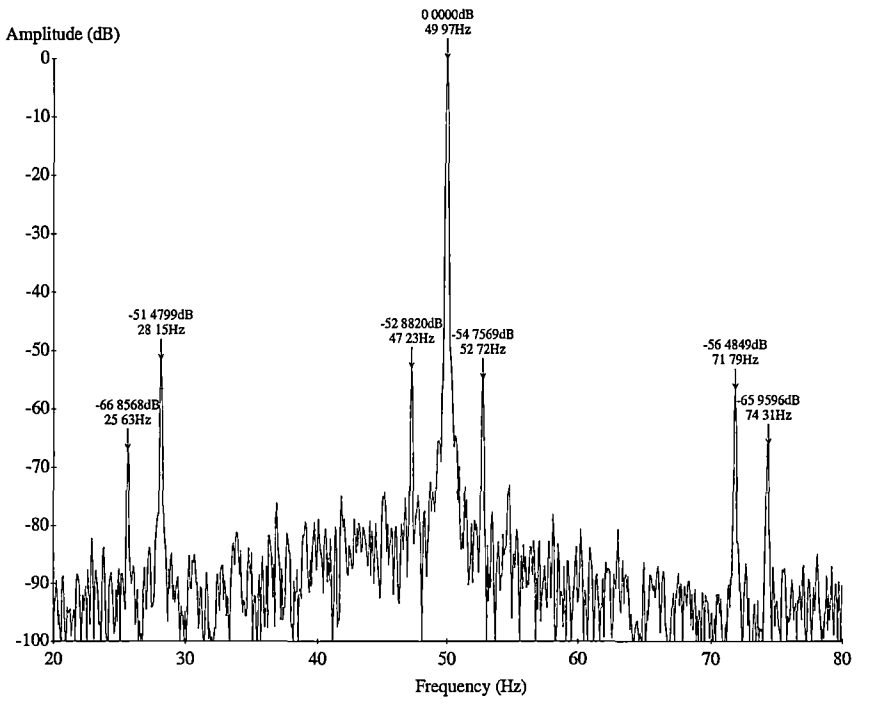

Figure 3.2: Sidebands on supply frequency with the good rotor

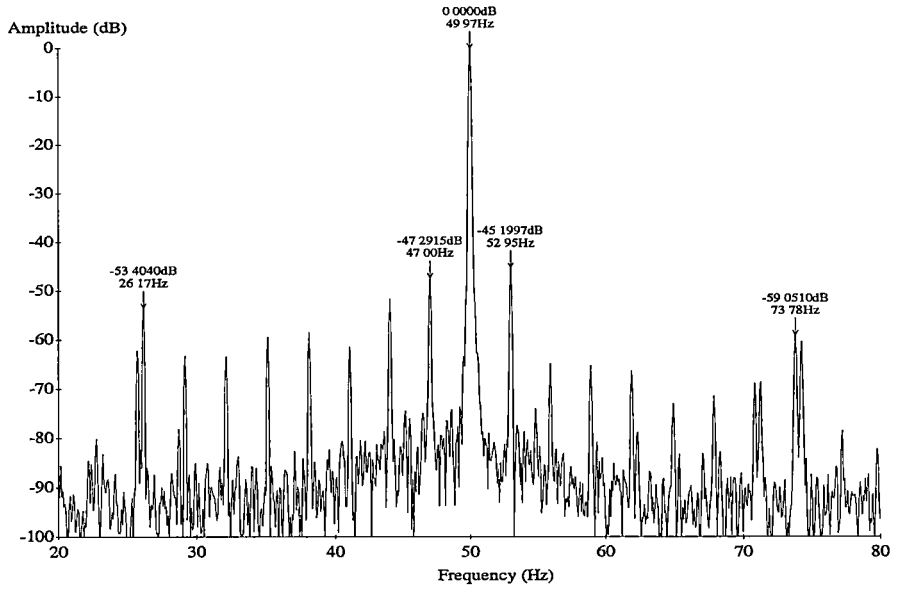

Figure 3.3: Sidebands on supply frequency with the one cut rotor

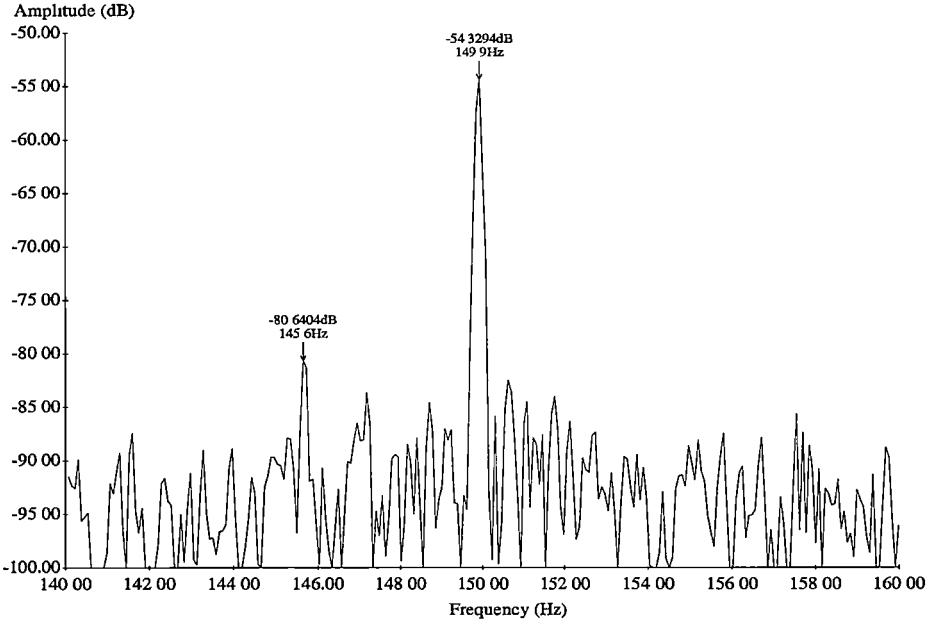

Figure 3.4: The sidebands on 150Hz with the good rotor

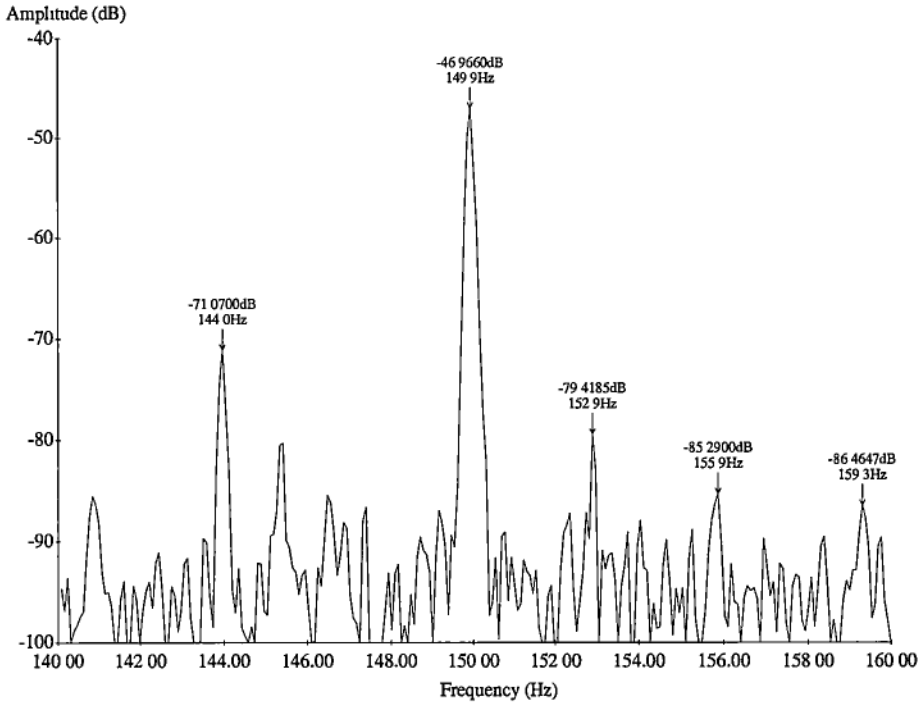

F

igure 3.5: The sidebands on 150Hz with the one cut rotor

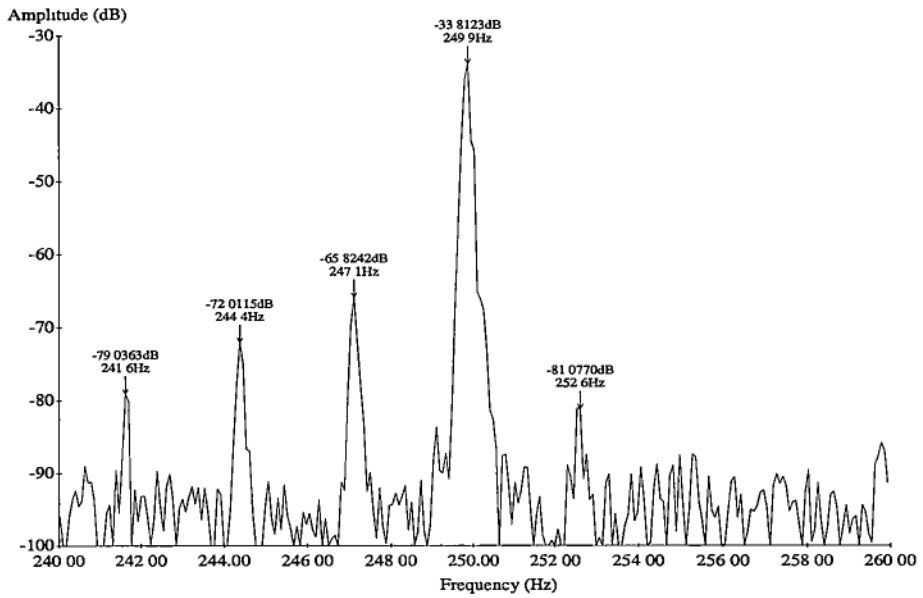

F

igure 3.6: The sidebands on 250Hz with the good rotor

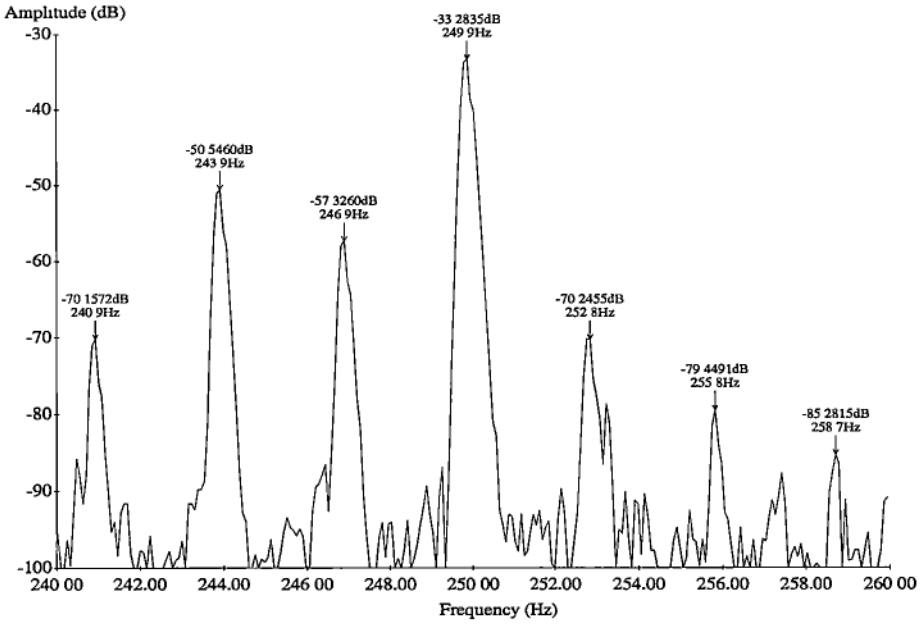

F

igure 3.7: The sidebands on 250Hz with the one cut rotor

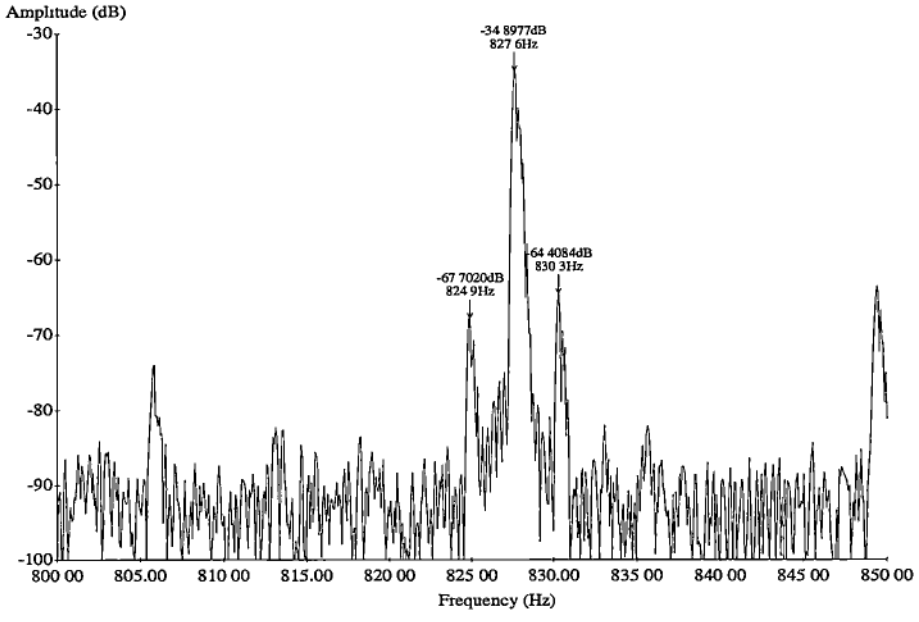

F

igure 3.8: The sidebands on the fundamental slot harmonic with the good rotor

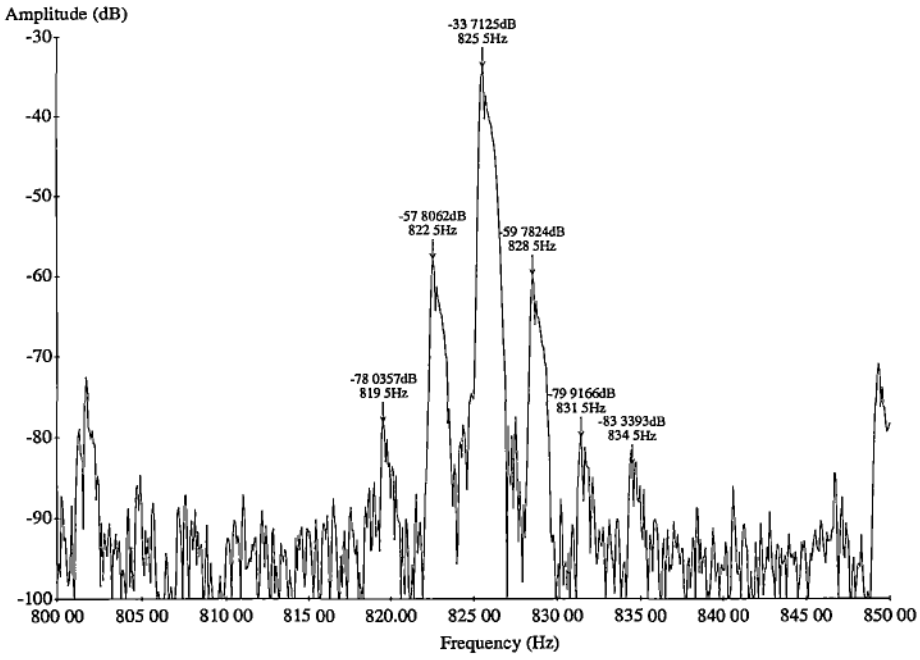

Figure 3.9: The sidebands on the fundamental slot harmonic with the one cut rotor

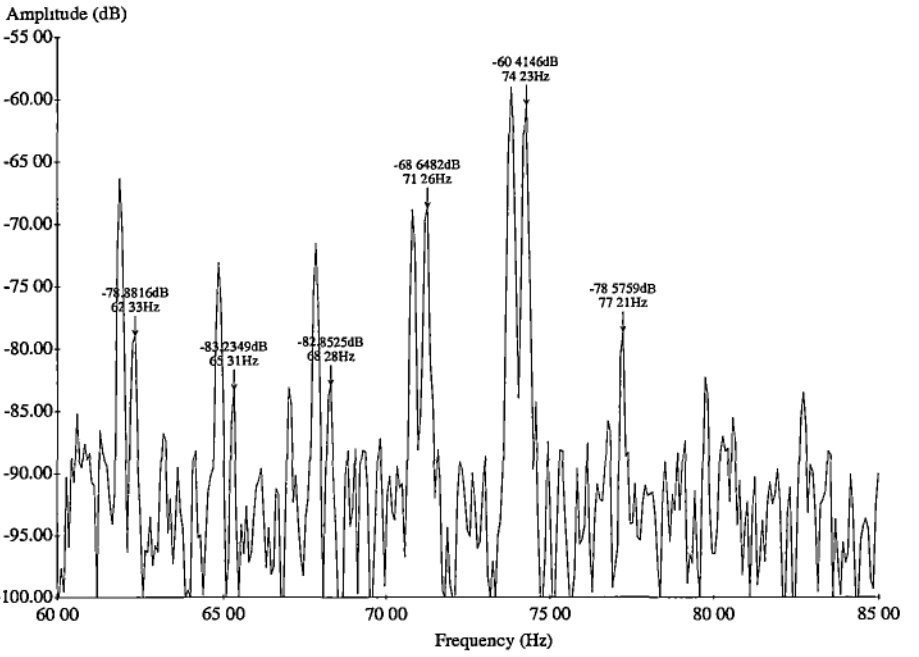

Figure 3.10: The sidebands on $f_s + f_r$ components

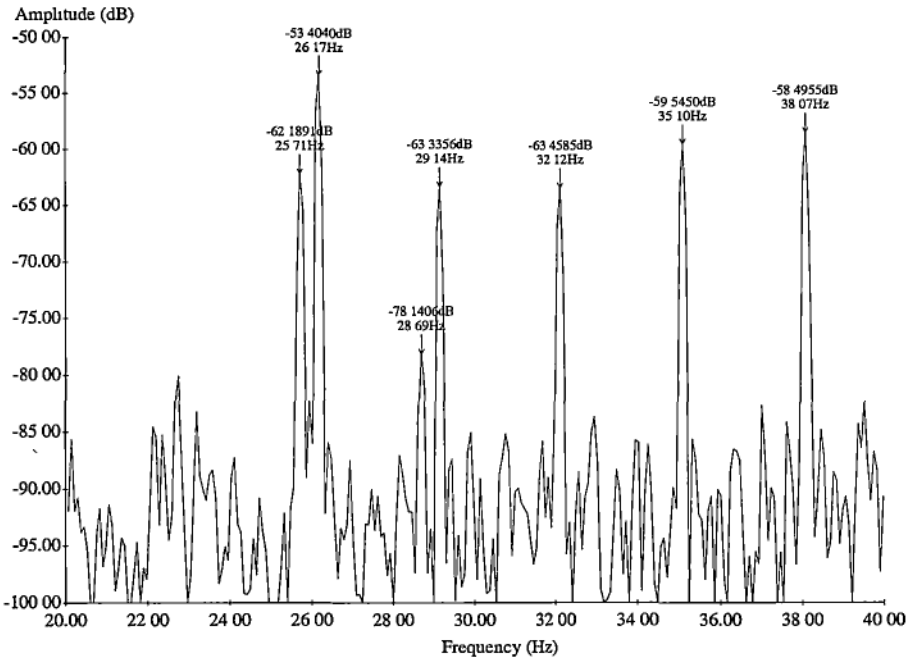

Figure 3.11: The sidebands on $f_s - f_r$ components

The accuracy of the prediction from 'single test' diagnostic algorithm [76] and equation (3.3) [16,18] is verified by using the $(1-2s)f_s$ component from the above measurements. For the good rotor case, from the prediction of the 'single test', the motor will mostly likely have a cracked rotor bar since the relative amplitude of $(1-2s)f_s$ components is between –50 and –60dB (-52.9dB). However, from equation (3.3), the predicted number of broken rotor bar is 0.14, which suggests that the rotor is in good condition or has a very small crack. The presence of $\pm 2sf_s$ components is due to normal manufacturing tolerance variation in the rotor bar resistance and end ring joints resistance.

In the case with one broken rotor bar, the prediction from Kliman is that there is probably a broken rotor bar, as the amplitude of the $(1-2s)f_s$ is –47.3dB (ie greater than –50dB) and the prediction from equation (3.3) gives 0.43 broken rotor bar, equivalent to a cracked bar. However, the prediction from the two broken rotor bars case gives 1.9 broken rotor bars, which almost matches the actual number, while the Kliman criterion say that there is definitely a broken rotor bar.

The tests also verified that when rotor damage increases, not only the relative amplitude of $(1 \pm 2s)f_s$ increase, but also the $\pm 2nsf_s$ sideband components on $f_s \pm f_r$ components, third, fifth and slot harmonics. The change of the relative amplitude of these components shows the severity of the rotor defect, and the appearance of all $\pm 2nsf_s$ sidebands centred on $f_s \pm f_r$ components, slot harmonics, 50, 150, and 250, harmonics is also a distinct feature of the damaged rotor [76].

3.6 Electrical Interference from Variable Speed Drives (VSD) for Induction Motors

The prediction of extra frequencies in the stator current produced by rotor defects such as a broken rotor bar and rotor eccentricity, for a motor on 50Hz sinusoidal (mains) supply are in the section 3.3. Fault-related frequencies should still be present in the stator current of motors connected to a VSD. The VSD produces a variable frequency output waveform by converting the mains input into DC by either a controlled or uncontrolled rectifier, and then inverting it to produce AC of variable magnitude and frequency. A very common type is the pulse-width modulated (PWM) inverter supplied by a diode (uncontrolled) rectifier as shown in block diagram form in figure 4.1 [99]. The PWM inverter uses a sinusoidal modulating wave with a triangular carrier wave to drive the power semiconductor switches, which chop the DC voltage source into a series of pulses whose envelope approximates a sinusoidal voltage. The frequency of the modulating sinewave determines the output frequency of the drive.

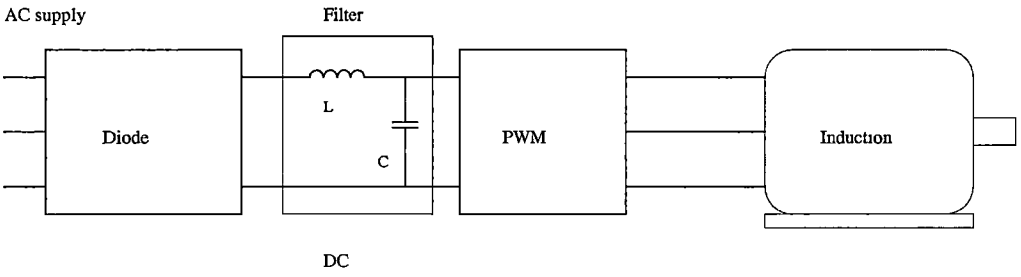

Figure 3.12: Pulse width modulated inverter drive

There are two difficulties with a PWM drive: the first is that the voltage and current waveforms are not sinusoidal, the second is that the frequency may change during the sampling period. However, in addition to these, there is another non-trivial problem: the electrical interference it produces due to the chopped nature of the stator voltage. Figure 3.13 shows a current waveform measured on the Pope motor supplied by a PWM drive at fixed frequency. Current was monitored using a Fluke Hall-effect type clip-on ammeter. The same type was used successfully for the measurements described in section 3.5. It provides 1 millivolt per ampere, and is rated up to 1000 amp DC or 700 amp AC. The ammeter used in figure 3.13 obviously suffers from massive interference from the particular PWM drive, even with some shielding added to the ammeter. An analogue filter can reduce but not eliminate this level of noise, which still causes a problem with the data acquisition.

As an alternative, a fully shielded wire-wound current transformer with a matched load, the Fischer Custom Communications Inc. RF current probe (Appendix A4.2), was used. This has excellent immunity to noise, as in figure 3.14. However, during the measurements of motor currents in industry, we found that there was often not enough distance between the three-phase cables in the motor control cubicle to clip the Fischer probe over a cable. Probe outside diameter is about 100mm. Another drawback is that it has a phase error of about 30° at 50Hz which is a problem when currents had to be measured accurately enough to be able to compute the input motor power.

Because of these drawbacks of the Fischer probe, a split core current transformer (CT) was designed to have an acceptable level of interference in the current

waveform that goes to the computer. The CT provides 1 volt per 20 ampere and has 3.6° phase error for 80 amp 50Hz current (Appendix A4.3). Figure 3.15 shows the current waveform of a PWM drive using the CT. There are very few spikes compared with figure 3.13 and 3.14. The lower frequency response was not a problem since we were not interested in the very high frequencies.

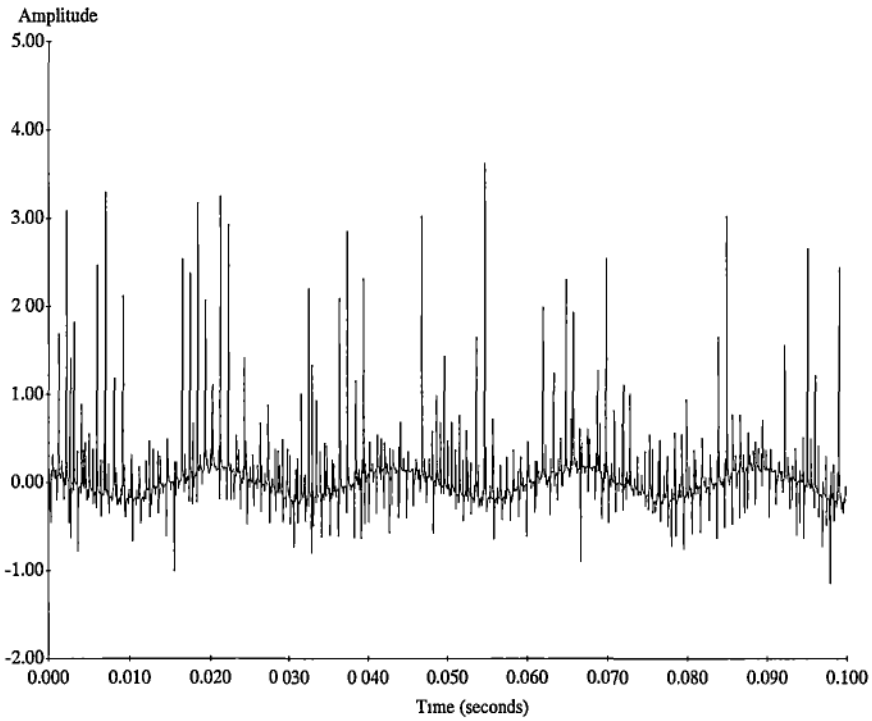

Figure 3.13: Current waveform for PWM drive picked up by Hall-effect clamp-on ammeter

[It should be noted that Mr. R. Langman did the initial design of the split core CT.]

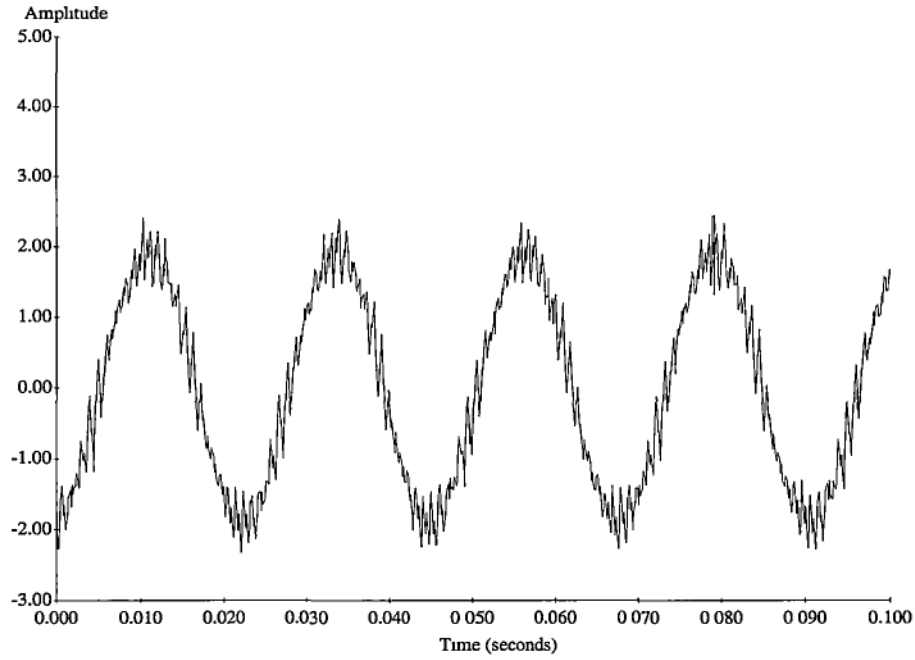

Figure 3.14: Current waveform for PWM drive picked up by Fischer RF current clamp

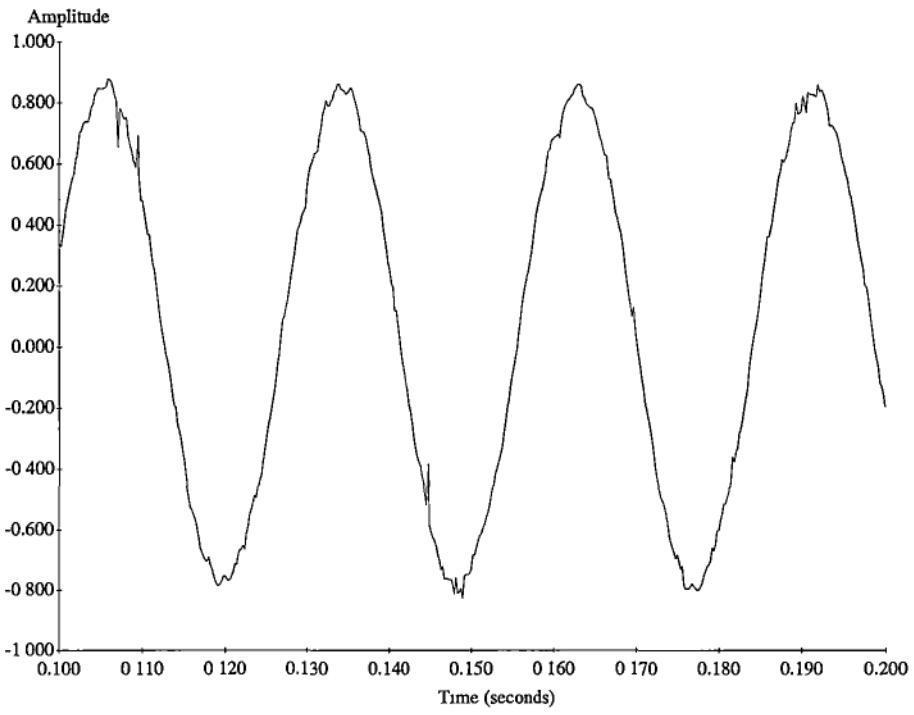

Figure 3.15: Current waveform for PWM drive picked up by CT

3.7 Test Results of the 7.5kW Pope Motor Supplied at Fixed Frequency from a Variable Speed Drive (VSD)

The 7.5kW Pope motor with a good rotor was supplied by an ABB SAMI SG variable speed drive (Appendix A3.3). It was operated at fixed frequency, 50Hz, at full load condition. The line current waveform was captured by the split core CT. Figure 3.16 shows the current spectrum from 20 to 80Hz. The background noise level is 15 to 20dB higher compared to the mains supply case (figure 3.2). The double slip-frequency sidebands exist at 47.07Hz and 52.87Hz with -50.3dB and -56.5dB respectively. The $f_s \pm f_r$ sidebands also exist at 26.63Hz and 73.32Hz.

The $\pm 2nsf_s$ sidebands centred on $f_s \pm f_r$ components, slot harmonics, third, and fifth harmonics could not be distinguished due to the higher noise level. If the $(1-2sf_s)$ amplitude is used to predict the broken rotor bar, Kliman's criterion [76], states that it is mostly likely to have a cracked bar. Using equation (3.3), the predicted number of broken rotor bars is 0.31, double that of the mains supply case.

When the rotor with one cut rotor bar was fitted to the motor, the new spectrum has amplitude shown in figure 3.17 (motor was delivering full-load output at rated speed). The double slip-frequency sidebands are -45.4dB and -46.8dB respectively. Figures 3.18 and 3.19 show the $\pm 2nsf_s$ sideband components centred on fifth and slot harmonics. No prominent $\pm 2nsf_s$ sidebands can be found around the $f_s \pm f_r$ components, the slot harmonics, third and fifth harmonics. Equation (3.3) predicts the motor having 0.54 broken rotor bar. Kliman's criterion predicts one broken rotor bar.

For the rotor with two cut bars, the relative amplitude of double slip-frequency sidebands are -32.0dB and -34.6dB. Equation (3.3) predicts 2.3 broken rotor bars. Figure 3.20 shows the $f_s + f_r$ component at 74.23Hz and $f_s + f_r - 2sf_s$ component at 71.26Hz. Prominent $\pm 2nsf_s$ sidebands can be found on third, fifth, and slot harmonics.

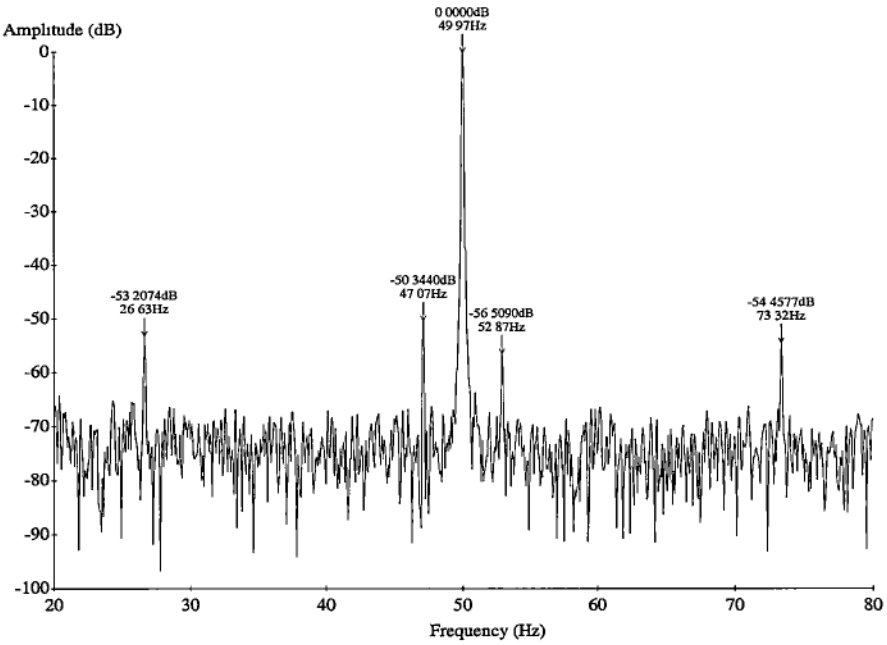

Figure 3.16: The sidebands on the fundamental supply frequency with the good rotor

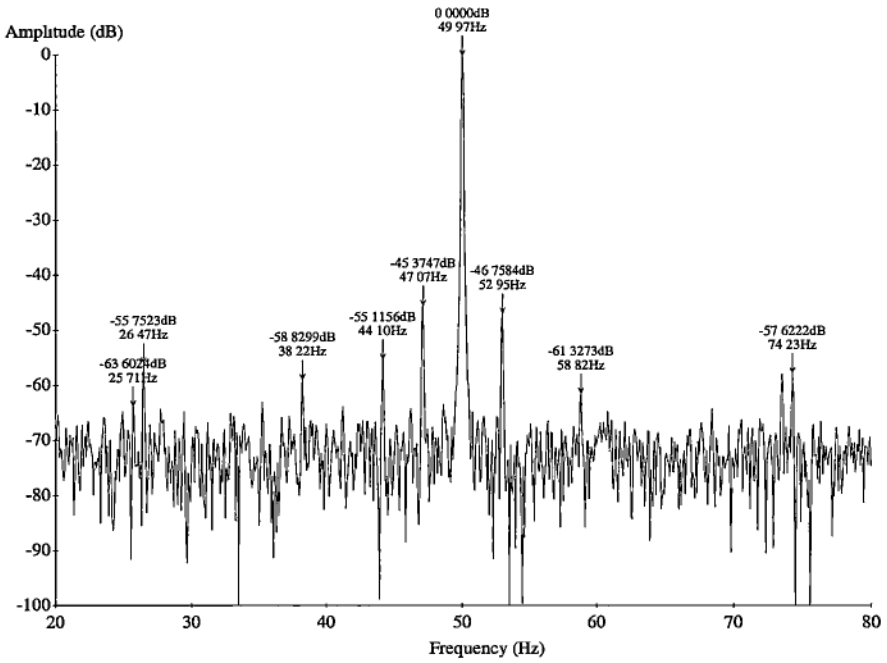

Figure 3.17: The sidebands on the fundamental supply frequency with the one cut rotor

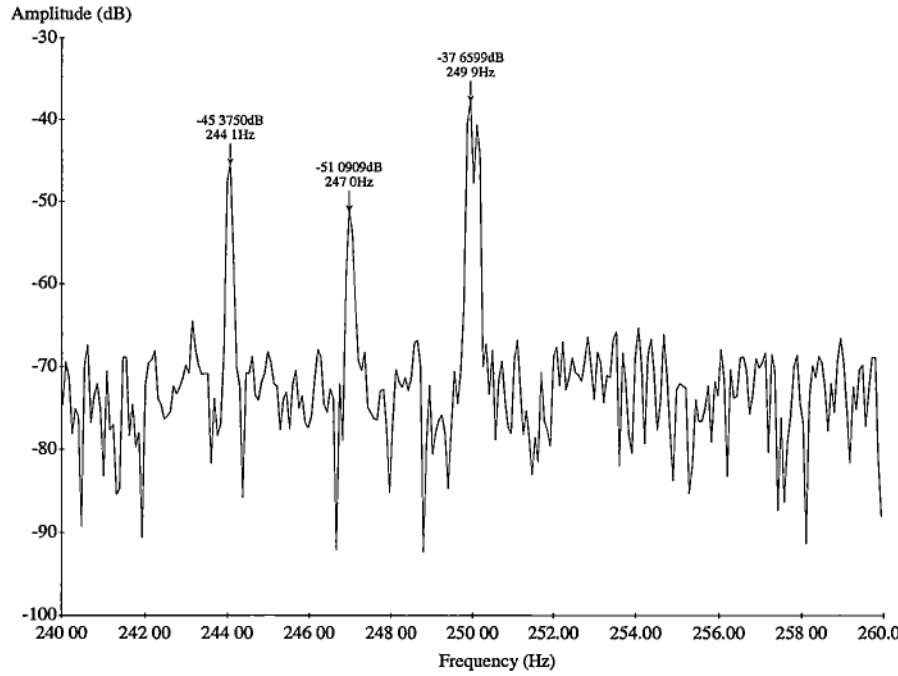

Figure 3.18: The $\pm 2nsf_s$ sidebands on 250Hz with the one cut rotor

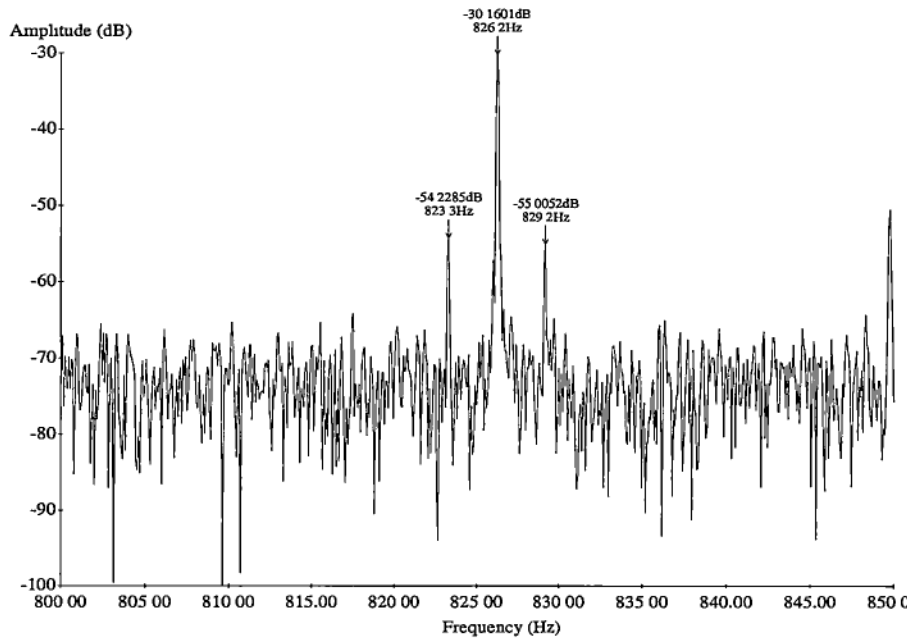

Figure 3.19: The $\pm 2sf_s$ sidebands on the fundamental slot harmonic with the one cut rotor

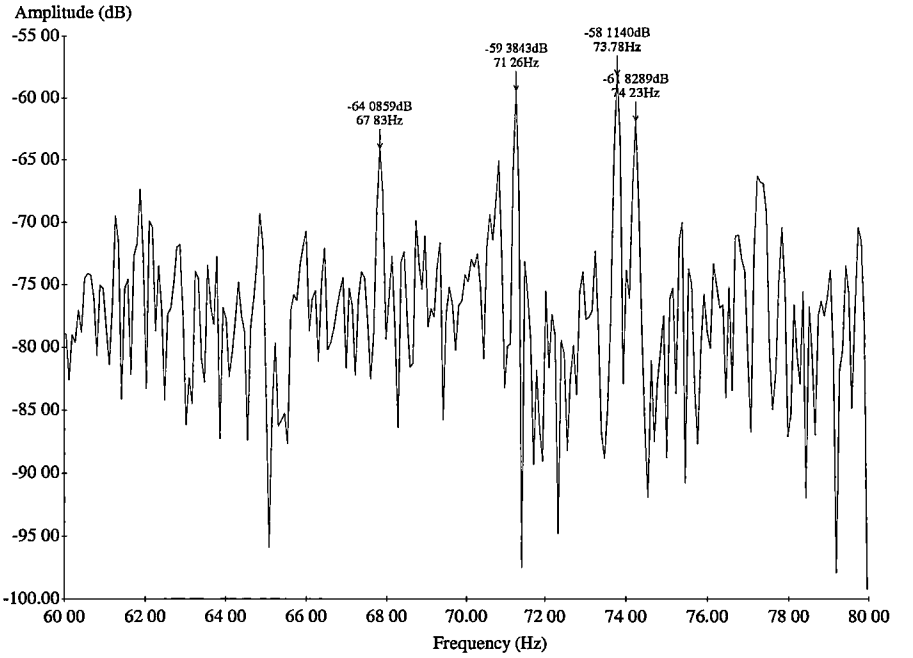

Figure 3.20: The $\pm 2sf_s$ sidebands on $f_s + f_r$ component with the two cut rotor

3.8 Induction Motors with Variable Supply Frequency

The double slip-frequency $\pm 2sf_s$ sidebands should still be present in the stator current waveform of induction motors supplied with variable frequency. However, their detection becomes more complicated. Essentially, it is a problem of dealing with a "non-stationary" signal, ie the fundamental frequency varies during the sampling period. If a data record of current waveform is sampled at a constant rate, the Fourier Transform will produce a blurred spectrum with no distinct peaks and a high noise level, as in figure 3.21 (measured on the Pope motor, with the frequency changed from 50Hz to 45Hz during the 12 seconds sampling period). Note that the sidebands themselves vary as the supply frequency changes. For induction motors of more than 100kW that may have a slip at rated load of less than 0.01, the $\pm 2sf_s$ sidebands are within $\pm 2\%$ of fundamental. Clearly, the $2sf_1$ sidebands of figure 3.17 would be hidden.

Hardware and software ways of avoiding the blurred spectrum have previously been

attempted by Innes [22], and are summarised in the following sections.

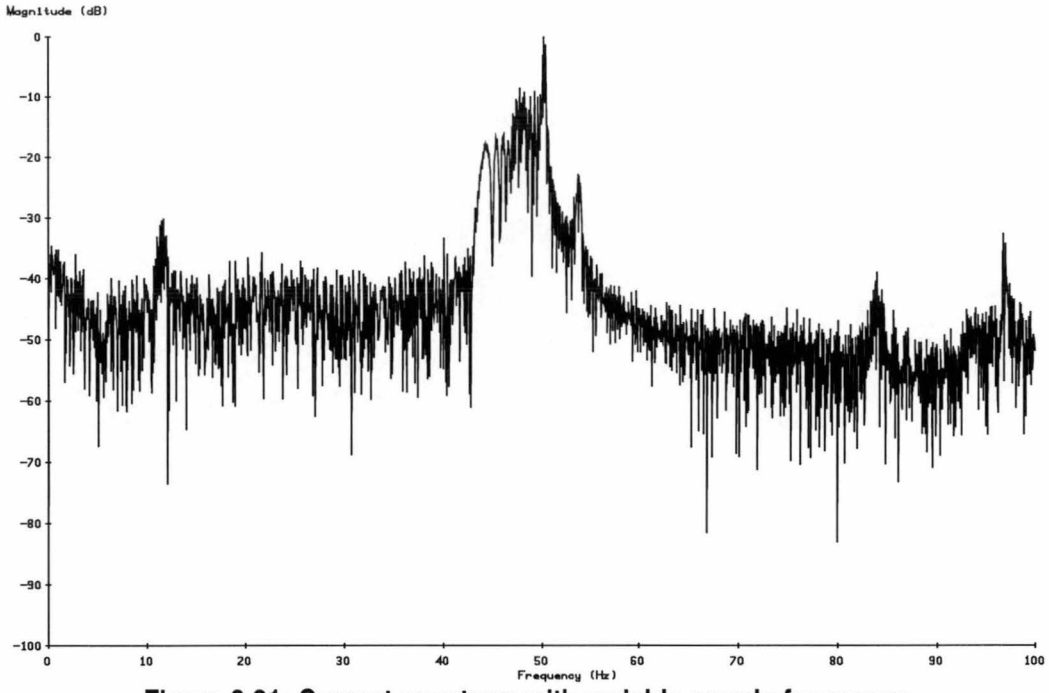

Figure 3.21: Current spectrum with variable supply frequency

3.8.1 Application of the Phase Lock Loop to Variable Speed Drives

Innes [22] developed a Phase Locked Loop (PLL) synchronous sampling technique and applied it to variable speed operation. His current spectrum of the 7.5kW Pope motor supplied by a PWM waveform is shown in figure 3.22. The motor supply frequency varied over approximately 5Hz in 14 seconds while the data was being recorded. The sidebands and supply frequency are quite clear, compared to figure 3.21 for the same motor and test conditions but using a constant sampling rate. (Note that the frequency scale in figure 3.22 is misleading, ie it should be marked in "per unit of fundamental frequency", so that 50.33Hz becomes 1.00).

The PLL hardware was tried on a number of drives, both in the field and the laboratory. It was found to perform well in some circumstances and rather badly in others. One difficulty was found to lie with the limited tracking range of the PLL. It is quite difficult to design a PLL with a wide tracking range and a good step response at such low frequencies. Its operation was constrained by the limited tracking range of approximately ±18Hz, centred about 50Hz.

A second, serious, problem was a "jitter" on the output waveform of one particular variable speed drive in the laboratory, an ABB SAMI GS (Appendix A3.3), even when operating at a "constant" output frequency. This jitter was occasionally of large enough magnitude to cause the PLL circuit to lose lock, causing non-synchronous sampling to occur until it regained lock. This produces spectra with broadening of the supply frequency peak.

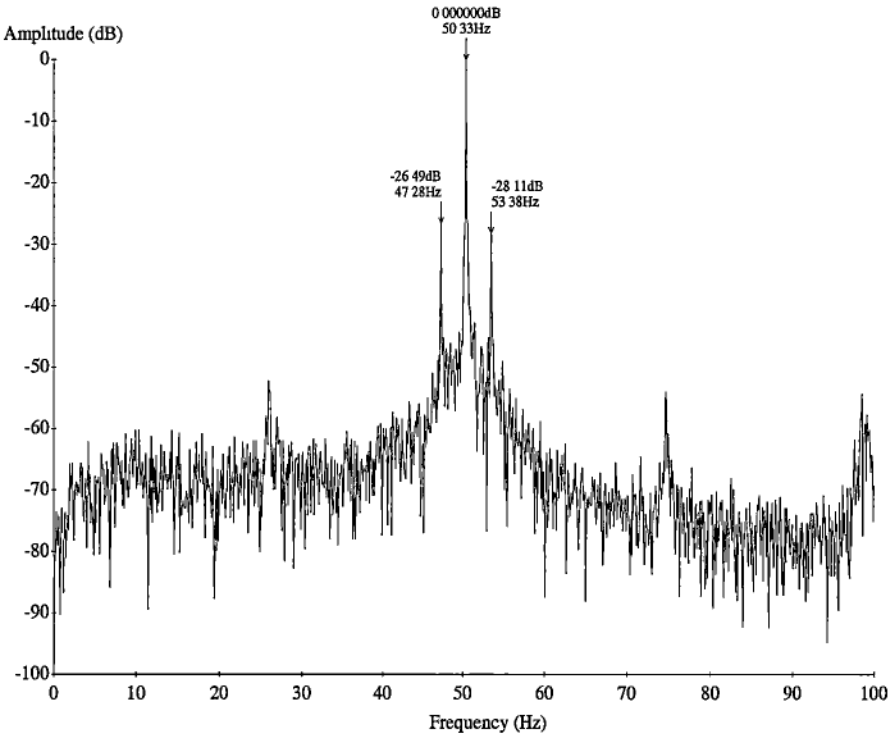

Figure 3.22: Stator current spectrum for fixed frequency sampling with varying supply voltage frequency.

It was thought that the jitter may be due to the variation in turn-on and turn-off time of the semiconductor switches in the drive, as a result of varying amounts of current being switched [100]. It is likely that all drives may suffer this problem to a greater or lesser degree. Hence, the PLL method may not be that useful. However, if the circuit could be implemented as part of the drive itself, then the PLL could be driven from the power electronics control signals. This would solve the problem, as these signals should not suffer from frequency jitter.

3.8.2 Short Time Fourier Transform (STFT)

The detection of double slip frequencies for a variable frequency drive is a non-stationary signal processing problem. Fourier analysis can no longer cope because it assumes that the signal is stationary over the sampling period. However, there are two types of analysis that can in theory deal with a non-stationary signal. The first is Time-Frequency analysis, such as the Short Time Fourier Transform, and the second is Wavelet analysis. The basic difference is that STFT has constant resolution in both time and frequency, whereas in Wavelet analysis, the time and frequency resolutions are inter-dependent.

Both these are recent developments, partially due to the large amount of computing power required. STFT calculates the Fourier Transform of the signal $f(t)$ by applying a short window function $g(t)$ centred at a particular time τ. The window is a shift in time along the data set and consecutive overlapped transforms are performed. Effectively, the STFT assumes that the signal remains stationary over the length of the window [101]. If the window is relatively short, this assumption local stationary is often valid. The time and frequency resolution of the STFT are dependent upon the window function. Choosing a short window will result in a transform exhibiting good time resolution but this reduces the sampling number used in the Fourier Transform calculation and the frequency resolution reduces. The relationship between resolution in time (Δt) and frequency (Δf) is governed by the uncertainty principle [102]

$$\Delta t \Delta f \geq \frac{1}{4\pi} \tag{3.12}$$

where Δt is the transform resolution in the time domain and Δf is the transform resolution in the frequency domain.

Innes applied the STFT to measure stator current waveforms when the supply frequency is varying [22]. The waveforms were taken from the 7.5kW Pope motor with a damaged rotor. (The STFT was calculated using the TFSA 4.0 package [68] and MATLAB® [69]. It is displayed as grey scale images where white indicates the highest amplitude and black the lowest. The amplitudes are plotted on a logarithmic

scale. Unless otherwise stated, the window length used is 1024 points. Filtering of the current waveform was achieved using the signal processing toolbox of MATLAB®).

The STFT was first used on a mains frequency current waveform, (which is stationary), and the results are shown in figure 3.23. It does not have sufficient frequency resolution to resolve the twice slip-frequency sidebands. The frequency resolution can be increased by lengthening the window to include more data points. Naturally, this decreases the time resolution. The rotor slot frequency at 800Hz is about the only thing visible.

Figure 3.24 shows the STFT when the drive frequency is steadily increased from 30Hz to 60Hz. The fundamental frequency is visible at the bottom of the image and can be seen to increase slightly over time, as would be expected. The twice slip-frequency sidebands are not visible at all. The other frequency components in the time-frequency plane are the result of the modulation process. The two components below 1000Hz decrease in frequency while the two above increase. The drive output frequency components include multiples of the carrier plus and minus multiples of the carrier frequency. As the modulating (drive) frequency increases, the sidebands will move away from the multiples of the carrier frequency. This occurs in figure 3.24 up until 0.8 seconds. At this point in time, it would appear that the drive modulation process changes, causing the jump in frequencies. The new frequencies are present until about 1 second, at which point the spectrum returns to a similar situation to the start, except that it would appear that the carrier frequency has increased, and thus all components have increased in frequency.

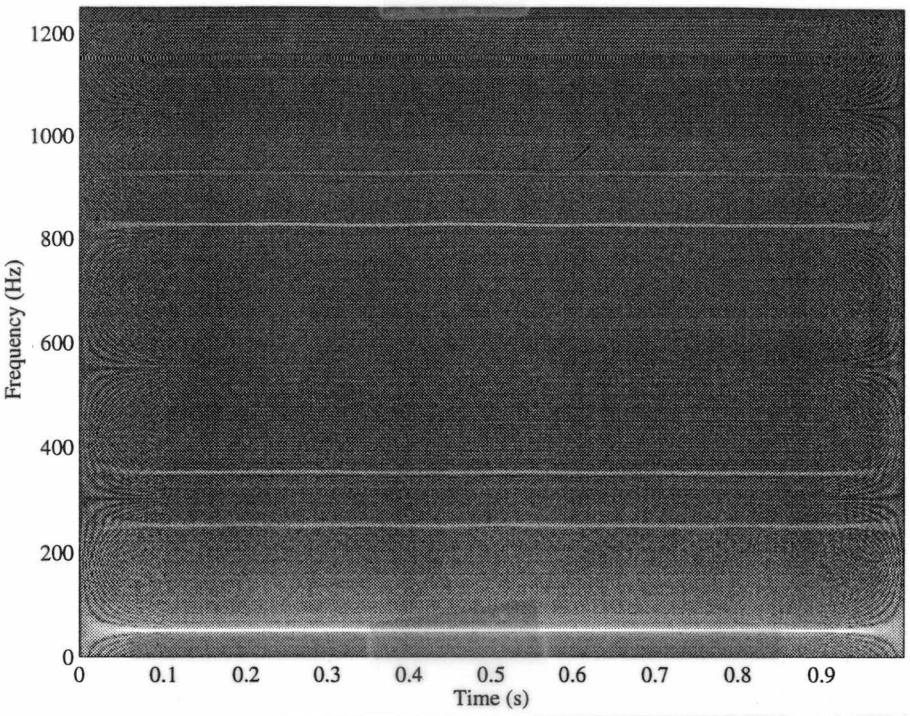

Figure: 3.23: STFT of stator current waveform with mains supply

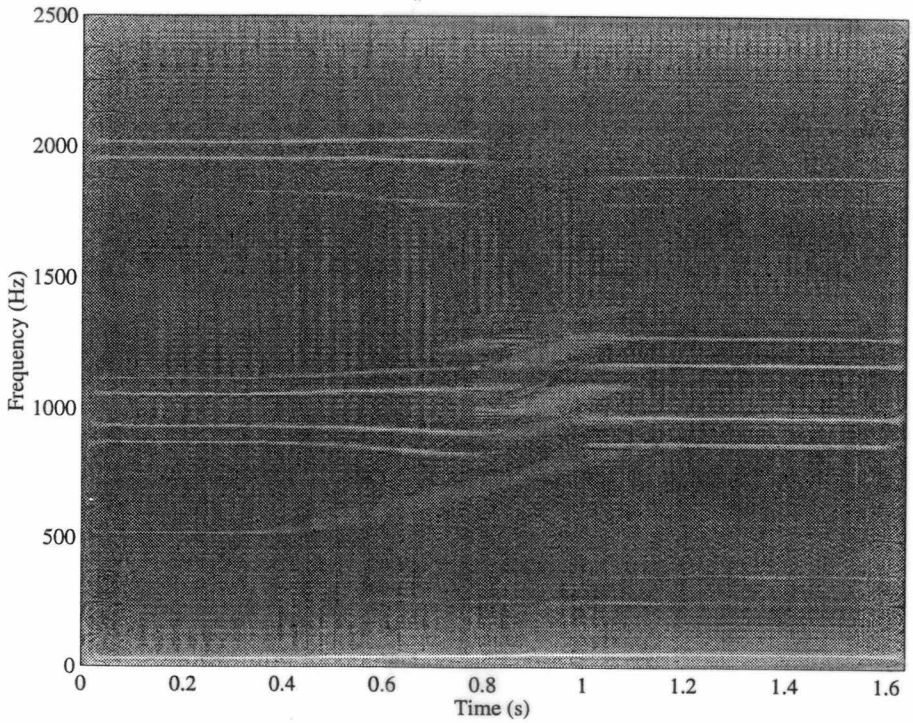

Figure 3.24: STFT of stator current waveform with drive frequency ramping from 30Hz to 60Hz

Innes also applied Wavelet analysis on the same current waveform. Little useful information was provided from the result [22]. The application of these methods to the analysis of stator current waveforms was not successful. It seems that the frequency resolution is never good enough to distinguish the twice slip-frequency sidebands from the supply frequency and that this is a general problem in detecting low-level signals in the presence of larger signals.

3.9 Summary

This chapter has presented the theoretical expression for the magnetic field harmonics in the air gap of an induction motor. It takes into account the effects of slotting, saturation, and rotor eccentricities and predicts extra frequencies that could appear in the stator current as a result. The effect of a broken rotor bar on the magnetic field in the air gap and on the $f_s \pm f_r$ components is determined. Values of the fault frequency components in the stator current are predicted. This basic information is vital for the detection of broken rotor bars in an induction motor supplied by a variable speed drive.

The main fault frequencies that appear in the stator current spectrum for broken rotor bar detection are the double slip-frequency sidebands, resulting from the modulation of the supply frequency. The layout of the stator winding, and its distribution factors and coil span factors, will have a very significant effect on which frequencies will actually appear in the current. Another distinct feature of the damaged rotor spectrum is the appearance of sidebands centred on the $f_s \pm f_r$ components, all the time and slot harmonics.

Prediction of broken rotor bars was also discussed. The predictions from Thomson [16,18] and Kliman [76] are applied to experimental results from a laboratory motor with deliberately cut rotor bars, with both mains and variable frequency supply. There is moderate agreement.

The electrical interference produced from the variable frequency drive was discussed in this chapter. It included a study of the suitability of different types of current transducers. The difficulties of broken rotor bars detection for induction motors with

variable supply frequency were also addressed. Problems of previous approaches of broken rotor bars detection with varying supply frequency were discussed and summarised.

An alternative non-invasive technique and accompanying instrumentation for condition monitoring of induction motors will be introduced in chapter 4. The input power signal is computed from measurements of two line currents and two line-to-line voltages. Inter-turn short-circuit fault of stator windings and broken rotor bars detection are attempted using spectrum analysis of this signal. The effect of supplying with variable speed drive on the method is investigated by experimental result.

Chapter 4

On-line Voltage and Current Monitoring of Induction Motors - *Input Motor Power Monitoring*

4.1 Introduction

On-line voltage and current (V-I) monitoring of induction motors is widely used for the estimation of parameter of healthy motors for control purposes. A comprehensive summary is given by Vas [10].

As far as condition monitoring goes, Cho et al [70] used measurements of stator voltage, current, frequency and speed to process into a near-least-square-error estimator to estimate motor impedances. The estimated rotor resistance is compared with its nominal value to detect broken rotor bars. Off-line measurements are needed to obtain the temperature/resistance variation, which is a disadvantage.

Hsu [67] calculated the air gap torque from V-I measurements to detect shorted stator coils and cracked rotor bars. Experimental results showed the existence of double

slip-frequency air gap torque for a defective rotor, and of a double fundamental supply frequency for a defective stator.

Penman et al [68] detected broken rotor bars by monitoring the transient torque that was computed using V-I measurements. Various ways to implement the numerical integration on data were investigated. Experiment showed that a broken rotor bar does indeed affect the transient electromagnetic torque.

Legowski et al [103] computed the instantaneous three-phase input motor power from V-I measurements, to detect the irregular mechanical load conditions. Experimental result showed that the input power waveform contains all the frequency components of the mechanical load oscillation.

Janda et al [66] proposed two methods to detect broken rotor bars in three-phase induction motors. The first was based on simple analog processing of instantaneous single-phase power that is the product of voltage and current. The second approach was based on extracting the negative sequence stator current by an appropriate analog filter. Both derived signals contain double slip-frequency components whose amplitude is related to the amount of rotor damage.

Sottile et al. [10] calculated negative-sequence impedance of induction motors from V-I measurements to try to detect incipient stator insulation failure. Experimental results from a motor (less than 200 horsepower) showed that the negative-sequence current decreased after a stator short-circuit winding fault, implying a net increase in the motor's negative-sequence impedance. It also illustrated how small supply voltage unbalance can mask these effects but how monitoring the motor's negative-sequence impedance could still be used to detect incipient failure in situation where small voltage unbalance exist.

All these V-I measurements were with mains supply. This chapter describes an on-line method for detecting stator and rotor defects in three-phase squirrel-cage induction motors. It applies to both mains and variable frequency supplies. The instantaneous three-phase input power is computed from measurements of two line-to-line voltages and two line currents. Fourier analysis identifies fault-related frequencies. The predicted fault-related frequency is based on Penman's analysis [9].

The change of the relative amplitude of the fault related frequency components are monitored. Tests were carried out on both laboratory motors with deliberately shorted stator coils and rotor damage, with mains and PWM supply. The effect of different load conditions and operating frequencies were also investigated experimentally.

4.2 Frequencies of Input Motor Power Signal with Mains Supply

4.2.1 Time Harmonics

When an induction motor is supplied by a balanced three-phase voltage, the instantaneous power is DC. With unbalanced impedances, such as inter-turn short-circuit, the input power will be DC plus a component of twice supply frequency ($2\omega_s$). The change of amplitude of this component can indicate a defect in the stator winding.

In practice, the stator currents drawn by a balanced three-phase stator winding from mains and/or PWM supply will be a series of odd time harmonics. As the power is current times voltage, the input power will contain these frequency components:

$$(m_{\omega s} \pm n_{\omega s})\omega_s \tag{4.1}$$

where $m_{\omega s}$ and $n_{\omega s}$ are odd integers.

Hence, for $|m_{\omega s} \pm n_{\omega s}| = 2$, with significant high level of corresponding time harmonics, the $2\omega_s$ component in the power signal due to unbalanced impedance may be covered up.

4.2.2 Unsymmetrical Stator Fault (Penman's Analysis [9])

Penman et al. [9] considered a short-circuited turn in a stator coils of a three-phase induction motor as type of unsymmetrical stator fault. By analysis of the MMF pattern, such a condition induces components of flux density in a rotor reference frame, which are the frequencies of the induced current in rotor.

$$B = \frac{1}{2}\sum_{n=odd} B_n \cos\left\{\left[1 \pm n_{\theta s}\frac{(1-s)}{pp}\right]\omega_s t \pm n_{\theta s}\theta_r\right\} \tag{4.2}$$

When the components of equation (4.2) are further modulated in instantaneous power, and a corresponding set of harmonics f_{power_sd} appears in general form as

$$f_{power\_sd} = \left[(n_{\omega s} \pm 1) \pm n_{\theta s}\frac{(1-s)}{pp}\right] f_s \tag{4.3}$$

where $n_{\omega s}$ and $n_{\theta s}$ are the order of time and space harmonics.

4.2.3 Air Gap Variation and Rotor Defects

The extra sideband components of the time harmonics of the stator current caused by the air gap variation and rotor defects were discussed in Chapter 3. The corresponding set of harmonics in the power may be expressed as follow.

$$f_{ar} = \left\{\begin{matrix}(n_{rt}R \pm n_{de})\dfrac{(1-s)}{pp} \pm \\ 2n_{sa} \pm n_{\omega s}\end{matrix}\right\} f_s \xrightarrow{Modulation} f_{power\_ar} = \left\{\begin{matrix}(n_{rt}R \pm n_{de})\dfrac{(1-s)}{pp} \pm \\ (n_{\omega s} \pm 1) \pm 2n_{sa}\end{matrix}\right\} f_s \tag{4.4}$$

$$f_{be} = \left\{n_{\theta s}\frac{(1-s)}{pp} \pm n_{\omega s} \pm 2n_{be}s\right\} f_s \xrightarrow{Modulation} f_{power\_be} = \left\{(n_{\omega s} \pm 1) \pm \frac{(1-s)}{pp} \pm 2n_{be}s\right\} f_s \tag{4.5}$$

$$f_{bs} = \left\{\frac{R(1-s)}{pp} \pm n_{\omega s} \pm 2n_{be}s\right\} f_s \xrightarrow{Modulation} f_{power\_bs} = \left\{(n_{\omega s} \pm 1) \pm \frac{R(1-s)}{pp} \pm 2n_{be}s\right\} f_s \tag{4.6}$$

The fault-related sidebands of the fundamental of the stator current now appear in the low frequency range (less than ω_s) and sidebands on even harmonics of the instantaneous input power signal. For example, the $(1 \pm 2ns)f_s$ sidebands of the stator current due to rotor defects will become as $2nsf_s$ components and $(2 \pm 2ns)f_s$ sidebands in the power. Notice that some of the components in equation (4.4) can be submerged by the frequency components caused by unsymmetrical stator defects.

4.3 Hardware

The test motor was a three-phase six-pole, 415V, 4.5kW, 955rpm, delta connected, squirrel-cage induction motor made by AEI Ltd. It has 57 rotor slots and 48 stator slots. The number of coils per group is non-integer (two and two thirds), ie fractional-slot stator windings. The DC phase resistance is 4.3Ω (cold). In order to simulate an inter-turn short-circuit in the stator winding, the 'start' of a coil and the 'end' of the adjacent coil was connected to two external terminals 'A' and 'B'. When these two terminals were shorted, the corresponding DC phase resistance dropped to 4.1Ω. No further information of the winding structure is available.

When the test motor was running at full load, and the inter-turn short-circuit fault was introduced, the current i_{sc} in the faulty coil was 45A. The short-circuit could only be allowed for a few seconds to avoid the damage to the coil. i_{sc} was measured by a split core current ammeter displaying the RMS reading. It was found that i_{sc} did not change for different loading conditions, and that vibration was noticeable when the short-circuit occurred.

In order to avoid damaging the coil when the short-circuit was introduced, terminals 'A' and 'B' were connected to a variable resistor R1 (in series with a switch S1) to limit i_{sc}. Varying R1 can simulate different fault levels. The test rig is shown in figure 4.1.

The motor input power ($p_{in} = v_{12}i_1 + v_{32}i_3$) is obtained by measuring two line-to-line voltages (v_{12} and v_{32}) and two line currents (i_1 and i_3) using the split core current transformers, and the opto-isolator box for voltage that provides complete isolation between motor and I/O card. The corresponding signals are amplified, low-pass-filtered and then sampled in a single instrument that contains a four-channel instrumentation amplifier with five different gain settings (1, 3, 10, 30 and 100). The four-channel six-pole low-pass filter is available with corner frequency 2000Hz. The four-channel sample-and-hold amplifier is triggered externally by the A/D strobes generated from the data acquisition card. Each signal is sampled at 5kHz and 65536 data are recorded. Each set of measurements takes about 13 seconds. Output from

this instrument is digitised using a computer equipped with a 12-bit A/D card. p_{in} is computed and the sampled signals i_1, v_{12}, and p_{in} are stored in files. In each spectrum analysis of the input power signals, the average (DC) power is used as the zero dB level.

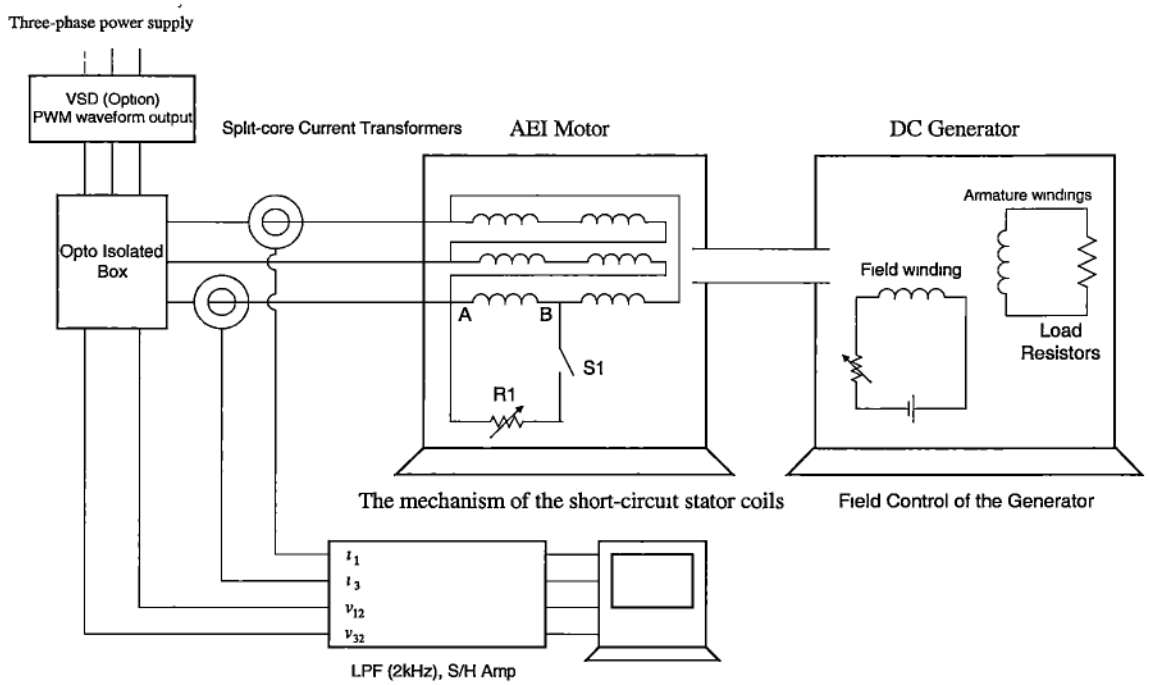

Figure 4.1: The set up of the measurements

4.4 Test Results with Mains Supply

4.4.1 Short-circuit Stator Coil

The AEI motor was loaded by a DC generator and resistor combination that can provide different load conditions. The motor was run at 0.045 per unit slip Figure 4.2 shows the sidebands (5+s)/3 and (7-s)/3 of the second harmonic (100Hz) of the unfaulted motor power. They are at 84.15Hz with –82.2 dB and 115.9Hz with –80.6dB. No sidebands appear on higher even time harmonics. Slot harmonics are insignificant in this particular motor.

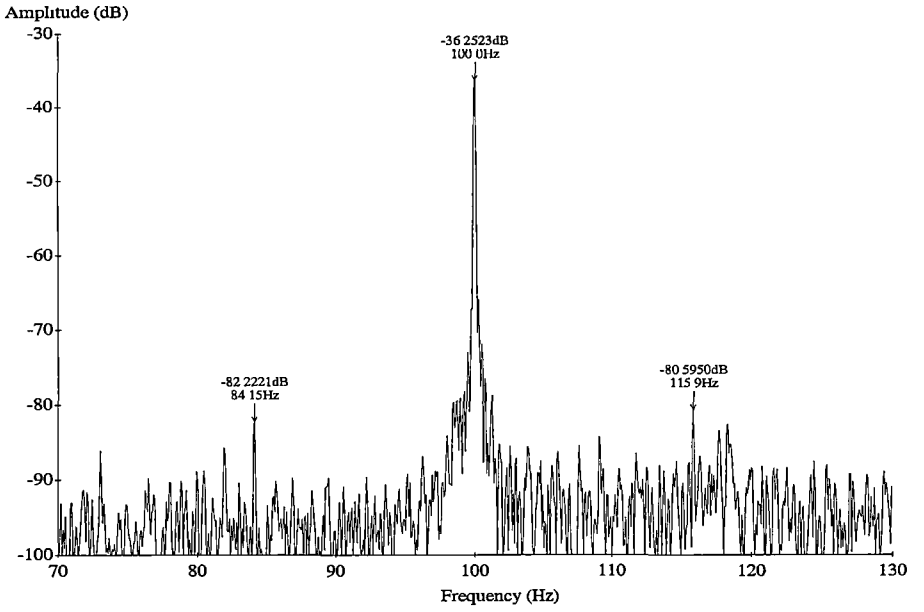

Figure 4.2: Frequency spectrum of the instantaneous power signal of AEI motor in healthy condition

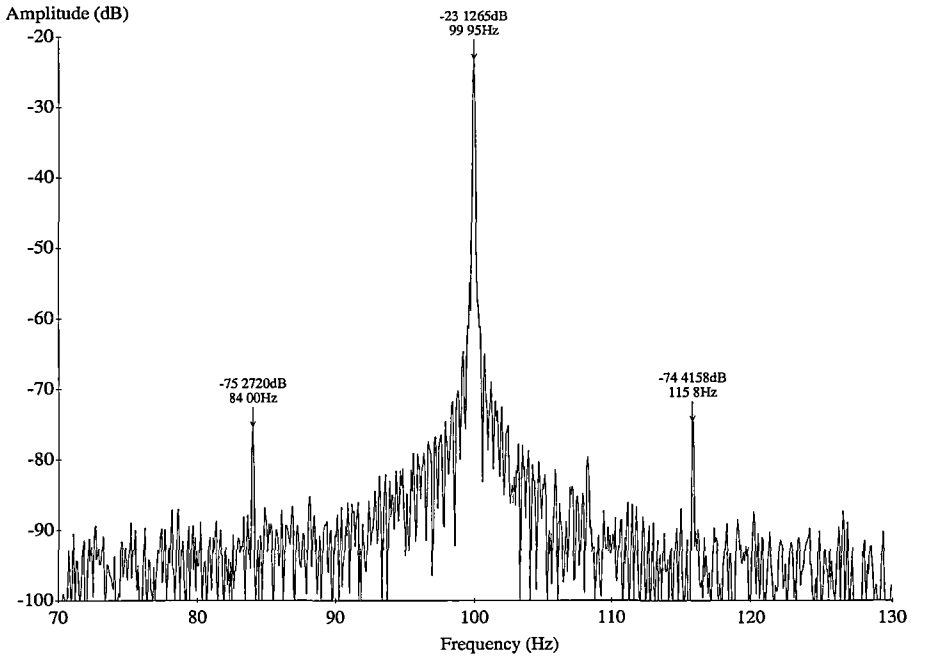

Figure 4.3: Frequency spectrum of the instantaneous power signal of AEI motor with 16A short-circuit current at the faulty stator coils

		Relative amplitude (dB)				
Frequency factor	Conditions	Slip=0.003	Slip=0.015	Slip=0.025	Slip=0.035	Slip=0.040
(5+s)/3	$i_{sc}=0$	-63.9	-67.0	-77.9	-77.6	-79.0
	$i_{sc}=16.5$A	-50.9	-51.6	-58.2	-60.1	-63.1
Amplitude change due to stator defect		13.0	15.4	19.7	17.5	15.9
2	$i_{sc}=0$	-20.4	-29.0	-41.0	-42.7	-44.3
	$i_{sc}=16.5$A	-18.0	-20.8	-25.3	-24.0	-27.7
Amplitude change due to stator defect		2.4	8.2	15.7	16.7	16.6
(7-s)/3	$i_{sc}=0$	-64.4	-67.0	-76.4	-77.6	-79.0
	$i_{sc}=16.5$A	-50.9	-52.2	-59.4	-61.2	-63.0
Amplitude change due to stator defect		13.5	14.8	17	16.4	16.0

Table 4.1: The effect of load variation on amplitude change of the stator defect related components

With the same motor load, the stator coil was shorted by closing switch S1. R1 was adjusted to limit the short-circuit current i_{sc} to 16 amps. Only the components of (5+s) f_s/3, (7-s) f_s/3 and $2\omega_s$ show 10 dB increase compared to the unfaulted case, as shown in figure 4.3.

When measurements were carried out from no load to full load, R1 was adjusted to limit i_{sc} to 16.5A. Amplitudes of (5+s) f_s/3, (7-s) f_s/3 and $2\omega_s$ frequencies are in table 4.1.

In another test, the AEI motor operated at 0.04 per unit slip, and R1 was varied to limit i_{sc} over a range of values, from 3.2A to 35A. Amplitudes of (5+s) f_s/3, (7-s) f_s/3 and $2\omega_s$ are in table 4.2.

The amplitude change of these components at different load and at different shorted coil current are plotted in figures 4.4 and 4.5. From figure 4.4, it can be seen that the effect of load variation on the $2f_s$ component is significant. As the harmonics in the supply decreases with the load, the $2f_s$ component caused by the fault may not be distinguished at low load conditions because it is less than the $2\omega_s$ caused by the time harmonics of the supply voltage and current. However, figure 4.5 shows that the

effect of load variation on the components (5+s) $f_s/3$ and (7-s) $f_s/3$ is less than that of $2f_s$.

		Relative amplitude (dB)				
Frequency factor	Conditions	$i_{sc1} = 35.0$A	$i_{sc1} = 16.0$A	$i_{sc1} = 9.5$A	$i_{sc1} = 5.3$A	$i_{sc1} = 3.2$A
(5+s)/3	$i_{sc} = i_{sc1}$	-60.1	-63.1	-69.2	-73.1	-78.5
	$i_{sc} = 0$	-79.0	-79.0	-79.0	-79.0	-79.0
Amplitude change due to stator defect		18.9	15.9	9.8	5.9	0.5
2	$i_{sc} = i_{sc1}$	-21.9	-27.4	-32.9	-37.5	-44.5
	$i_{sc} = 0$	-49.3	-49.3	-49.3	-49.3	-49.3
Amplitude change due to stator defect		22.4	16.9	11.4	6.8	0.2
(7-s)/3	$i_{sc} = i_{sc1}$	-61.0	-63.0	-66.8	-70.6	-76.8
	$i_{sc} = 0$	-79.0	-79.0	-79.0	-79.0	-79.0
Amplitude change due to stator defect		18	16	12.2	8.4	2.2

Table 4.2: The effect of shorted coil current variation on amplitude change of the stator defect related components

As the level of i_{sc} is related to unbalance of the stator impedance, the amplitude change of the fault components is proportional to the level of imbalance. It can be seen from figure 4.5 that the amplitude change of the fault-related components becomes noticeable when the shorted coil current is significant.

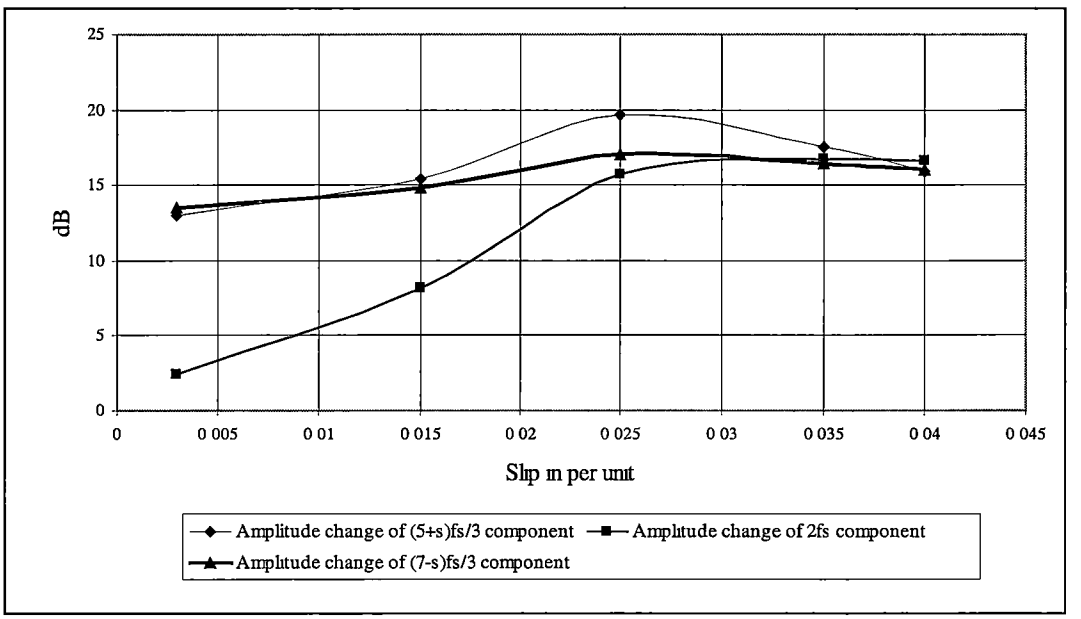

Figure 4.4: The effect of load variation on amplitude change of the stator defect related components

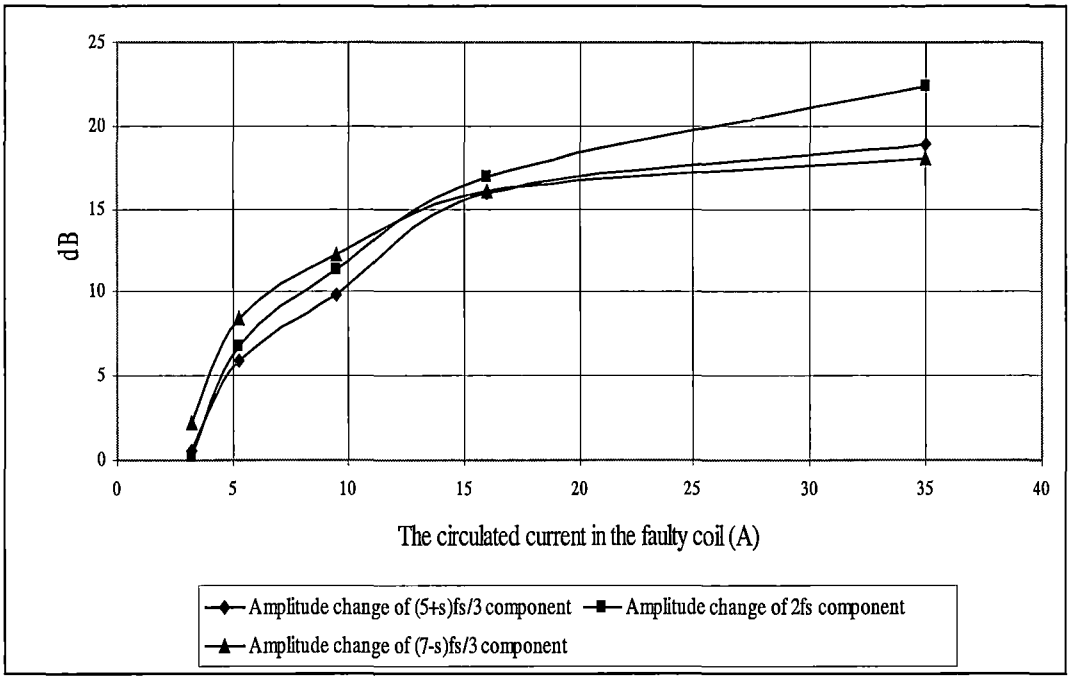

Figure 4.5: The effect of shorted coil current on amplitude change of the stator defect related components

4.4.2 Broken Rotor Bars

Figure 4.6 shows the spectrum of input power when the motor with the good rotor. The only distinct peak in the low frequency range (0 to 40Hz) is the speed frequency at 16.17Hz with –48.8dB. The $2sf_s$ component is about –70dB.

The rotor of the same motor was then deliberately damaged by having a bar cut through at the end ring. It was first loaded at 0.029 per unit slip. Figure 4.7 shows the corresponding frequency spectrum of the instantaneous power from 0 to 40Hz. The component at 2.9Hz has the largest amplitude with –47.0dB, compared to –70dB, the 'good rotor' case, shown in figure 4.6.

The $4sf_s$ (5.79Hz at –59.5dB) and $6sf_s$ (8.77Hz at –73.8dB) components are visible. There are another two groups of fault-related components in the same frequency range; the $\pm 2nsf_s$ sidebands of f_r components (13.28Hz, 16.17Hz, 19.07Hz, and 22.05Hz) and $2f_r$ (26.55Hz, 29.45Hz, 32.35Hz and 35.32Hz). The amplitude of these components are about –70dB.

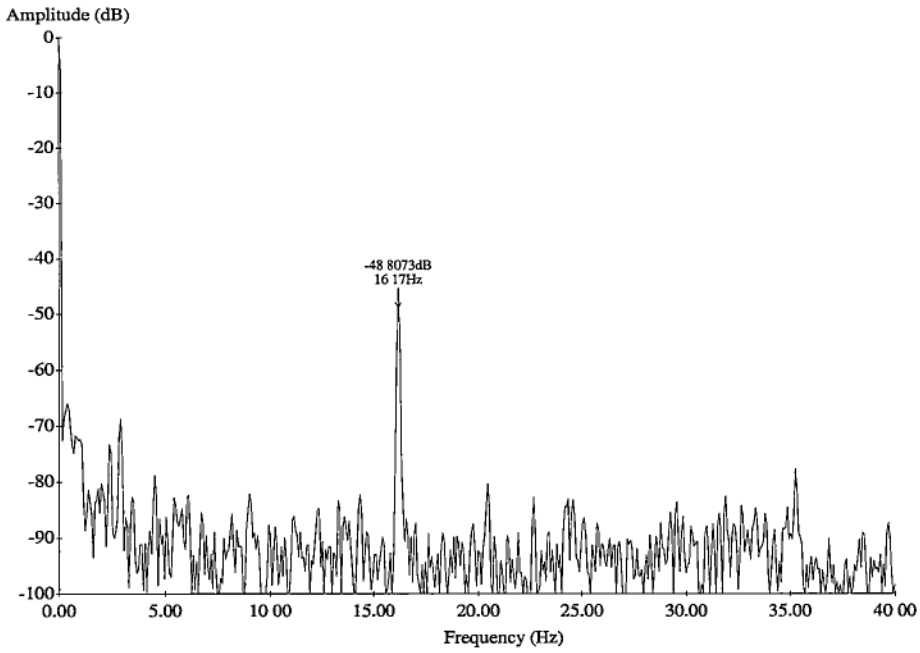

Figure 4.6: Frequency spectrum of the instantaneous power signal of AEI motor in healthy condition at 0.029 per unit slip

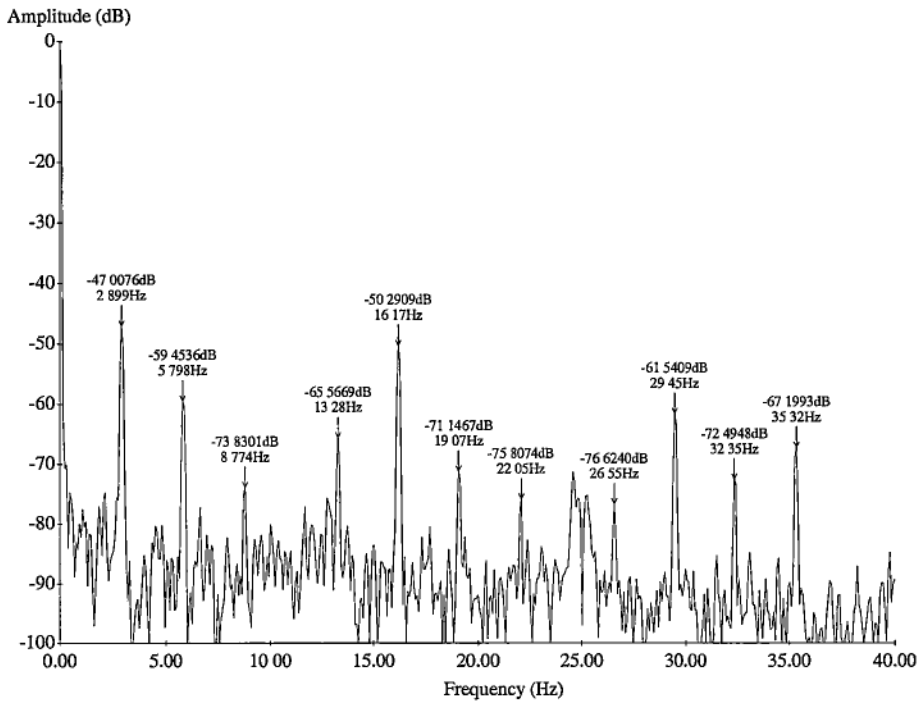

Figure 4.7: Frequency spectrum of the instantaneous power signal of AEI motor with the one cut rotor at 0.029 per unit slip

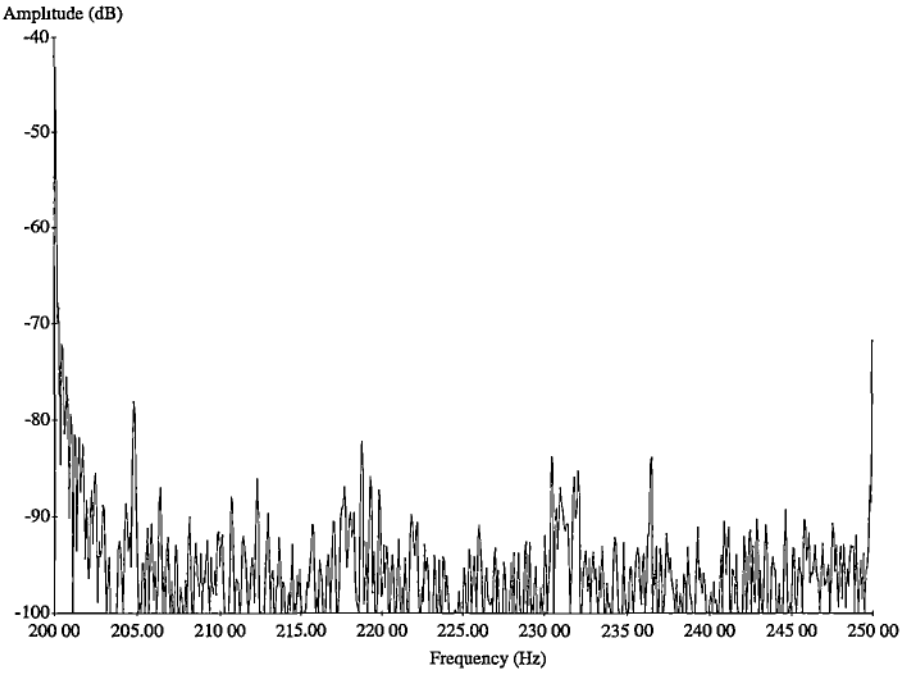

Figure 4.8: Same spectrum as in figure 4.6 but at 200Hz to 250Hz range

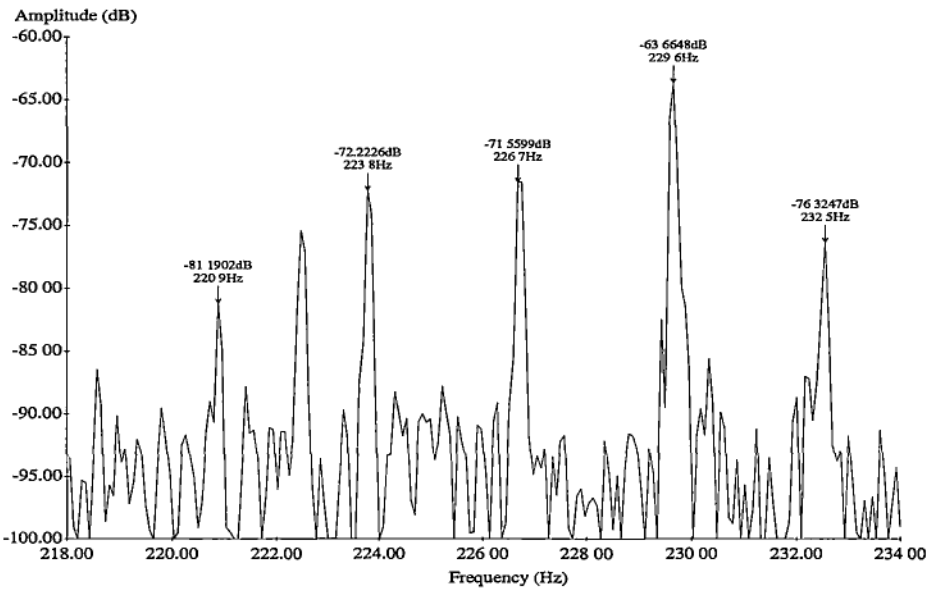

Figure 4.9: Same spectrum as in figure 4.7 but at 200Hz to 250Hz range and highlighting the rotor defect-related frequencies

Another interesting result at the fourth time harmonic is the $\pm 2nsf_s$ sidebands on the $[4+2(1-s)/pp]f_s$ component. Significant peaks can be found at 220.9Hz ($[4-6s+2(1-s)/pp]f_s$), 223.8Hz ($[4-4s+2(1-s)/pp]f_s$), 226.7Hz ($[4-2s+2(1-s)/pp]f_s$) and 232.5Hz ($[4+2s+2(1-s)/pp]f_s$). The results are shown in figure 4.9. Figure 4.8 shows that these are almost undetectable for a good rotor.

More measurements were carried out on the same motor from low load to full load. Results are summarised in table 4.3. Several trends are present:

- More information is available for identifying the fault rotor when the load is increased.
- At no load, the $2nsf_s$ components and sidebands are either too low in amplitude or too close together, and could not be distinguished.
- The $\pm 2nsf_s$ sideband components were all at very low amplitude ie more than 60dB down (from the DC power).
- The $2sf_s$, $4sf_s$ and $6sf_s$ is the group of rotor fault-related components that has the largest change in amplitude when the rotor is damaged, as shown in figure 4.10.
- The $\pm 2nsf_s$ sidebands of f_r and $2f_r$ components are the second large group of rotor fault-related frequency components. They even could be noticed at low load condition, shown in figure 4.11.

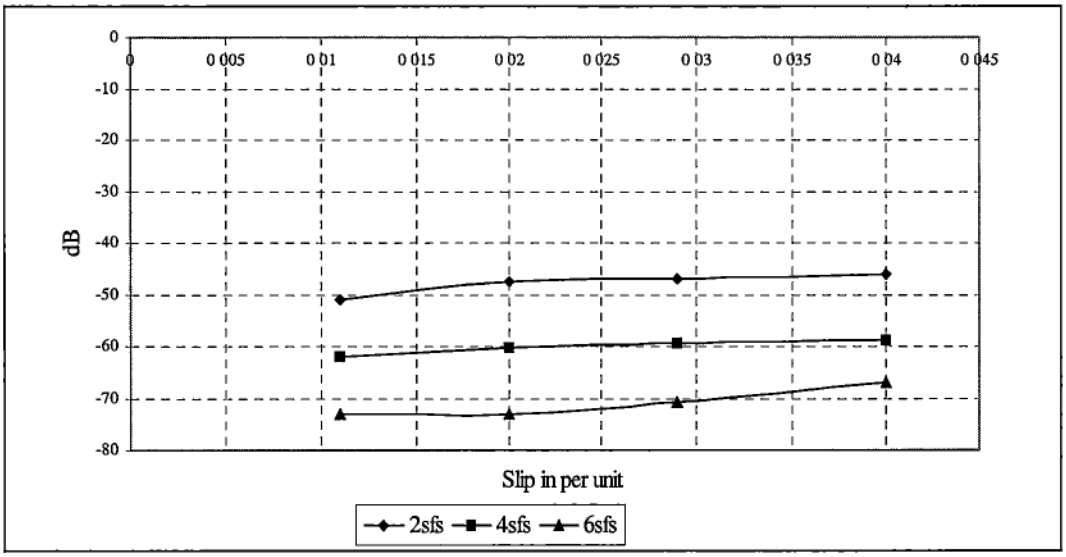

Figure 4.10: The effect of load variation on amplitude change of the $2sf_s$, $4sf_s$ and $6sf_s$ components with a broken bar in the rotor

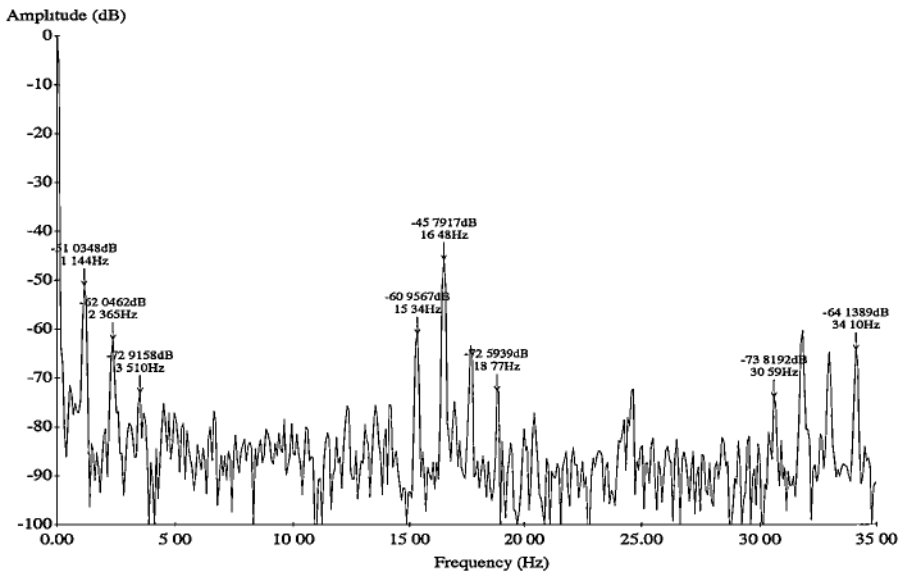

Figure 4.11: Frequency spectrum of the instantaneous power signal of AEI motor with the one rotor bar. Slip = 0.011 pu (low load)

Frequency factor	Slip=0.004		Slip=0.011		Slip=0.020		Slip=0.029		Slip=0.040	
	Hz	dB	Hz	dB	Hz	dB	Hz	dB	Hz	dB
2s			1.14	-51.0	2.14	-47.6	2.90	-47.0	3.97	-46.0
4s			2.37	-62.0	4.27	-60.4	5.80	-59.5	7.94	-58.9
6s			3.51	-72.9	6.49	-72.9	8.77	-73.8	12.05	-67.1
fr-2s			15.34	-61.0	14.19	-64.5	13.28	-65.6		
fr	16.63	-42.2	16.48	-45.8	16.33	-48.4	16.17	-50.3	16.02	-51.9
fr+2s			17.62	-63.4	18.64	-67.4	19.07	-71.1	19.99	-76.3
fr+4s					20.60	-74.8	22.05	-75.1		
2fr-4s			30.59	-73.8	28.38	-74.5	26.55	-76.6	23.96	-77.1
2fr-2s			31.81	-60.4	30.52	-61.3	29.45	-61.5	28.00	-62.3
2fr	33.57	-68.1	32.96	-64.7	32.65	-68.9	32.35	-72.5	31.97	-71.4
2fr+2s			34.10	-64.1	34.79	-65.3	35.32	-67.2	35.97	-69.4
4-8s+2(1-s)/3					222.2	-83.9			212.2	-74.1
4-6s+2(1-s)/3					224.2	-81.8	220.9	-81.2	216.0	-78.2
4-4s+2(1-s)/3			230.7	-67.5	226.4	-73.0	223.8	-72.2	220.0	-72.6
4-2s+2(1-s)/3			229.5	-73.8	228.5	-70.5	226.7	-71.6	224.0	-71.0
4+2(1-s)/3	233.3	-67.3	231.9	-63.2	230.7	-65.7	229.6	-63.7	228.0	-63.1
4+2s+2(1-s)/3					232.8	-77.1	232.5	-76.3	231.9	-76.7
4+4s+2(1-s)/3					234.9	-81.2			235.9	-85.2
4+6s+2(1-s)/3									240.0	-83.5
4+8s+2(1-s)/3									244.0	-81.3
4+10s+2(1-s)/3									248.1	-83.6
2-6s									87.8	-85.5
2-4s			97.66	-70.1	95.75	-72.6	94.22	-76.3	92.0	-80.0
2-2s			98.88	-62.2	97.96	-70.1	97.12	-72.6	95.98	-75.0
2	100	-18.4	100	-29.0	100	-38.0	100	-42.3	100	-49.0
2+2s							103.0	-77.6	104	-78.1
2+4s							106.6	-76.5		
2+6s									112.1	-86.8
4-8s									184.0	-83.3
4-6s					194.0	-81.2	191.4	-81.0	188.0	-79.3
4-4s			197.8	-74.5	196.1	-78.1	194.3	-72.7	192.0	-72.3
4-2s			198.9	-70.5	197.9	-68.2	197.2	-76.7	196.0	-78.9
4+2s			201.2	-78.0						
4+4s			202.4	-80.3	204.0	-81.1	206.7	-79.5		
4+6s					206.1	-83.3			212.2	-74.1
4+8s										
6-8s					291.7	-77.5	288.5	-75.4	284.0	-71.8
6-6s					293.8	-78.5	291.5	-78.4	288.0	-82.3
6-4s					295.9	-74.3	294.4	-72.9	292.0	-72.9
6-2s					298.2	-65.1	297.3	-64.2	295.9	-66.8
6+4s									308.0	-82.1
4+6s									312.2	-79.9
6+8s									316.0	-80.2

Table 4.3: The effect of load variation on the rotor fault-related components

4.5 Extra Frequencies of Input Motor Power Signal with PWM Waveform Supply

The motor currents of variable frequency drives with PWM waveform voltage output are nonsinusoidal. If the stator windings are balanced delta, or star-connected with an isolated neutral, the triplen harmonics should not produce any motor current. Different schemes of PWM switching strategies may be used to eliminate selected low order time harmonics. For example, figures 4.12 and 4.15 show the stator current spectra of the AEI motor supplied by a Renold VFD drive and a Zener VSC 2000 drive, at 40Hz fixed frequency (a 2kHz low pass filter was used).

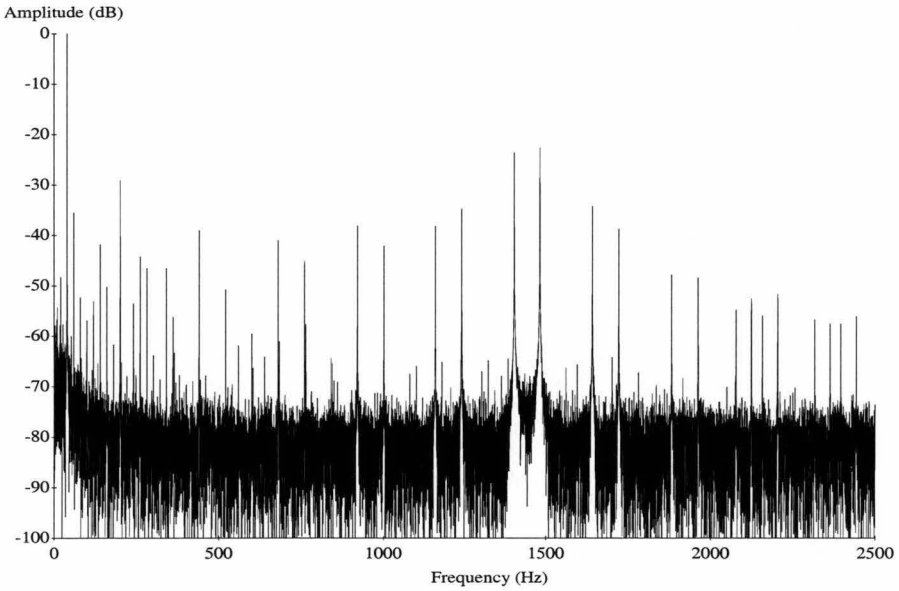

Figure 4.12: Stator current spectrum of the AEI motor supplied by Renold drive at 40Hz, full load, healthy condition

The output current waveform from the Renold drive has significant harmonics at $(5+6n)f_s$ and $(7+6n)f_s$ where n is positive integer, including zero. The largest pair of harmonics are the $35f_s$ and $37f_s$ at about –20dB. The rest of the components are about –45dB.

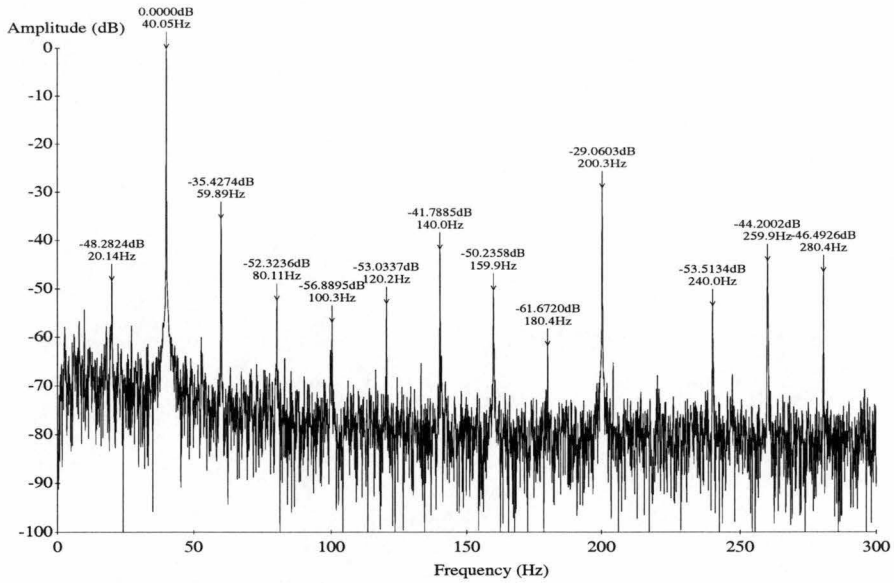

Figure 4.13: Stator current spectrum of the AEI motor supplied by Renold drive at 40Hz, full load, healthy condition (0 to 300Hz)

Looking closely at the low frequency range (0 to 700Hz in figure 4.12), several prominent peaks are visible. Figures 4.13 and 4.14 show zooms of the same spectrum but from 0 to 300Hz and 300 to 750Hz. The prominent peaks are labelled in the diagrams, and summarised in table 4.4. The fifth harmonic, 200.3Hz has the largest amplitude, -29.1dB. Besides the time harmonics, peaks are:

$(100-f_s)$=59.89Hz, $|(100-3f_s)|$=20.14Hz, $|(100-5f_s)|$=100.3Hz,

$|(100-6f_s)|$=140.0Hz $|(100-7f_s)|$=180.4Hz $|(100-9f_s)|$=259.9Hz

Innes [22] identified one component, $100-f_s$, and defined it as 'reflected frequency'. The origin of this component may be the rectification of the mains to produce the DC link voltage. The ripples in this DC voltage pass through the modulation process and form the reflected frequency.

The reflected frequency and its related components in the current are summarised in table 4.5. These components are present in voltage, and corresponding components are in the instantaneous power signal as shown in table 4.4. Only the fundamental, second time harmonic, and reflected frequency components in voltage are included.

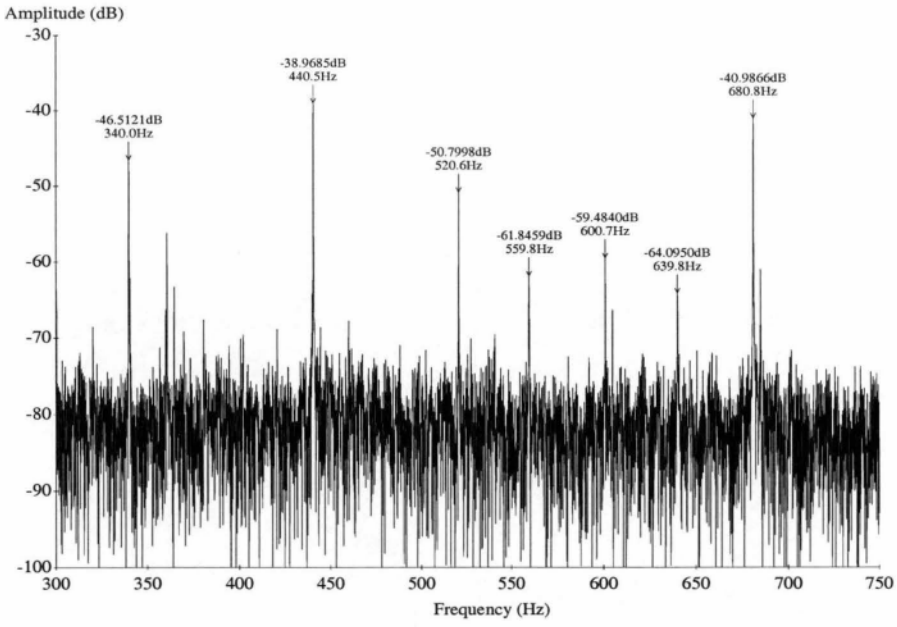

Figure 4.14: Stator current spectrum of the AEI motor supplied by Renold drive at 40Hz, full load, healthy condition (300 to 750Hz)

Frequency components in current Hz		Frequency components in voltage Hz					
		f_s	$-f_s$	$2f_s$	$-2f_s$	$100-f_s$	f_s-100
		40.05	-40.05	80.1	-80.1	59.9	-59.9
$2f_s$	80.1	120.15	40.05	160.20	0.00	180.05	20.20
$3f_s$	120.2	160.25	80.15	200.30	40.10	180.10	60.30
$4f_s$	159.9	199.95	119.85	240.00	79.80	219.80	100.00
$5f_s$	200.3	240.35	160.25	280.40	120.20	260.20	140.40
$6f_s$	240.0	280.05	199.95	320.10	159.90	299.90	180.10
$7f_s$	280.4	320.45	240.35	360.50	200.30	340.30	220.50
$11f_s$	440.5	480.55	400.45	520.60	360.40	500.40	380.60
$13f_s$	520.6	560.65	480.55	600.70	440.50	580.50	460.70
$14f_s$	559.8	599.85	519.75	639.90	1080.40	619.70	499.90
$15f_s$	600.7	640.75	560.65	680.80	520.60	660.60	540.80
$16f_s$	639.8	679.85	599.75	719.90	559.70	699.70	579.90
$17f_s$	680.8	720.85	640.75	760.90	600.70	740.70	620.90
$100-f_s$	59.9	99.95	19.85	700.65	-20.20	119.80	0.00
$100-3f_s$	-20.14	19.91	-60.19	59.96	-100.24	39.76	-80.04
$100-5f_s$	-100.3	-60.25	-140.35	-20.20	-180.40	-40.40	-160.20
$100-6f_s$	-140.0	-99.95	-180.05	-59.90	-220.10	-80.10	-199.90
$100-7f_s$	-180.4	-140.35	-220.45	-100.30	-260.50	-120.50	-240.30
$100-9f_s$	-259.9	-219.85	-299.95	-179.80	-340.00	-200.00	-319.80
$100-11f_s$	-340.0	-299.95	-380.05	-259.90	-420.10	-280.10	-399.90
		Frequency components in the instantaneous input power signal Hz					

Table 4.4: The harmonics of the current, voltage and power of AEI motor supplied by Renold drive

Frequency components in current	$2f_s$	$3f_s$	$4f_s$	$5f_s$	$6f_s$	$7f_s$
Hz	80.1	120.2	159.9	200.3	240.0	280.4
dB	-52.3	-53.0	-50.2	-29.1	-53.5	-46.5
Frequency components in current	$11f_s$	$13f_s$	$14f_s$	$15f_s$	$16f_s$	$17f_s$
Hz	440.5	520.6	559.8	600.7	639.8	680.8
dB	-39.0	-50.8	-61.8	-59.5	-64.1	-41.0
Frequency components in current	$100-f_s$	$100-3f_s$	$100-5f_s$	$100-6f_s$	$100-7f_s$	$100-9f_s$
Hz	59.9	-20.14	-100.3	-140.0	-180.4	-259.9
dB	-35.4	-48.3	-56.9	-41.8	-61.7	-44.2
Frequency components in current	$100-11f_s$					
Hz	-340.0					
dB	-46.5					

Table 4.5: The harmonics of the stator current of AEI motor supplied by Renold drive

For the Zener drive, there are two groups of harmonics with significant amplitude, as shown in figure 4.15. They are: $1000\pm f_s$, $1000\pm 2f_s$, $1000\pm 4f_s$ and $2000\pm f_s$, $2000\pm 2f_s$, $2000\pm 4f_s$. The largest pair of harmonics in the 1000Hz group is $1000\pm 2f_s$; and $2000\pm 2f_s$ in the 2000Hz group; at about –25dB. The rest are below –50dB.

The amplitude of prominent peaks up to 350Hz are in table 4.6. The significant time harmonics at the low frequency range are only up to 7th harmonic, at 279.4Hz, –50.2dB. The reflected frequency and its related harmonics are in (100- f_s)=60.04Hz, |(100-6 f_s)|=139.80Hz, |(100-9 f_s)|=260.0Hz, and |(100-11 f_s)|=339.80Hz.

Frequency components in current	$2f_s$	$3f_s$	$4f_s$	$5f_s$	$6f_s$	$7f_s$
Hz	79.8	119.7	159.6	199.6	239.9	279.4
dB	-79.8	-47.6	-46.1	-55.5	-62.2	-50.2
Frequency components in current	$100-f_s$	$100-6f_s$	$100-9f_s$	$100-11f_s$		
Hz	60.0	-139.8	-260.0	-339.8		
dB	-57.2	-62.9	-45.0	-46.5		

Table 4.6: The harmonics of the stator current of AEI motor supplied by Zener drive

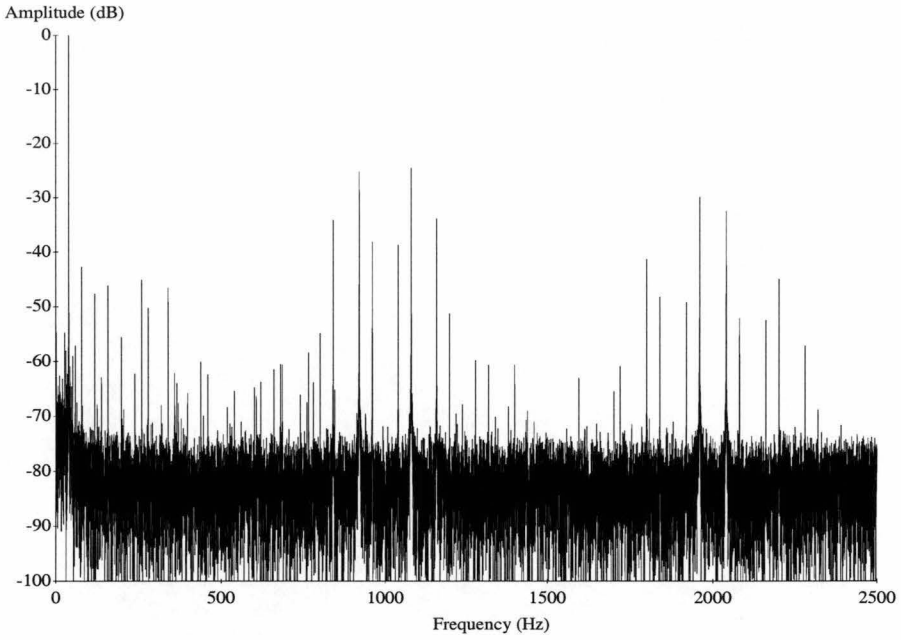

Figure 4.15: Stator current spectrum of the AEI motor supplied by Zener drive at 40Hz, full load, healthy condition

The amplitude of these components is lower than the stator current output from the Renold drive. The predicted frequency components of power from the Zener drive are summarised in table 4.7. Only the fundamental, second time harmonic, and reflected frequencies of voltage waveform are included.

Frequency components in current Hz		Frequency components in voltage Hz					
		f_s	$-f_s$	$2f_s$	$-2f_s$	$100-f_s$	f_s-100
		40.05	-40.05	80.1	-80.1	59.9	-59.9
$2f_s$	79.8	119.85	39.75	159.90	-0.30	139.70	19.90
$3f_s$	119.7	159.75	79.65	199.80	39.60	179.60	59.80
$4f_s$	159.6	199.65	119.55	239.70	79.50	219.50	99.70
$5f_s$	199.6	239.65	159.55	279.70	119.50	259.50	139.70
$6f_s$	239.9	279.95	199.85	320.00	159.80	299.80	180.00
$7f_s$	279.4	319.45	239.35	359.50	199.30	339.30	219.50
$100-f_s$	60.04	100.09	19.99	140.14	-20.06	119.94	0.14
$100-6f_s$	-139.8	-99.75	-179.85	-59.70	-219.90	-79.90	-199.70
$100-9f_s$	-260.0	-219.95	-300.05	-179.90	-340.10	-200.10	-319.90
$100-11f_s$	-339.8	-299.75	-379.85	-259.70	-419.90	-279.90	-399.70
		Frequency components in the instantaneous input power signal Hz					

Table 4.7: The harmonics of the stator current of AEI motor supplied by Zener drive

The reflected frequency and its related harmonics are an interesting phenomenon, especially if they are present for all drives, because it can potentially coincide with one of the fault-related sideband peaks in current or in power. This could make it appear as though a fault were present when there is none.

The extra frequencies caused by the stator and rotor defects that were discussed in the previous section should still exist in the instantaneous input power signal when supplied with variable frequency drive. Similar sets of measurements as were done on the AEI motor with mains supply, but now supplied from the Renold and the Zener drives.

4.6 Test Results with Variable Frequency Supply

4.6.1 Short-circuit Stator Coils

The frequency spectrum of the instantaneous input power of the AEI motor supplied by the Renold drive at 40Hz, 0.046 pu slip motor, in healthy condition, is shown in figure 4.16 (0 to 300Hz range). The background noise level is about –70dB, which is 20dB higher than the mains supply cases. The fault-related components predicted from Penman's analysis are not distinguishable. The $4f_s$ component at 160.2Hz has the largest amplitude, 31.6dB down from the DC power.

With a short-circuit stator coil, (i_{sc} was limited at 15A) the $2f_s$ component increased more than 10dB, shown in figure 4.17 (and compared to figure 4.16). No significant change in amplitude of the other components can be seen. Prominent peaks and their amplitudes are summarised in table 4.8.

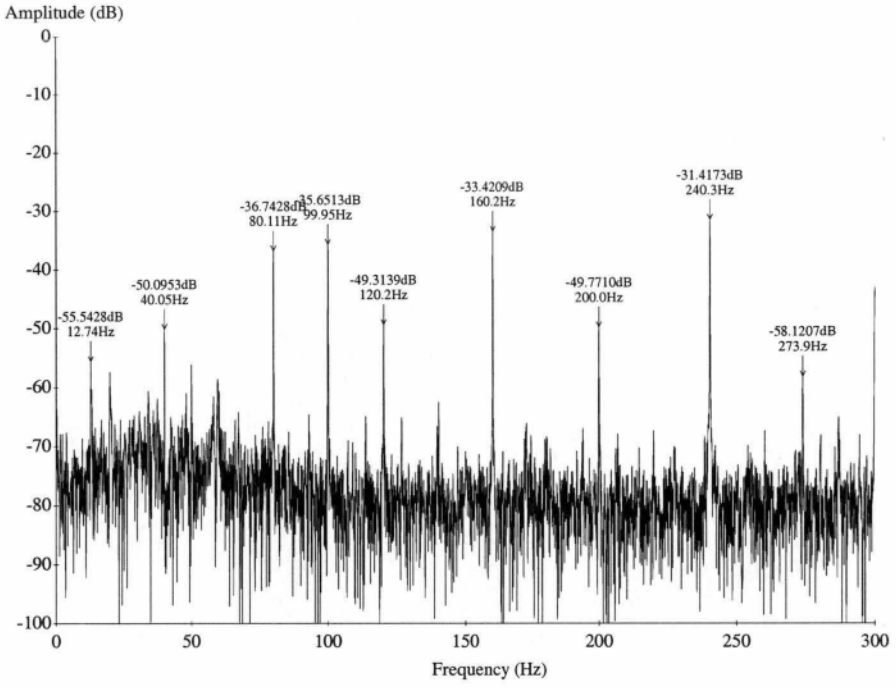

Figure 4.16: The spectrum of the power signal, supplied by Renold drive, at 40Hz, full load, in healthy condition

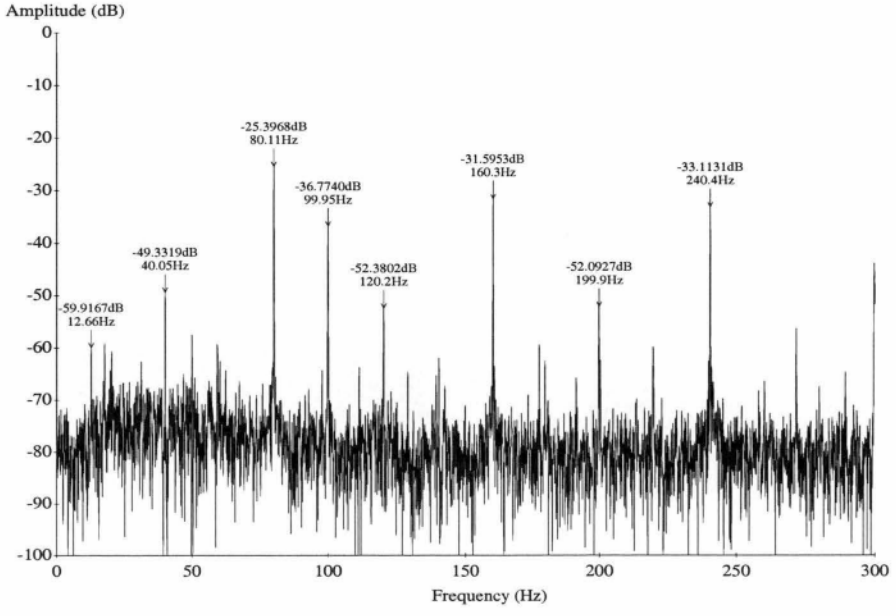

Figure 4.17: The spectrum of the power signal, supplied by Renold drive, at 40Hz, full load, with 15A short-circuit current in the faulty stator coil

When the AEI motor was supplied by the Zener drive, and operated at the same condition, the corresponding frequency spectrum of the power signal is shown in figure 4.18. The reflected frequency and the 5th harmonic were suppressed to –61.3dB and –60.5dB respectively. The second harmonic increased to –28.5dB for 15A short-circuit stator coil current, as shown in figure 4.19. The prominent peaks and their amplitudes are summarised in table 4.8.

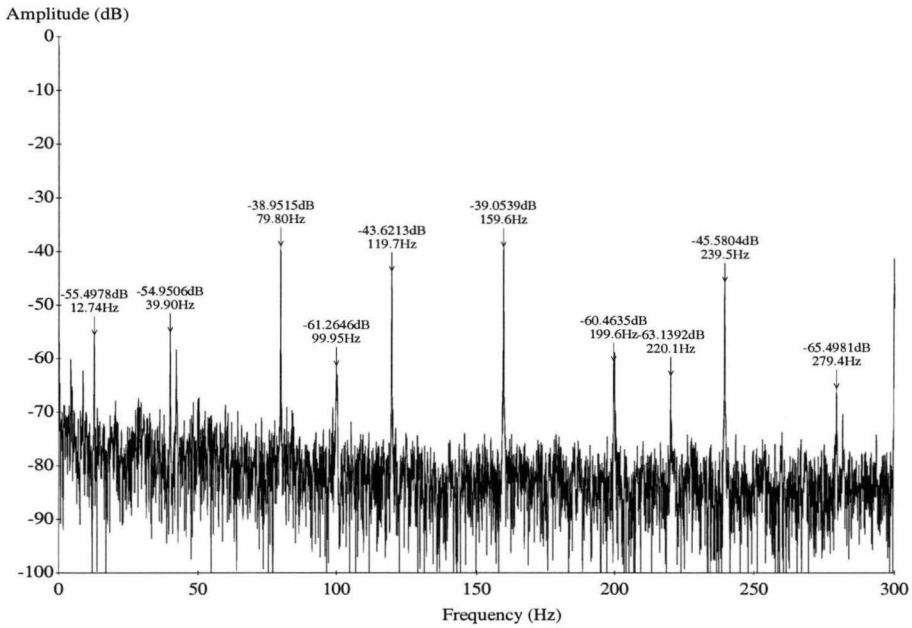

Figure 4.18: The spectrum of the power signal, supplied by Zener drive, at 40Hz, full load, in healthy condition

		Renold drive		Zener drive	
		No fault	i_{sc}=15A	No fault	i_{sc}=15A
	Hz	dB	dB	dB	dB
f_r	12.74	-55.5	-60.0	-55.5	-59.8
f_s	40.05	-50.1	-49.3	-55.0	-50.6
$2f_s$	80.11	-36.7	-25.4	-39.0	-28.5
$100-f_s$	99.95	-35.7	-36.7	-61.3	-65.0
$3f_s$	120.2	-49.3	-52.4	-43.6	-43.8
$4f_s$	160.2	-33.4	-31.6	-39.1	-38.4
$5f_s$	200.0	-49.8	-52.1	-60.5	-59.9
$6f_s$	240.3	-31.4	-33.1	-45.6	-46.6
$100-10f_s$	300.0	-43.0	-44.7	-41.5	-41.0

Table 4.8

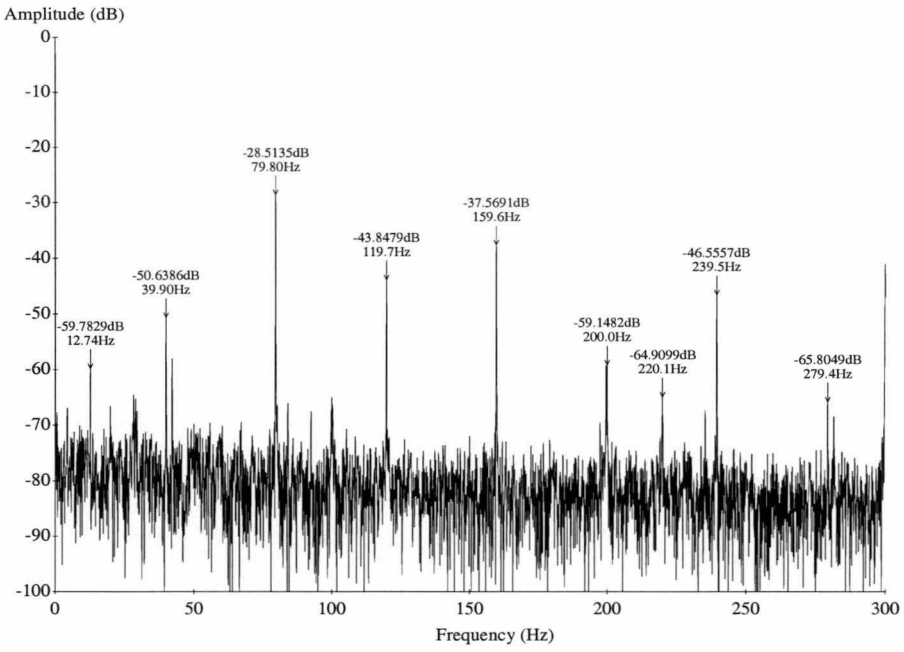

Figure 4.19: The spectrum of the power signal, supplied by Zener drive, at 40Hz, full load, with 15A short-circuit current in the faulty stator coil

4.6.1.1 The effect of different short-circuit current in the 'faulty' coil on second harmonic

Measurements of the $2f_s$ component in power at different shorted coil currents are summarised in table 4.9 and plotted in figure 4.20. It is expected that the relative amplitude of the $2f_s$ component in power will increase (with i_{sc}) and in fact significant increase occurs even at a relatively low shorted-coil current. The Renold drive has, in general, a larger amplitude of second harmonic than the Zener drive, which may be due to the higher amplitude of harmonic produced by the Renold drive.

	The relative amplitude of $2f_s$ component in power dB	
	Renold drive	Zener drive
No fault, i_{sc}=0A	-36.7	-39.0
i_{sc}=10A	-27.3	-33.2
i_{sc}=15A	-25.4	-28.5
i_{sc}=20A	-23.5	-25.6
i_{sc}=25A	-22.8	-23.6

Table 4.9

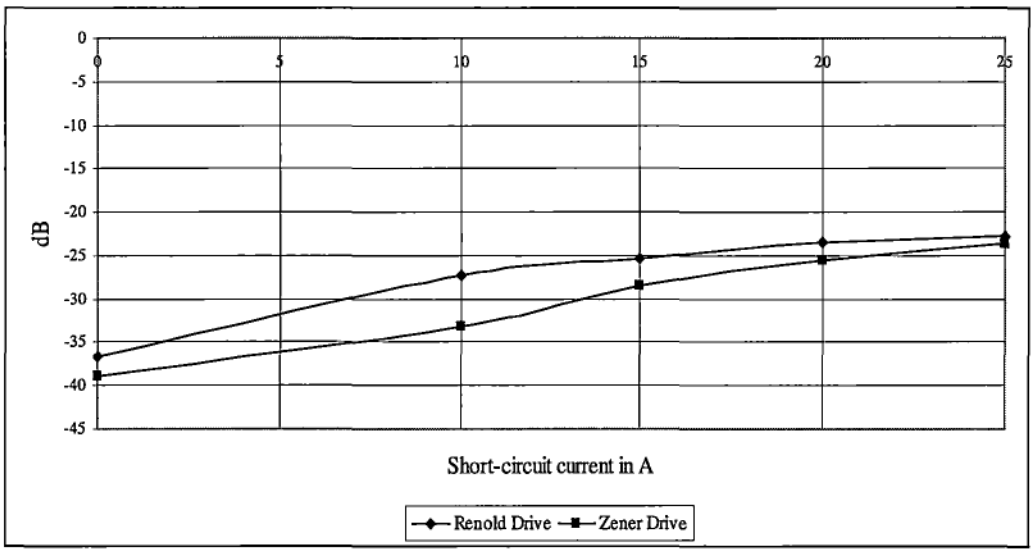

Figure 4.20: Variation of the second harmonic due to different short-circuit current

4.6.1.2 The effect of load variation on second harmonic

With supply frequency fixed at 40Hz, measurements were taken from no load to full load. i_{sc} was limited at 19A, and values of second harmonic in power are summarised in table 4.10.

	The relative amplitude of $2f_s$ component in power dB					
	Renold drive			Zener drive		
	No fault	i_{sc}=19A	dB change	No fault	i_{sc}=19A	dB change
Slip=0.046	-36.7	-23.5	13.2	-39.0	-25.6	13.4
Slip=0.024	-32.0	-21.6	10.4	-35.4	-23.2	12.2
Slip=0.014	-28.1	-19.7	8.4	-30.3	-22.1	8.2
Slip=0.001	-17.3	-14.0	3.3	-21.4	-15.5	5.9

Table 4.10

As the load is reduced, the stator current is dominated by the magnetising current; the third harmonic current increases, as also does the $2f_s$ power component. The change of the amplitude of the $2f_s$ power component due to the shorted-coil becomes unnoticeable at low load as illustrated in figure 4.21. The results again show that in general, the $2f_s$ power component from the Zener drive is relatively lower than that from the Renold drive.

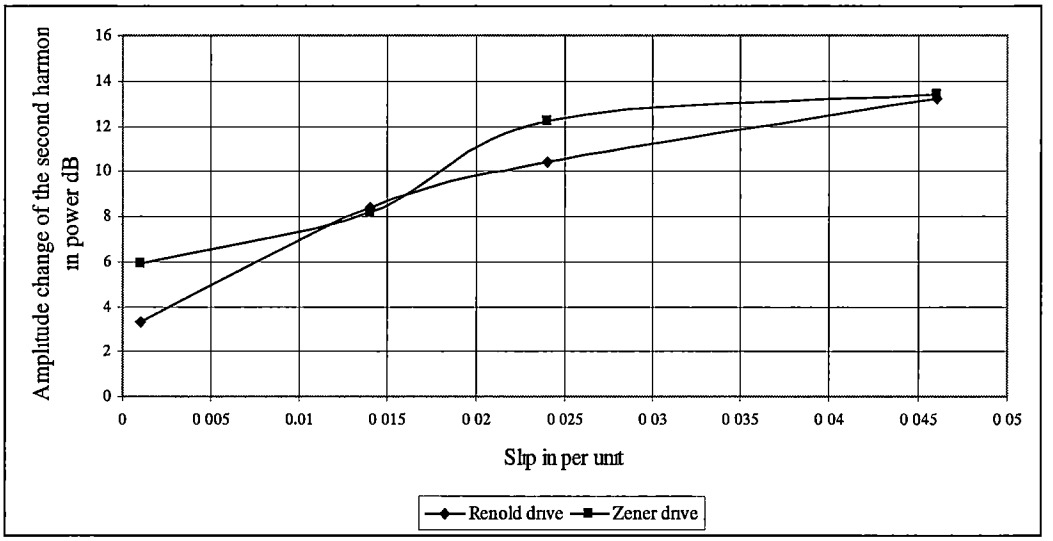

Figure 4.21: Variation of the second harmonic due to different load

4.6.1.3 The effect of different operating frequency on second harmonic

The test motor was fully loaded with supply frequency fixed at 45Hz, 40Hz, 30Hz, and 20Hz. The short-circuit current in the 'faulty' stator coil was limited to 19A. The results of second harmonic in power are summarised in table 4.11 and figure 4.22.

Operating Frequency Hz	The relative amplitude of $2f_s$ component in power dB					
	Renold drive			Zener drive		
	No fault	i_{sc}=19A	dB change	No fault	i_{sc}=19A	dB change
45	-44.3	-24.9	19.4	-43.1	-28.4	15.7
40	-36.7	-23.5	13.2	-39.0	-25.6	13.4
30	-22.4	-19.0	3.4	-35.1	-22.6	12.5
20	-15.8	-13.0	2.3	-31.0	-20.6	10.4

Table 4.11

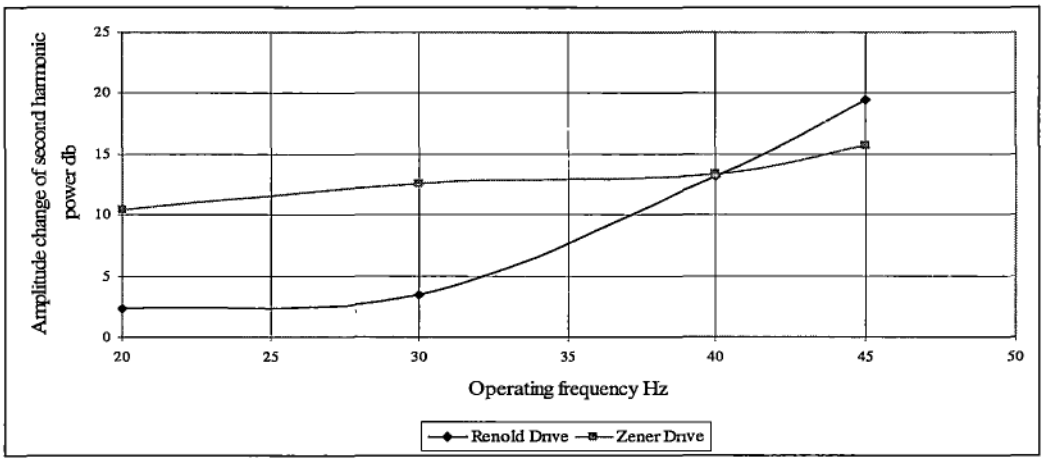

Figure 4.22: Variation of the second harmonic due to different operating frequency

The amplitude of $2f_s$ power component (Zener drive) decreases by 5dB as supply frequency decreases from 45Hz to 20Hz. The Renold drive shows a 15dB decrease in the $2f_s$ power component at low supply frequency which implies that the time harmonics in the supply increases. It may be due to following reasons:

- When the supply frequency is low, the equivalent motor reactance is reduced. The high-order time harmonics cannot be filtered out adequately by the machine reactance.

- As the anti-alising low-pass filter (2kHz) was initially designed for 50Hz fundamental, the highest harmonics would be the 40^{th}. However, when the operating frequency is reduced to 20Hz, this upper limit will be increased to the 100^{th} harmonic. The signals will contain much higher harmonics.

- Different schemes of PWM switching strategies may also affect the harmonic contents of the voltage and current waveforms output from the drives. For example, figure 4.23 shows the frequency spectrum of the instantaneous power of the AEI motor supplied by the Renold drive operating at 20Hz. The harmonics contents amplitudes of more than –40dB appear over the whole range of frequencies. Figure 4.24 shows the frequency spectrum of the power when the AEI motor is supplied by the Zener drive. Groups of harmonics of more than –40dB only appear around DC, 1000Hz and 2000Hz. Significant harmonic suppression is achieved elsewhere.

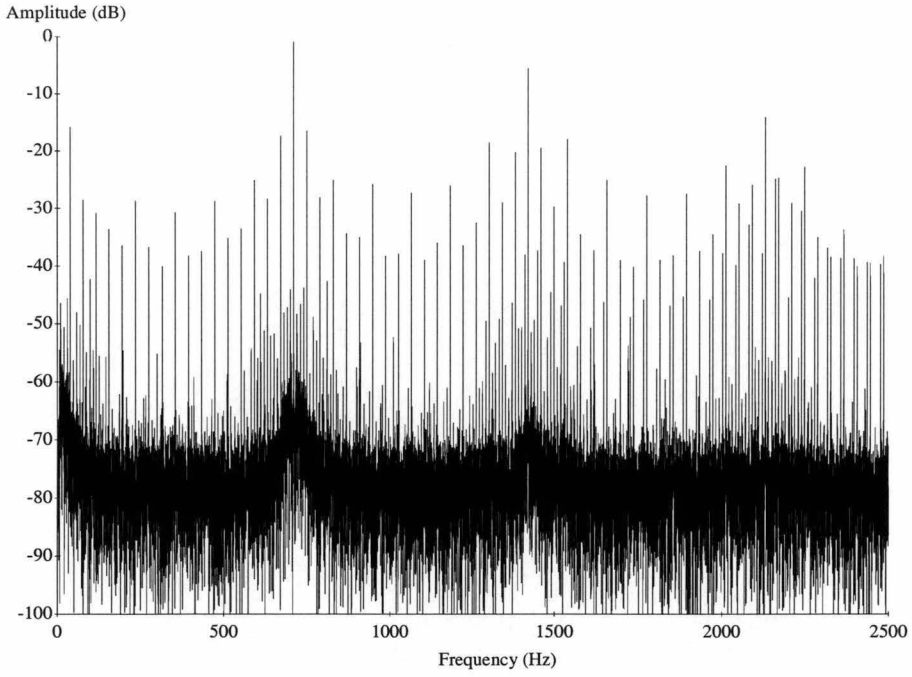

Figure 4.23: The spectrum of the input power of AEI motor supplied by Renold drive operating at 20Hz

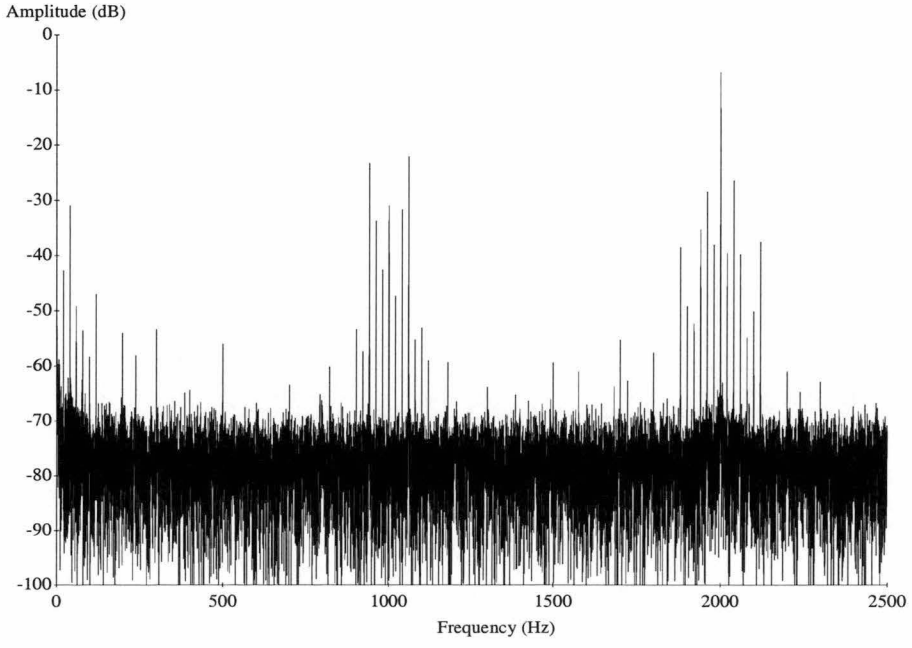

Figure 4.24: The spectrum of the input power of AEI motor supplied by Zener drive operating at 20Hz

4.6.2 Broken Rotor Bars

The AEI motor with one cut bar rotor was supplied by the Zener drive at fixed frequency, 40Hz, and loaded to 0.042 per unit slip. Figure 4.26 shows the frequency spectrum of the corresponding power signal from 0 to 25Hz. The $2sf_s$ and $4sf_s$ components are (at 3.36Hz) –47.8dB and (at 6.79Hz) -63.8dB.

Another rotor fault-related frequency component in this range is $2(f_r - sf_s)$ (22.13Hz) at –61.3dB. The 4.349Hz and 8.698Hz components are independent of load, although they are not significant (only 10dB above the noise floor). They even appear even when the motor is in a healthy condition, as shown in figure 4.25. The cause of these components is mystery.

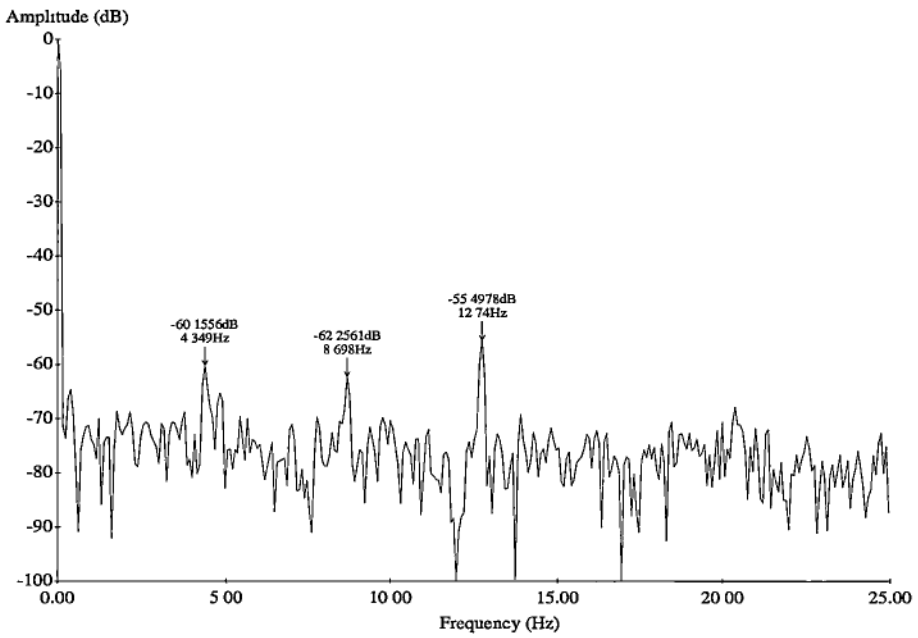

Figure 4.25: The spectrum of the input power of AEI motor supplied by Zener drive operating at 40Hz, 0.042 per unit slip in healthy condition

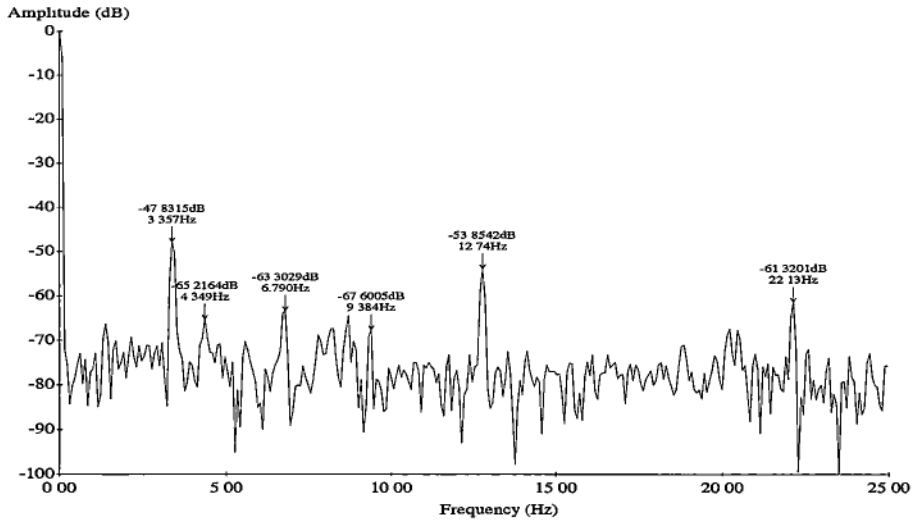

Figure 4.26: The spectrum of the input power of AEI motor supplied by Zener drive operating at 40Hz, 0.042 per unit slip with the one cut rotor bar

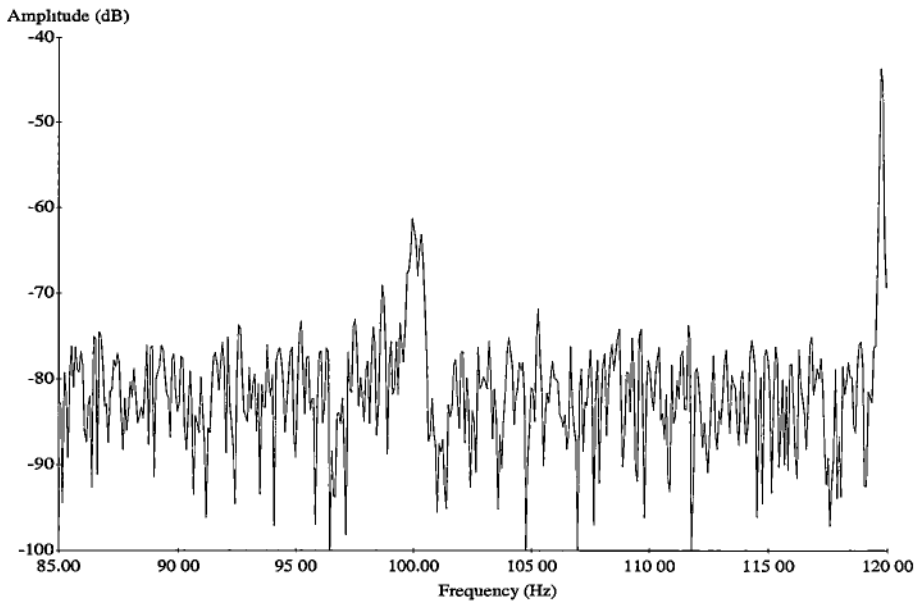

Figure 4.27: The $\pm 2nf_s$ sidebands on $2(f_s + f_r)$ component (same spectrum as figure 4.24, healthy motor)

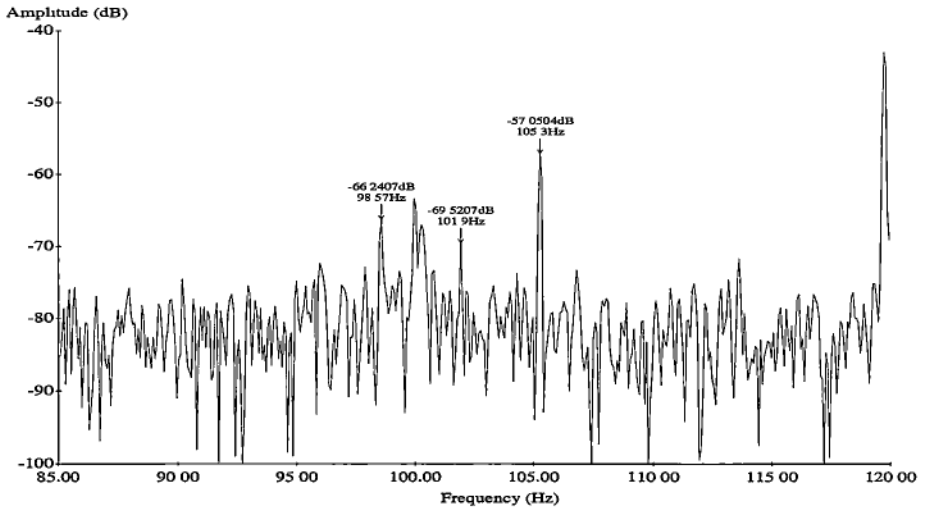

Figure 4.28: The $\pm 2nf_s$ sidebands on $2(f_s + f_r)$ component (same spectrum as figure 4.25, one cut rotor bar)

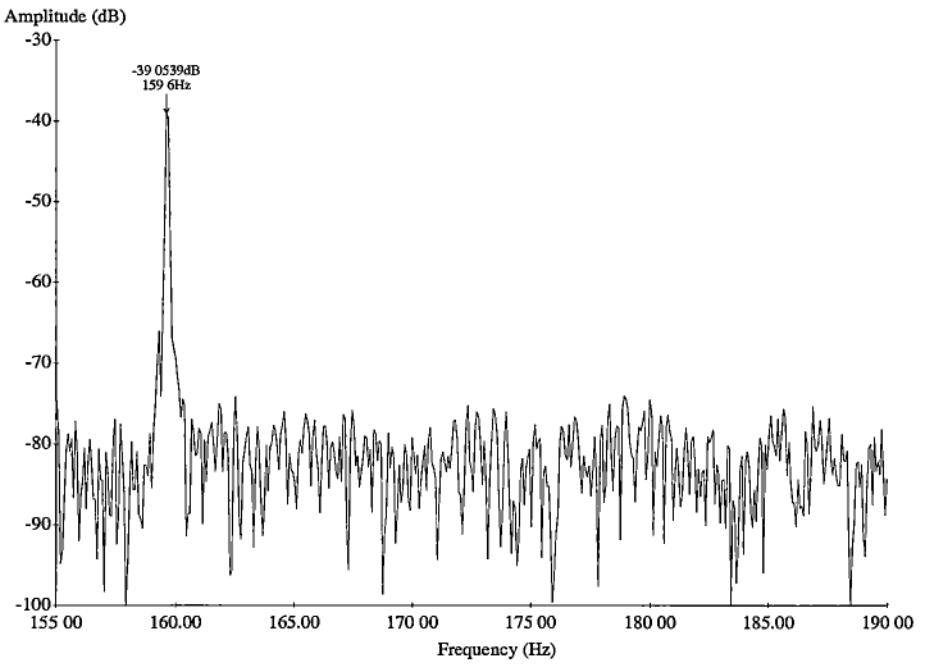

Figure 4.29: The $\pm 2nf_s$ sidebands on $2(2f_s + f_r)$ component (same spectrum as figure 4.24, healthy motor)

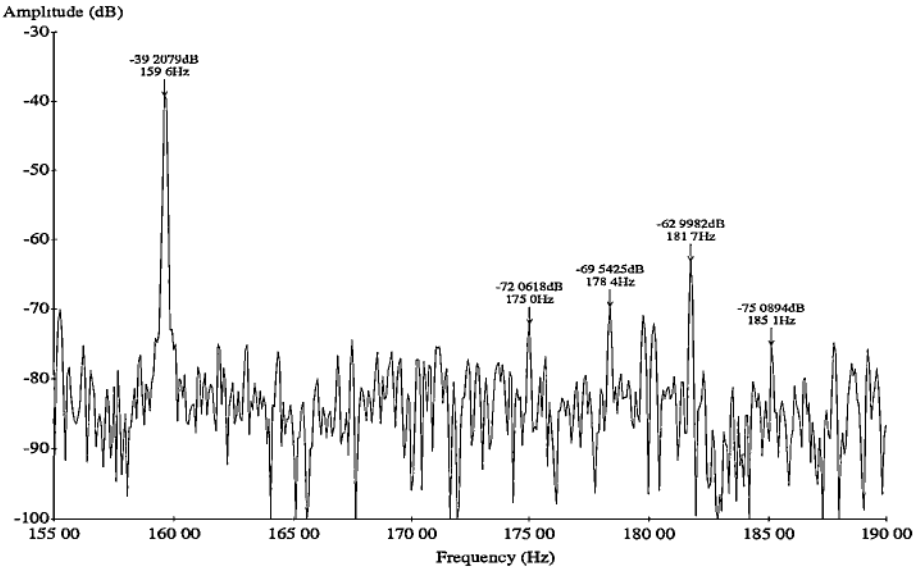

Figure 4.30: The $\pm 2nf_s$ sidebands on $2(2f_s + f_r)$ component (same spectrum as figure 4.24, with one cut rotor bar)

Another group of rotor fault-related components are the $\pm 2nsf_s$ sidebands of $2(f_s + f_r)$ and $2(2f_s + f_r)$. They are labelled in figures 4.28 and 4.30. The corresponding components from the good rotor case are shown in figures 4.27 and 4.29. The low sidebands of $\pm 2nsf_s$ of 6th harmonics also exist and their amplitudes are in column 5 of table 4.12.

4.6.2.1 The effect of load variation on the rotor fault-related components

More measurements were carried out on the same motor supplied with the same drive from low load to full load. Results are summarised in table 4.12.

Compared to the mains supply cases, the pattern appeared on table 4.12 is similar to table 4.3, but in general with less useful information available. It may be because the background noise level of the spectrum analysis has increased. Extra frequency components generated from variable speed drives make the search for the fault-related components more difficult.

	Slip=0.0015		Slip=0.019		Slip=0.025		Slip=0.042	
	Hz	dB	Hz	dB	Hz	dB	Hz	dB
2s			1.37	-50.3	2.06	-49.3	3.36	-47.8
4s					4.12	-61.0	6.71	-63.3
(1-s)/3 - 2s					10.91	-62.9	9.38	-67,6
(1-s)/3	13.28	-40.4	13.05	-49.2	12.97	-50.1	12.74	-53.9
2(1-s)/3 - 2sfs			24.87	-59.1	23.88	-59.4	22.13	-61.3
2-4s+2(1-s)/3					101.7	-65.8	98.57	-66.2
2-2s+2(1-s)/3			104.7	-61.3	103.7	-65.4	101.9	-69,5
2+2(1-s)/3			106.0	-55.4	105.7	-57.1	105.3	-57.1
4-6s+2(1-s)/3			181.8	-69.0			175.0	-72.1
4-4s+2(1-s)/3			183.2	-65.1	181.5	-65.6	178.4	-69.5
4-2s+2(1-s)/3			184.6	-61.8	183.5	-62.9	181.7	-63.0
4+2(1-s)/3							185.1	-75.1
6-4s					235.4	-69.2	232.7	-68.6
6-2s			238.2	-64.3	237.4	-69.0	236.1	-66.3

Table 4.12: The effect of load variation on the rotor fault-related components with Zener drive supply

4.6.2.2 The effect of operating frequency on the rotor fault-related components

Table 4.13 summarises the amplitude of the fault-related components at different supply frequencies. It can be seen that there is less information when the frequency is reduced. The background noise level of the spectrum decreases as frequency increase as in figure 4.31 and 4.32. There is about 10dB difference in background noise. The reasons why the signals have higher harmonics content at lower supply frequencies are discussed in section 4.6.1.

	45Hz		40Hz		30Hz		20Hz	
	Hz	dB	Hz	dB	Hz	dB	Hz	dB
2s	4.501	-45.4	3.967	-46.7	2.89	-48.5	1.83	-49.1
4s	9.00	-62.2	7.94	-63.1				
(1-s)/3 - 2s	9.69	-62.5	8.7	-60.9				
(1-s)/3	14.19	-54.0	12.66	-54.6	9.54	-55.5	6.33	-55.2
2(1-s)/3 - 2sfs	23.96	-61.3	21.29	-60.7	12.44	-65.6	10.83	-61.2
2(1-s)/3	28.46	-67.7					12.66	-60.4
2(1-s)/3 + 2s	32.96	-69.4			16.1	-60.8		
2-4s+2(1-s)/3	109.3	-67.4	97.1	-64.0	73.09	-63.4		
2-2s+2(1-s)/3	113.7	-72.0			76.07	-63.4		
2+2(1-s)/3	118.2	-58.9	105.1	-58.1	78.96	-56.5		
2+2s+2(1-s)/3	122.5	-73.4						
4-6s+2(1-s)/3	173.0	-71.2	173.0	-71.2				
4-4s+2(1-s)/3	176.9	-68.7	176.9	-68.7	138.9	-68.5		
4-2s+2(1-s)/3	180.9	-61.8	180.9	-61.8	136.0	-63.3		
6-4s	260.4	-69.8	231.5	-69.4	174.0	-71.8	116.0	-68.4
6-2s	264.8	-67.7	235.4	-67.7	176.9	-68.9	117.9	-66.5

Table 4.13: The effect of different operating frequency on the rotor fault-related components with Zener drive supply

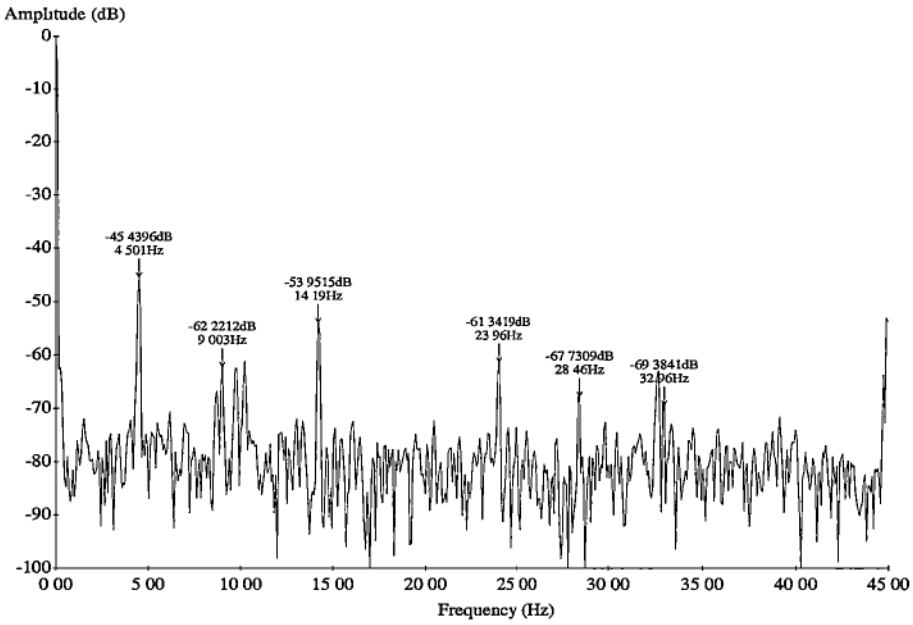

Figure 4.31: The spectrum of the input power of AEI motor supplied by Zener drive operating at 45Hz, with the one cut rotor

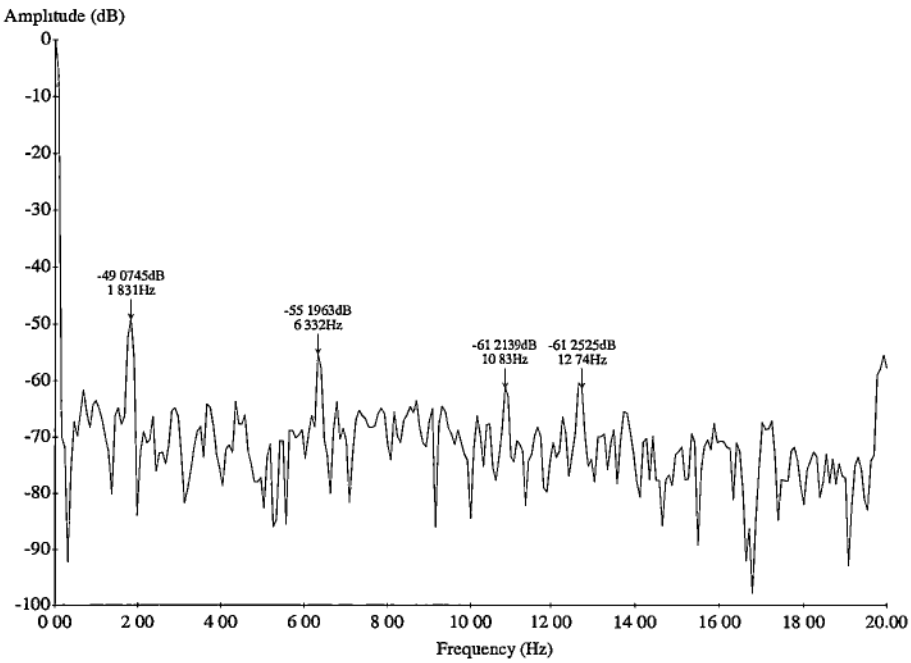

Figure 4.32: The spectrum of the input power of AEI motor supplied by Zener drive operating at 20Hz, with the one cut rotor

4.6.2.3 The effect of varying operating frequency on the $\pm 2nsf_s$ components

As all the rotor fault-related components in current and power are slip-dependent, they will be overlapped by each other when the operating frequency is varying. However, the low frequency components in power, such as $2nsf_s$,can still give some useful information about the rotor. For example, the AEI motor with the one cut rotor bar was run at 0.045 per unit slip, with the frequency slowly varied from 40Hz to 35Hz. The $2sf_s$ component in power only varied from 3.61Hz to 3.15Hz, and is quite distinct and sharp in figure 4.33.

The frequency was then varied at the rate of 10Hz per minute. When this rate is doubled, the peak becomes wider, as shown in figure 4.34, and eventually becomes invisible.

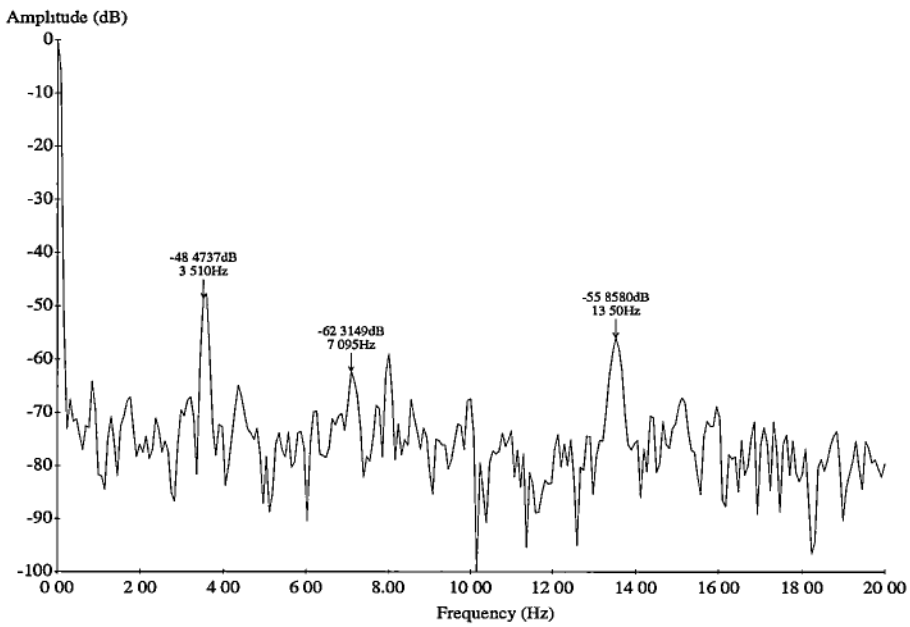

Figure 4.33: The spectrum of the input power of AEI motor supplied by Zener drive with operating frequency varied from 40 to 35Hz (10Hz/60s), with the one cut rotor

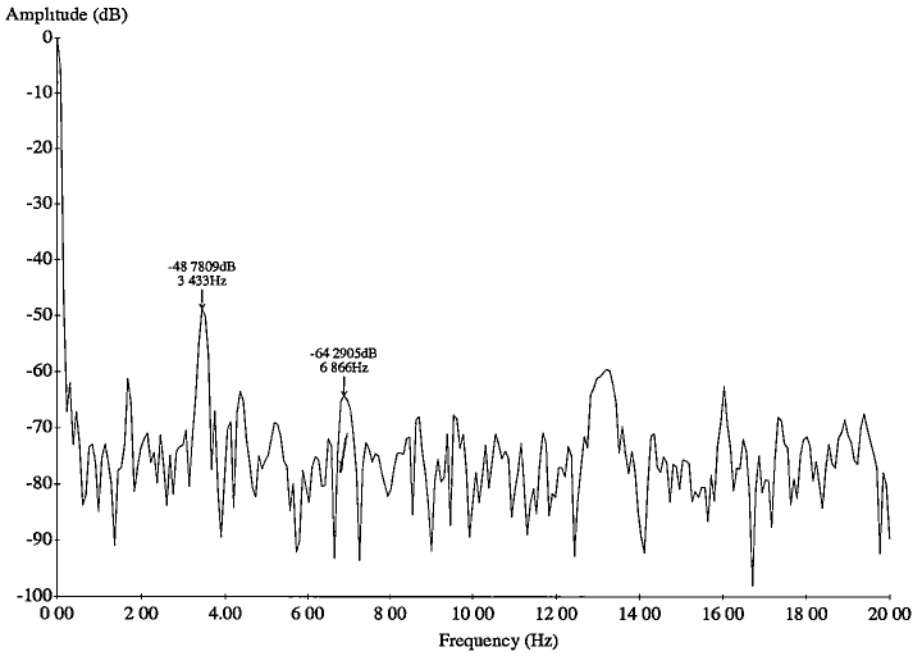

Figure 4.34: The spectrum of the input power of AEI motor supplied by Zener drive with operating frequency varied from 40 to 35Hz (20Hz/60s), with the one cut rotor

4.7 Summary

This chapter describes an attempt to detect short-circuit stator coils and broken rotor bars from the instantaneous input power of the motor, computed from measurement of two line-to-line voltages and two line currents.

A Fourier transform gives frequencies that can be identified with stator or rotor damage. In brief, a short-circuit stator coil produces an unbalance in the stator impedance, that will produce second harmonic in the power. Extra fault-related frequency components in power are also predicted from Penman's analysis [9]. By monitoring the change of their relative amplitude, a stator defect may be identified.

The extra frequencies that could be in stator current, due to a rotor defect, were discussed in Chapter 3. This information is vital for the detection of broken rotor bars using instantaneous power. The predicted rotor fault-related power frequencies are based on the results from Chapter 3.

In the case of variable frequency supply, laboratory studies were based on two PWM variable frequency drives (Renold and Zener drive). It was found that PWM strategies could produce output harmonics at a number of groups of frequency. These are only a problem if they mask any fault-related frequency components. Most of the components are quite high in the frequency range, but this is dependent on the parameters used to implement the PWM waveform. They may mask the slot harmonics (The effect of drive harmonics could be completely disregarded if the drive and condition monitoring system were integrated. The drive could then use an optimised PWM technique to eliminate any frequency components that may mask the fault-related frequency components).

This chapter also describes an experimental study of the effects of the drive frequency, load variation, different fault level (stator fault only) on the amplitude of the fault-related frequency components. Several interesting aspects were seen from tests on a laboratory motor with a deliberately shorted turn in one stator winding, and a damaged rotor.

4.7.1 Shorted turns in stator winding

- There is high current in the shorted turn, which is independent of the load on the motor.
- (5+s) $f_s/3$ and (7-s) $f_s/3$ components in the power signal are produced by a shorted stator coil.
- The sensitivity of using $2f_s$ component in power to detect stator fault is dependent on the harmonic content of the supply.
- The relative amplitude of the fault-related components is increased with increasing current in the 'faulty' coil (controlled by a variable resistor in the shorted coil).

4.7.2 Broken rotor bars

- The main fault frequencies that appear in the power are the double slip-frequency and its multiples.

- Another group of fault-related components in power are the $\pm 2nsf_s$ sidebands of f_r, $2f_r$ and $2(nf_s + 2f_r)$ in the AEI motor.

- $\pm 2nsf_s$ sidebands of even time harmonics in power is another distinct feature although the layout of the stator winding, and its distribution factors and coil span factors, will have a very significant effect on the amplitude of the fault components discussed above.

4.7.3 Supplied with variable frequency

- The availability of fault-related peaks in the spectrum of the power signal is dependent on the PWM strategies and operating frequencies, that affect the harmonic contents and background noise level of spectrum of power signal. The fault-related (both stator and rotor) components that have relatively low amplitude can be covered up by the background noise. The problem may be solved if a variable corner-frequency anti-aliasing low pass filter is used.

- If supply frequency is varying slowly, experimental results showed that the frequency spectrum of the power signal provides almost the same clarity of information for rotor fault as for operation at fixed frequency.

Chapter 5

Maintenance and Current Monitoring of DC Motors

5.1 Introduction

These days, DC generators are all but obsolete, being replaced by solid-state rectifiers. However, the same is not true of DC motors; their speed-torque characteristics mean they are still useful in some industrial applications. Significant features include adjustable speed over a wide range, constant mechanical power output or constant torque, rapid acceleration or deceleration, and responsiveness to feedback signals. These are ideal for roll-mill drives marine applications and mine winders, all of which are critical items of plant. Although the requirements for periodic checking of brush wear and necessary brush replacement, plus the high capital cost, are often listed as disadvantages of DC motors, and modern variable frequency supplies with induction motors have a performance almost as good as that of the DC motor, there are still DC motors in use. They are likely to stay in use for several years.

The modern condition-based maintenance systems that have been described in chapter 2 are all aimed at induction motors. This chapter deals with the problems

caused by poor commutation and the maintenance of the DC motor in some detail, because very few people have addressed this since 1964 (the last UK conference devoted to DC motors). The effects of open-circuit, short-circuit armature coils, and poor commutation are studied experimentally, and spectrum analysis of the motor armature and field current is critically examined as a means of detecting these defects.

5.2 Armature or Rotor Faults

DC motors can show some of the same sort of problems as do AC motors (eg. rotor eccentricity, bearings, and insulation failure) plus an extra one; poor commutation and sparking at the brushes. This can result in blackening, pitting, and wear of both commutator and brushes. These conditions rapidly become worse in a few hours or days, burning away the copper and carbon, until there is a ring of 'fire' around the commutator and a short circuit of the supply occurs.

Rotor or armature defects of the DC motor are mostly attributable to bad riser joints, or to open- or short-circuit of an armature coil. The short-circuit may take place between the risers and it may take place between adjacent turns of a multi-turn coil. Very often a large local current will circulate in the faulty coil, resulting in the burn-out of the coil. It then becomes open-circuit, that causes very severe sparking. Bad joints cause blackening or burning of the faulty joint, repeated at pole-pitch intervals due to the resulting imbalance in the armature currents [105].

5.3 Maintenance of DC Motors

Visual inspection of the commutator and brushgear is probably the only method that is used in industry to assess the condition of DC motors. It is one of the simplest, and most familiar, method of assessing motor condition. However, it depends on direct eye access which is not always easy, there are no official specifications dealing with this method, and the interpretation of inspection results requires experience. Different people will interpret in different ways.

5.3.1 Inspection of Destructive Commutator Condition

During the shutdown period, the most important check of the DC motors is the condition of the commutator surface. Sparking causes pitting of the commutator. When excessive sparking occurs, copper transfer occurs from the trailing edges of the commutator bars, which will then become burned or etched.

The patterns of commutator bar burning may indicate different problems of the commutator [28,105]. When only two adjacent bars are discoloured, arcing across the mica below the surface is indicated and may be caused by conductive material buildup, such as copper, between commutator bars. It can lead to flashover when bar-to-bar voltages are high.

If the commutator bars are discoloured at regular intervals around the commutator circumference, for example, the second, third or fourth bar being of a darker colour than the others, it is commonly referred to as slot bar burning [28], and indicates poor commutation generally.

Pitch bar burning starts under the cathode brush when a rotor defect occurs [28]. Excessive arcing, metal transfer, and associated burning occur every time the defect passes under the cathode brush. Usually, the burned bars will be spaced at 360/pp degrees around the commutator, where pp is the number of pole-pairs. For example, a four-pole motor will have burned bars 180 degrees apart, or a six-pole motor 120 degrees. Each burned area may have one or more burned bars. This causes the brushes to bounce and eventually break if the commutator is not resurfaced.

By contrast, the field windings carry DC that is only varied occasionally. Faults in these windings are rare, but they must still be kept free of carbon dust that is given off by the brushes.

5.3.2 Electrical Tests During a Maintenance Period

There are some electrical tests that may be made during the shutdown period.

(i) The bar-to-bar test [5] is used to check for some winding faults or bad joints. Essentially, it measures the resistance. A DC current is passed through the armature

at points on the commutator spaced by a pole pitch. The voltage reading will be uniform if the winding is sound. For some multi-turn windings, the reading will be varied in a recurring pattern.

(ii) The brush drop curve test [5] can be used to get a rough guide to the interpole strength. It is a quite straightforward method of measuring the voltage between brush and commutator at, say, three positions across the brush thickness. Under ideal conditions the current density will be uniform and fairly constant readings will be obtained. If a high voltage drop is at the entering edge and a low or reverse voltage drop at the leaving edge, then the interpoles are too strong. The converse will indicate weak interpoles.

(iii) The AC current test [5] can be used to check short-circuit turns in the field coils. When an AC current is passed through a field coil, any that sustain shorted turns will show up because they require reduced voltage compared to a healthy coil

(iv) The surface temperature of the commutator under different service conditions may indicate abnormal operating conditions [106]. A radiation pyrometer was developed by the British Scientific Instrument Research Association (to the requirements of British Railways) especially for this purpose.

(v) Kennedy and Gates [107] used a proximity probe, fixed on to the back of a brush, to measure the surface irregularity of the commutator. This test may be used to check the concentricity of commutator and shaft, armature balance, and alignment.

5.3.3 On-line Inspection of Sparking, and the Commutation Chart

Some sparking does not mean bad commutation. For example, motors with variable loads spark quite noticeably at either or both edges of the brush as the current rises and falls, and yet may not be regarded as having too much sparking.

However, excessive sparking can cause disastrous damage to the motor, and so it is important to have some method to indicate the degree of sparking on a motor. Figure 5.1 shows an example of a commutation chart. Sparkless or black commutation is

No. 1. Pinpoint sparking is No. $1\frac{1}{16}$. Light sparking is $1\frac{1}{4}$ and so on [5]. The classifications in between $1\frac{1}{4}$ and $2\frac{1}{2}$ could be rather subjective.

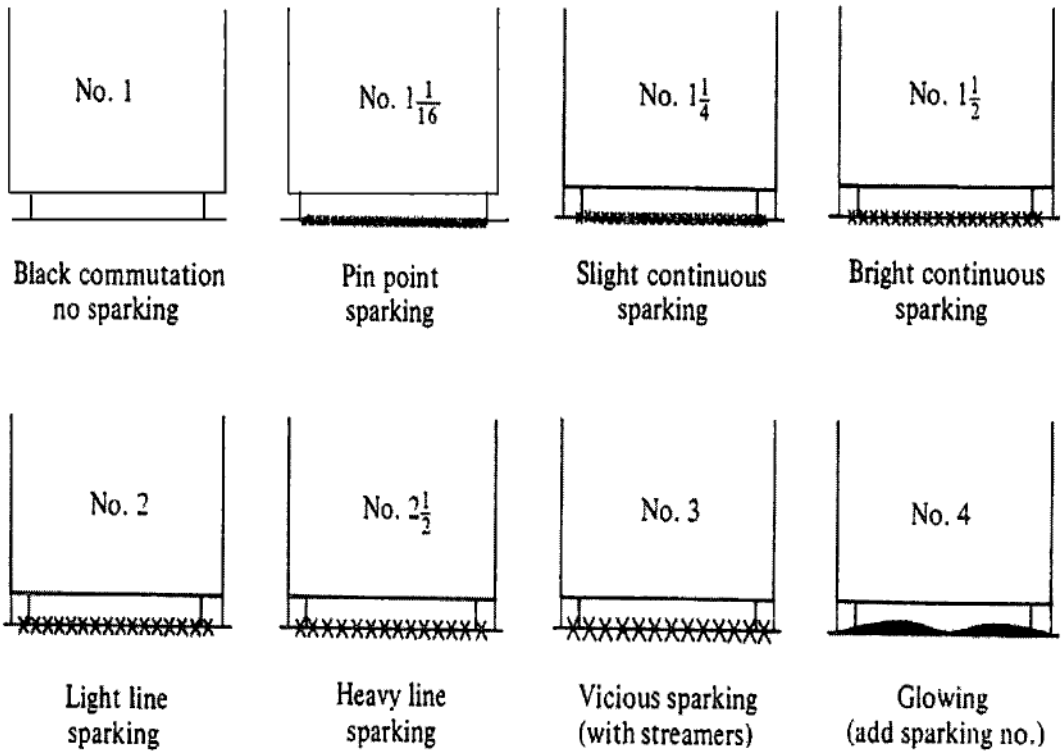

Figure 5.1 Commutation chart to define sparking [5]

The colour of sparking may give some guide to health of the motor [5]:

- Dull yellow sparks are normally harmless.
- White sparks, unless intense, are not serious but may increase brush wear.
- When high rates of brush wear occurs, particles of red hot carbon come from the brush and may give red sparks.
- Blue and green brilliant sparks may indicate a serious winding fault.

Most sparking occurs on the trailing edge of the brushes but sparking on the entering edge can be caused by mechanical imperfections resulting in the brush actually bouncing off the commutator.

Obviously these methods are subjective and far from infallible. For example, the eyesight of the observer and the amount of light (daylight or artificial light) will affect the appearance of sparking. Attempts have been made to assess sparking by measuring one of its physical or electrical effects for commutation testing, such as the amplitude of the high frequency signal generated by a sparking commutator [108], using light sensitive cells [109] and photoelectric sparking sensor [110]. None of these provide a simple sparking meter.

5.4 Frequency Components of DC Motor Currents

Motor current spectral analysis can be applied to detect defects and it has the advantage that it can be easily carried out in the substation at a distance from the motor.

When the armature and field current of a DC motor are supplied by a rectifier, the current waveforms are ideally DC plus ripple frequencies. A three-phase full-wave rectifier will have a fundamental ripple frequency at 300Hz, while a single phase one has it at 100Hz.

The slot openings of the armature will induce permeance variations in the air gap, which results in slot frequency and its harmonics being induced in the current waveforms.

5.5 Tests on Laboratory DC Motors

Three DC motors were tested. The armature of each was supplied by a three phase rectified voltage and it was loaded by a generator (either AC or DC) and resistor combination, shown in figure 5.2.

Motor armature and field currents, were monitored with a clip-on "Rogowski" coil described in the next section. The corresponding output voltage was amplified, low-pass filtered and then digitised using a computer equipped with a 12-bit A/D card (Appendix B). The sampling rate is 10kHz, and 65536 data points are captured for each measurement.

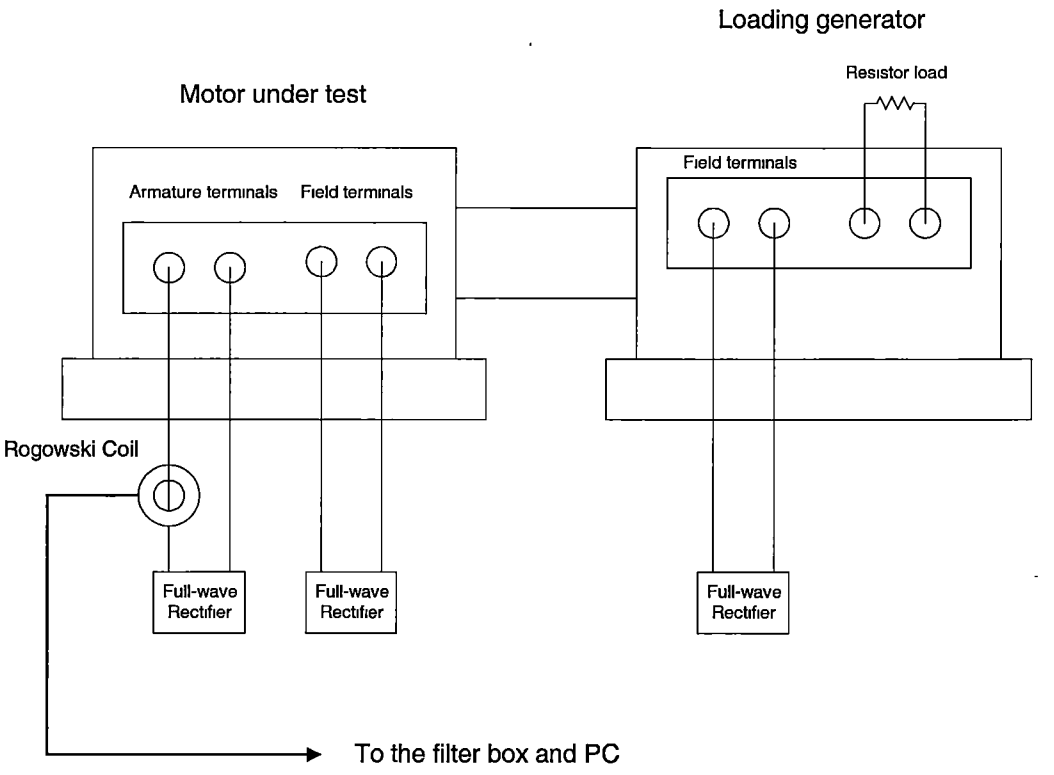

Figure 5.2 Testing of laboratory DC motors

5.5.1 Air-core Current Transformer for DC Motor Current Monitoring

In order to monitor the DC motor currents, an appropriate current transducer had to be designed. The conventional current transformer cannot be used because DC saturates the core, and any superimposed AC currents are not noticed. Furthermore, the electrical noise inside the control cubicle of a thyristor-controlled DC motor prevents successful operation of a Hall Effect clip-on ammeter (Appendix B). Instead an air-core clip-on "Rogowski" coil was designed to monitor the fault-related frequencies in armature and field current. The coil is not made with ferromagnetic material in its core, so that it cannot be driven into saturation by the DC. When a conductor carrying current *i*, passes through a Rogowski coil, the coil generates a voltage e_g proportional to the coil's mutual inductance M, and the time rate of change of current [111-112], ie $e_g(t) = \mathrm{M}\frac{di(t)}{dt}$. The RMS voltage E corresponding to a current of frequency ω rad/sec and RMS amplitude I, is $\mathrm{E} = \omega \mathrm{MI}$.

Obviously, the Rogowski coil ignores DC. The amplitude of the output voltage is proportional to the frequency. It means that the higher frequency components will have larger amplification. These characteristics are good for detecting the slot harmonics and the commutator bar frequency, as they are relatively high frequency but very small amplitude related to the DC level. The design of the Rogowski coil is outlined in Appendix A4.4.

Because it ignored DC there is a difficulty in knowing the absolute amplitude of voltage from the Rogowski coil. By comparison the voltage from a CT on a induction motor always has the zero dB level as the supply frequency. However, the zero dB frequency of armature or field current may be the rectifier ripple frequency, the slot frequency, or the commutator bar frequency (or their harmonics). For comparison purposes, in the following sections, the zero dB frequency of the spectrum analysis is the rectifier ripple frequency (100Hz or 300Hz). If necessary, this can be related to the DC current by looking at the spectrum of the current obtained from the Hall Effect ammeter. Both amplitudes are large enough not to be adversely affected by spikes of current caused by thyristor.

5.5.2 The Effect of the Interpole Strength on DC Motor Currents

The motor for this test was an old 2.9HP, 4-pole DC motor (M45, Appendix A2.1) with 28 slots and 83 segments. It has separate terminals for the interpole winding. The motor was first run at full load at 1040 rpm with the interpole winding connected. The rotational frequency f_r is equal to 17.33Hz. No sparking could be seen. The commutator bar frequency $\left(f_{cb} = 83 \times f_r\right)$ was expected to be about 1438.4Hz (17.33Hz×83).

The armature and field current waveforms were recorded using the Rogowski coil. Figure 5.3 shows the frequency spectrum of the armature current in the 0 to 500Hz range. The zero dB frequency is the slot frequency f_{slot}, $28 f_r$. The ripple frequency from the rectifier supply is at 300.1Hz with an amplitude of -2.9dB relative to the slot frequency. The commutator bar frequency is at 1438Hz, with amplitude of -26dB (about 5% of the slot harmonic amplitude), as shown in figure 5.5. The sidebands, that are separated from the commutator bar frequency by $\pm f_r$ and $\pm 2 f_r$, are also

prominent. These results are summarised in table 5.1. Figure 5.7 shows the commutator bar frequency of the corresponding field current spectrum with results summarised in table 5.3.

If there was sparking, a burst of sparks would be expected every time a commutator bar moved under a brush. By by-passing the interpoles on the motor, pin-point sparking (referred to in figure 5.1) occurred. The motor speed was 997 rpm and f_r is equal to 16.63Hz. Figure 5.6 shows the commutator bar frequency and the sidebands that are separated by $\pm f_r$ and $\pm 2f_r$. The amplitude of the bar frequency increased to -19.5dB related to slot frequency. Figure 5.8 shows the field current spectrum. The results are summarised in table 5.2 and 5.4.

In order to check whether any amplitude change of the slot frequency is due to the sparking, the zero dB frequency (slot frequency) of the spectrum was converted to rectifier ripple frequency (300Hz for armature current and 100Hz for field current). The conversion results show that the slot frequency component in the armature and the field current was slightly increased. A significant amplitude change occurred to the commutator bar frequency and its nf_r sidebands in the armature and the field current spectra. The amplitude of the four-times-speed frequency was relatively larger than the rest of the speed harmonics, due to the salient poles (it is a four-pole motor).

When commutation occurs, the turns of the commutating coil lie on the main pole axis. The occurrence of sparking at the brushes when the commutating coil leaves the brush is due to the rapid adjustment of the coil current amplitude to the branch armature current amplitude. This current adjustment must be accompanied by a corresponding change in flux in the field poles, which results in a corresponding amplitude change at the same commutator bar frequency in the field current.

Frequency (Hz)	300.1	484.9	1403	1420	1438	1455	1472
Frequency factor	$6f_1$	f_{slot}	$f_{cb}-2f_r$	$f_{cb}-f_r$	f_{cb}	$f_{cb}+f_r$	$f_{cb}+2f_r$
dB (related f_{slot})	-2.9	0	-49.0	-36.2	-26.0	-32.2	-46.0
dB (related to 300Hz)	0	2.9	-46.1	-33.3	-23.1	-29.3	-43.1

Table 5.1 The results of the armature current spectrum of M45 with interpole connected

Frequency (Hz)	300	465.5	1347	1363	1380	1397	1413
Frequency factor	$6f_1$	f_{slot}	$f_{cb}-2f_r$	$f_{cb}-f_r$	f_{cb}	$f_{cb}+f_r$	$f_{cb}+2f_r$
dB (related f_{slot})	-6.4	0	-35.1	-23.0	-19.5	-27.5	-37.3
dB (related to 300Hz)	0	6.4	-28.7	-16.8	-13.1	-21.1	-30.9

Table 5.2 The results of the armature current spectrum of M45 without interpole

Frequency (Hz)	100.1	485.7	1405	1423	1440	1457	1475
Frequency factor	$6f_1$	f_{slot}	$f_{cb}-2f_r$	$f_{cb}-f_r$	f_{cb}	$f_{cb}+f_r$	$f_{cb}+2f_r$
dB (related to f_{slot})	-4.9	0	-39.8	-24.9	-19.2	-23.7	-32.1
dB (related to 100Hz)	0	4.9	-34.8	-19.9	-14.2	-18.7	-27.1

Table 5.3 The results of the field current spectrum of M45 with interpole connected

Frequency (Hz)	100.1	465.2	1346	1362	1379	1396	1412
Frequency factor	$6f_1$	f_{slot}	$f_{cb}-2f_r$	$f_{cb}-f_r$	f_{cb}	$f_{cb}+f_r$	$f_{cb}+2f_r$
dB (related f_{slot})	-7.8	0	-25.8	-14.3	-10.8	-17.9	-23.0
dB (related to 100Hz)	0	7.8	-18.0	-6.5	-3.0	-10.1	-15.2

Table 5.4 The results of the field current spectrum of M45 without interpole

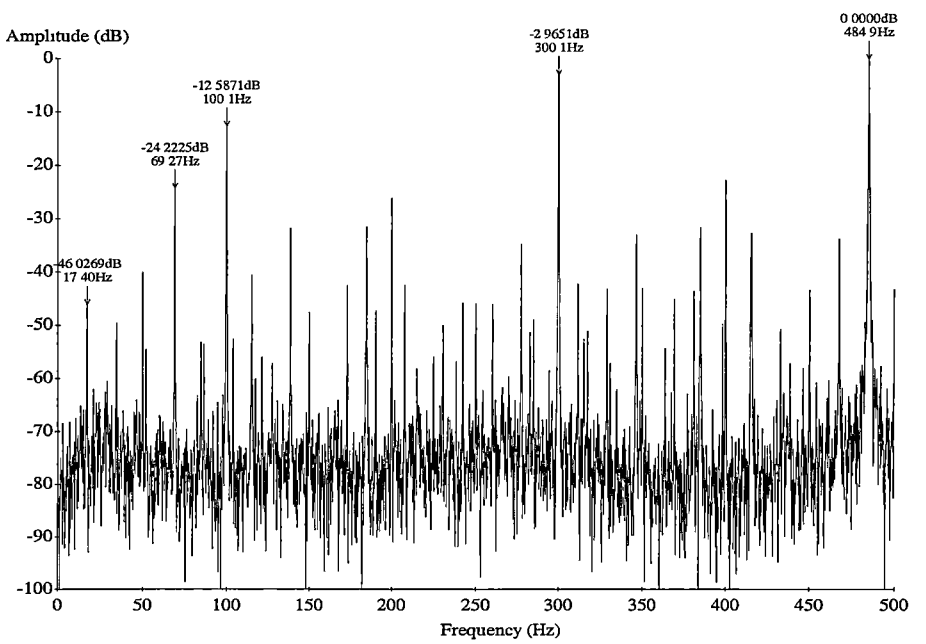

Figure 5.3: Frequency spectrum of the derivative of armature current with interpole winding connected (M45)

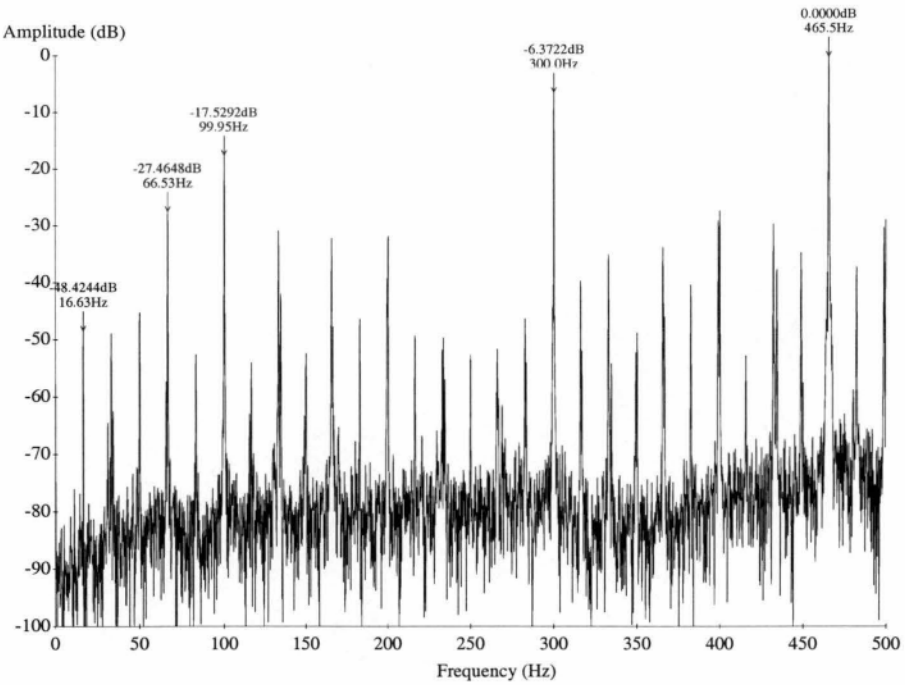

Figure 5.4: Frequency spectrum of the derivative of field current with interpole winding connected (M45)

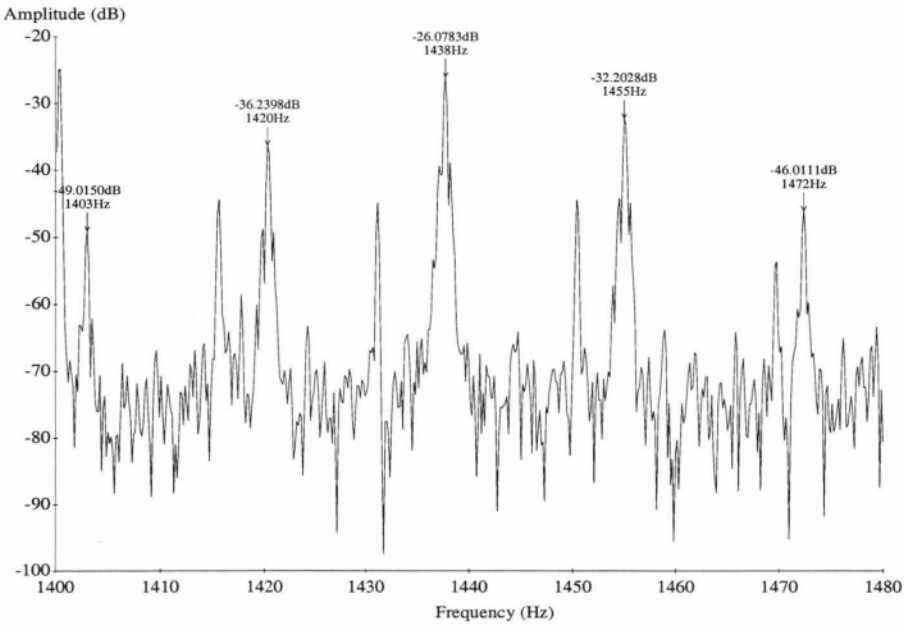

Figure 5.5: The commutator bar frequency harmonics of armature current with interpole winding connected (M45)

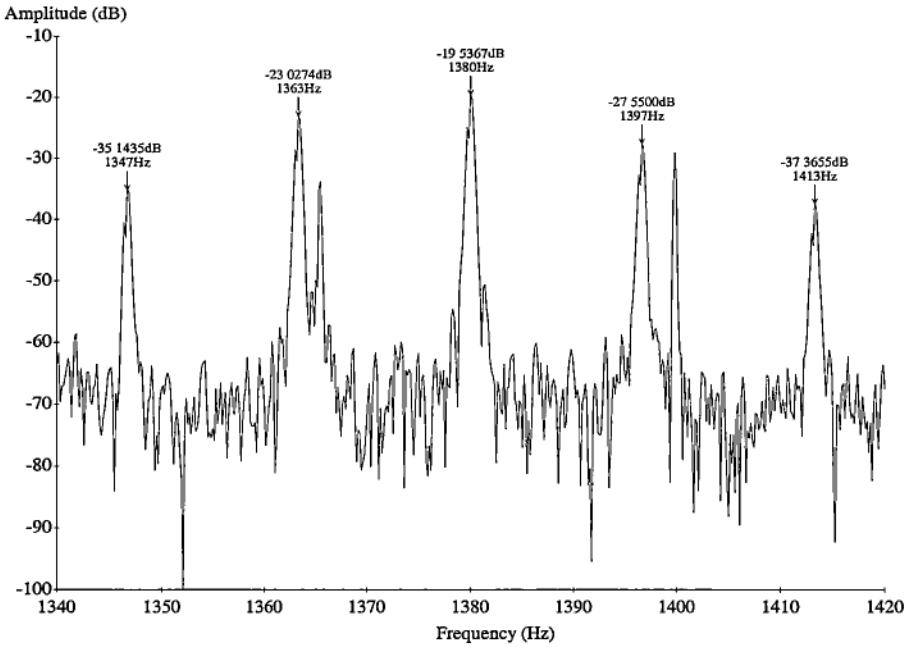

Figure 5.6: The commutator bar frequency harmonics of field current with interpole winding connected (M45)

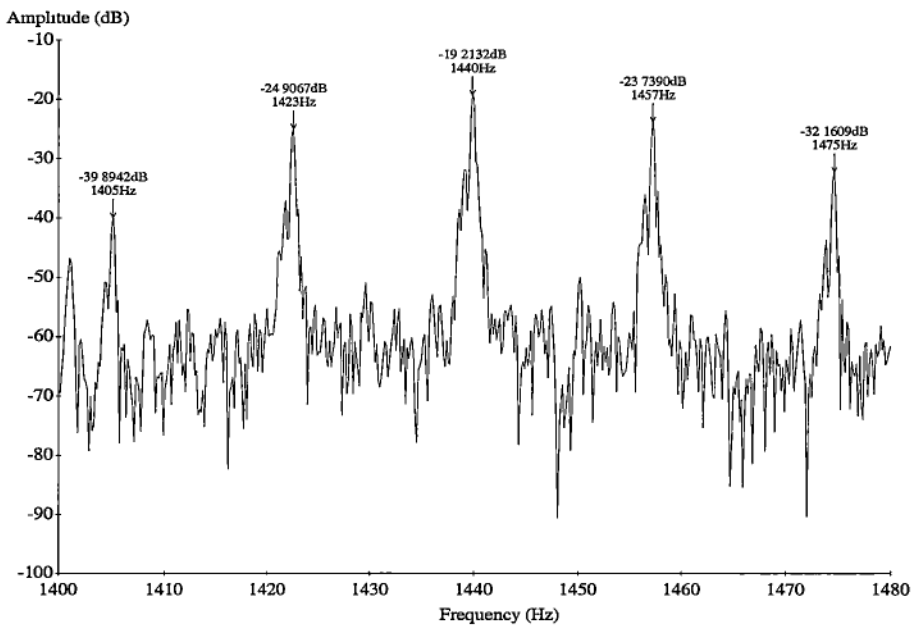

Figure 5.7: The commutator bar frequency harmonics of armature current without interpole winding (M45)

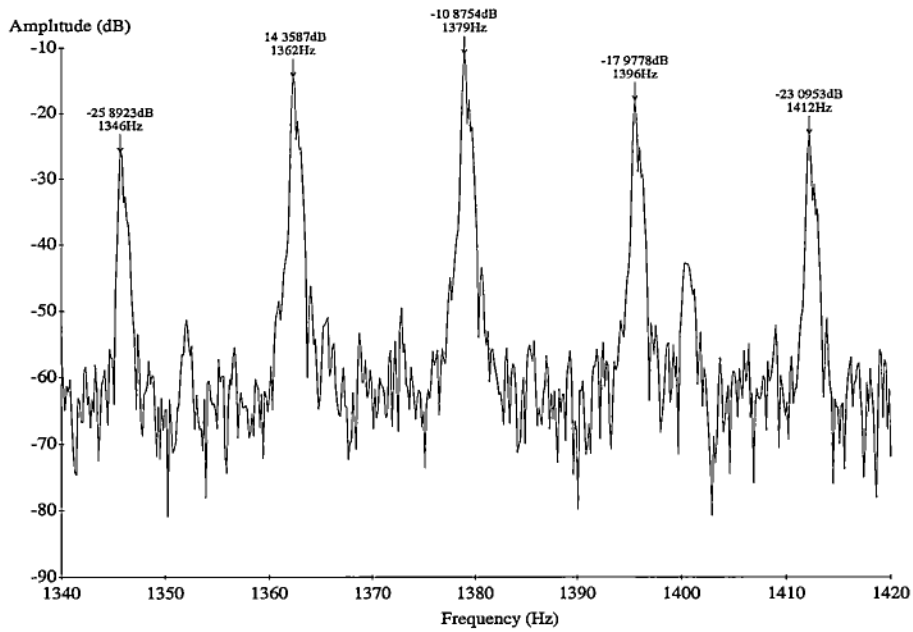

Figure 5.8: The commutator bar frequency harmonics of field current without interpole winding (M45)

5.5.3 The Effect of Open-circuit and Short-circuit Armature Coil on DC Motor Currents: 0.5HP Davey Motor

The first motor for this test was a 2-pole 0.5HP lap winding motor (F.W. Davey & Co, rated at 1500rpm, V_a=180V, i_a=2A, V_f=220V, i_f=0.2A, more detail in Appendix A2.3). It did not have interpoles. It has 16 slots and 48 commutator bars (three coils per slot). The healthy motor was first run at 1720 rpm at rated load and speed. The rotational speed frequency f_r was 28.67Hz. Figure 5.9 shows the frequency spectrum of the armature current in the zero to 300Hz range. The zero dB frequency is 300Hz, which is the rectifier ripple frequency. Multiples of speed frequency and time harmonics are visible. The amplitude of two times and four times the speed frequency is relatively high, as it was a 2-pole motor. The amplitude of significant components is summarised in table 5.5. A similar frequency pattern is found in the field current, as shown in figure 5.11. The zero dB frequency of the field current spectrum was the commutator bar frequency, this was converted to 300Hz rectifier ripple frequency at zero dB (a three-phase full wave rectifier was used for the field supply) and is shown in table 5.7.

	f_r	$2f_r$	$3f_r$	$4f_r$	$5f_r$	$6f_r$	$7f_r$	$8f_r$	$6f_1$	f_{slot}	f_{cb}
(Hz)	28.6	57.2	85.9	114.5	143.1	171.7	200.4	229.0	300.1	458.1	1374
(dB)	-52.1	-18.6	-49.0	-18.9	-53.9	-39.3	-54.6	-34.4	0	-2.0	-19.6

Table 5.5: The armature current spectrum of the Davey motor with good armature

	f_r	$2f_r$	$3f_r$	$4f_r$	$5f_r$	$6f_r$	$7f_r$	$8f_r$	$6f_1$	f_{slot}	f_{cb}
(Hz)	27.6	55.4	83.0	110.6	138.4	166.0	193.6	221.4	300.1	442.8	1328
(dB) related to f_{slot}	-34.1	-17.4	-28.1	-13.2	-27.6	-17.4	-28.1	-17.5	-1.1	0	-18.0
(dB) related to 300Hz	-33.0	-16.3	-27.0	-12.1	-26.5	-16.3	-27.0	-16.4	0	1.1	-16.9

Table 5.6: The armature current spectrum of the Davey motor with an open-circuit armature coil

One armature coil was deliberately disconnected from a commutator bar. The DC level of the armature current dropped to two-thirds normal value. Figure 5.10 shows the frequency spectrum of the armature current. The zero dB frequency was the slot frequency and was converted to 300Hz, the rectifier ripple frequency. The background noise level increased by about 20dB. The amplitude of the multiples of the speed frequency increased significantly except at two times and four times the speed frequency. Results are summarised in table 5.6.

The corresponding field current spectrum is shown in figure 5.12, and results are summarised in table 5.8. The zero dB frequency of the field current is 300Hz, the rectifier ripple frequency. No significant change of background noise level or speed harmonics can be found in the field current spectrum.

	f_r	$2f_r$	$3f_r$	$4f_r$	$5f_r$	$6f_r$	$7f_r$	$8f_r$	$6f_1$	f_{slot}	f_{cb}
(Hz)	29.2	58.4	87.7	116.9	146.1	175.3	204.6	233.8	299.8	467.5	1403
(dB) related to f_{cb}	-33.9	-10.2	-30.3	-20.4	-31.0	-35.9	-31.1	-22.6	-5.4	-6.5	0
(dB) related to 300Hz	-25.8	-4.8	-24.9	-15.0	-25.6	-30.5	-25.7	-17.2	0	-1.1	5.4

Table 5.7: The results of the field current spectrum of the Davey motor with good armature

	f_r	$2f_r$	$3f_r$	$4f_r$	$5f_r$	$6f_r$	$7f_r$	$8f_r$	$6f_1$	f_{slot}	f_{cb}
(Hz)	26.7	53.4	80.1	106.8	133.5	160.2	186.9	213.7	300.1	427.3	1282
(dB)	-27.4	-8.56	-25.2	-16.7	-19.7	-23.4	-16.7	-25.7	0	-6.6	-0.55

Table 5.8: The results of the field current spectrum of the Davey motor with an open-circuit armature coil

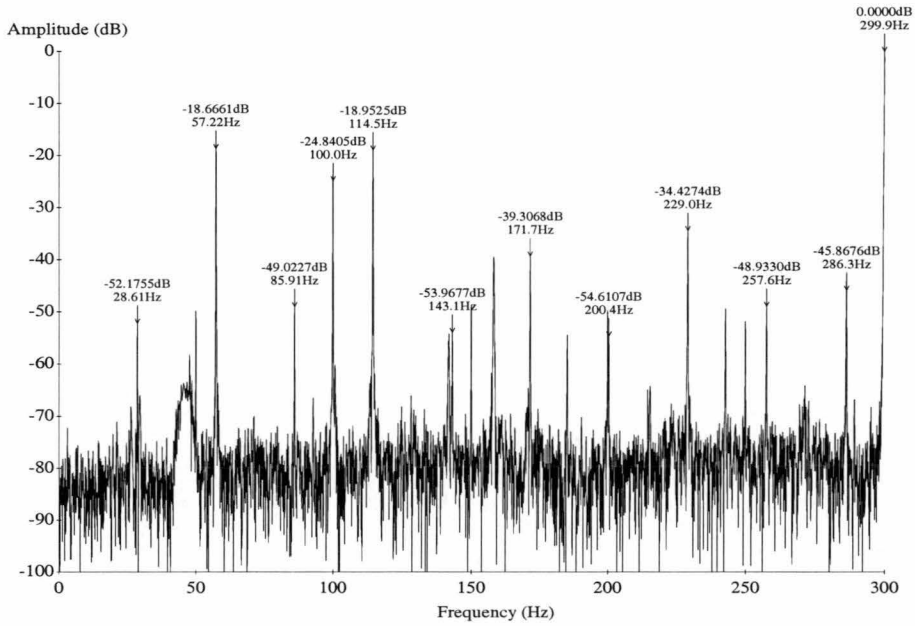

Figure 5.9: Frequency spectrum of the derivative of armature current with a good armature (Davey motor)

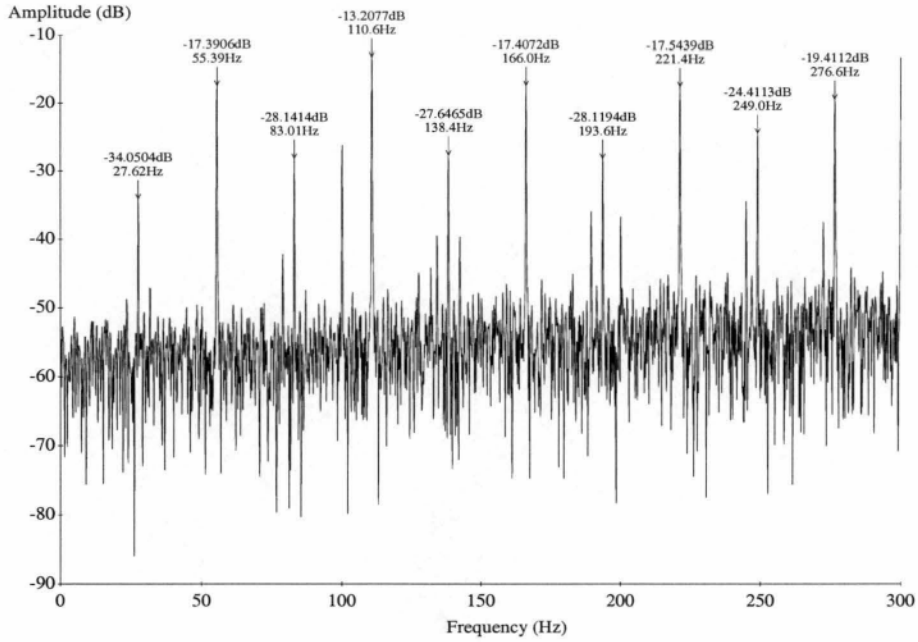

Figure 5.10: Frequency spectrum of the derivative of armature current with an open-circuit armature coil (Davey motor)

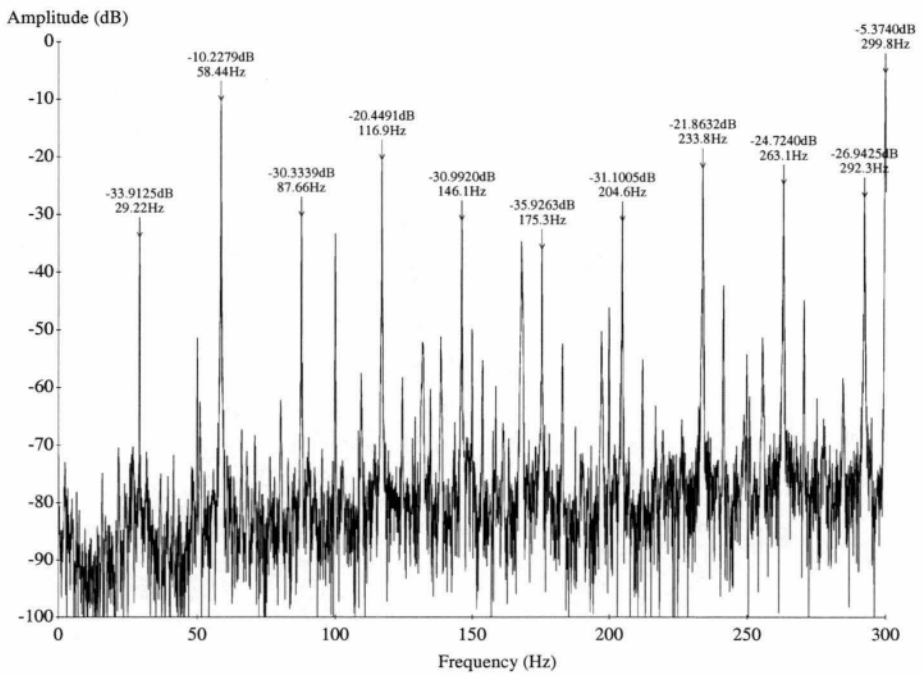

Figure 5.11: Frequency spectrum of the derivative of field current with a good armature (Davey motor)

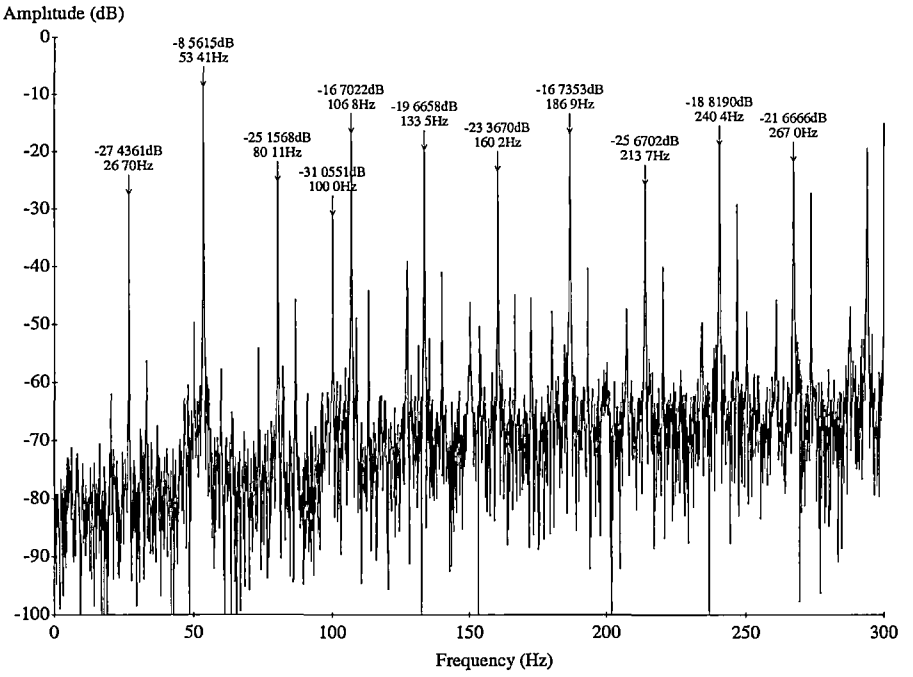

Figure 5.12: Frequency spectrum of the derivative of field current with an open-circuit armature coil (Davey motor)

In order to simulate a short-circuit in the armature winding, the 'start' of the first coil is shorted to the 'end' of the third coil. Two segments away a Hall plate was attached to the motor frame to get an estimation of the short-circuit current by the amplitude of its magnetic field, because there was no way of getting at the shorted coil itself. When the motor was stationary, a known current was injected into adjacent commutator segments, and the maximum Hall plate voltage was noted as the rotor was turned by hand. The 'calibrated' Hall plate voltage gives a rough idea on the amplitude of the current in the shorted coil and showed that i_{sc} is proportional to armature voltage. As a result, only a fraction (57.4 volt) of rated armature voltage was supplied to the motor, to avoid damage to the shorted coil. The field current was 0.2A and the motor was loaded to 2A of armature current. Figure 5.13 and 5.14 show the corresponding frequency spectrum of the armature and field current. Both spectra are dominated by speed frequency and its multiples. The relative amplitude of these components is summarised in tables 5.9 and 5.10.

The zero dB component is 300Hz (from a three-phase rectifier). The relative amplitude of the speed frequency in the armature current shows a 30dB increase

compared with the 'healthy armature' case. The rest of the multiples of frequency components have 10 to 20dB increases in amplitude. The commutator bar frequency component in armature current is low, 31.2dB down from the 300Hz ripple. As the motor was run at very low speed, 485rpm, longer commutation time is provided for the current reverse process in the commutating coils. Less sparking occurs at the trailing brush tip and hence the commutator bar frequency component in armature current is of low amplitude.

	f_r	$2f_r$	$3f_r$	$4f_r$	$5f_r$	$6f_r$	$7f_r$	$8f_r$	$6f_1$	f_{slot}	f_{cb}
(Hz)	8.1	16.2	24.3	32.2	40.3	48.4	56.5	64.5	300	128.9	387.0
(dB)	-23.0	-9.0	-35.8	-18.4	-26.2	-18.8	-35.6	-33.7	0	-6.0	-31.2

Table 5.9: The results of the armature current spectrum of the Davey motor with a short-circuit armature coil

In the spectrum of the corresponding field current, only the double, triple, and the six times multiple of speed frequency components have as much as 10dB increase in their relative amplitude.

	f_r	$2f_r$	$3f_r$	$4f_r$	$5f_r$	$6f_r$	$7f_r$	$8f_r$	$6f_1$	f_{slot}	f_{cb}
(Hz)	8.1	16.2	24.3	32.4	40.4	48.5	56.6	64.5	300	129.2	387.7
(dB)	-30.6	-0.9	-18.9	-22.0	-26.6	-17.4	-33.7	-22.5	0	-12.2	-6.2

Table 5.10: The results of the field current spectrum of the Davey motor with a short-circuit armature coil

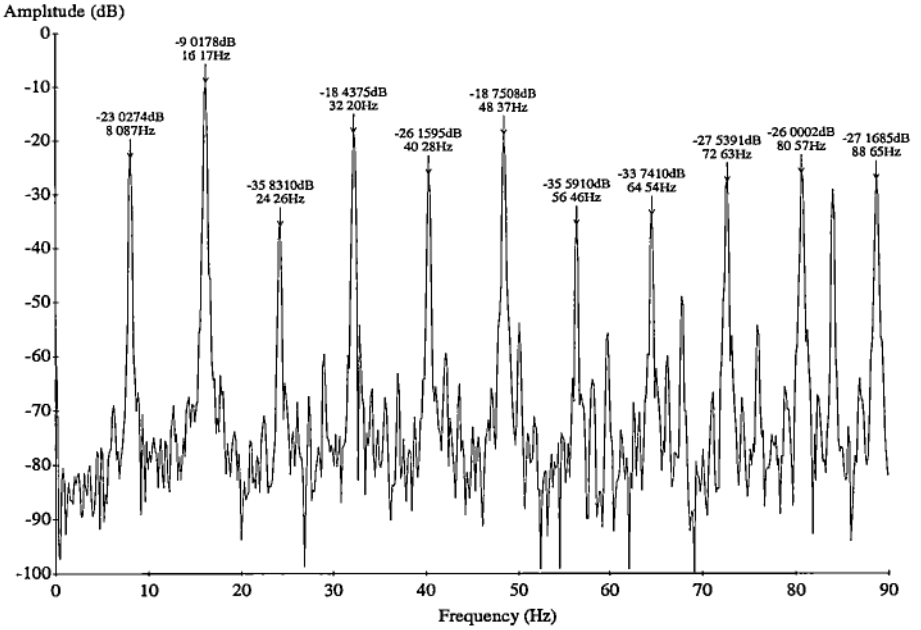

Figure 5.13: Frequency spectrum of the derivative of the armature current with a short-circuit armature coil (Davey motor)

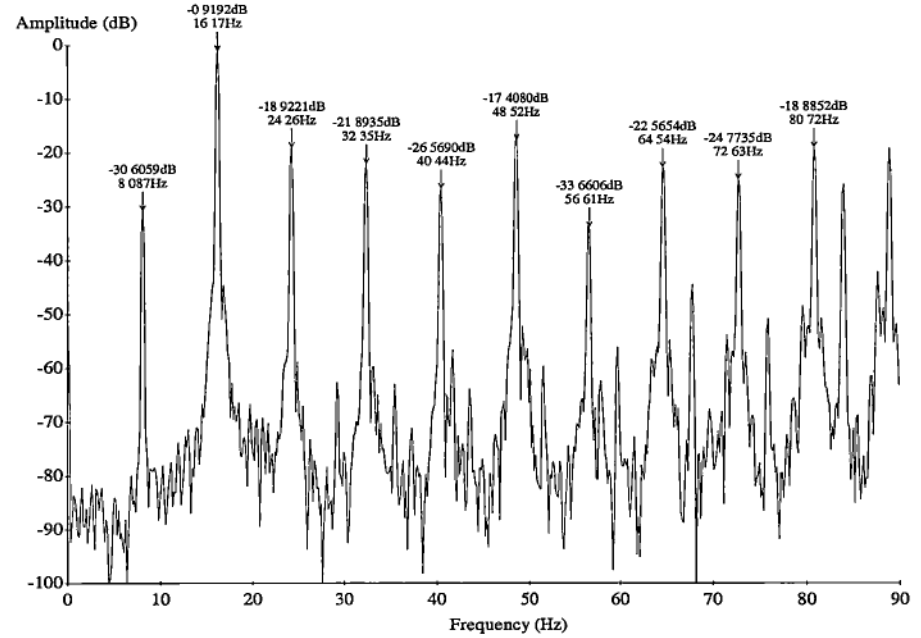

Figure 5.14: Frequency spectrum of the derivative of the field current with a short-circuit armature coil (Davey motor)

5.5.4 5kW Motor with Open-circuit Armature Coils (M87)

The motor for the load test was rated at 5kW, 500V. It had a 4-pole, wave winding (M87, Appendix A2.2) with 39 slots and 117 commutator bars. The speed was 1330 rpm when the motor had a good armature so f_r is 22.17Hz. Figure 5.15 shows the frequency spectrum of the armature current. The zero dB frequency is 300Hz. Multiples of speed frequency and time harmonics dominate. The amplitude of four times speed frequency is relatively larger than the rest. A similar frequency pattern can be found in the field current, shown in figure 5.17. The zero dB frequency for this is 100Hz.

With one open-circuit armature coil, the load test could only be carried out at half load because serious sparking started and there was a risk of flashover. Spikes occurred on the waveform in the time domain. The background noise level of the armature current spectrum increased about 20dB, due to the sparking, as shown in figure 5.16. The amplitude of the multiples of the speed frequency increased significantly, except for fundamental speed frequency.

However, no spikes occurred on the field current waveform. The background noise level of the field current spectrum is the same as with a good armature, as shown in figure 5.18. No significant amplitude change of the speed harmonics was found. Results are summarised in tables 5.11, 5.12, 5.13 and 5.14.

	f_r	$2f_r$	$3f_r$	$4f_r$	$5f_r$	$6f_r$	$7f_r$	$8f_r$	$6f_1$	f_{slot}	f_{cb}
(Hz)	22.1	44.4	66.5	88.6	110.9	133.1	155.2	177.5	300.1	864.7	2594
(dB)	-41.6	-51.5	-45.5	-39.0	-50.6	-46.2	-56.1	-47.1	0	-37.0	-32.1

Table 5.11: The results of armature current of M87 with good armature

	f_r	$2f_r$	$3f_r$	$4f_r$	$5f_r$	$6f_r$	$7f_r$	$8f_r$	$6f_1$	f_{slot}	f_{cb}
(Hz)	23.2	46.7	68.9	93.0	113.5	139.8	163.0	186.2	300.1	907.6	2723
(dB)	-39.8	-31.6	-33.6	-23.5	-32.2	-29.9	-32.1	-26.0	0	-32.0	-37.3

Table 5.12: The results of armature current of M87 with an open-circuit armature coil

	f_r	$2f_r$	$3f_r$	$4f_r$	$5f_r$	$6f_r$	$7f_r$	$8f_r$	$6f_1$	f_{slot}	f_{cb}
(Hz)	23.2	46.4	69.7	92.9	116.1	139.3	162.5	185.9	100.1	904.5	2723
(dB)	-51.0	-40.3	-42.4	-36.9	-48.3	-38.7	-51.1	-39.9	0	-36.3	-44.0

Table 5.13: The results of field current of M87 with a good armature

	f_r	$2f_r$	$3f_r$	$4f_r$	$5f_r$	$6f_r$	$7f_r$	$8f_r$	$6f_1$	f_{slot}	f_{cb}
(Hz)	22.1	44.4	66.5	88.6	110.8	133.1	155.2	177.3	99.5	864.7	2594
(dB)	-45.3	-48.8	-41.8	-38.7	-42.5	-46.7	-43.4	-37.9	0	-37.3	-40.8

Table 5.14: The results of field current of M87 with an open-circuit armature coil

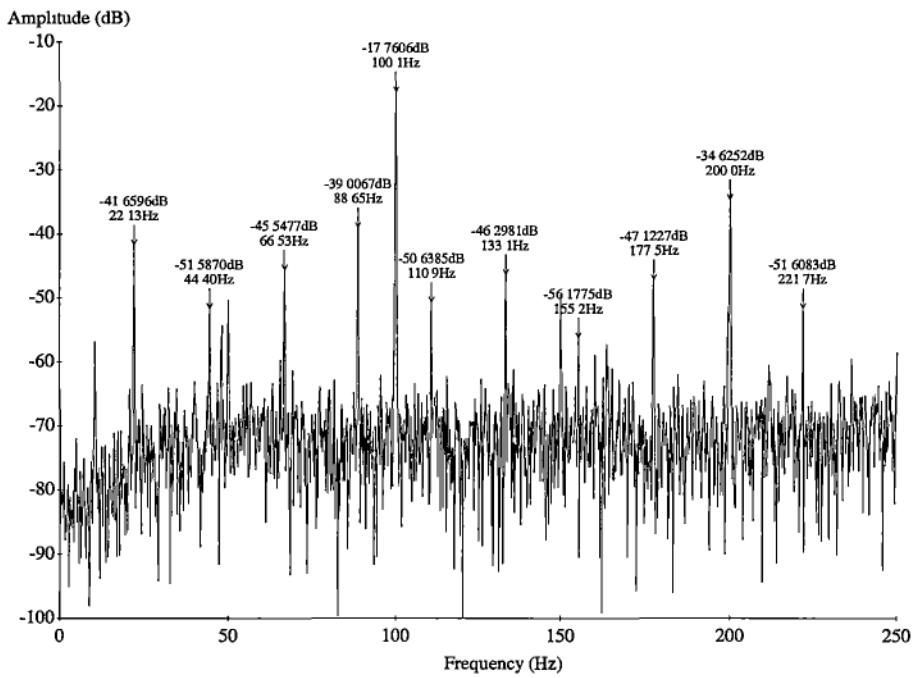

Figure 5.15: Frequency spectrum of the derivative of armature current with a good armature (M87)

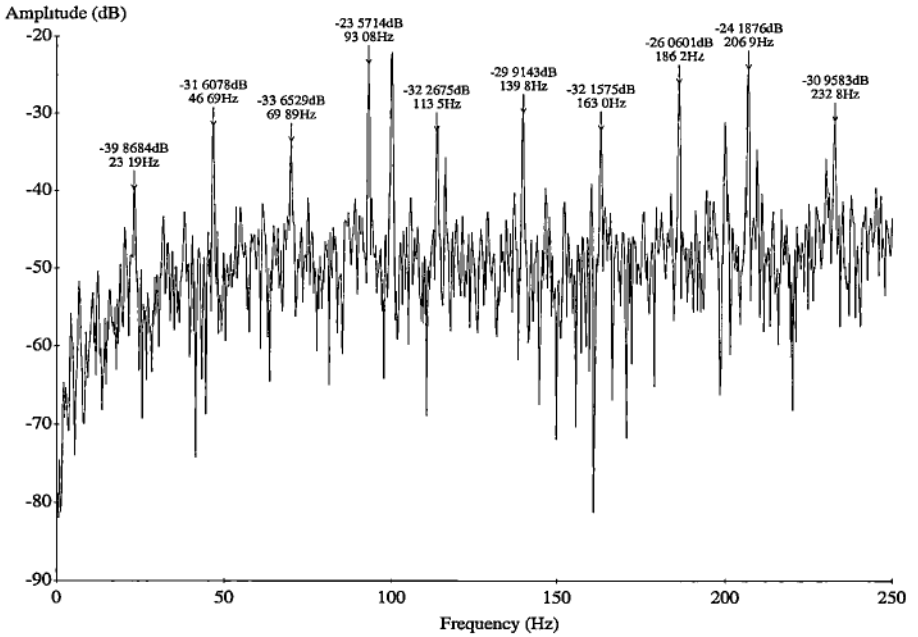

Figure 5.16: Frequency spectrum of the derivative of armature current with an open-circuit armature coil (M87)

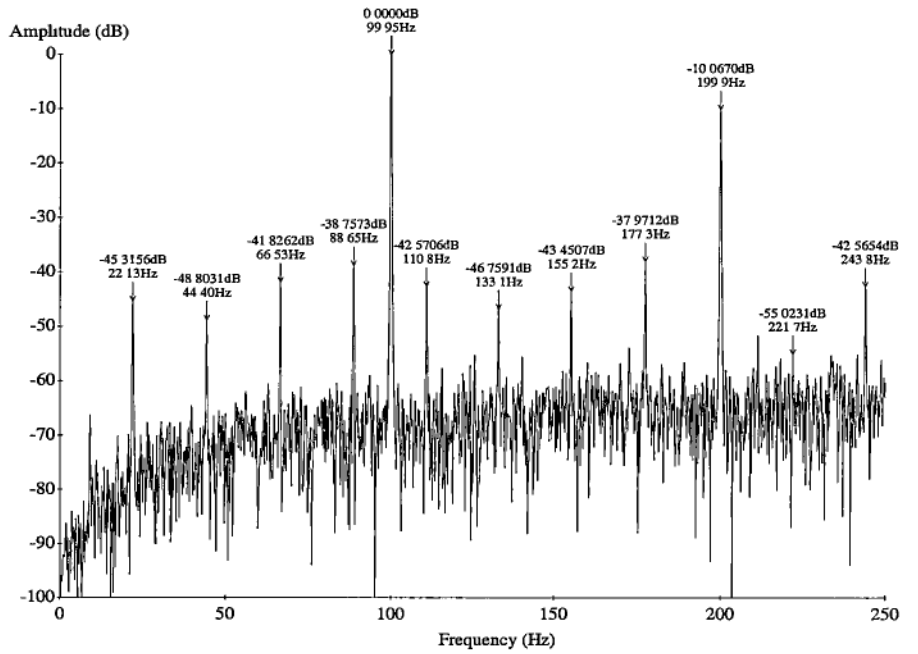

Figure 5.17: Frequency spectrum of the derivative of field current with a good armature (m87)

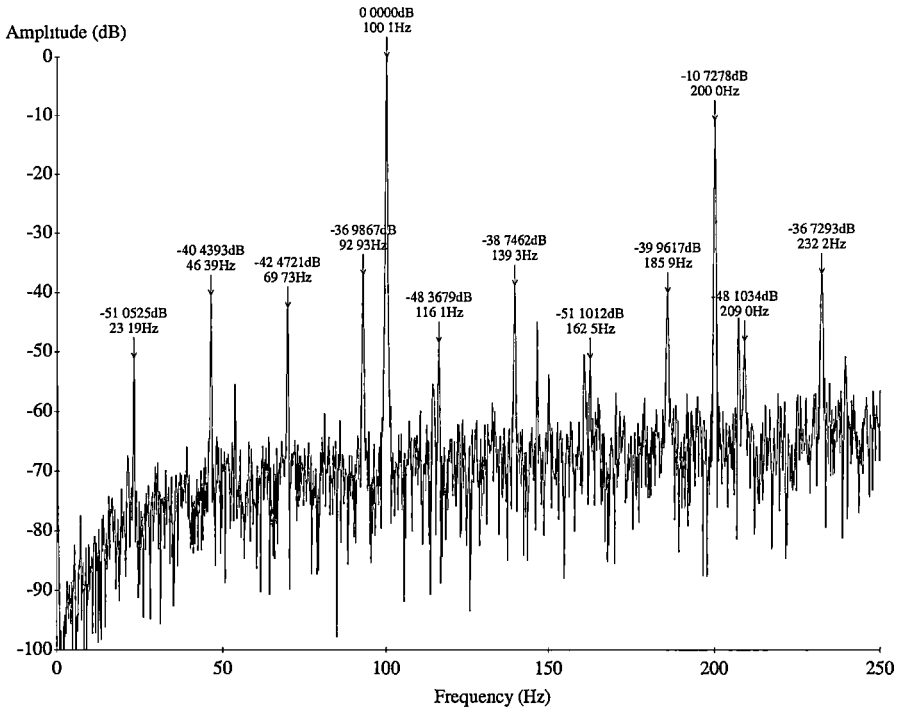

Figure 5.18: Frequency spectrum of the derivative of field current with an open-circuit armature coil (M87)

When there is an open-circuit coil in one of the two parallel armature circuits, a massive change in current occurs when the faulty coil passes under the brush. It induces disastrous spikes and noise in the armature current waveform.

When there is a short in one armature coil, a large current is induced in the shorted coil, which induces a large flux change and generate magnetic pull to the rotor. Hence, speed frequency and its multiples become dominant.

Experiment shows that the field current spectrum does not reflect the change armature circuit because the armature winding and the field winding are in electrical space quadrature, and the magnetic coupling factor is very low.

5.6 Summary

It is essential that commutation be correct. Sparking will cause excessive wear of the brushes and the commutator. The nature of the effect is governed by the brushgear, the interpole strength and motor defects. This chapter first summarised the methods available for "measurement" of sparking, and for fault identification. Visual observation of sparking is most widely used in industry to assess DC motor condition. Off-line tests for winding defects may be used (but were not done at either of the two paper mills where we took measurements) and no serious attempt has been made to do on-line monitoring techniques to detect DC motor defects.

This chapter describes the preliminary tests that were carried out on three laboratory DC motors. The motors were run on full load steady state, with and without defect windings. The armature and field current waveforms were monitored by an air-core Rogowski coil. Spectrum analysis of the waveforms detected the amplitude change of some frequency components, due to the defects.

Results showed that the armature and field current spectrum of a healthy motor is dominated by rectifier ripple frequency and the speed harmonics (integer multiples of speed frequency).

The effect of incorrect interpole strength on the DC motor currents was investigated; by-passing the interpole windings caused pin-point sparking. The frequencies due to incorrect interpole strength can be expressed as $f_{iips} = f_{cb} \pm nf_r$, where n is integer 1, 2, 3, .., f_{cb} is commutator bar frequency, ie number of commutator segment times speed frequency, and f_r is rotor speed frequency.

Two motors were tested with and without armature defects. The two pole motor (one brush pair), with a fault showed the amplitude of the multiples of the speed frequency of armature current to increase. The speed frequency has a larger increase in amplitude than the rest. For a four-pole motor (two brush pairs) with a fault, the amplitude of the even speed harmonics has a larger amplitude increase than the rest. The amplitude of the speed frequency does not change. These observations show that

the frequency component due to armature defects can be expressed as $f_{ocac} = N_{bp} f_r$, where N_{bp} is number of brush pairs.

However, the effect of these defects on the field current is not significant, due to the low magnetic coupling factor between the field and armature circuit.

As the fault-related frequencies can be present in a good armature, and the existence of armature damage has to be indicated by a significant *change* in the amplitude of a particular frequency, a numerical model is needed to get a better understanding of what is a significant change. Chapter 6 describes numerical models of the Davey motor with open-circuit or short-circuit armature coil at steady state operation. Coupled coil theory was used, and all individual armature coils were modelled. The results discussed in this chapter are backed up by predictions from the model.

Chapter 6

Numerical Modelling of DC Motors with Open-circuit and Short-circuit Armature Coils

Chapter 5 gives some preliminary test results on laboratory motors to demonstrate the effect of an open-circuit or a short-circuit armature coil on the armature and field current waveform. The experimental results show that the fault-related frequencies (predominantly speed frequency and its multiples) are often present in the armature and field current of a healthy motor, and that armature coil damage can only be reliably indicated by a significant change in the amplitude of the particular frequencies. In order to get a better understanding of what is a significant change of amplitude, a DC motor with an open-circuit or short-circuit armature coil was modelled in order to compute the waveform of the armature and field current at steady state condition.

In general, there are two distinct methods of simulating electric machines: finite element analysis and coupled circuit analysis. Finite element analysis effectively breaks the machine up into very small regions and then solves the magnetic field equations subject to constraints at the boundaries of each of these regions [114]. A

complete flux pattern in the machine can thus be built up. It requires a large amount of computer processing power and time to solve the equations. Finite element analysis is not used in this thesis for this reason. This type of model is mostly used for design purposes, but it does not give voltage or current waveforms directly and is therefore of less use for the purposes of this research than the coupled coil model.

The alternative to finite element analysis is to model the machine as a set of inductively coupled coils and hence from its equivalent circuit. Any voltages and currents can then be calculated directly by solving the equivalent circuit equations.

The simple two-winding equivalent circuit is the most common one for a healthy DC motor in steady state operation. There is one stator field winding that consist of a two or four series connected coils depending on the number of poles, and one armature winding that consist of the various coils interconnected at the commutator. It can not model a shorted coil.

Jones [125-126] used the coupled coil (also known as unified-machine) theory to elucidate the mechanism of commutation and the performance of DC motors. Four coils were used in the model: (i) The stator field winding, (i) the interpoles (that form a second stator winding in electrical space quadrature with the field winding), (iii) the main armature, excluding the commutating coils, (iv) the commutating coils. Each stage of analysis was supported with a comprehensive series of experimental results. A particularly valuable feature is the development of methods for the measurement of the machine inductance.

Guhmann and Filbert [113] detected and localised faults in the rotor of low-power universal motors by analysing the current signal in time and frequency domain. Five 250W, 12,000 rpm, 32 commutator segments universal motors were specially prepared for the tests. Motor 1 had an unconnected armature winding. Motor 2 had one commutator segment with a different height to the others. Motor 3 had a short circuit between adjacent commutator segments. Motor 4 had an eccentric commutator, and motor 5 was a healthy motor. Since the current waveforms were not sampled with a constant sampling rate, the frequency spectra were plotted as multiples of the rotating frequency. The current spectra were calculated by using linear prediction method (Burg Algorithm). The results of low-power universal

motors in good condition and different kind of fault conditions were presented in time and frequency domain. However, no general conclusion was made for the extra frequency components caused by different kind of faults.

Application of a parameter estimation method to the diagnosis of low-power DC and AC motor drive systems has been reported by Filbert, Schneider and Nold [113, 115-121]. An electric motor drive system can be described by energy balance equations, and continuous time models can be used. The state values given from the energy balance equations have to be measured and the loss function has to be minimised by an estimator such as least-squares. As balance equations are used to describe a functional model of a motor, which is a power converter, detectable faults must be related to a significant change of the power distribution in the motor, such as winding defects or brushes. Faults that only produce acoustic noise or vibration, such as bearing, gear, or commutator faults, cannot be detected by the parameter estimation method.

Krisch [122] investigated the commutation of a DC machine with a wave winding. Based on the assumption that the coil in each slot is identical, only one coil needed to be modelled. The commutation properties of the wave winding was computed and compared to experimental measurement. He concluded that the frequency of the pulsation of the armature current equals (number of commutator segments) times (speed frequency), and the current density on the leaving brush edge might be several times more than that of nominal value for late commutation.

A recent paper on DC motors is by Glowacz [123]. He modelled two DC motors with the field and armature coils as connected individual coils. One of them was a 52 slot lap-winding motor, and the other one was a 53 slot wave-winding motor. The inductance of the coils was determined by the air gap permeance function, expressed as a Fourier Series. The effects of the short- and open-circuit of the armature coils were simulated. This six-page conference paper briefly described the development of this model. Only short-circuit armature coil measurement results were given and compared. No conclusions were made for any fault-related frequency components of motor current. No references were in English.

One of the references that Glowacz referred to for the determination of the machine inductances was Schröder and Oberretl's paper [124]. It is a German paper, which was translated for me by a German student in the Department of Electrical Engineering and Computer Science of the University of Tasmania. This paper described a method of calculation of all current and voltage (eg bar-to-bar voltage) waveforms of a DC motor. It is based on field-harmonic theory, which takes all armature reactions between stator and rotor into account. The rotor position dependent self- and mutual inductances are obtained by finite element calculations and then resolved into Fourier series. The brush-commutator is simulated by brush contact resistances, which depend on the rotor positions. The function of brush resistance over time is periodically extended to an odd function and eventually resolved into Fourier series. The calculation was based on a very simple three-slot machine such as would be used for a model railway engine hardly an industrial applications. The brush-commutator contact resistance, armature current, field current, armature coil current and bar-to-bar voltage were measured and compared to the calculated values. The authors made no conclusions.

This chapter examines a healthy DC motor model for steady state operation, using coupled coil theory. The model is then adapted for the modelling of an open-circuit armature coil. A similar approach models a short-circuit armature coil. These models specifically used the construction details of a laboratory motor to simulate individual field coils, armature coils, and 'faulty' coil. Some simulation results of the armature and field current from this model are reported and are compared with the experimental measurements.

6.1 The Coupled Coils Theory

Consider a system with k magnetically coupled electric circuits. Assume that each circuit can be represented by concentrated coils so that all fluxes in a coil link every turn of that coil. In general, the flux produced by each coil can be separated into two components, ie the self-flux and $(n-1)$ components of mutual flux. The self-flux of the k^{th} coil consists of the magnetising flux, Φ_{mk}, which links all the other coils, and the leakage flux, Φ_{lk}. The leakage component is denoted with a l subscript and a

magnetising component denoted by a *m* subscript. The flux linking each coil may be expressed

$$\Phi_k = \Phi_{lk} + \Phi_{mk} + \sum_{\substack{j=1 \\ j \neq k}}^{n} \Phi_{nj} \tag{6.1}$$

With N_k turns of coil *k*, the flux linkages are

$$\lambda_k = N_k \Phi_k = \lambda_{lk} + \lambda_{mk} + \sum_{\substack{j=1 \\ j \neq k}}^{n} \lambda_{nj} \tag{6.2}$$

These components may be written in terms of the air gap permeance, Λ, as

$$\begin{aligned} \lambda_{lk} &= N_k \Phi_{lk} = \Lambda_{lk} N_k^2 i_k \\ \lambda_{mk} &= N_k \Phi_{mk} = \Lambda_{mk} N_k^2 i_k \\ \lambda_{lk} &= N_k \Phi_{kj} = \Lambda_{kj} N_k N_j i_j \end{aligned} \tag{6.3}$$

where i_k is the current of coil *k*.

Hence, the following inductances may be defined:

Self inductance:

$$L_k = L_{lk} + L_{mk} = (\Lambda_{lk} + \Lambda_{mk}) N_k^2 = \frac{N_k \Phi_{kk}}{i_k} \tag{6.4}$$

Mutual inductance between coil *k* and coil *j*:

$$M_{kj} = M_{jk} = \Lambda_{kj} N_k N_j = \frac{N_k \Phi_{kj}}{i_j} \tag{6.5}$$

as the permeance $\Lambda_{kj} = \Lambda_{jk}$.

The total flux linkage for each of the *n* coils can be expressed in matrix form using equations (6.3-6.5):

$$\lambda = \mathbf{L}\mathbf{i} \Rightarrow \begin{bmatrix} \lambda_1 \\ \lambda_2 \\ \lambda_3 \\ \vdots \\ \lambda_n \end{bmatrix} = \begin{bmatrix} L_1 & M_{12} & M_{13} & \cdots & M_{1n} \\ M_{21} & L_2 & M_{23} & \cdots & M_{2n} \\ M_{31} & M_{32} & L_3 & \cdots & M_{3n} \\ \vdots & \vdots & \vdots & \ddots & \vdots \\ M_{n1} & M_{n2} & M_{n3} & \cdots & L_n \end{bmatrix} \begin{bmatrix} i_1 \\ i_2 \\ i_3 \\ \vdots \\ i_n \end{bmatrix} \tag{6.6}$$

The voltage equation of coil k is:

$$v_k = R_k i_k + \frac{d\lambda_k}{dt} \tag{6.7}$$

The voltage equations of the system in matrix form are:

$$\mathbf{v} = \mathbf{R}\mathbf{i} + \frac{d\lambda}{dt} \tag{6.8}$$

and if inductance matrix, **L**, and current matrix **i**, are time varying, then equation (6.8) becomes:

$$\mathbf{v} = \mathbf{R}\mathbf{i} + \mathbf{i}\frac{d\mathbf{L}}{dt} + \mathbf{L}\frac{d\mathbf{i}}{dt} \tag{6.9}$$

Equation (6.9) can be written as the first order differential equation of the form $\frac{dy}{dt} = f(t, y(t))$ as

$$\frac{d\mathbf{i}}{dt} = \mathbf{L}^{-1}\mathbf{v} - \mathbf{L}^{-1}\left(\mathbf{R} + \frac{d\mathbf{L}}{dt}\right)\mathbf{i} \tag{6.10}$$

This is usually expressed as an initial value problem and can be solved numerically. Models can either use equation (6.9), or equations (6.6) and (6.8) can be used simultaneously.

6.2 The First Approach of Coupled Coil Model of the DC Machine with Individual Armature Sub Coils Modelled

Coupled coil theory models a DC machine by considering both the field and armature to consist of sets of concentrated coils. In order to develop such a model, the construction details of the motor have to be known. For the rotor, this includes the

number of coils, number of slots, the physical dimensions of the brushes and the commutator bars, and the physical arrangement and connection of the armature coils.

This model is based on a 2-pole, 1/2 HP, 16 slots, and 48 segments motor (Davey machine, Appendix A2.3). It has a simplex-lap winding with 16 coils. Each coil is made up of three 17-turn sub coils in series, as shown in figure 6.1. Coil 1 is made up of sub coils 1a, 1b, and 1c. The coil span is 7 slots and the brush width is 4 times the commutator bar width. Figure 6.2 shows a portion of the connection of the armature winding and the brush-commutator set.

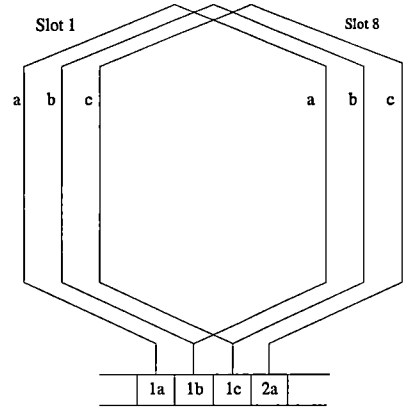

Figure 6.1: Three sub coils per slot of Davey machine

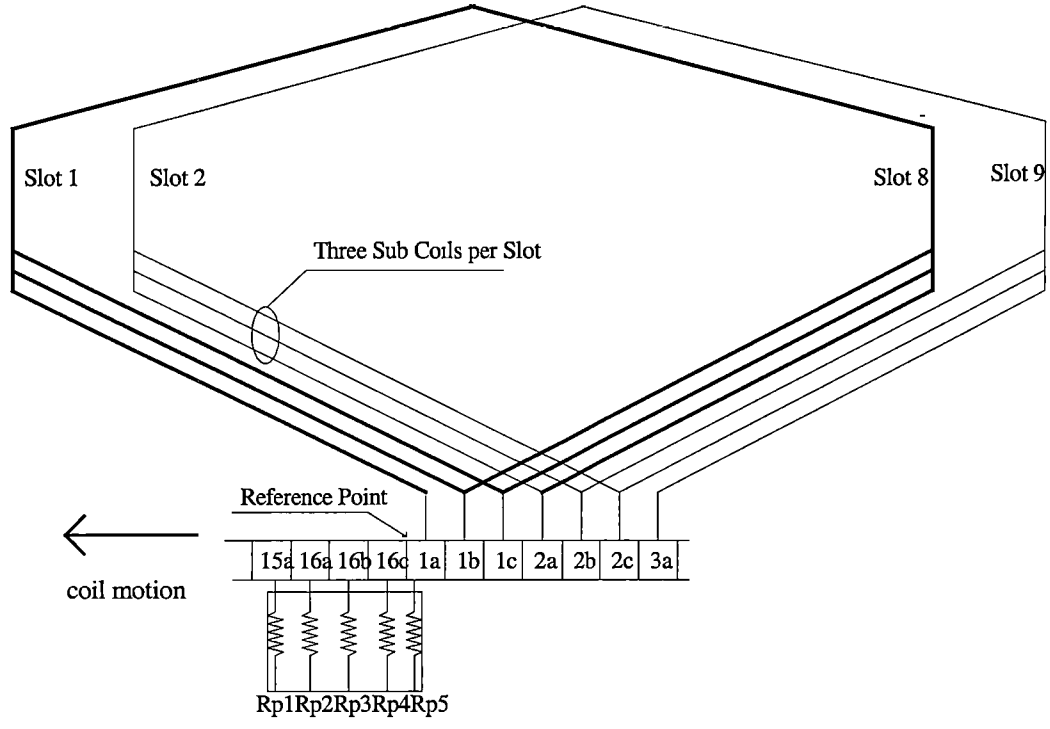

Figure 6.2: The armature circuit of the Davey Machine

The first approach was based on the sub coils. The operation of the machine was simulated with 48 intervals per revolution (48 segments 7.5 mechanical degrees apart). It is assumed that the reference point (rotor position = zero mechanical degrees) is that when the brush only contacts segments 15c, 16a, 16b, and 16c. When the rotor moves, segment 1a moves toward the brush, ie sub coil 16c starts to commutate. The brush contacts segments 15c, 16a, 16b, 16c, and 1a. Five contact resistors can model each brush. R_{pk} are the positive brush contact resistors, where k=1, 2, 3, 4 and 5. These resistance values depend on the segment-brush contact surface and are time varying. R_{nk} are the corresponding contact resistors of negative brush that are not shown in figure 6.2.

Figure 6.3 shows the equivalent circuit of the armature of the Davey machine. The armature circuit was modelled as 10 individual coils in two parallel paths. Each path is formed by 20 sub coils in series and is modelled by two coils named as S_1 and S_2. Four coils are under commutation at positive brush named, C_{pm}, where m=1, 2, 3 and 4. At this rotor position, they correspond to sub coils 15c, 16a, 16b and 16c respectively. Coils C_{nm} are commutated under negative brush, corresponding to sub coils 7c, 8a, 8b, and 8c. As the machine is modelled as a generator, the generated voltage is supplied to a load resistor. It is expected that the harmonic contents in the field and armature current are the same when the machine is operated at motor mode or generator mode. The field circuit, which is not shown here, can simply be represented by a coil supplied by a constant voltage.

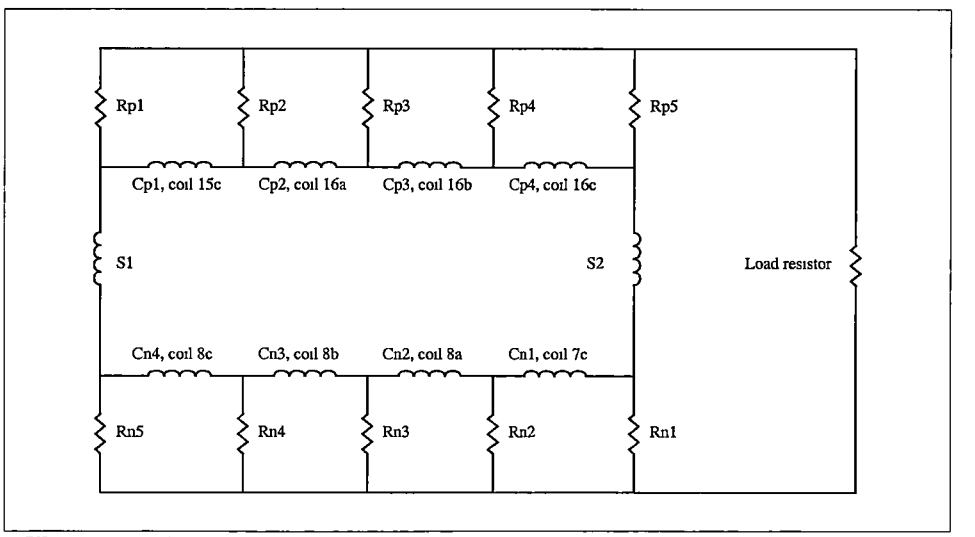

Figure 6.3: The equivalent circuit of the Davey machine-complete model

All the coils in the equivalent circuit are magnetically coupled to each other. It is assumed that all the fluxes in each coil link every turn of that coil, ie "concentrated". The total flux linking any one of the coils is the superposition of the self-flux and the mutual fluxes. The differential equations of the rotor can be written as an equation (6.10), in which resistance and inductance matrixes are now 11 by 11.

In order to solve equation (6.10) numerically, the calculation of the inverse of the inductance matrix is involved. As the sub coils in each slot have the same physical structure and position, the flux linkages of these sub coils are the same. Since there are always at least three coils under commutation, it means that there will be at least two rows of the inductance matrix numerically very close or equal. For example, at the rotor position shown in figure 6.2, the corresponding inductance matrix is

$$\mathbf{L} = \begin{bmatrix}
L_{ff} & M_{f_15c} & M_{f_16a} & M_{f_16b} & M_{f_16c} & M_{f_7c} & M_{f_8a} & M_{f_8b} & M_{f_8c} & M_{f_s2} & M_{f_s1} \\
M_{f_15c} & L_{15c} & m_{15c_16a} & m_{15c_16b} & m_{15c_16c} & m_{15c_7c} & m_{15c_8a} & m_{15c_8b} & m_{15c_8c} & m_{15c_s2} & m_{15c_s1} \\
M_{f_16a} & m_{15c_16a} & L_{16a} & m_{16a_16b} & m_{16a_16c} & m_{16a_7c} & m_{16a_8a} & m_{16a_8b} & m_{16a_8c} & m_{16a_s2} & m_{16a_s1} \\
M_{f_16b} & m_{15c_16b} & m_{16a_16b} & L_{16b} & m_{16b_16c} & m_{16b_7c} & m_{16b_8a} & m_{16b_8b} & m_{16b_8c} & m_{16b_s2} & m_{16b_s1} \\
M_{f_16c} & m_{15c_16c} & m_{16a_16c} & m_{16b_16c} & L_{16c} & m_{16c_7c} & m_{16c_8a} & m_{16c_8b} & m_{16c_8c} & m_{16c_s2} & m_{16c_s1} \\
M_{f_7c} & m_{15c_7c} & m_{16a_7c} & m_{16b_7c} & m_{16c_7c} & L_{7c} & m_{7c_8a} & m_{7c_8b} & m_{7c_8c} & m_{7c_s2} & m_{7c_s1} \\
M_{f_8a} & m_{15c_8a} & m_{16a_8a} & m_{16b_8a} & m_{16c_8a} & m_{7c_8a} & L_{8a} & m_{8a_8b} & m_{8a_8c} & m_{8a_s2} & m_{8a_s1} \\
M_{f_8b} & m_{15c_8b} & m_{16a_8b} & m_{16b_8b} & m_{16c_8b} & m_{7c_8b} & m_{8a_8b} & L_{8b} & m_{8b_8c} & m_{8b_s2} & m_{8b_s1} \\
M_{f_8c} & m_{15c_8c} & m_{16a_8c} & m_{16b_8c} & m_{16c_8c} & m_{7c_8c} & m_{8a_8c} & m_{8b_8c} & L_{8c} & m_{8c_s2} & m_{8c_s1} \\
M_{f_s2} & m_{15c_s2} & m_{16a_s2} & m_{16b_s2} & m_{16c_s2} & m_{7c_s2} & m_{8a_s2} & m_{8b_s2} & m_{8c_s2} & L_{s2} & m_{s2_s1} \\
M_{f_s1} & m_{15c_s1} & m_{16a_s1} & m_{16b_s1} & m_{16c_s1} & m_{7c_s1} & m_{8a_s1} & m_{8b_s1} & m_{8c_s1} & m_{s2_s1} & L_{s1}
\end{bmatrix} \tag{6.11}$$

As the sub coils 16_a, 16_b and 16_c are in the same slot, then

$$\begin{aligned}
&M_{f_16a} = M_{f_16b} = M_{f_16c} \\
&m_{16a_7c} = m_{16b_7c} = m_{16c_7c} \\
&m_{16a_8a} = m_{16b_8a} = m_{16c_8a} \\
&m_{16a_8b} = m_{16b_8b} = m_{16c_8b} \\
&m_{16a_8c} = m_{16b_8c} = m_{16c_8c} \\
&m_{16a_s1} = m_{16b_s1} = m_{16c_s1} \\
&m_{16a_s2} = m_{16b_s2} = m_{16c_s2} \\
&L_{16a} = L_{16b} = L_{16c} \approx m_{16a_16b} = m_{16a_16c} = m_{16b_16c}
\end{aligned} \tag{6.12}$$

Therefore, the third, fourth and fifth rows of the **L** matrix are numerically very close or equal. A similar pattern will be obtained for the seventh, eighth and ninth row of

the matrix. The inductance matrix becomes singular and it is impossible to obtain the corresponding inverse matrix.

As the three sub coils connected in series in the same slot have the same flux linkage, they can be treated as a single coil. Hence, the second approach of the DC machine modelling is based on such coils (ie one coil per slot) and will be discussed in the next section.

6.3 Coupled Coil Model of the Davey Machine with One Coil per Slot

This model of the Davey machine has the following assumptions:

- The model merges three sub coils into one equivalent armature coil, there are thus 16 coil and 16 slots
- the width of the commutator segment is three times the original,
- the magnetic circuits are linear,
- the unipolar flux is neglected,
- the effect of the eddy current in iron is neglected,
- the entire brush-commutator segment contact surface conducts current uniformly,
- the commutator-brush set is approximated by variable resistors which are independent of current density and surface contact dimensions but dependent on rotor position,
- the total brushes voltage drop is assumed to be 1 volt,
- the ratio between negative and positive brush resistance is 1.25:1,
- the width of the insulation strip between the commutator segments is neglected.

In the following text, the term 'coil(s)' refers to a coil that is formed by three sub coils connected in series at the same slot. The coils are 22.5° apart in space from each other and the flux linkages of these coils are different. Hence, the singular inductance matrix caused by the physical structure of the sub coils is avoided. The commutator segment width is assumed to be three times the original. The commutation time of each coil is three times longer than the previous case. All resistance and inductance measurements of the motor are described in section 6.6.

In figure 6.5a, the relative positions of the positive brush and commutator segments are shown for the instant at which commutation is just beginning for coil 16. The rotor position in mechanical degrees θ_{rm} is equal to zero. Before coil 16 starts to commutate, the positive brush partially contacts segments 15 and 16. Two resistors can be used to model the positive brush, R_{p1} and R_{p2}. The corresponding equivalent resistors of the negative brush are R_{n1} and R_{n2}, which are not shown. At this instant, the ends of coils 15 and 7 are connected to positive and negative brushes respectively. 7 coils form each of the parallel paths. Thus the Davey machine can be modelled by 5 concentrated coils: the field circuit, the two parallel paths of armature coils, and the two coils under commutation by the brushes.

Figure 6.5b shows the position of the positive brush partially on segments 15, 16 and 1. Coils 15 and 16 are connected to the positive brush (and coils 7 and 8 are connected to the negative brush) at $7.5^{\circ} > \theta_{rm} \geq 0$. Three resistors can be used to model each brush, R_{pm} and R_{nm}, where m=1, 2 and 3. Each parallel path consists of six coils. At this interval, the Davey machine can be modelled by 7 concentrated coils: the field coil, the two parallel paths of armature coils, and four coils connected to the brushes.

Figure 6.5c shows the corresponding positive brush position at the instant when the commutation of coil 15 ends, $\theta_{rm} = 7.5^{\circ}$. When $22.5^{\circ} > \theta_{rm} \geq 7.5^{\circ}$, coils 16 and 8 are under commutation, ie the positive brush partially contacts segments 16 and 1 (or negative brush is partially on segments 8 and 9). Again, a 5-coil equivalent circuit can be used to model the Davey machine.

The brush-commutator sets are modelled by two the positive brush resistance R_{bp} and the negative brush resistance R_{bn}. The combined value of R_{pb} and R_{nb} is determined by assuming the total brush voltage drop is 1 volt at rated current. Each brush-commutator contact resistance is proportional to the brush-commutator contact surface, and varies with rotor position. For example, when $30^{\circ} > \theta_{rm} \geq 45^{\circ}$ the positive brush is formed by R_{p1}, and R_{p2} in parallel. The dashed and the solid lines in figure 6.4 show the contact resistance R1 (R_{p1}), between the brush and segment 1,

and R2 (R_{p2}) for segment 2 varying with rotor position. When segment 2 is moved towards the brush, R2 decreases from infinite to R_{com}, that corresponds with the resistance value when segment 2 is totally covered by the brush. When segment 1 is moved apart from the brush, R1 increases from R_{com} to infinite. The pattern of R2 is the same as R1 but having a 22.5 mechanical degrees phase shift related to R1. It should be noted that the resistance axis of figure 6.4 is terminated at one ohm in order to display the pattern of R1 and R2.

The operation of the Davey machine was simulated with 16 intervals of rotor positions in a revolution. The 7-coil equivalent circuit and 5-coil equivalent circuit are used to model the steady state operation of the Davey machine at each interval. The combination of coils used in the equivalent circuits is summarised in table 6.1 at different rotor positions. The equivalent circuits are discussed in detail in the following sections.

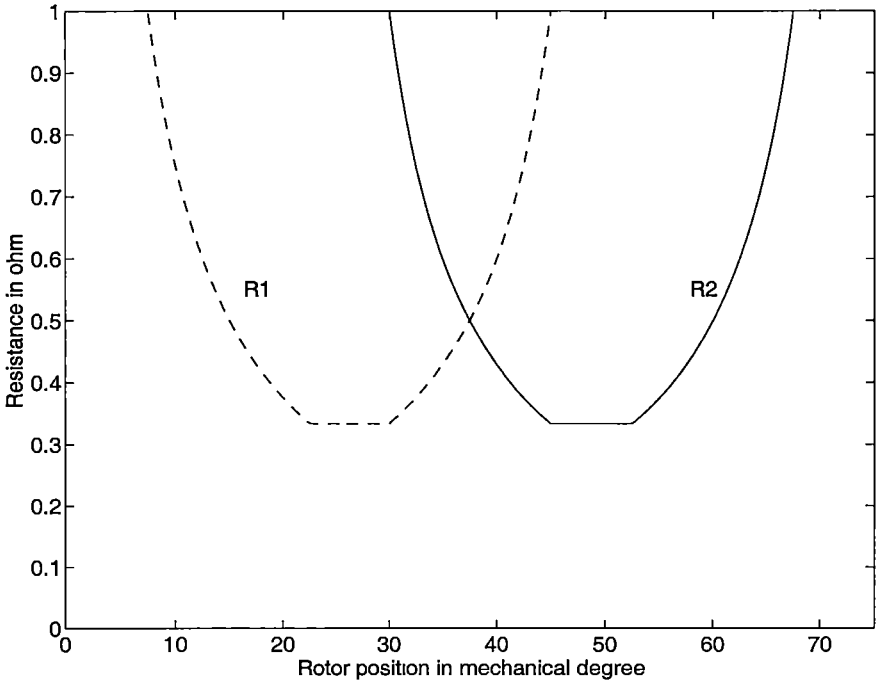

Figure 6.4: The brush-segment contact resistance of Davey machine

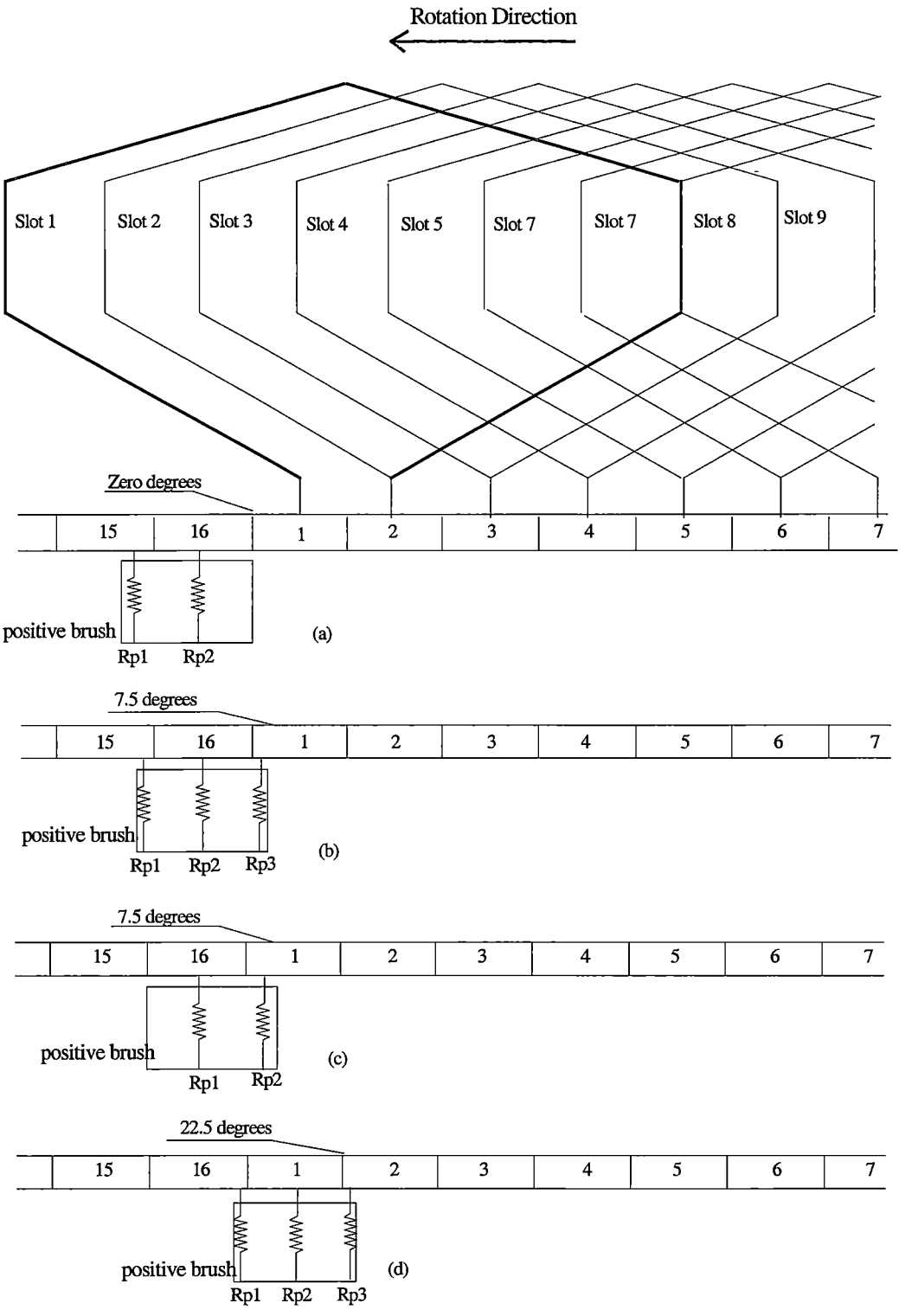

Figure 6.5: The armature circuit of the Davey Machine at different rotor positions

Rotor position θ_{rm}	C_{p1} / C_{n1} coil number	C_{p2} / C_{n2} coil number	S_1 / S_2 coil number
$0 > \theta_{rm} \geq 7.5$	15 / 7	16 / 8	9,10,11,12,13,14 / 1, 2, 3, 4, 5, 6
$7.5 > \theta_{rm} \geq 22.5$	16 / 8		9,10,11,12,13,14,15 / 1,2,3,4,5,6,7
$22.5 > \theta_{rm} \geq 30$	16 / 8	1 / 9	10,11,12,13,14,15 / 2,3,4,5,6,7
$30 > \theta_{rm} \geq 45$	1 / 9		10,11,12,13,14,15,16 / 2,3,4,5,6,7,8
$45 > \theta_{rm} \geq 52.5$	1 / 9	2 / 10	11,12,13,14,15,16 / 3,4,5,6,7,8
$52.5 > \theta_{rm} \geq 67.5$	2 / 10		11,12,13,14,15,16,1 / 3,4,5,6,7,8,9
$67.5 > \theta_{rm} \geq 75$	2 / 10	3 / 11	12,13,14,15,16,1 / 4,5,6,7,8,9
$75 > \theta_{rm} \geq 90$	3 / 11		12,13,14,15,16,1,2 / 4,5,6,7,8,9,10
$90 > \theta_{rm} \geq 97.5$	3 / 11	4 / 12	13,14,15,16,1,2 / 5,6,7,8,9,10
$97.5 > \theta_{rm} \geq 112.5$	4 / 12		13,14,15,16,1,2,3 / 5,6,7,8,9,10,11
$112.5 > \theta_{rm} \geq 120$	4 / 12	5 / 13	14,15,16,1,2,3 / 6,7,8,9,10,11
$120 > \theta_{rm} \geq 135$	5 / 13		14,15,16,1,2,3,4 / 6,7,8,9,10,11,12
$135 > \theta_{rm} \geq 142.5$	5 / 13	6 / 14	15,16,1,2,3,4 / 7,8,9,10,11,12
$142.5 > \theta_{rm} \geq 157.5$	6 / 14		15,16,1,2,3,4,5 / 7,8,9,10,11,12,13
$157.5 > \theta_{rm} \geq 165$	6 / 14	7 / 15	16,1,2,3,4,5 / 8,9,10,11,12,13
$165 > \theta_{rm} \geq 180$	7 / 15		16,1,2,3,4,5,6 / 8,9,10,11,12,13,14
$180 > \theta_{rm} \geq 187.5$	7 / 15	8 / 16	1,2,3,4,5,6 / 9,10,11,12,13,14
$187.5 > \theta_{rm} \geq 202.5$	8 / 16		1,2,3,4,5,6,7 / 9,10,11,12,13,14,15
$202.5 > \theta_{rm} \geq 210$	8 / 16	9 / 1	2,3,4,5,6,7 / 10,11,12,13,14,15
$210 > \theta_{rm} \geq 225$	9 / 1		2,3,4,5,6,7,8 / 10,11,12,13,14,15,16
$225 > \theta_{rm} \geq 232.5$	9 / 1	10 / 2	3,4,5,6,7,8 / 11,12,13,14,15,16
$232.5 > \theta_{rm} \geq 247.5$	10 / 2		3,4,5,6,7,8,9 / 11,12,13,14,15,16,1
$247.5 > \theta_{rm} \geq 255$	10 / 2	11 / 3	4,5,6,7,8,9 / 12,13,14,15,16,1
$255 > \theta_{rm} \geq 270$	11 / 3		4,5,6,7,8,9,10 / 12,13,14,15,16,1,2
$270 > \theta_{rm} \geq 277.5$	11 / 3	12 / 4	5,6,7,8,9,10 / 13,14,15,16,1,2
$277.5 > \theta_{rm} \geq 292.5$	12 / 4		5,6,7,8,9,10,11 / 13,14,15,16,1,2,3
$292.5 > \theta_{rm} \geq 300$	12 / 4	13 / 5	6,7,8,9,10,11 / 14,15,16,1,2,3
$300 > \theta_{rm} \geq 315$	13 / 5		6,7,8,9,10,11,12 / 14,15,16,1,2,3,4
$315 > \theta_{rm} \geq 322.5$	13 / 5	14 / 6	7,8,9,10,11,12 / 15,16,1,2,3,4
$322.5 > \theta_{rm} \geq 337.5$	14 / 6		7,8,9,10,11,12,13 / 15,16,1,2,3,4,5
$337.5 > \theta_{rm} \geq 345$	14 / 6	15 / 7	8,9,10,11,12,13 / 16,1,2,3,4,5
$345 > \theta_{rm} \geq 360$	15 / 7		8,9,10,11,12,13,14 / 16,1,2,3,4,5,6

Table 6.1: The combination of armature coils used in the equivalent circuits

6.3.1 7-coil Equivalent Circuit of the Davey Machine

Figure 6.6 shows the 7-coil equivalent circuit of the Davey machine. In the armature circuit, coil S_1 and S_2 represent the two paths that are formed by 6 coils connected in series. R_{s1} and R_{s2} are the corresponding path resistance. Four coils are under commutation. Coils C_{p1} and C_{p2} are commutated by the positive brush while coils C_{n1} and C_{n2} are commutated by the negative brush. R_{cp1}, R_{cp2}, R_{cn1}, and R_{cn2} are the corresponding coil resistance. Each brush is modelled by three brush-segment contact resistors. They are R_{pk} and R_{nk}, where k=1, 2 and 3. These brush-segment contact resistors are rotor position varying.

The field circuit is simply represented by a coil in series with a resistor and supplied by a pure DC voltage.

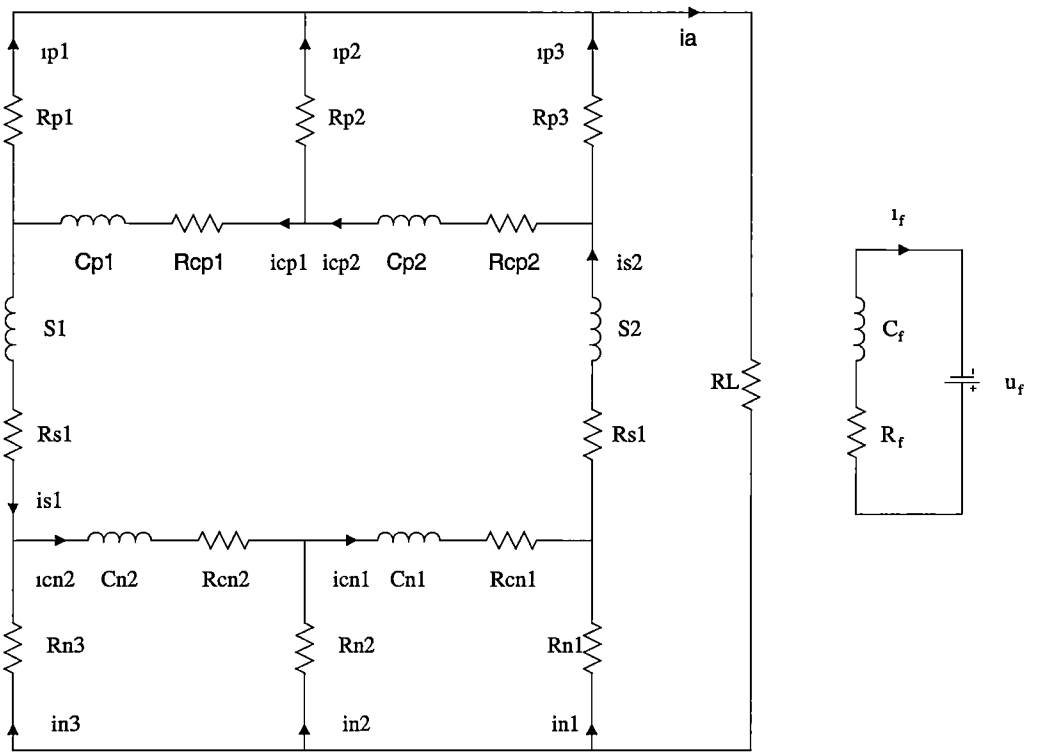

Figure 6.6: The 7-coil equivalent circuit of the Davey machine

Let i_f, i_{cp1}, i_{cp2}, i_{cn1}, i_{cn2}, i_{s1} and i_{s2} be the coil currents; and i_{p1}, i_{p2}, i_{p3}, i_{n1}, i_{n2} and i_{n3} be the brush currents. From figure 6.6, the coil voltage can be expressed in terms of the voltage drops of the brush resistors. For coil C_{p1},

$$U_{cp1} = i_{cp1} \cdot R_{cp1} + \dot{\lambda}_{cp1} = i_{p2} \cdot R_{p2} - i_{p1} \cdot R_{p1} \tag{6.13}$$

The brush resistor currents can also be expressed in terms of the coil currents,

$$i_{p1} = i_{cp1} - i_{s1} \tag{6.14}$$

$$i_{p2} = i_{cp2} - i_{cp1} \tag{6.15}$$

Substitute equations (6.14) and (6.15) into (6.13) gives

$$\left(R_{cp1} + R_{p1} + R_{p2}\right) i_{cp1} - R_{p2} \cdot i_{cp2} - R_{p1} \cdot i_{s1} + \dot{\lambda}_{cp1} = 0 \tag{6.16}$$

The derivation of the voltage equations of the coils is shown in Appendix B. Only the result is given in this section. Seven differential equations can be obtained and written in matrix form as $\mathbf{v} = \mathbf{R}\mathbf{i} + \mathbf{i}\frac{d\mathbf{L}}{dt} + \mathbf{L}\frac{d\mathbf{i}}{dt}$, where

$$\mathbf{v} = \left[U_f \;\; 0 \;\; 0 \;\; 0 \;\; 0 \;\; 0 \;\; 0\right]^T; \tag{6.17}$$

$$\mathbf{i} = \left[i_f \;\; i_{cp1} \;\; i_{cp2} \;\; i_{s2} \;\; i_{cn1} \;\; i_{cn2} \;\; i_{s1}\right]^T \tag{6.18}$$

$\mathbf{R} =$

$$\begin{bmatrix}
R_f & 0 & 0 & 0 & 0 & 0 & 0 \\
0 & R_{cp1} + R_{p1} + R_{p2} & -R_{p2} & 0 & 0 & 0 & -R_{p1} \\
0 & -R_{p2} & R_{cp2} + R_{p2} + R_{p3} & -R_{p3} & 0 & 0 & 0 \\
0 & 0 & -R_{p3} & R_{s2} + R_{p3} + R_{n1} + R_L & -R_{n1} & 0 & -R_L \\
0 & 0 & 0 & -R_{n1} & R_{cn1} + R_{n1} + R_{n2} & -R_{n2} & 0 \\
0 & 0 & 0 & 0 & -R_{n2} & R_{cn2} + R_{n2} + R_{n3} & -R_{n3} \\
0 & -R_{p1} & 0 & -R_L & 0 & -R_{n3} & R_{s1} + R_{p1} + R_{n3} + R_L
\end{bmatrix} \tag{6.19}$$

$$\mathbf{L} = \begin{bmatrix} L_{ff} & M_{f\_cp1} & M_{f\_cp2} & M_{f\_s2} & M_{f\_cn1} & M_{f\_cn2} & M_{f\_s1} \\ M_{cp1\_f} & L_{cp1} & m_{cp1\_cp2} & m_{cp1\_s2} & m_{cp1\_cn1} & m_{cp1\_cn2} & m_{cp1\_s1} \\ M_{cp2\_f} & m_{cp2\_cp1} & L_{cp2} & m_{cp2\_s2} & m_{cp2\_cn1} & m_{cp2\_cn2} & m_{cp2\_s1} \\ M_{s2\_f} & m_{s2\_cp1} & m_{s2\_cp2} & L_{s2} & m_{s2\_cn1} & m_{s2\_cn2} & m_{s2\_s1} \\ M_{cn1\_f} & m_{cn1\_cp1} & m_{cn1\_cp2} & m_{cn1\_s2} & L_{cn1} & m_{cn1\_cn2} & m_{cp1\_s1} \\ M_{cn2\_f} & m_{cn2\_cp1} & m_{cn2\_cp2} & m_{cn2\_s2} & m_{cn2\_cn1} & L_{cn2} & m_{cn2\_s1} \\ M_{s1\_f} & m_{s1\_cp1} & m_{s1\_cp2} & m_{s1\_s2} & m_{s1\_cn1} & m_{s1\_cn2} & L_{s1} \end{bmatrix} \quad (6.20)$$

U_f, R_f and L_{ff} are the field voltage, resistance and self inductance respectively. All the subscripts, parameters and variables are referred to in figure 6.6. In equation (6.20), L is the self inductance of coils. M is the mutual inductance between the field and the coils and m is the mutual inductance between coils of the armature circuit.

In order to solve the system equations, it is necessary to obtain the various coefficient matrices, $\mathbf{R}$, $\mathbf{L}$ and $\frac{d\mathbf{L}}{dt}$. They are dependent on the rotor position and must be obtained for every iteration, and will be discussed in the following sections.

6.3.1.1 Coil resistance of the 7-coil equivalent circuit

R_{coil} is defined as the coil resistance of each armature coil (16 armature coils in the Davey machine). Hence, in the resistance matrix,

$$R_{cp1} = R_{cp2} = R_{cn1} = R_{cn2} = R_{coil} \quad (6.21)$$

$$R_{s1} = R_{s2} = 6R_{coil} \quad (6.22)$$

6.3.1.2 Brush-segment contact resistance of the 7-coil equivalent circuit

During commutation, it is assumed that current is distributed uniformly over the brush surface to give a constant current density. The brush-segment of the coils undergoing commutation is inversely proportional to the interface surface areas between segments and brush.

Let R_{bp} be the brush resistance for the whole positive brush surface and assume that is ohmic. At a given instant, the brush-segment contact area of segment 'a' is A_a and

is proportional to G_a. The brush-segment contact area of segment 'c' is A_c and is proportional to G_c. Both G_a and G_c are rotor position dependent. The brush-segment contact area of segment b is A_b and is proportional to G_b. G_b is constant and equal to the segment width W_c. Then at a given instant, the contact areas

$$G_a + G_b + G_c = brushwidth = W_b \tag{6.23}$$

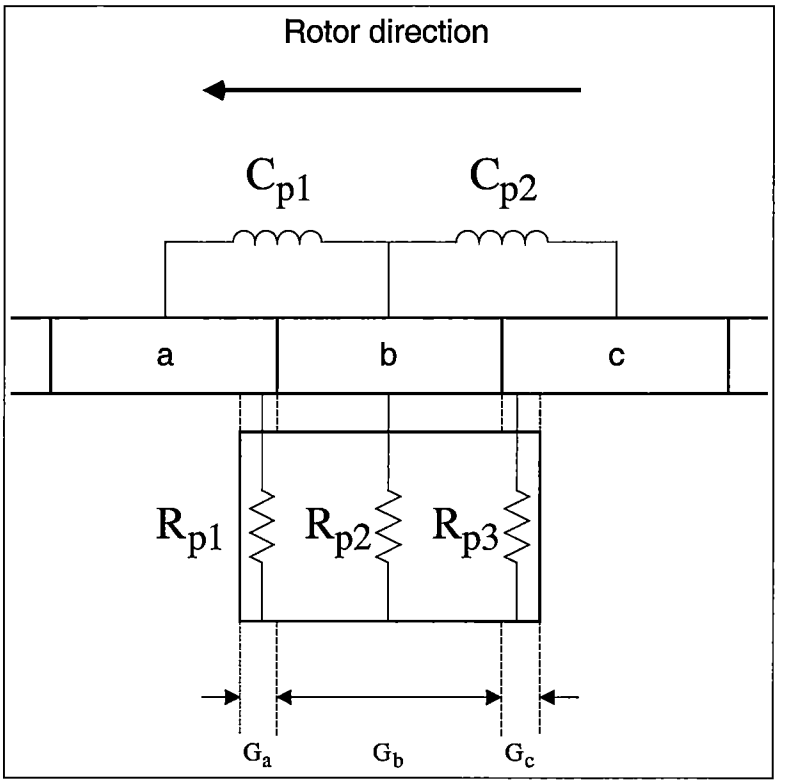

Figure 6.7: Brush-segment contact resistance of 7-coil equivalent circuit

The corresponding contact resistances are

$$R_{p1} = R_{bp}\frac{W_b}{G_a} \tag{6.24}$$

$$R_{p2} = R_{bp}\frac{W_b}{W_c} = R_{wc} \tag{6.25}$$

$$R_{p3} = R_{bp}\frac{W_b}{G_c} \tag{6.26}$$

The brush currents are inversely proportional to the resistance, ie directly proportional to G_a, G_b and G_c. As the change of G_a and G_c is linear with time, so also are the currents, giving "straight-line" commutation or "resistance" commutation, shown in figure 6.7.

Figure 6.8 shows the value of R_{p1}, R_{p2} and R_{p3} of the 7-coil equivalent circuit varying with the rotor position, assuming that $R_{bp} = 0.22\Omega$, the resistance between the positive brush and segments a and c varies with rotor position θ_{rm}. At this region, R_{p1} and R_{p3} cross over; ie R_{p1} decreases from infinite to $4R_{bp}$ and R_{p3} increases from $4R_{bp}$ to infinite; while R_{p2} is kept constant. The same assumption is made for the commutation process by the negative brush.

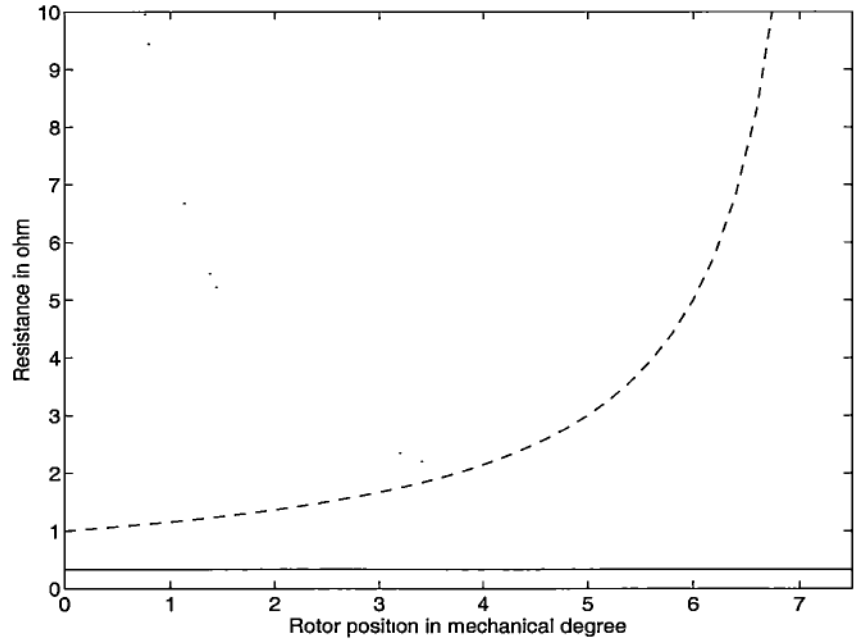

Figure 6.8: The brush-segment contact resistance for the 7-coil equivalent circuit

6.3.1.3 Self inductance of the coils in the 7-coil equivalent circuit

For the Davey machine, let L_k, be the self inductance of k^{th} armature coil; M_{f_k} be the field-armature mutual inductance of k^{th} armature coil; and m_{j_k} be the mutual inductance between j^{th} and k^{th} armature coils, where $j \neq k$.

$$\begin{aligned} M_{f\_k} &= M_{k\_f} \\ m_{j\_k} &= m_{k\_j} \end{aligned} \tag{6.27}$$

where j and k are integers for 1 to 16.

The coils used in the equivalent circuit are dependent on rotor position, shown in table 6.1. Hence, the inductance of the equivalent circuit also varies with rotor positions. For example, when $0 < \theta_{rm} \leq 7.5^{o}$,

Coil C_{p1} = Coil 15, Coil C_{p2} = Coil 16, Coil C_{n1} = Coil 7,

Coil C_{n2} = Coil 8, Coil S1 = Coil 9; 10, 11, 12, 13, and 14 in series, and

Coil S2 = Coil 1; 2, 3, 4, 5, and 6 in series.

The inductance matrix of the 7-coil equivalent circuit can be expressed in terms of L_k, M_{f_k} and m_{j_k} as

$$L_{cp1} = L_{15}, \quad L_{cp2} = L_{16}, \quad L_{cn1} = L_7, \quad L_{cn2} = L_8,$$

$$L_{s1} = L_9 + L_{10} + L_{11} + L_{12} + L_{13} + L_{14} + 2\begin{pmatrix} m_{9\_10} + m_{9\_11} + m_{9\_12} + m_{9\_13} + m_{9\_14} + \\ m_{10\_11} + m_{10\_12} + m_{10\_13} + m_{10\_14} + \\ m_{11\_12} + m_{11\_13} + m_{11\_14} + \\ m_{12\_13} + m_{12\_14} + \\ m_{13\_14} \end{pmatrix}, \text{ and}$$

$$L_{s2} = L_1 + L_2 + L_3 + L_4 + L_5 + L_6 + 2\begin{pmatrix} m_{1\_2} + m_{1\_3} + m_{1\_4} + m_{1\_5} + m_{1\_6} + \\ m_{2\_3} + m_{2\_4} + m_{2\_5} + m_{2\_6} + \\ m_{3\_4} + m_{3\_5} + m_{3\_6} + \\ m_{4\_5} + m_{4\_6} + \\ m_{5\_6} \end{pmatrix}$$

6.3.1.4 Mutual inductance between the field coil and the other coils in the 7-coil equivalent circuit

$M_{f\_cp1} = M_{cp1\_f} = M_{f\_15}$,

$M_{f\_cp2} = M_{cp2\_f} = M_{f\_16}$,

$M_{f\_s2} = M_{s2\_f} = M_{f\_1} + M_{f\_2} + M_{f\_3} + M_{f\_4} + M_{f\_5} + M_{f\_6}$,

$M_{f\_cn1} = M_{cn1\_f} = M_{f\_7}$; $M_{f\_cn2} = M_{cn2\_f} = M_{f\_8}$, and

$M_{f\_s1} = M_{s1\_f} = M_{f\_9} + M_{f\_10} + M_{f\_11} + M_{f\_12} + M_{f\_13} + M_{f\_14}$

6.3.1.5 Mutual inductance between the coils of the 7-coil equivalent circuit

$m_{cp1\_cp2} = m_{cp2\_cp1} = m_{15\_16}$,

$m_{cp1\_s2} = m_{s2\_cp1} = m_{1\_15} + m_{2\_15} + m_{3\_15} + m_{4\_15} + m_{5\_15} + m_{6\_15}$,

$m_{cp1\_cn1} = m_{cn1\_cp1} = m_{7\_15}$,

$m_{cp1\_cn2} = m_{cn2\_cp1} = m_{8\_15}$,

$m_{cp1\_s1} = m_{s1\_cp1} = m_{9\_15} + m_{10\_15} + m_{11\_15} + m_{12\_15} + m_{13\_15} + m_{14\_15}$,

$m_{cp2\_cn1} = m_{cn1\_cp2} = m_{7\_16}$,

$m_{cp2\_cn2} = m_{cn2\_cp2} = m_{8\_16}$,

$m_{cp2\_s2} = m_{s2\_cp2} = m_{1\_16} + m_{2\_16} + m_{3\_16} + m_{4\_16} + m_{5\_16} + m_{6\_16}$,

$m_{cp2\_s1} = m_{s1\_cp2} = m_{9\_16} + m_{10\_16} + m_{11\_16} + m_{12\_16} + m_{13\_16} + m_{14\_16}$,

$m_{s2\_cn1} = m_{cn1\_s2} = m_{1\_7} + m_{2\_7} + m_{3\_7} + m_{4\_7} + m_{5\_7} + m_{6\_7}$,

$$m_{s2\_cn2} = m_{cn2\_s2} = m_{1\_8} + m_{2\_8} + m_{3\_8} + m_{4\_8} + m_{5\_8} + m_{6\_8},$$

$$m_{s2\_s1} = m_{s1\_s2} = \begin{bmatrix} m_{1\_9} + m_{2\_9} + m_{3\_9} + m_{4\_9} + m_{5\_9} + m_{6\_9} + \\ m_{1\_10} + m_{2\_10} + m_{3\_10} + m_{4\_10} + m_{5\_10} + m_{6\_10} + \\ m_{1\_11} + m_{2\_11} + m_{3\_11} + m_{4\_11} + m_{5\_11} + m_{6\_11} + \\ m_{1\_12} + m_{2\_12} + m_{3\_12} + m_{4\_12} + m_{5\_12} + m_{6\_12} + \\ m_{1\_13} + m_{2\_13} + m_{3\_13} + m_{4\_13} + m_{5\_13} + m_{6\_13} + \\ m_{1\_14} + m_{2\_14} + m_{3\_14} + m_{4\_14} + m_{5\_14} + m_{6\_14} \end{bmatrix},$$

$$m_{cn1\_cn2} = m_{cn2\_cn1} = m_{7\_8},$$

$$m_{cn1\_s1} = m_{s1\_cn1} = m_{7\_9} + m_{7\_10} + m_{7\_11} + m_{7\_12} + m_{7\_13} + m_{7\_14}, \text{ and}$$

$$m_{cn2\_s1} = m_{s1\_cn2} = m_{8\_9} + m_{8\_10} + m_{8\_11} + m_{8\_12} + m_{8\_13} + m_{8\_14}$$

6.3.2 5-coil Equivalent Circuit of the Davey Machine

Figure 6.9 shows the 5-coil equivalent circuit of the Davey machine. Each of the parallel paths is formed by 7 coils connected in series. In the equivalent circuit, only coil C_{p1} and C_{n1} are commutated by the brushes. R_{p1}, R_{p2}; R_{n1}, and R_{n2} are used to model the brushes.

The derivation of the voltage equations of the 5-coil circuit is shown in Appendix B. There are five differential equations for this model and, written in matrix form as equation (6.9), where the voltage matrix is

$$\mathbf{v} = \begin{bmatrix} U_f & 0 & 0 & 0 & 0 \end{bmatrix}^T; \tag{6.28}$$

The current matrix is

$$\mathbf{i} = \begin{bmatrix} i_f & i_{cp1} & i_{s2} & i_{cn1} & i_{s1} \end{bmatrix}^T \tag{6.29}$$

$$\mathbf{R} = \begin{bmatrix} R_f & 0 & 0 & 0 & 0 \\ 0 & R_{cp1}+R_{p1}+R_{p2} & -R_{p2} & 0 & -R_{p1} \\ 0 & -R_{p2} & R_{s2}+R_{p2}+R_{n1}+R_L & -R_{n1} & -R_L \\ 0 & 0 & -R_{n1} & R_{cn1}+R_{n1}+R_{n2} & -R_{n2} \\ 0 & -R_{p1} & -R_L & -R_{n2} & R_{s1}+R_{p1}+R_{n2}+R_L \end{bmatrix} \tag{6.30}$$

$$\mathbf{L} = \begin{bmatrix} L_{ff} & M_{f\_cp1} & M_{f\_s2} & M_{f\_cn1} & M_{f\_s1} \\ M_{cp1\_f} & L_{cp1} & m_{cp1\_s2} & m_{cp1\_cn1} & m_{cp1\_s1} \\ M_{s2\_f} & m_{s2\_cp1} & L_{s2} & m_{s2\_cn1} & m_{s2\_s1} \\ M_{cn1\_f} & m_{cn1\_cp1} & m_{cn1\_s2} & L_{cn1} & m_{cn1\_s1} \\ M_{s1\_f} & m_{s1\_cp1} & m_{s1\_s2} & m_{s1\_cn1} & L_{s1} \end{bmatrix} \tag{6.31}$$

6.3.2.1 Coil resistance of the 5-coil equivalent circuit

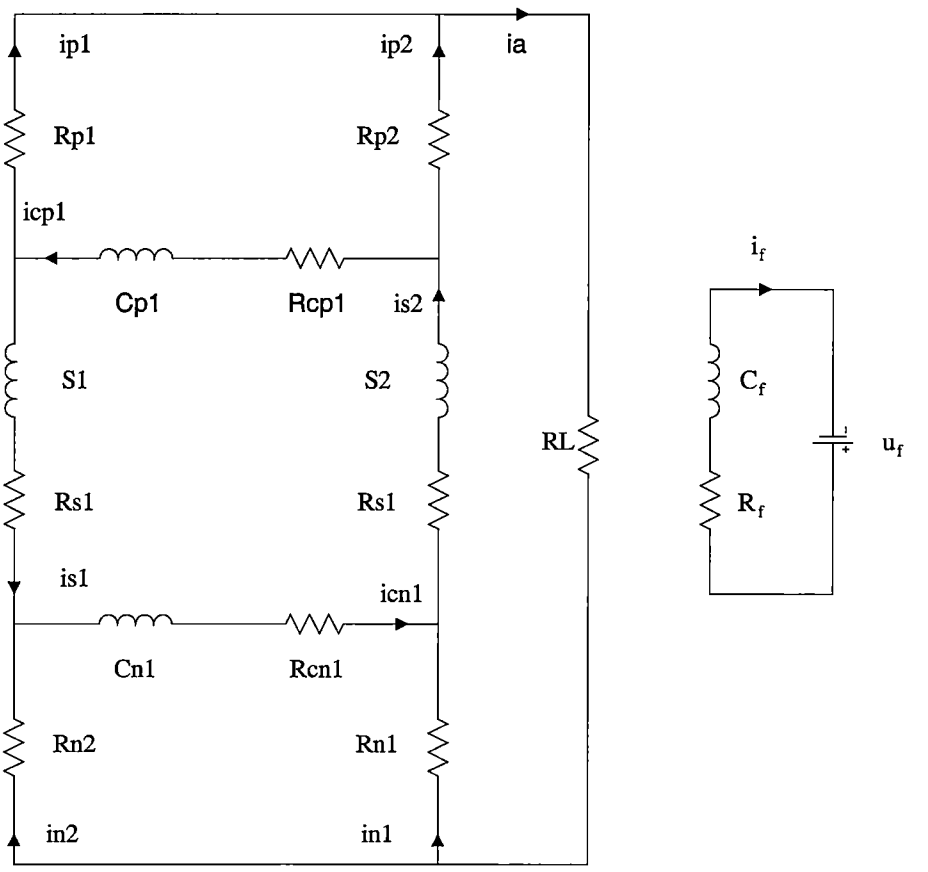

Figure 6.9: The 5-coil equivalent circuit of the Davey machine

The coil resistance of the 5-coil equivalent circuit is,

$$R_{cp1} = R_{cn1} = R_{coil} \tag{6.32}$$

$$R_{s1} = R_{s2} = 7R_{coil} \tag{6.33}$$

6.3.2.2 Brush-segment resistance of the 5-coil equivalent circuit

Figure 6.10 shows the equivalent circuit of the positive brush of the 5-coil equivalent circuit. At a given instant,

$$G_b + G_c = brushwidth = W_b \tag{6.34}$$

The corresponding contact resistance is

$$R_{p1} = R_{bp} \frac{W_b}{G_b} \tag{6.35}$$

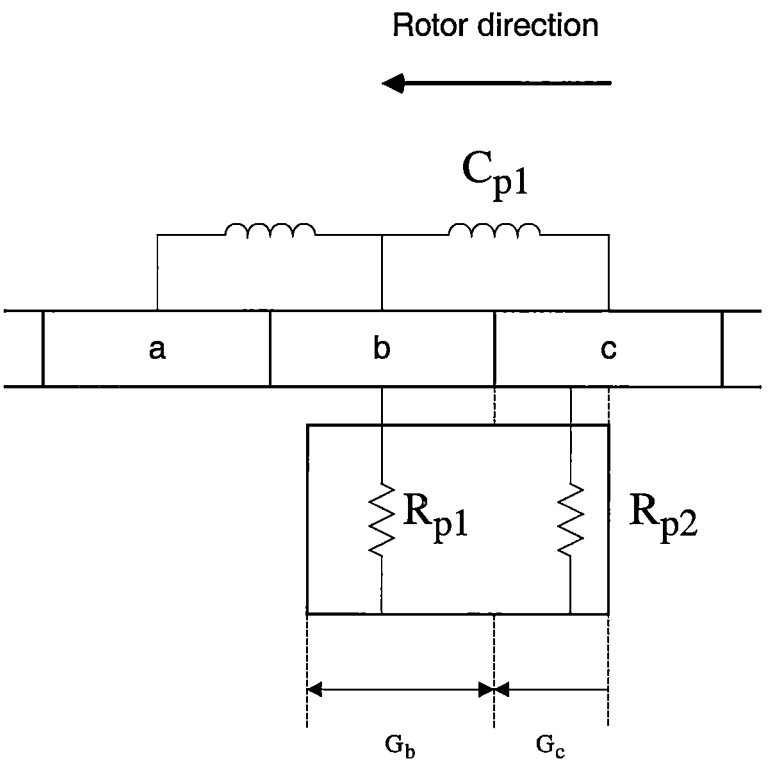

Figure 6.10: Brush-segment resistance of 5-coil equivalent circuit

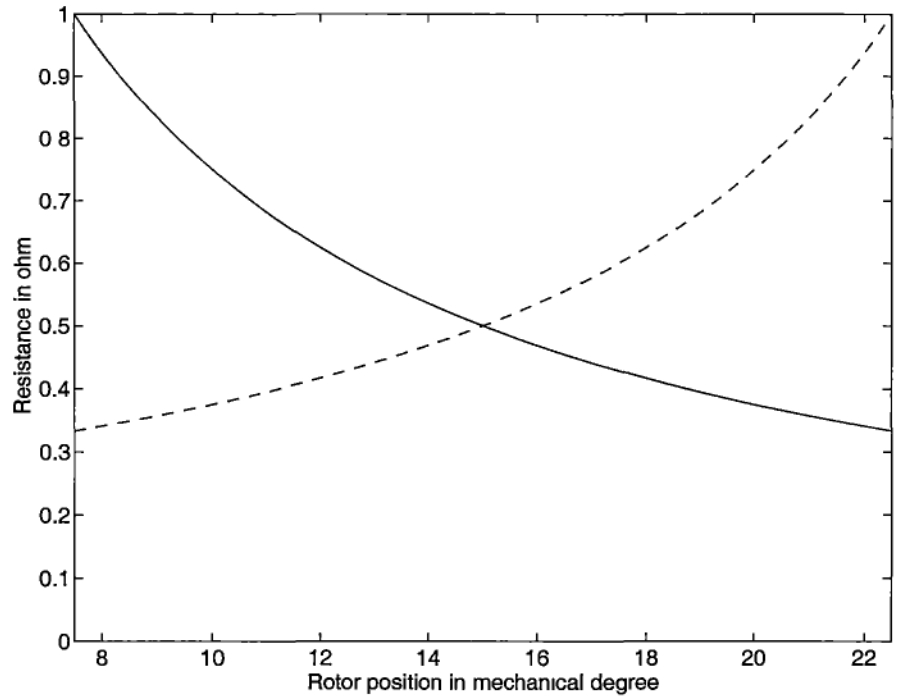

Figure 6.11: The brush-segment contact resistance for the 5-coil equivalent circuit

$$R_{p2} = R_{bp} \frac{W_b}{G_c} \tag{6.36}$$

Figure 6.11 shows the values of R_{p1} and R_{p2} of the 5-coil equivalent circuit. They vary with the rotor position. The same assumption is made for the commutation process of the negative brush-segment.

6.3.2.3 Self inductance of the coils in 5-coil equivalent circuit

The coils used in the 5-coil equivalent circuit at different rotor position are summarised in table 6.1. For example, when $7.5^\circ < \theta_{rm} \leq 22.5^\circ$,

Coil C_{p1} = Coil 16, Coil C_{n1} = Coil 8,

Coil S1 = Coil 9; 10, 11, 12, 13, 14 and 15 in series, and

Coil S2 = Coil 1; 2, 3, 4, 5, 6 and 7 in series.

The inductance matrix of the 5-coil equivalent circuit can be expressed in terms of L_k, M_{f_k} and m_{j_k} as

$$L_{cp1} = L_{16}, \qquad L_{cn1} = L_8,$$

$$L_{s1} = L_9 + L_{10} + L_{11} + L_{12} + L_{13} + L_{14} + L_{15} + 2\begin{pmatrix} m_{9\_10} + m_{9\_11} + m_{9\_12} + m_{9\_13} + m_{9\_14} + m_{9\_15} \\ m_{10\_11} + m_{10\_12} + m_{10\_13} + m_{10\_14} + m_{10\_15} \\ m_{11\_12} + m_{11\_13} + m_{11\_14} + m_{11\_15} \\ m_{12\_13} + m_{12\_14} + m_{12\_15} \\ m_{13\_14} + m_{13\_15} \\ m_{14\_15} \end{pmatrix},$$

$$L_{s2} = L_1 + L_2 + L_3 + L_4 + L_5 + L_6 + L_7 + 2\begin{pmatrix} m_{1\_2} + m_{1\_3} + m_{1\_4} + m_{1\_5} + m_{1\_6} + m_{1\_7} \\ m_{2\_3} + m_{2\_4} + m_{2\_5} + m_{2\_6} + m_{2\_7} \\ m_{3\_4} + m_{3\_5} + m_{3\_6} + m_{3\_7} \\ m_{4\_5} + m_{4\_6} + m_{4\_7} \\ m_{5\_6} + m_{5\_7} + \\ m_{6\_7} \end{pmatrix}$$

6.3.2.4 Mutual inductance between the field coil and the other coils of the 5-coil equivalent circuit

$M_{f\_cp1} = M_{cp1\_f} = M_{f\_16}$, $M_{f\_cn1} = M_{cn1\_f} = M_{f\_8}$,

$M_{f\_s2} = M_{s2\_f} = M_{f\_1} + M_{f\_2} + M_{f\_3} + M_{f\_4} + M_{f\_5} + M_{f\_6} + M_{f\_7}$, and

$M_{f\_s1} = M_{s1\_f} = M_{f\_9} + M_{f\_10} + M_{f\_11} + M_{f\_12} + M_{f\_13} + M_{f\_14} + M_{f\_15}$

6.3.2.5 Mutual inductance between the coils of the 5-coil equivalent circuit

$m_{cp1\_s2} = m_{s2\_cp1} = m_{1\_16} + m_{2\_16} + m_{3\_16} + m_{4\_16} + m_{5\_16} + m_{6\_16} + m_{7\_16}$,

$m_{cp1\_cn1} = m_{cn1\_cp1} = m_{8\_16}$,

$m_{cp1\_s1} = m_{s1\_cp1} = m_{9\_16} + m_{10\_16} + m_{11\_16} + m_{12\_16} + m_{13\_16} + m_{14\_16} + m_{15\_16}$,

$m_{s2\_cn1} = m_{cn1\_s2} = m_{1\_8} + m_{2\_8} + m_{3\_8} + m_{4\_8} + m_{5\_8} + m_{6\_8} + m_{7\_8}$,

$$m_{s2\_s1} = m_{s1\_s2} = \begin{bmatrix} m_{1\_9} + m_{2\_9} + m_{3\_9} + m_{4\_9} + m_{5\_9} + m_{6\_9} + m_{7\_9} + \\ m_{1\_10} + m_{2\_10} + m_{3\_10} + m_{4\_10} + m_{5\_10} + m_{6\_10} + m_{7\_10} + \\ m_{1\_11} + m_{2\_11} + m_{3\_11} + m_{4\_11} + m_{5\_11} + m_{6\_11} + m_{7\_11} + \\ m_{1\_12} + m_{2\_12} + m_{3\_12} + m_{4\_12} + m_{5\_12} + m_{6\_12} + m_{7\_12} + \\ m_{1\_13} + m_{2\_13} + m_{3\_13} + m_{4\_13} + m_{5\_13} + m_{6\_13} + m_{7\_13} + \\ m_{1\_14} + m_{2\_14} + m_{3\_14} + m_{4\_14} + m_{5\_14} + m_{6\_14} + m_{7\_14} + \\ m_{1\_15} + m_{2\_15} + m_{3\_15} + m_{4\_15} + m_{5\_15} + m_{6\_15} + m_{7\_15} \end{bmatrix},$$

$$m_{cn1\_s1} = m_{s1\_cn1} = m_{8\_9} + m_{8\_10} + m_{8\_11} + m_{8\_12} + m_{8\_13} + m_{8\_14} + m_{8\_15}$$

6.4 Coupled Coil Model of the Davey Machine with short-circuit coil in Armature

A short-circuit coil is modelled by putting a short between two adjacent commutator segments, ie segment 1 and 2, as shown in figure 6.12. From figure 6.12A, the relative position of the positive brush and commutators for the instant at which commutation is carrying for coil 15 and just beginning for coil 16. Coil 1 is shorted and Coil 16 is started to commutate. The positive brush contacts segments 15 and 16. Two resistors may be used to model the positive brush, R_{p1} and R_{p2}. The corresponding equivalent resistors for the negative brush are R_{n1} and R_{n2}, which are not shown in the figures (Coil 7 is under commutation by the negative brush while Coil 8 is just stared). As the short-circuit coil (Coil 1) is modelled separately, at this instant, one of the parallel path is formed by 6 coils and the other path is formed by 7 coils. The Davey machine is thus modelled by six concentrated coils: the field coil, two parallel paths of armature coils, two coils under commutation, and the short-circuit coil.

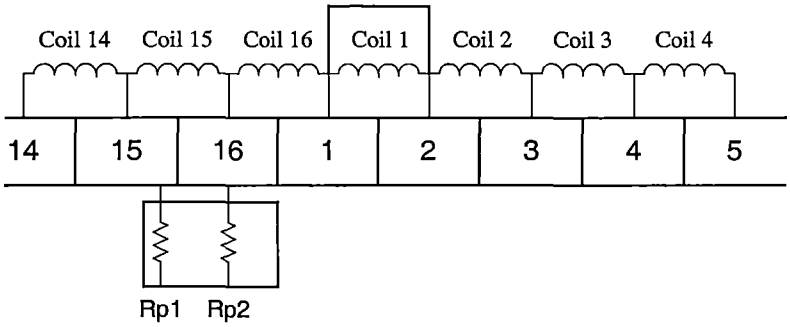

(A) Rotor position at zero degrees

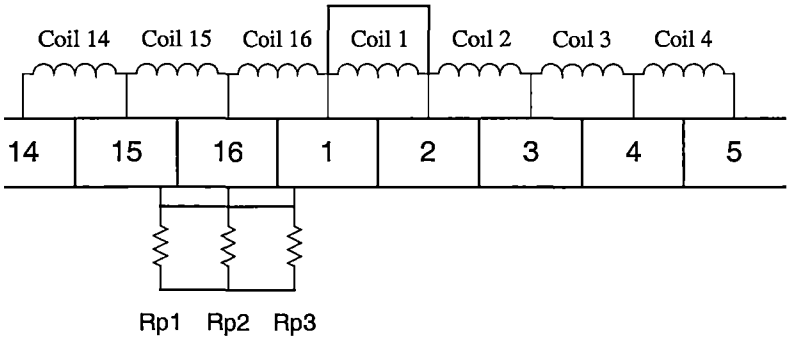

(B) Rotor position at 0 - 7.5 degrees

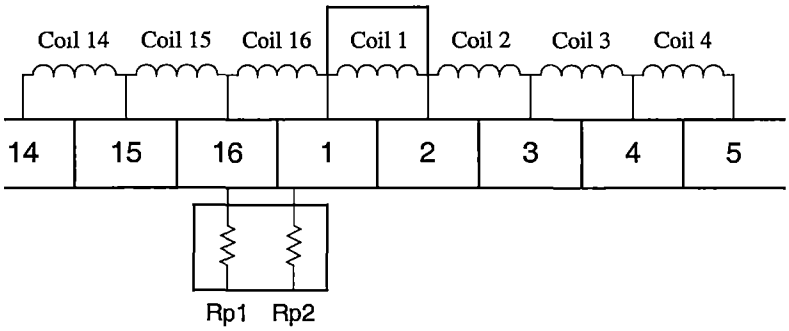

(C) Rotor position at 7.5 - 22.5 degrees

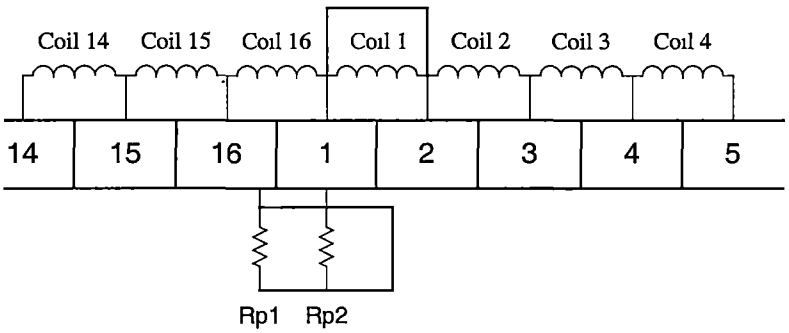

(D) Rotor position at 22.5 - 30 degrees

Figure 6.12: The armature circuit of the Davey machine at different rotor positions

When rotor position is between zero and 7.5 degrees, shown in figure 6.12B, the positive brush is on segments 15, 16 and 1. Coils 15 and 16 are under commutation by the positive brush (Coil 7 and 8 are under commutation by the negative brush). Three resistors model each brush, R_{p1}, R_{p2}, and R_{p3} for the positive brush; and R_{n1}, R_{n2}, and R_{n3} for the negative brush. At this instant, the short-circuit coil is still in one of the parallel path and eight concentrated coils model the Davey machine.

For rotor between 7.5 and 22.5 degrees, the condition is similar as the rotor at zero degree. Six concentrated coils model the machine, shown in figure 6.12C.

When the rotor position is 22.5 degrees, shown in figure 6.12D, the short-coil coil is started to commutate. As segments 1 and 2 are shorted, two resistors model the positive brush while three resistors are needed for the negative brush. Each parallel path will have 6 coils in series, and seven concentrated coils are used in the model.

Figure 6.13A shows the rotor position between 30 and 45 degrees. The positive brush contacts segments 1 and 2, which are shorted together. Only one resistor is used to model the positive brush and is assumed to be constant for this period. It still needs two resistors to model the negative brush. Two coils are under commutation including the short-circuit coil. Five concentrated coils model the machine.

Figure 6.13B to D show the successive intervals for the rotor positions that are similar to those at 22.5 to 30 degrees, 7.5 to 22.5 degrees and 0 to 7.5 degrees intervals. Seven, six, and eight concentrated coils respectively model the machine.

The operation of the Davey machine was simulated with 16 intervals of rotor position in a revolution. Two different equivalent circuits are used in each interval. The combination of coils used in different equivalent circuit in different rotor positions is summarised in table 6.2. The equivalent circuits are discussed in detail in the following sections.

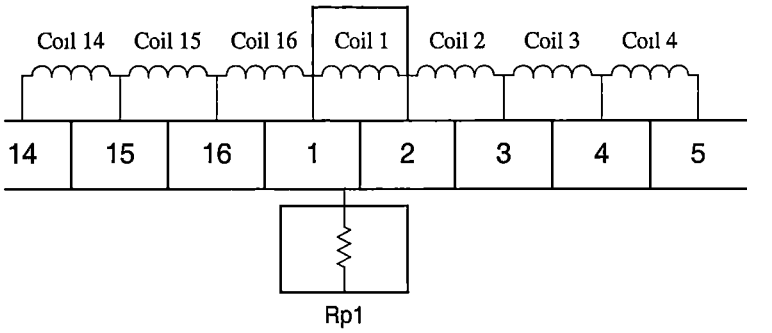

(A) Rotor position at 30 - 45 degrees

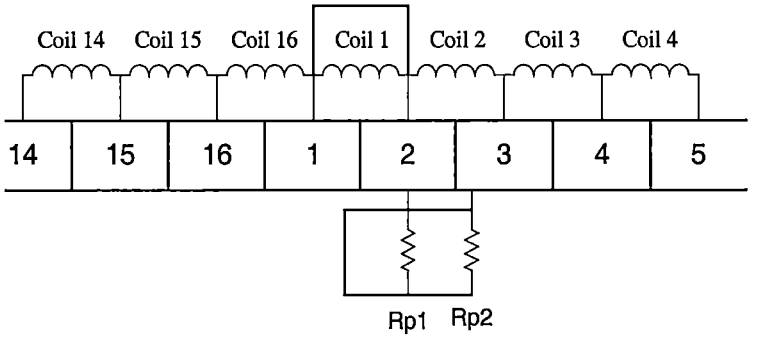

(B) Rotor position at 45 - 52.5 degrees

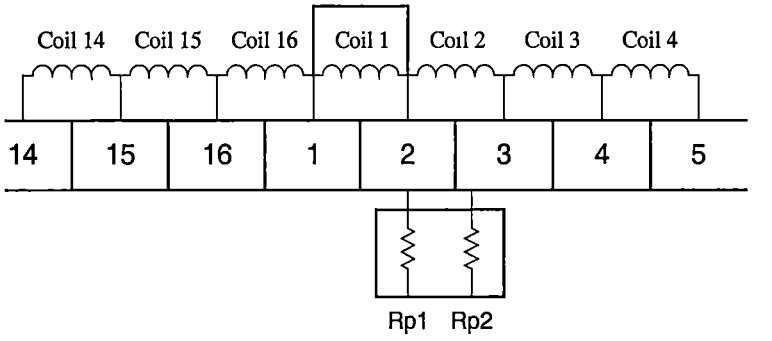

(C) Rotor position at 52.5 - 67.5 degrees

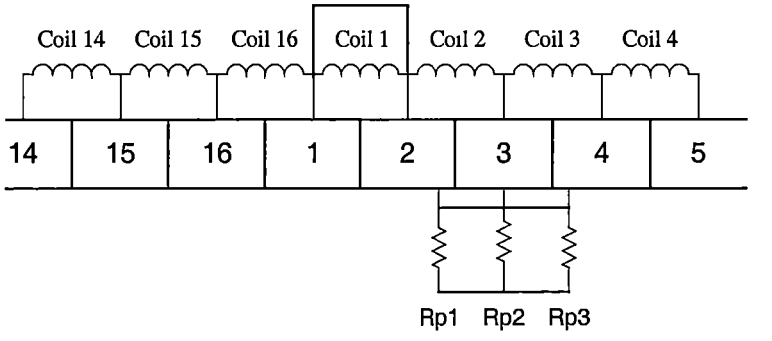

(D) Rotor position at 67.5 - 75 degrees

Figure 6.13: The armature circuit of the Davey machine at different rotor positions

Rotor position θ_{rm}	C_{p1} / C_{n1}	C_{p2} / C_{n2}	S_1 / S_2	No. of equivalent coils
$0 > \theta_{rm} \geq 7.5$	15 / 7	16 / 8	9,10,11,12,13,14 /2, 3, 4, 5, 6	8
$7.5 > \theta_{rm} \geq 22.5$	16 / 8		9,10,11,12,13,14,15 /2,3,4,5,6,7	6
$22.5 > \theta_{rm} \geq 30$	16 / 8	1 / 9	10,11,12,13,14,15 / 2,3,4,5,6,7	7
$30 > \theta_{rm} \geq 45$	1 / 9		10,11,12,13,14,15,16 / 2,3,4,5,6,7,8	5
$45 > \theta_{rm} \geq 52.5$	1 / 9	2 / 10	11,12,13,14,15,16 / 3,4,5,6,7,8	7
$52.5 > \theta_{rm} \geq 67.5$	2 / 10		11,12,13,14,15,16/ 3,4,5,6,7,8,9	6
$67.5 > \theta_{rm} \geq 75$	2 / 10	3 / 11	12,13,14,15,16/ 4,5,6,7,8,9	8
$75 > \theta_{rm} \geq 90$	3 / 11		12,13,14,15,16,2 / 4,5,6,7,8,9,10	6
$90 > \theta_{rm} \geq 97.5$	3 / 11	4 / 12	13,14,15,16,2 / 5,6,7,8,9,10	8
$97.5 > \theta_{rm} \geq 112.5$	4 / 12		13,14,15,16,2,3 / 5,6,7,8,9,10,11	6
$112.5 > \theta_{rm} \geq 120$	4 / 12	5 / 13	14,15,16,2,3 / 6,7,8,9,10,11	8
$120 > \theta_{rm} \geq 135$	5 / 13		14,15,16,2,3,4 / 6,7,8,9,10,11,12	6
$135 > \theta_{rm} \geq 142.5$	5 / 13	6 / 14	15,16,2,3,4 / 7,8,9,10,11,12	8
$142.5 > \theta_{rm} \geq 157.5$	6 / 14		15,16,2,3,4,5 / 7,8,9,10,11,12,13	6
$157.5 > \theta_{rm} \geq 165$	6 / 14	7 / 15	16,2,3,4,5 / 8,9,10,11,12,13	8
$165 > \theta_{rm} \geq 180$	7 / 15		16,2,3,4,5,6 / 8,9,10,11,12,13,14	6
$180 > \theta_{rm} \geq 187.5$	7 / 15	8 / 16	2,3,4,5,6 / 9,10,11,12,13,14	8
$187.5 > \theta_{rm} \geq 202.5$	8 / 16		2,3,4,5,6,7 / 9,10,11,12,13,14,15	6
$202.5 > \theta_{rm} \geq 210$	8 / 16	9 / 1	2,3,4,5,6,7 / 10,11,12,13,14,15	7
$210 > \theta_{rm} \geq 225$	9 / 1		2,3,4,5,6,7,8 / 10,11,12,13,14,15,16	5
$225 > \theta_{rm} \geq 232.5$	9 / 1	10 / 2	3,4,5,6,7,8 / 11,12,13,14,15,16	7
$232.5 > \theta_{rm} \geq 247.5$	10 / 2		3,4,5,6,7,8,9 / 11,12,13,14,15,16	6
$247.5 > \theta_{rm} \geq 255$	10 / 2	11 / 3	4,5,6,7,8,9 / 12,13,14,15,16,1	8
$255 > \theta_{rm} \geq 270$	11 / 3		4,5,6,7,8,9,10 / 12,13,14,15,16,2	6
$270 > \theta_{rm} \geq 277.5$	11 / 3	12 / 4	5,6,7,8,9,10 / 13,14,15,16,2	8
$277.5 > \theta_{rm} \geq 292.5$	12 / 4		5,6,7,8,9,10,11 / 13,14,15,16,2,3	6
$292.5 > \theta_{rm} \geq 300$	12 / 4	13 / 5	6,7,8,9,10,11 / 14,15,16,2,3	8
$300 > \theta_{rm} \geq 315$	13 / 5		6,7,8,9,10,11,12 / 14,15,16,2,3,4	6
$315 > \theta_{rm} \geq 322.5$	13 / 5	14 / 6	7,8,9,10,11,12 / 15,16,2,3,4	8
$322.5 > \theta_{rm} \geq 337.5$	14 / 6		7,8,9,10,11,12,13 / 15,16,2,3,4,5	6
$337.5 > \theta_{rm} \geq 345$	14 / 6	15 / 7	8,9,10,11,12,13 / 16,2,3,4,5	8
$345 > \theta_{rm} \geq 360$	15 / 7		8,9,10,11,12,13,14 / 16,2,3,4,5,6	6

Table 6.2: The combination of armature coils used in the equivalent circuits to model short-circuit in armature winding

6.4.1 8-coil Equivalent Circuit of the Davey Machine with a Short-circuit Coil in Armature

When four coils are under commutation and the short-circuit coil is in one of the parallel paths, an 8-coil equivalent circuit models the Davey machine. For example, when rotor position is between zero and 7.5 degrees, the short-circuit coil C_{sc} (Coil 1) is in the S2 parallel path, shown in figure 6.14.

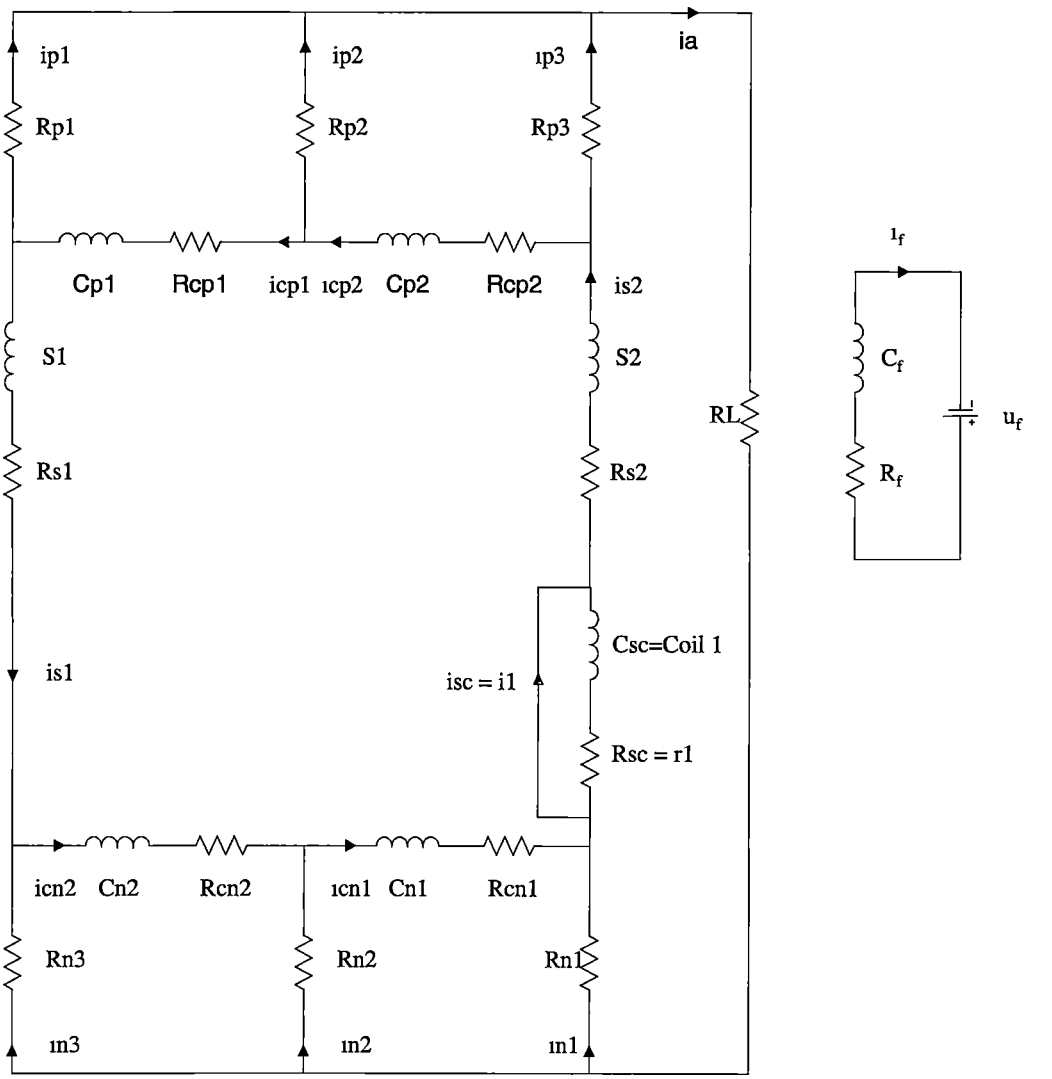

Figure 6.14: The 8-coil equivalent circuit of the Davey machine to model short-circuit armature coil

There are eight differential equations for this circuit, written in matrix form as equation (6.9), where the voltage matrix is

$$\mathbf{v} = [U_f \quad 0 \quad 0 \quad 0 \quad 0 \quad 0 \quad 0 \quad 0]^T \tag{6.37}$$

The current matrix is

$$\mathbf{i} = [i_f \quad i_{cp1} \quad i_{cp2} \quad i_{s2} \quad i_{cn1} \quad i_{cn2} \quad i_{s1} \quad i_1]^T \tag{6.38}$$

The resistor matrix **R** is

$$\begin{bmatrix}
R_f & 0 & 0 & 0 & 0 & 0 & 0 & 0 \\
0 & R_{cp1}+R_{p1}+R_{P2} & -R_{p2} & 0 & 0 & 0 & -R_{p1} & 0 \\
0 & -R_{p2} & R_{cp2}+R_{p2}+R_{P3} & -R_{p3} & 0 & 0 & 0 & 0 \\
0 & 0 & -R_{p3} & R_{s2}+R_L+R_{p3}+R_{n1} & -R_{n1} & 0 & -R_L & 0 \\
0 & 0 & 0 & -R_{n1} & R_{cn1}+R_{n1}+R_{n2} & -R_{n2} & 0 & 0 \\
0 & 0 & 0 & 0 & -R_{n2} & R_{cn2}+R_{n2}+R_{n3} & -R_{n3} & 0 \\
0 & -R_{p1} & 0 & -R_L & 0 & -R_{n3} & R_{s1}+R_L+R_{n3}+R_{p1} & 0 \\
0 & 0 & 0 & 0 & 0 & 0 & 0 & r_1
\end{bmatrix} \tag{6.39}$$

The inductance matrix **L** is

$$\begin{bmatrix}
L_{ff} & M_{f_cp1} & M_{f_cp2} & M_{f_s2} & M_{f_cn1} & M_{f_cn2} & M_{f_s1} & M_{f_Csc} \\
M_{cp1_f} & L_{cp1} & m_{cp1_cp2} & m_{cp1_s2} & m_{cp1_cn1} & m_{cp1_cn2} & m_{cp1_s1} & m_{cp1_Csc} \\
M_{cp2_f} & m_{cp2_cp1} & L_{cp2} & m_{cp2_s2} & m_{cp2_cn1} & m_{cp2_cn2} & m_{cp2_s1} & m_{cp2_Csc} \\
M_{s2_f} & m_{s2_cp1} & m_{s2_cp2} & L_{s2} & m_{s2_cn1} & m_{s2_cn2} & m_{s2_s1} & m_{s2_Csc} \\
M_{cn1_f} & m_{cn1_cp1} & m_{cn1_cp2} & m_{cn1_s2} & L_{cn1} & m_{cn1_cn2} & m_{cn1_s1} & m_{cn1_Csc} \\
M_{cn2_f} & m_{cn2_cp1} & m_{cn2_cp2} & m_{cn2_s2} & m_{cn2_cn1} & L_{cn2} & m_{cn2_s1} & m_{cn2_Csc} \\
M_{s1_f} & m_{s2_cp1} & m_{s2_cp2} & m_{s1_s2} & m_{s2_cn1} & m_{s1_cn2} & L_{s1} & m_{s1_Csc} \\
M_{Csc_f} & m_{Csc_cp1} & m_{Csc_cp2} & m_{Csc_s2} & m_{Csc_cn1} & m_{Csc_cn2} & m_{Csc_s1} & L_{Csc}
\end{bmatrix} \tag{6.40}$$

6.4.1.1 Coil Resistance of the 8-coil Equivalent Circuit

The coil resistances of the 8-coil equivalent circuit are,

$$R_{cp1} = R_{cp2} = R_{cn1} = R_{cn2} = R_{coil} \tag{6.41}$$

$$R_{s1} = 6R_{coil} \tag{6.42}$$

$$R_{s2} = 5R_{coil} \tag{6.43}$$

$$R_{sc} = R_1 = R_{coil} \tag{6.44}$$

6.4.1.2 Brush-segment contact resistance of the 8-coil Equivalent Circuit

The contact resistances of the positive and negative brush-segment are the same as those discussed in section 6.3.1.2, refer to equations (6.24), (6.24) and (6.24) and figure 6.7.

6.4.1.3 Self inductance of the 8-coil Equivalent Circuit

The coils used in the 8-coil equivalent circuit at different rotor position are summarised in table 6.2. To illustrate the inductance matrix of the 8-coil equivalent circuit, consider the instant when the rotor position is between zero and 7.5 degrees.

Coil C_{p1} = Coil 15, Coil C_{p2} = Coil 16, Coil C_{n1} = Coil 7,

Coil C_{n2} = Coil 8, Coil S_1 = Coil 9, 10, 11, 12, 13, and 14 in series, and

Coil S_2 = Coil 2, 3, 4, 5, and 6 in series, and Coil C_{sc} = Coil 1.

The self inductance of the coils is

$L_{cp1} = L15$, $L_{cp2} = L16$, $L_{cn1} = L7$, $L_{cn2} = L8$, $L_{sc} = L1$,

$$L_{s1} = L_9 + L_{10} + L_{11} + L_{12} + L_{13} + L_{14} + 2\begin{pmatrix} m_{9\_10} + m_{9\_11} + m_{9\_12} + m_{9\_13} + m_{9\_14} + \\ m_{10\_11} + m_{10\_12} + m_{10\_13} + m_{10\_14} + \\ m_{11\_12} + m_{11\_13} + m_{11\_14} + \\ m_{12\_13} + m_{12\_14} + \\ m_{13\_14} \end{pmatrix}, \text{ and}$$

$$L_{s2} = L_2 + L_3 + L_4 + L_5 + L_6 + 2\begin{pmatrix} m_{2\_3} + m_{2\_4} + m_{2\_5} + m_{2\_6} + \\ m_{3\_4} + m_{3\_5} + m_{3\_6} + \\ m_{4\_5} + m_{4\_6} + \\ m_{5\_6} \end{pmatrix}$$

6.4.1.4 Mutual inductance between the field coil and the other coils in the 8-coil equivalent circuit

$M_{f\_cp1} = M_{cp1\_f} = M_{f\_15}$, $M_{f\_cp2} = M_{cp2\_f} = M_{f\_16}$,

$M_{f\_s2} = M_{s2\_f} = M_{f\_2} + M_{f\_3} + M_{f\_4} + M_{f\_5} + M_{f\_6}$,

$M_{f\_cn1} = M_{cn1\_f} = M_{f\_7}$; $M_{f\_cn2} = M_{cn2\_f} = M_{f\_8}$,

$M_{f\_s1} = M_{s1\_f} = M_{f\_9} + M_{f\_10} + M_{f\_11} + M_{f\_12} + M_{f\_13} + M_{f\_14}$, and

$M_{f\_Csc} = M_{f\_1}$

6.4.1.5 Mutual inductance between the coils of the 8-coil equivalent circuit

$m_{cp1\_cp2} = m_{cp2\_cp1} = m_{15\_16}$, $m_{cp1\_cn1} = m_{cn1\_cp1} = m_{7\_15}$,

$m_{cp1\_cn2} = m_{cn2\_cp1} = m_{8\_15}$, $m_{cp2\_cn1} = m_{cn1\_cp2} = m_{7\_16}$,

$m_{cp1\_s2} = m_{s2\_cp1} = m_{2\_15} + m_{3\_15} + m_{4\_15} + m_{5\_15} + m_{6\_15}$,

$m_{cp1\_s1} = m_{s1\_cp1} = m_{9\_15} + m_{10\_15} + m_{11\_15} + m_{12\_15} + m_{13\_15} + m_{14\_15}$,

$m_{cp2\_cn2} = m_{cn2\_cp2} = m_{8\_16}$, $m_{cn1\_cn2} = m_{cn2\_cn1} = m_{7\_8}$,

$m_{cp2\_s2} = m_{s2\_cp2} = m_{2\_16} + m_{3\_16} + m_{4\_16} + m_{5\_16} + m_{6\_16}$,

$m_{cp2\_s1} = m_{s1\_cp2} = m_{9\_16} + m_{10\_16} + m_{11\_16} + m_{12\_16} + m_{13\_16} + m_{14\_16}$,

$m_{s2\_cn1} = m_{cn1\_s2} = m_{2\_7} + m_{3\_7} + m_{4\_7} + m_{5\_7} + m_{6\_7}$,

$$m_{s2\_cn2} = m_{cn2\_s2} = m_{2\_8} + m_{3\_8} + m_{4\_8} + m_{5\_8} + m_{6\_8},$$

$$m_{s2\_s1} = m_{s1\_s2} = \begin{bmatrix} m_{2\_9} + m_{3\_9} + m_{4\_9} + m_{5\_9} + m_{6\_9} + \\ m_{2\_10} + m_{3\_10} + m_{4\_10} + m_{5\_10} + m_{6\_10} + \\ m_{2\_11} + m_{3\_11} + m_{4\_11} + m_{5\_11} + m_{6\_11} + \\ m_{2\_12} + m_{3\_12} + m_{4\_12} + m_{5\_12} + m_{6\_12} + \\ m_{2\_13} + m_{3\_13} + m_{4\_13} + m_{5\_13} + m_{6\_13} + \\ m_{2\_14} + m_{3\_14} + m_{4\_14} + m_{5\_14} + m_{6\_14} \end{bmatrix},$$

$$m_{cn1\_s1} = m_{s1\_cn1} = m_{7\_9} + m_{7\_10} + m_{7\_11} + m_{7\_12} + m_{7\_13} + m_{7\_14},$$

$$m_{cn2\_s1} = m_{s1\_cn2} = m_{8\_9} + m_{8\_10} + m_{8\_11} + m_{8\_12} + m_{8\_13} + m_{8\_14},$$

$$m_{cp1\_Csc} = m_{Csc\_cp1} = m_{1\_15}, \qquad m_{cp2\_Csc} = m_{Csc\_cp2} = m_{1\_16},$$

$$m_{cn1\_Csc} = m_{Csc\_cp1} = m_{1\_8}, \qquad m_{cn2\_Csc} = m_{Csc\_cn2} = m_{1\_7},$$

$$m_{Csc\_s1} = m_{s1\_Csc} = m_{1\_9} + m_{1\_10} + m_{1\_11} + m_{1\_12} + m_{1\_13} + m_{1\_14}, \text{ and}$$

$$m_{Csc\_s2} = m_{s2\_Csc} = m_{1\_2} + m_{1\_3} + m_{1\_4} + m_{1\_5} + m_{1\_6}$$

6.4.2 6-coil Equivalent Circuit of the Davey Machine with a Short-circuit Coil in Armature

When two coils are under commutation and the short-circuit coil is in one of the parallel paths, a 6-coil equivalent circuit models the Davey machine. For example, when rotor position is between 7.5 and 22.5 degrees, the short-circuit coil (Coil 1) is in the S2 parallel path, shown in figure 6.15.

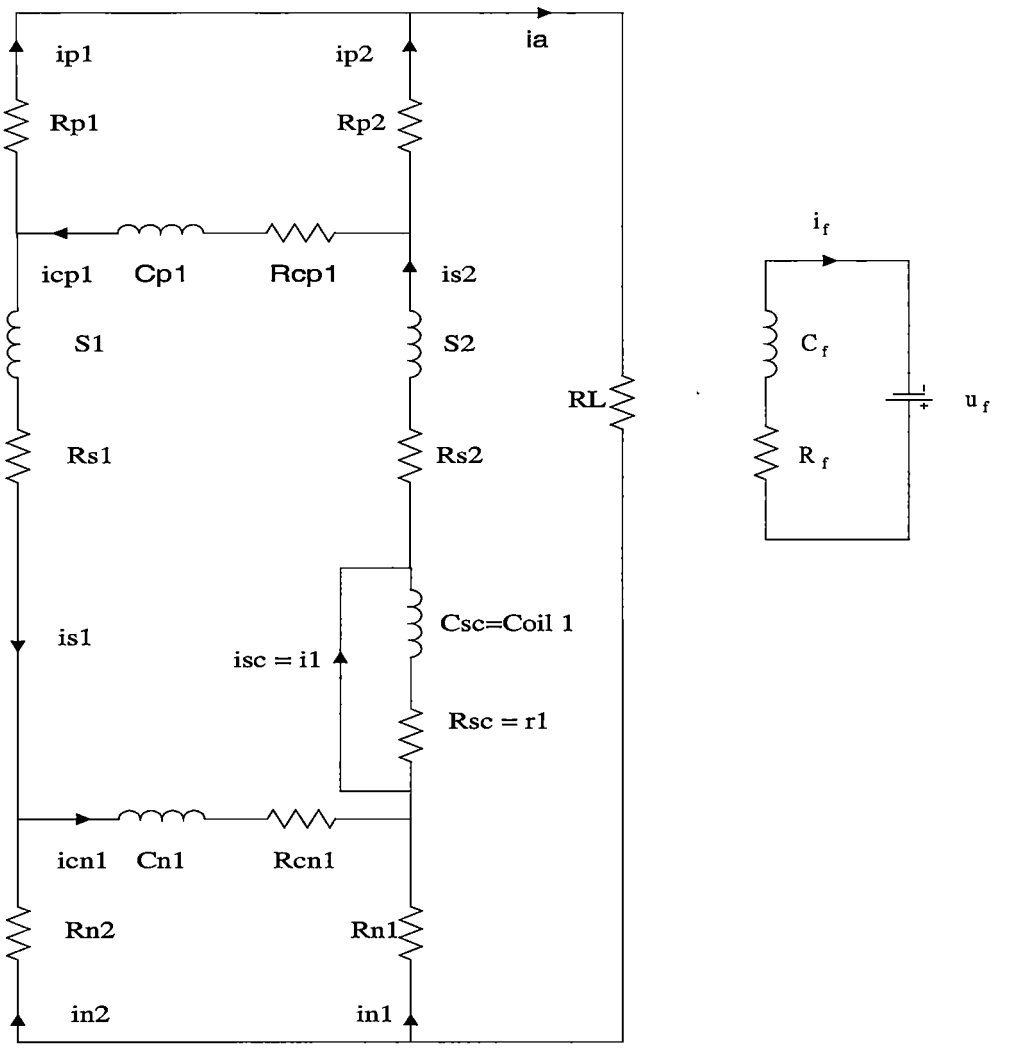

Figure 6.15: The 6-coil equivalent circuit of the Davey machine to model short-circuit armature coil

There are six differential equations for this circuit, written in matrix form as equation (6.9), where the voltage matrix is

$$\mathbf{v} = [U_f \quad 0 \quad 0 \quad 0 \quad 0 \quad 0]^T \tag{6.45}$$

The current matrix is

$$\mathbf{i} = [i_f \quad i_{cp1} \quad i_{s2} \quad i_{cn1} \quad i_{s1} \quad i_1]^T \tag{6.46}$$

The resistor matrix **R** is

$$\begin{bmatrix} R_f & 0 & 0 & 0 & 0 & 0 \\ 0 & R_{cp1}+R_{p1}+R_{P2} & -R_{p2} & 0 & -R_{p1} & 0 \\ 0 & -R_{p2} & R_{s2}+R_L+R_{p2}+R_{n1} & -R_{n1} & -R_L & 0 \\ 0 & 0 & -R_{n1} & R_{cn1}+R_{n1}+R_{n2} & -R_{n2} & 0 \\ 0 & -R_{p1} & -R_L & -R_{n2} & R_{s1}+R_L+R_{n2}+R_{p1} & 0 \\ 0 & 0 & 0 & 0 & 0 & r_1 \end{bmatrix} \quad (6.47)$$

The inductance matrix **L** is

$$\begin{bmatrix} L_{ff} & M_{f\_cp\ 1} & M_{f\_s2} & M_{f\_cn\ 1} & M_{f\_s1} & M_{f\_Csc} \\ M_{f\_cp\ 1} & L_{cp1} & m_{cp1\_s2} & m_{cp1\_cn1} & m_{cp1\_s1} & m_{cp1\_Csc} \\ M_{f\_s2} & m_{cp1\_s2} & L_{s2} & m_{s2\_cn1} & m_{s2\_s1} & m_{s2\_Csc} \\ M_{f\_cn\ 1} & m_{cp1\_cn1} & m_{s2\_cn1} & L_{cn1} & m_{cn1\_s1} & m_{cn1\_Csc} \\ M_{f\_s1} & m_{cp1\_s1} & m_{s2\_s1} & m_{cn1\_s1} & L_{s1} & m_{s1\_Csc} \\ M_{f\_Csc} & m_{cp1\_Csc} & m_{s2\_Csc} & m_{cn1\_Csc} & m_{s1\_Csc} & L_{Csc} \end{bmatrix} \quad (6.48)$$

6.4.2.1 Coil Resistance of the 6-coil Equivalent Circuit

The coil resistances of the 6-coil equivalent circuit are,

$$R_{cp1} = R_{cn1} = R_{coil} \quad (6.49)$$

$$R_{s1} = 7R_{coil} \quad (6.50)$$

$$R_{s2} = 6R_{coil} \quad (6.51)$$

$$R_{sc} = R_1 = R_{coil} \quad (6.52)$$

6.4.2.2 Brush-segment contact resistance of the 6-coil Equivalent Circuit

The contact resistances of the positive and negative brush-segment are the same as those discussed in section 6.3.2.2, refer to equations (6.35) and (6.36) and figure 6.10.

6.4.2.3 Self inductance of the 6-coil Equivalent Circuit

The coil combinations used in the 6-coil equivalent circuit for different rotor position are summarised in table 6.2. To illustrate the inductance matrix, consider the instant when the rotor position is between 7.5 and 22.5 degrees.

Coil C_{p1} = Coil 16, Coil C_{n1} = Coil 8, Coil C_{sc} = Coil 1,

Coil S_1 = Coil 9, 10, 11, 12, 13, 14 and 15 in series, and

Coil S_2 = Coil 2, 3, 4, 5, 6 and 7 in series.

The self inductance of the coils is

$L_{cp1} = L16$, $L_{cn1} = L8$, $L_{sc} = L1$,

$$L_{s1} = L_9 + L_{10} + L_{11} + L_{12} + L_{13} + L_{14} + L_{15}$$
$$2\begin{pmatrix} m_{9\_10} + m_{9\_11} + m_{9\_12} + m_{9\_13} + m_{9\_14} + m_{9\_15} \\ m_{10\_11} + m_{10\_12} + m_{10\_13} + m_{10\_14} + m_{10\_15} \\ m_{11\_12} + m_{11\_13} + m_{11\_14} + m_{11\_15} \\ m_{12\_13} + m_{12\_14} + m_{12\_15} \\ m_{13\_14} + m_{13\_15} \\ m_{14\_15} \end{pmatrix}, \text{ and}$$

$$L_{s2} = L_2 + L_3 + L_4 + L_5 + L_6 + L_7$$
$$2\begin{pmatrix} m_{2\_3} + m_{2\_4} + m_{2\_5} + m_{2\_6} + m_{2\_7} \\ m_{3\_4} + m_{3\_5} + m_{3\_6} + m_{3\_7} \\ m_{4\_5} + m_{4\_6} + m_{4\_7} \\ m_{5\_6} + m_{5\_7} \\ m_{6\_7} \end{pmatrix}$$

6.4.2.4 Mutual inductance between the field coil and the other coils in the 6-coil equivalent circuit

$$M_{f\_cp1} = M_{cp1\_f} = M_{f\_15},\ M_{f\_cn1} = M_{cn1\_f} = M_{f\_7},$$

$$M_{f\_s2} = M_{s2\_f} = M_{f\_2} + M_{f\_3} + M_{f\_4} + M_{f\_5} + M_{f\_6} M_{f\_7},$$

$M_{f\_s1} = M_{s1\_f} = M_{f\_9} + M_{f\_10} + M_{f\_11} + M_{f\_12} + M_{f\_13} + M_{f\_14} M_{f\_15}$, and

$M_{f\_Csc} = M_{f\_1}$

6.4.2.5 Mutual inductance between the coils of the 6-coil equivalent circuit

$m_{cp1\_s2} = m_{s2\_cp1} = m_{2\_16} + m_{3\_16} + m_{4\_16} + m_{5\_16} + m_{6\_16} + m_{7\_16}$,

$m_{cp1\_cn1} = m_{cn1\_cp1} = m_{8\_16}$,

$m_{cp1\_s1} = m_{s1\_cp1} = m_{9\_16} + m_{10\_16} + m_{11\_16} + m_{12\_16} + m_{13\_16} + m_{14\_16} + m_{15\_16}$,

$m_{s2\_cn1} = m_{cn1\_s2} = m_{2\_8} + m_{3\_8} + m_{4\_8} + m_{5\_8} + m_{6\_8} + m_{7\_8}$,

$m_{cn1\_s1} = m_{s1\_cn1} = m_{8\_9} + m_{8\_10} + m_{8\_11} + m_{8\_12} + m_{8\_13} + m_{8\_14} + m_{8\_15}$,

$m_{cp1\_Csc} = m_{Csc\_cp1} = m_{1\_16}$, $m_{cn1\_Csc} = m_{Csc\_cp1} = m_{1\_8}$,

$m_{Csc\_s1} = m_{s1\_Csc} = m_{1\_9} + m_{1\_10} + m_{1\_11} + m_{1\_12} + m_{1\_13} + m_{1\_14} + m_{1\_15}$,

$m_{Csc\_s2} = m_{s2\_Csc} = m_{1\_2} + m_{1\_3} + m_{1\_4} + m_{1\_5} + m_{1\_6} + m_{1\_7}$,

$$m_{s2\_s1} = m_{s1\_s2} = \begin{bmatrix} m_{2\_9} + m_{3\_9} + m_{4\_9} + m_{5\_9} + m_{6\_9} + m_{7\_9} + \\ m_{2\_10} + m_{3\_10} + m_{4\_10} + m_{5\_10} + m_{6\_10} + m_{7\_10} + \\ m_{2\_11} + m_{3\_11} + m_{4\_11} + m_{5\_11} + m_{6\_11} + m_{7\_11} + \\ m_{2\_12} + m_{3\_12} + m_{4\_12} + m_{5\_12} + m_{6\_12} + m_{7\_12} + \\ m_{2\_13} + m_{3\_13} + m_{4\_13} + m_{5\_13} + m_{6\_13} + m_{7\_13} + \\ m_{2\_14} + m_{3\_14} + m_{4\_14} + m_{5\_14} + m_{6\_14} + m_{7\_14} + \\ m_{2\_15} + m_{3\_15} + m_{4\_15} + m_{5\_15} + m_{6\_15} + m_{7\_15} \end{bmatrix}$$

6.4.3 7-coil Equivalent Circuit of the Davey Machine with a Short-circuit Coil in Armature

When four coils are under commutation, including the short-circuit coil, each parallel path is formed of 6 coils in series. A 7-coil equivalent circuit models the Davey machine. For example, when rotor position is between 22.5 and 30 degrees, the short-circuit coil (Coil 1) has started to commutate, as shown in figure 6.16.

There are seven differential equations for this circuit, written in matrix form as equation (6.9), where the voltage matrix is

$$\mathbf{v} = [U_f \quad 0 \quad 0 \quad 0 \quad 0 \quad 0 \quad 0]^T \tag{6.53}$$

The current matrix is

$$\mathbf{i} = [i_f \quad i_{cp1} \quad i_1 \quad i_{s2} \quad i_{cn1} \quad i_{cn2} \quad i_{s1}]^T \tag{6.54}$$

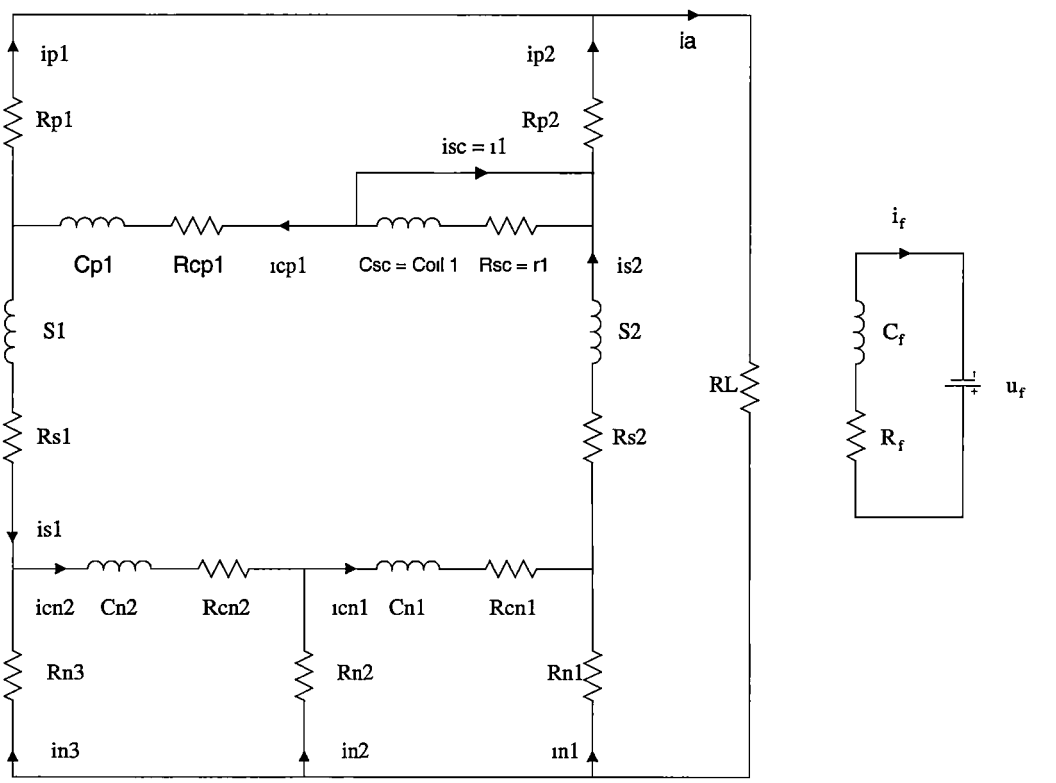

Figure 6.16: The 7-coil equivalent circuit of the Davey machine to model short-circuit armature coil

The resistor matrix **R** is

$$\begin{bmatrix} R_f & 0 & 0 & 0 & 0 & 0 & 0 \\ 0 & R_{cp1}+R_{p1}+R_{P2} & 0 & -R_{p2} & 0 & 0 & -R_{p1} \\ 0 & 0 & r_1 & 0 & 0 & 0 & 0 \\ 0 & -R_{p2} & 0 & R_{s2}+R_L+R_{p2}+R_{n1} & -R_{n1} & 0 & -R_L \\ 0 & 0 & 0 & -R_{n1} & R_{cn1}+R_{n1}+R_{n2} & -R_{n2} & 0 \\ 0 & 0 & 0 & 0 & -R_{n2} & R_{cn2}+R_{n2}+R_{n3} & -R_{n3} \\ 0 & -R_{p1} & 0 & -R_L & 0 & -R_{n3} & R_{s1}+R_L+R_{n3}+R_{p1} \end{bmatrix} \tag{6.55}$$

The inductance matrix **L** is

$$\begin{bmatrix} L_{ff} & M_{cp1\_f} & M_{Csc\_f} & M_{s2\_f} & M_{cn1\_f} & M_{cn2\_f} & M_{s1\_f} \\ M_{cp1\_f} & L_{cp1} & m_{Csc\_cp1} & m_{cp1\_s2} & m_{cp1\_cn1} & m_{cp1\_cn2} & m_{cp1\_s1} \\ M_{Csc\_f} & m_{Csc\_cp1} & L_{Csc} & m_{Csc\_s2} & m_{Csc\_cn1} & m_{Csc\_cn2} & m_{Csc\_s1} \\ M_{s2\_f} & m_{cp1\_s2} & m_{Csc\_s2} & L_{s2} & m_{s2\_cn1} & m_{cn2\_s2} & m_{s1\_s2} \\ M_{cn1\_f} & m_{cp1\_cn1} & m_{Csc\_cn1} & m_{s2\_cn1} & L_{cn1} & m_{cn1\_cn2} & m_{cn2\_s1} \\ M_{cn2\_f} & m_{cp1\_cn2} & m_{Csc\_cn2} & m_{cn2\_s2} & m_{cn1\_cn2} & L_{cn2} & m_{s1\_cn2} \\ M_{s1\_f} & m_{cp1\_s1} & m_{Csc\_s1} & m_{s1\_s2} & m_{cn2\_s1} & m_{s1\_cn2} & L_{s1} \end{bmatrix} \tag{6.56}$$

6.4.3.1 Coil Resistance of the 7-coil Equivalent Circuit

The coil resistances of the 7-coil equivalent circuit are,

$$R_{cp1} = R_{cn1} = R_{cn2} = R_{coil} \tag{6.57}$$

$$R_{s1} = 6R_{coil} \tag{6.58}$$

$$R_{s2} = 6R_{coil} \tag{6.59}$$

$$R_{sc} = R_{cp2} = R_{coil} \tag{6.60}$$

6.4.3.2 Brush-segment contact resistance of the 7-coil Equivalent Circuit

The contact resistances of the negative brush-segment are the same as those discussed in section 6.3.1.2. However, for the positive brush-segment, although the

positive brush partially contacts segment 16, 1 and 2, segments 1 and 2 are shorted together, shown in figure 6.17. Only R_{p1} and R_{p2} are used to model the positive brush-segment contact resistance. They vary with the rotor position and can be expressed as

$$R_{p1} = R_{bp}\frac{W_b}{G_a} \text{ and } R_{p2} = R_{bp}\frac{W_b}{G_b}$$

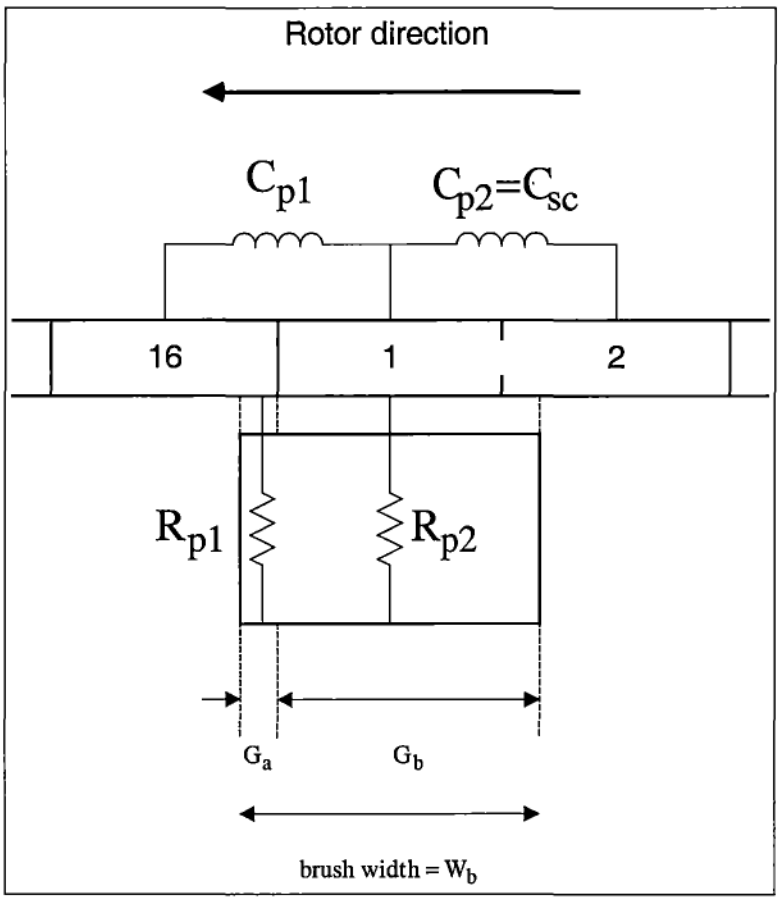

Figure 6.17: The positive brush-segment contact resistance of the 7-coil equivalent circuit with a short-circuit armature coil.

6.4.3.3 Self inductance of the 7-coil Equivalent Circuit

The coil combinations in the 7-coil equivalent circuit for different rotor position are summarised in table 6.2. To illustrate the inductance matrix, consider the instant when the rotor position is between 22.5 and 30 degrees.

Coil C_{p1} = Coil 16, Coil C_{p2} = Coil 1 = C_{sc}, Coil C_{n1} = Coil 8,

Coil C_{n2} = Coil 9, Coil S_1 = Coil 10, 11, 12, 13, 14 and 15 in series, and

Coil S_2 = Coil 2, 3, 4, 5, 6 and 7in series.

The self inductance of the coils is

$L_{cp1} = L16,$ $L_{cp2} = L1,$ $L_{cn1} = L8,$ $L_{cn2} = L9,$

$$L_{s1} = L_{10} + L_{11} + L_{12} + L_{13} + L_{14} + L_{15}$$
$$2\begin{pmatrix} m_{10\_11} + m_{10\_12} + m_{10\_13} + m_{10\_14} + m_{10\_15} \\ m_{11\_12} + m_{11\_13} + m_{11\_14} + m_{11\_15} \\ m_{12\_13} + m_{12\_14} + m_{12\_15} \\ m_{13\_14} + m_{13\_15} \\ m_{14\_15} \end{pmatrix}, \text{ and}$$

$$L_{s2} = L_2 + L_3 + L_4 + L_5 + L_6 + L_7$$
$$2\begin{pmatrix} m_{2\_3} + m_{2\_4} + m_{2\_5} + m_{2\_6} + m_{2\_7} \\ m_{3\_4} + m_{3\_5} + m_{3\_6} + m_{3\_7} \\ m_{4\_5} + m_{4\_6} + m_{4\_7} \\ m_{5\_6} + m_{5\_7} \\ m_{6\_7} \end{pmatrix}$$

6.4.3.4 Mutual inductance between the field coil and the other coils in the 7-coil equivalent circuit

$M_{f\_cp1} = M_{cp1\_f} = M_{f\_16},$ $M_{f\_cp2} = M_{cp2\_f} = M_{Csc\_f} = M_{f\_Csc} = M_{f\_1},$

$M_{f\_s2} = M_{s2\_f} = M_{f\_2} + M_{f\_3} + M_{f\_4} + M_{f\_5} + M_{f\_6} + M_{f\_7},$

$M_{f\_cn1} = M_{cn1\_f} = M_{f\_8},$ $M_{f\_cn2} = M_{cn2\_f} = M_{f\_9},$ and

$M_{f\_s1} = M_{s1\_f} = M_{f\_10} + M_{f\_11} + M_{f\_12} + M_{f\_13} + M_{f\_14} + M_{f\_15}$

6.4.3.5 Mutual inductance between the coils of the 7-coil equivalent circuit

$m_{cp1\_cp2} = m_{cp2\_cp1} = m_{Csc\_cp1} = m_{cp1\_Csc} = m_{1\_16}$,

$m_{cp1\_s2} = m_{s2\_cp1} = m_{2\_16} + m_{3\_16} + m_{4\_16} + m_{5\_16} + m_{6\_16} + m_{7\_16}$,

$m_{cp1\_cn1} = m_{cn1\_cp1} = m_{8\_16}$, $m_{cp1\_cn2} = m_{cn2\_cp1} = m_{9\_16}$,

$m_{cp1\_s1} = m_{s1\_cp1} = m_{10\_16} + m_{11\_16} + m_{12\_16} + m_{13\_16} + m_{14\_16} + +m_{15\_16}$,

$m_{cp2\_cn1} = m_{cn1\_cp2} = m_{cn1\_Csc} = m_{Csc\_cn1} = m_{1\_8}$,

$m_{cp2\_cn2} = m_{cn2\_cp2} = m_{Csc\_cn2} = m_{cn1\_Csc} = m_{1\_9}$,

$m_{cp2\_s2} = m_{s2\_cp2} = m_{s2\_Ccs} = m_{Csc\_s2} = m_{1\_2} + m_{1\_3} + m_{1\_4} + m_{1\_5} + m_{1\_6} + m_{1\_7}$,

$m_{cp2\_s1} = m_{s1\_cp2} = m_{Csc\_s1} = m_{s1\_Csc} = m_{1\_10} + m_{1\_11} + m_{1\_12} + m_{1\_13} + m_{1\_14} + m_{1\_15}$,

$m_{s2\_cn1} = m_{cn1\_s2} = m_{2\_8} + m_{3\_8} + m_{4\_8} + m_{5\_8} + m_{6\_8} + m_{7\_8}$,

$m_{s2\_cn2} = m_{cn2\_s2} = m_{2\_9} + m_{3\_9} + m_{4\_9} + m_{5\_9} + m_{6\_9} + m_{7\_9}$,

$$m_{s2\_s1} = m_{s1\_s2} = \begin{bmatrix} m_{2\_10} + m_{3\_10} + m_{4\_10} + m_{5\_10} + m_{6\_10} + m_{7\_10} + \\ m_{2\_11} + m_{3\_11} + m_{4\_11} + m_{5\_11} + m_{6\_11} + m_{7\_11} + \\ m_{2\_12} + m_{3\_12} + m_{4\_12} + m_{5\_12} + m_{6\_12} + m_{7\_12} + \\ m_{2\_13} + m_{3\_13} + m_{4\_13} + m_{5\_13} + m_{6\_13} + m_{7\_13} + \\ m_{2\_14} + m_{3\_14} + m_{4\_14} + m_{5\_14} + m_{6\_14} + m_{7\_14} + \\ m_{2\_15} + m_{3\_15} + m_{4\_15} + m_{5\_15} + m_{6\_15} + m_{7\_15} \end{bmatrix},$$

$m_{cn1\_cn2} = m_{cn2\_cn1} = m_{9\_8}$,

$m_{cn1\_s1} = m_{s1\_cn1} = m_{8\_10} + m_{8\_11} + m_{8\_12} + m_{8\_13} + m_{8\_14} + m_{8\_15}$, and

$m_{cn2\_s1} = m_{s1\_cn2} = m_{9\_10} + m_{9\_11} + m_{9\_12} + m_{9\_13} + m_{9\_14} + m_{9\_15}$

6.4.4 5-coil Equivalent Circuit of the Davey Machine with a Short-circuit Coil in Armature

When two coils are under commutation including the short-circuit, a 5-coil equivalent circuit models the Davey machine. For example, when rotor position is between 30 and 45 degrees, the short-circuit coil (Coil 1) is under commutation by the positive brush and each parallel path is formed by 7 coils in series, shown in figure 6.18.

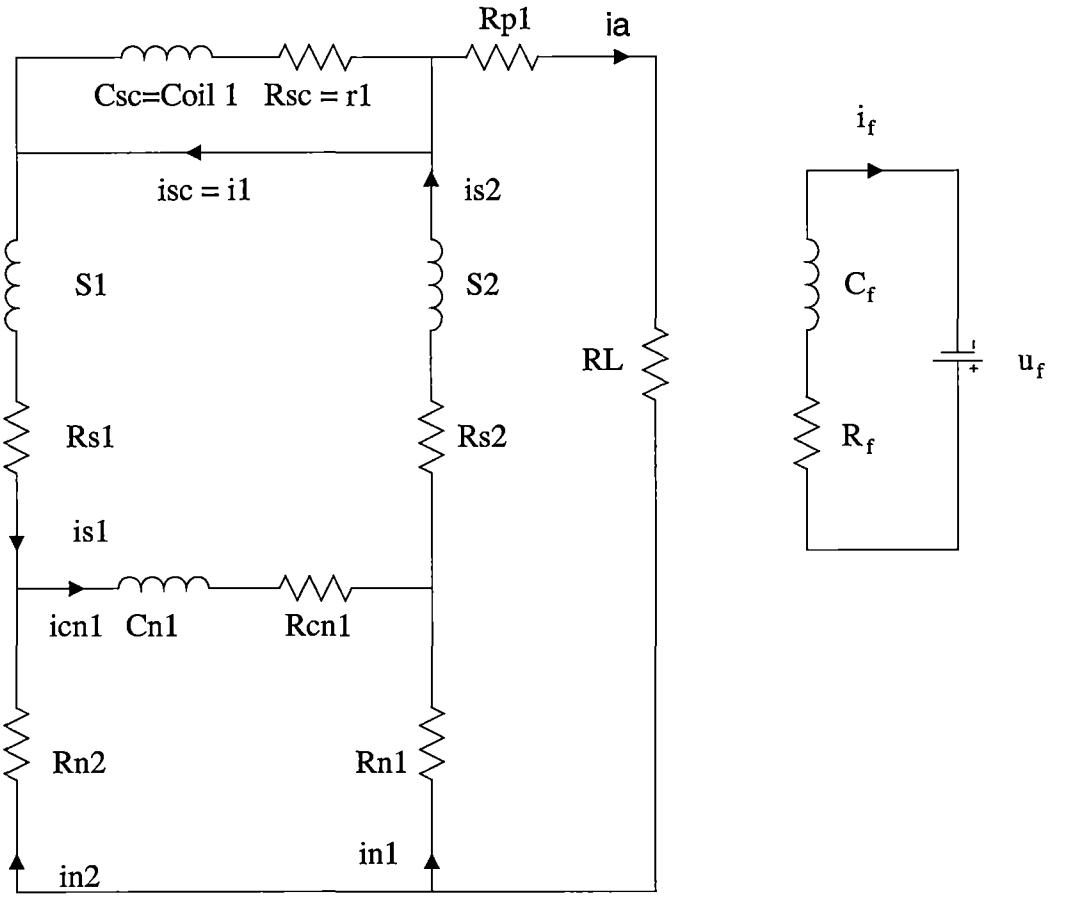

Figure 6.18: The 5-coil equivalent circuit of the Davey machine to model short-circuit armature coil

There are five differential equations for this circuit, written in matrix form as equation (6.9), where the voltage matrix is

$$\mathbf{v} = [U_f \quad 0 \quad 0 \quad 0 \quad 0]^T \tag{6.61}$$

The current matrix is

$$\mathbf{i} = [i_f \quad i_1 \quad i_{s2} \quad i_{cn1} \quad i_{s1}]^T \tag{6.62}$$

The resistor matrix **R** is

$$\begin{bmatrix} R_f & 0 & 0 & 0 & 0 \\ 0 & r_1 & 0 & 0 & 0 \\ 0 & 0 & R_{s2}+R_L+R_{p1}+R_{n1} & -R_{n1} & -R_{p1}-R_L \\ 0 & 0 & -R_{n1} & R_{cn1}+R_{n1}+R_{n2} & -R_{n2} \\ 0 & -R_{p1} & -R_L & -R_{n2} & R_{s1}+R_L+R_{n2}+R_{p1} \end{bmatrix} \tag{6.63}$$

The inductance matrix **L** is

$$\begin{bmatrix} L_{ff} & M_{f\_Csc} & M_{f\_s2} & M_{f\_cn1} & M_{f\_s1} \\ M_{f\_Csc} & L_{Csc} & m_{Csc\_s2} & m_{Csc\_cn1} & m_{Csc\_s1} \\ M_{f\_s2} & m_{Csc\_s2} & L_{s2} & m_{s2\_cn1} & m_{s2\_s1} \\ M_{f\_cn1} & m_{Csc\_cn1} & m_{s2\_cn1} & L_{cn1} & m_{cn1\_s1} \\ M_{f\_s1} & m_{Csc\_s1} & m_{s2\_s1} & m_{cn1\_s1} & L_{s1} \end{bmatrix} \tag{6.6}$$

6.4.4.1 Coil Resistance of the 5-coil Equivalent Circuit

The coil resistances of the 5-coil equivalent circuit are,

$$R_{cp1} = R_{Csc} = R_{cn1} = R_{coil} \tag{6.65}$$

$$R_{s1} = 7R_{coil} \tag{6.66}$$

$$R_{s2} = 7R_{coil} \tag{6.67}$$

6.4.4.2 Brush-segment contact resistance of the 5-coil Equivalent Circuit

The contact resistances of the negative brush-segment are the same as those discussed in section 6.3.2.2. However, for the positive brush-segment, although the positive brush partially contacts segment 1 and 2, only R_{p1} is used to model the positive brush-segment contact resistance since segment 1 and 2 are shorted together,

shown in figure 6.19. R_{p1} is assumed to be constant and equal to the positive brush resistance at this interval.

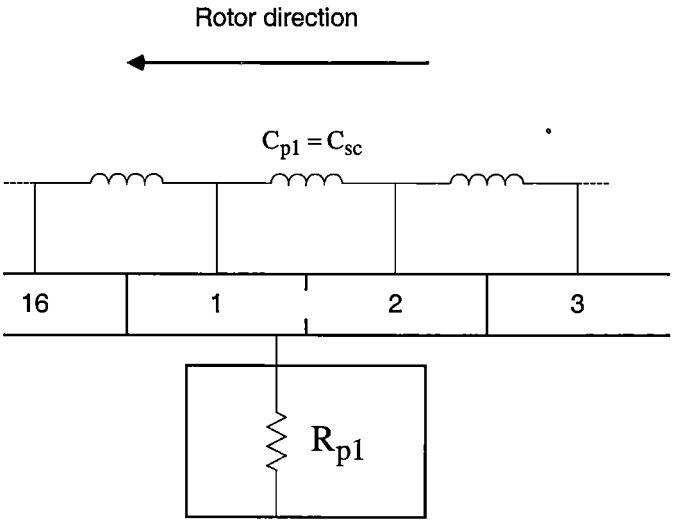

Figure 6.19: The positive brush-segment contact resistance of the 5-coil equivalent circuit with a short-circuit armature coil.

6.4.4.3 Self inductance of the 5-coil Equivalent Circuit

The coil combinations in the 5-coil equivalent circuit for different rotor position are summarised in table 6.2. To illustrate the inductance matrix, consider the instant when the rotor position is between 30 and 45 degrees.

Coil C_{p1} = Coil C_{sc} = Coil 1, Coil C_{n1} = Coil 8,

Coil S_1 = Coil 9, 10, 11, 12, 13, 14, 15 and 16 in series, and

Coil S_2 = Coil 2, 3, 4, 5, 6, 7 and 8 in series.

The self inductance of the coils are

$L_{cp1} = L_{Csc} = L1$, $L_{cn1} = L9$,

$$L_{s1} = L_{10} + L_{11} + L_{12} + L_{13} + L_{14} + L_{15} + L_{16}$$
$$2\begin{pmatrix} m_{10\_11} + m_{10\_12} + m_{10\_13} + m_{10\_14} + m_{10\_15} + m_{10\_16} \\ m_{11\_12} + m_{11\_13} + m_{11\_14} + m_{11\_15} + m_{11\_16} \\ m_{12\_13} + m_{12\_14} + m_{12\_15} + m_{12\_16} \\ m_{13\_14} + m_{13\_15} + m_{13\_16} \\ m_{14\_15} + m_{14\_16} + \\ m_{15\_16} \end{pmatrix}, \text{ and}$$

$$L_{s2} = L_2 + L_3 + L_4 + L_5 + L_6 + L_7 + L_8$$
$$2\begin{pmatrix} m_{2\_3} + m_{2\_4} + m_{2\_5} + m_{2\_6} + m_{2\_7} + m_{2\_8} \\ m_{3\_4} + m_{3\_5} + m_{3\_6} + m_{3\_7} + m_{3\_8} \\ m_{4\_5} + m_{4\_6} + m_{4\_7} + m_{4\_8} \\ m_{5\_6} + m_{5\_7} + m_{5\_8} \\ m_{6\_7} + m_{6\_8} \\ + m_{7\_8} \end{pmatrix}$$

6.4.4.4 Mutual inductance between the field coil and the other coils in the 5-coil equivalent circuit

$$M_{f\_cp1} = M_{cp1\_f} = M_{Csc\_f} = M_{f\_Csc} = M_{f\_1}, \qquad M_{f\_cn1} = M_{cn1\_f} = M_{f\_9},$$

$$M_{f\_s2} = M_{s2\_f} = M_{f\_2} + M_{f\_3} + M_{f\_4} + M_{f\_5} + M_{f\_6} + M_{f\_7} + M_{f\_8}, \text{ and}$$

$$M_{f\_s1} = M_{s1\_f} = M_{f\_16} + M_{f\_10} + M_{f\_11} + M_{f\_12} + M_{f\_13} + M_{f\_14} + M_{f\_15}$$

6.4.4.5 Mutual inductance between the coils of the 5-coil equivalent circuit

$$m_{cp1\_s2}=m_{s2\_cp1}=m_{s2\_Csc}=m_{Csc\_s2}=m_{1\_2}+m_{1\_3}+m_{1\_4}+m_{1\_5}+m_{1\_6}+m_{1\_7}+m_{1\_8},$$

$$m_{cp1\_cn1} = m_{cn1\_cp1} = m_{cn1\_Csc} = m_{Csc\_cn1} = m_{1\_9},$$

$$m_{cp1\_s1}=m_{s1\_cp1}=m_{s1\_Csc}=m_{Csc\_s1}=m_{1\_16}+m_{1\_15}+m_{1\_14}+m_{1\_13}+m_{1\_12}+m_{1\_11}+m_{1\_10},$$

$$m_{s2\_cn1} = m_{cn1\_s2} = m_{2\_9} + m_{3\_9} + m_{4\_9} + m_{5\_9} + m_{6\_9} + m_{7\_9} + m_{8\_9},$$

$$m_{cn1\_s1} = m_{s1\_cn1} = m_{9\_10} + m_{9\_11} + m_{9\_12} + m_{9\_13} + m_{9\_14} + m_{9\_15} + m_{9\_16},$$

and

$$m_{s2\_s1} = m_{s1\_s2} = \begin{bmatrix} m_{2\_10} + m_{3\_10} + m_{4\_10} + m_{5\_10} + m_{6\_10} + m_{7\_10} + m_{8\_10} + \\ m_{2\_11} + m_{3\_11} + m_{4\_11} + m_{5\_11} + m_{6\_11} + m_{7\_11} + m_{8\_11} + \\ m_{2\_12} + m_{3\_12} + m_{4\_12} + m_{5\_12} + m_{6\_12} + m_{7\_12} + m_{8\_12} + \\ m_{2\_13} + m_{3\_13} + m_{4\_13} + m_{5\_13} + m_{6\_13} + m_{7\_13} + m_{8\_13} + \\ m_{2\_14} + m_{3\_14} + m_{4\_14} + m_{5\_14} + m_{6\_14} + m_{7\_14} + m_{8\_14} + \\ m_{2\_15} + m_{3\_15} + m_{4\_15} + m_{5\_15} + m_{6\_15} + m_{7\_15} + m_{8\_15} + \\ m_{2\_16} + m_{3\_16} + m_{4\_16} + m_{5\_16} + m_{6\_16} + m_{7\_16} + m_{8\_16} \end{bmatrix}$$

6.5 Techniques for Numerically Solving Ordinary Differential Equations (ODE)

An ordinary differential equation (ODE) can always be written as a set of first order differential equations of the form :

$$\frac{dy}{dt} = f(t, y(t)) \tag{6.68}$$

With an initial value y_o given at t_o, it is required to find a function $y(t)$ defined over an interval (the length of the interval = step length (h)) which satisfies equation (6.68).

The simplest, and the most easily understood, numerical methods to solve an initial value problem are one-step methods. The general one-step method is an iteration of the form :

$$y_{k+1} = y_k + h\delta(x_k, y_k; h) \tag{6.69}$$

where $k = 0, 1, \ldots n\text{-}1$.

The function $\delta(x_k, y_k; h)$ is called the increment function, that can be used to obtain y_{k+1} from y_k. The step size, h, may be fixed, unless an error analysis indicates the change of h is necessary. Euler's method and the Runge-Kutta method are the two common one-step methods that will be considered here.

6.5.1 Euler's Methods

Euler's method is the simplest one-step method. Given that the starting point, x_0 and y_0, and the gradient of the curve, $y' = f(x, y)$ at that point, the next point on the curve could be approximated from x_0 -h to x_0 +h, for small values of h. So $y(x_0 + h)$ can be approximated by:

$$y(x_0 + h) \approx y(x_0) + hy'(x_0) = y_0 + hf(x_0, y_0) \tag{6.70}$$

Continuing the process of equation (6.70) gives the general Euler's method iteration :

$$y_{n+1} = y_n + hf(x_n, y_n) \tag{6.71}$$

where $x_n = x_0 + nh$.

The improved Euler's method (Heun's method) gets an estimate of y_{n+1}, as in the original Euler's method, but calls the result z_{n+1}. The average of $f(x_n, y_n)$ and $f(x_{n+1}, y_{n+1})$ is then taken in place of $f(x_n, y_n)$ in the next step, then

$$y_{n+1} = y_n + \frac{h}{2}\left(f(x_n, y_n) + f(x_n + h, y_n + hf(x_n, y_n))\right) \tag{6.72}$$

In general, the estimated value of $y(x_0 + h)$ from these two methods will not be on the solution curve $y(x)$, but for well-behaved functions and sufficiently small step size, a satisfactory approximation should result.

6.5.2 Runge-Kutta Methods

The inaccuracy of the Euler's method is due to the assumption that the gradient remains constant over the whole step. The Runge-Kutta method now to be described examines the gradient (or the increment function) at various points close to (x_n, y_n), in order to get a better idea of the behaviour of the gradient. The increment function is expressed as a weighted average of the gradient near (x_n, y_n) as

$$\delta(\mathrm{x}_k, y_k; \mathrm{h}) = w_1 f(p_1, q_1) + w_2 f(p_2, q_2) + \cdots + w_m f(p_m, q_m) \tag{6.73}$$

The weights w_k and the sample points (p_k, q_k) in equation (6.73) must be chosen carefully for best results. The Runge-Kutta methods are different schemes for choosing these values [127]. The fourth order of Runge-Kutta method requires four intermediate calculations of the weight functions as

$$y_{n+1} = y_n + \frac{\mathrm{h}}{6}(k_1 + 2k_2 + 2k_3 + k_4) \tag{6.74}$$

where

$$\begin{aligned} k_1 &= f(x_n, y_n) \\ k_2 &= f\left(x_n + \frac{\mathrm{h}}{2}, y_n + \frac{\mathrm{h}k_1}{2}\right) \\ k_3 &= f\left(x_n + \frac{\mathrm{h}}{2}, y_n + \frac{\mathrm{h}k_2}{2}\right) \\ k_4 &= f(x_n + \mathrm{h}, y_n + \mathrm{h}k_3) \end{aligned}$$

The fourth order of Runge-Kutta method is the most popular method because it is easy to implement, and virtually always succeeds in giving a good approximation. The drawbacks are that it is computationally inefficient, and errors are harder to control than other methods.

6.5.3 Other Methods of Solving ODEs

Other alternative methods of solving ODEs exist [128] such as Richardson extrapolation, also known as the Burlisch-Stoer method, and the predictor-corrector method. Both of these are more complex to implement than Runge-Kutta and also less likely to converge. However, they can be more accurate, and faster to compute.

The differential equations of all equivalent circuits can be written in the form of equation (6.36). Hence these equations can be solved to find the currents using the Runge-Kutta method.

6.6 Inductance Measurement on the Davey Machine

In order to solve the system equations, it is necessary to obtain the various resistances and inductances of the Davey motor. Since the machine is cylindrical, and the effects of slot opening are ignored, it follows that the self inductance of the field winding is independent of the rotor position. With this exception, the coefficients in the inductance matrix are all functions of rotor position. These coefficients where measured using a Direct Current Inductance (DCI) Bridge that was made in the Electrical Engineering Department of University of Tasmania [129]. All the tests were carried out with the machine stationary. The brush-gear was removed and contact leads were used to contact onto the commutator segments [125].

6.6.1 Field-armature Coil Mutual Inductance M_{f_n}

Figure 6.20 shows the developed diagram of the Davey machine for mutual inductance measurement. A DC supply and the reversing switch were connected to the armature as shown in figure 6.20 to set up the same flux as under normal operating condition.

In fact, measurement was taken of two symmetrically equivalent coils that are connected in parallel. 'Coil a' is equivalent to coils 1, 2, 3,4, 5, 6, 7, and 8 in series. 'Coil b' is coils 8, 9, 10, 11, 12, 13, 14, 15 and 16 in series. The induced voltage

from the field winding is integrated. The field-armature mutual inductance M_a was measured and equal to 3.87±0.01H.

Assuming that M_{f_n} are sinusoidal and can be expressed as

$$M_{f\_n} = M\sin(\omega_{rt}t + (n-1)\cdot w_c) \tag{6.75}$$

where M is the peak value of the field-armature coil mutual inductance, w_c is the segment width and equal to $\pi/8$, ω_{rt} is the angular speed of the rotor and n is an integer from 1 to 16.

Referring to figure 6.20, $\omega_{rt}t=0$, and M_a can be expressed in terms of M_{f_n} as

$$M_a = M\sum_{n=1}^{8}\sin((n-1)\cdot w_c) \tag{6.76}$$

Substitute $M_a = 3.87H$ into (6.41) gives M=0.78H. Hence,

$$M_{f\_n} = 0.756\sin(\omega_{rt}t + (n-1)\cdot w_c) \tag{6.77}$$

6.6.2 Self Inductances of Field and Armature Coils L_{ff} and L_1

L_{ff}=284H ± 5%, R_{ff} = 1100Ω

Coil 1 was disconnected from segment 1 to measure L_1. Measurements were carried out at different rotor positions. When $\omega_{rt}t=0$, maximum value of L_1 = 15.6mH. When $\omega_{rt}t=\pi/2$, minimum value of L_1 = 5.7mH. Hence, the self inductance of the armature coils can be expressed as

$$L_n = L_{ave} + L_{peak}\cos\left\{2\left(\omega_{rt}t - \pi - (n-1)\frac{\pi}{8}\right)\right\} \tag{6.78}$$

where L_{ave} is average value of L_1 and L_{peak} is the maximum variation of L_1.

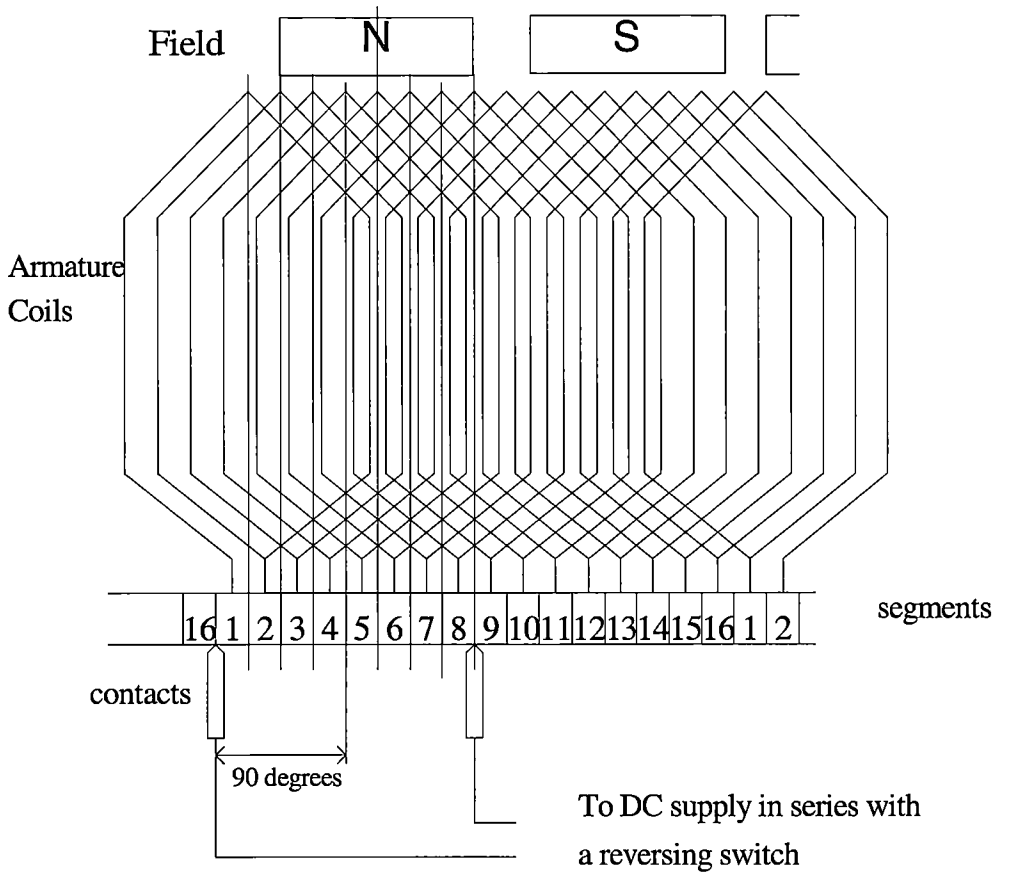

Figure 6.20: The developed diagram of the Davey machine for inductance measurement

It should be noted that the self-inductance of coil 1 has the minimum value when the turns lie on the field axis, not the armature axis. Jones [125] suggested that it is due to the leakage reluctance of the pole faces being less than the direct reluctance of the poles and yoke.

6.7 Numerical Solution of the Davey Machine Model

The mathematic model equations were solved using Matlab. Matrix inverses were calculated using Matlab matrix division operation that is actually computed by solving the upper and lower triangular system (LU-decomposition method).

A step size of 0.5 mechanical degrees (720 samples per revolution) was used for satisfactory simulation of the model. Simulating the Davey machine required about 25 hours of CPU time in order to produce one second of simulated time data. It takes

about 1.2 seconds of simulated time to reach the steady state condition. The program may no doubt be optimised to solve the equations faster but no serious effort has been put into this.

6.7.1 Simulation of the Davey Machine at Steady State Condition in Healthy Condition

A steady DC voltage was used for the field supply and the rotor speed was assigned to 1569rpm. Figure 6.21 and 6.22 show the simulation results of the armature and field current waveform of the Davey machine at steady state with a good armature, ie no open-circuit or short-circuit armature coils. A time step of (1/18828) sec was used. Two times speed frequency and the slot ripple are distinguishable.

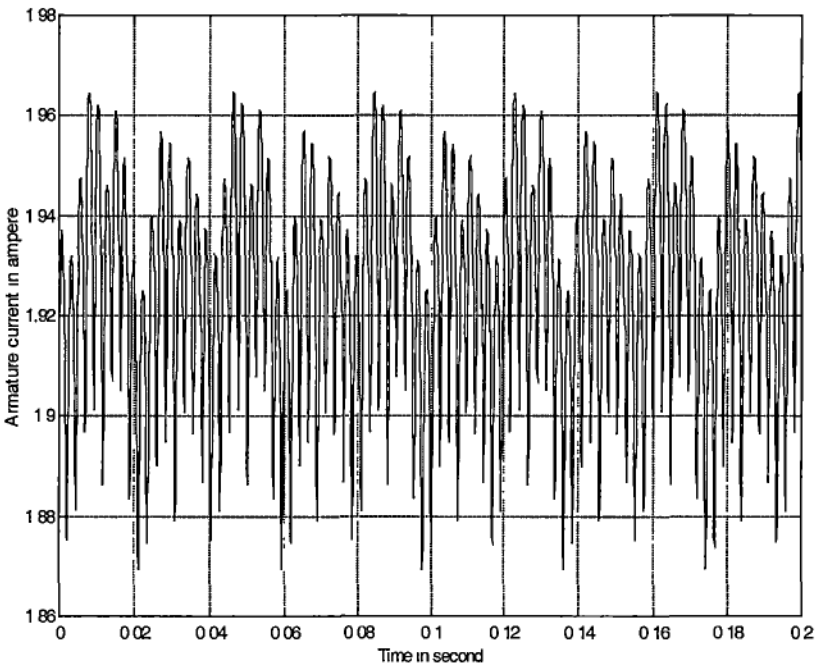

Figure 6.21: Simulated armature current of Davey machine in healthy condition

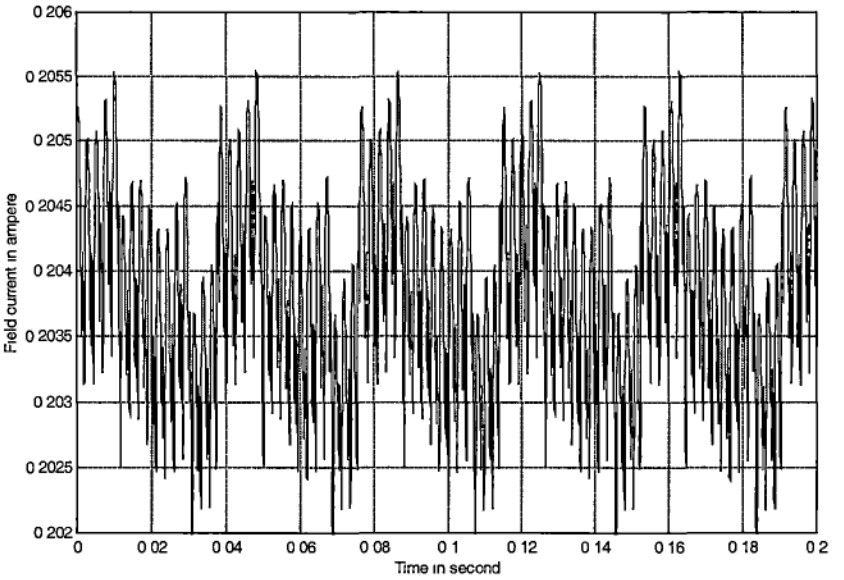

Figure 6.22: Simulated field current of Davey machine in healthy condition

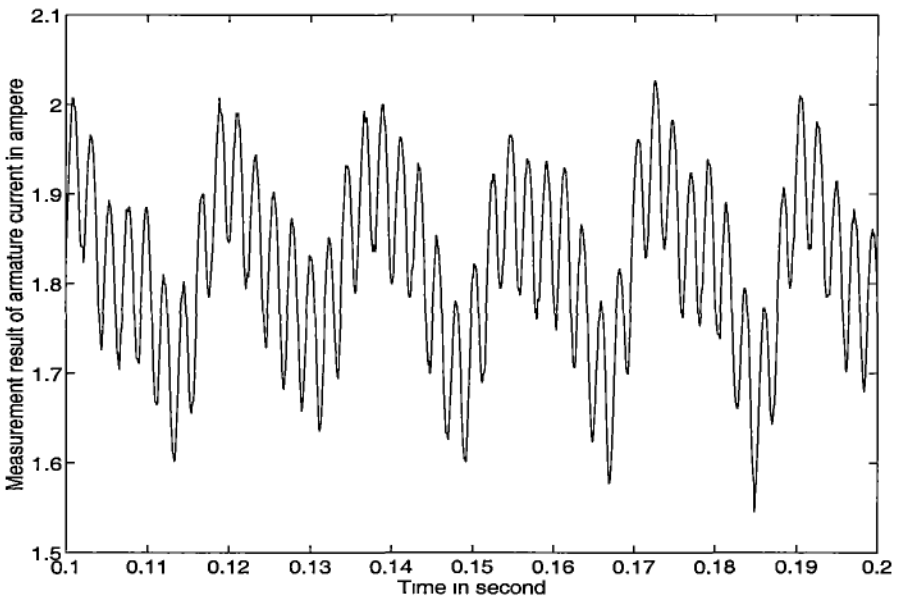

Figure 6.23: Armature current waveform of Davey machine with a good armature at steady state (measurement result)

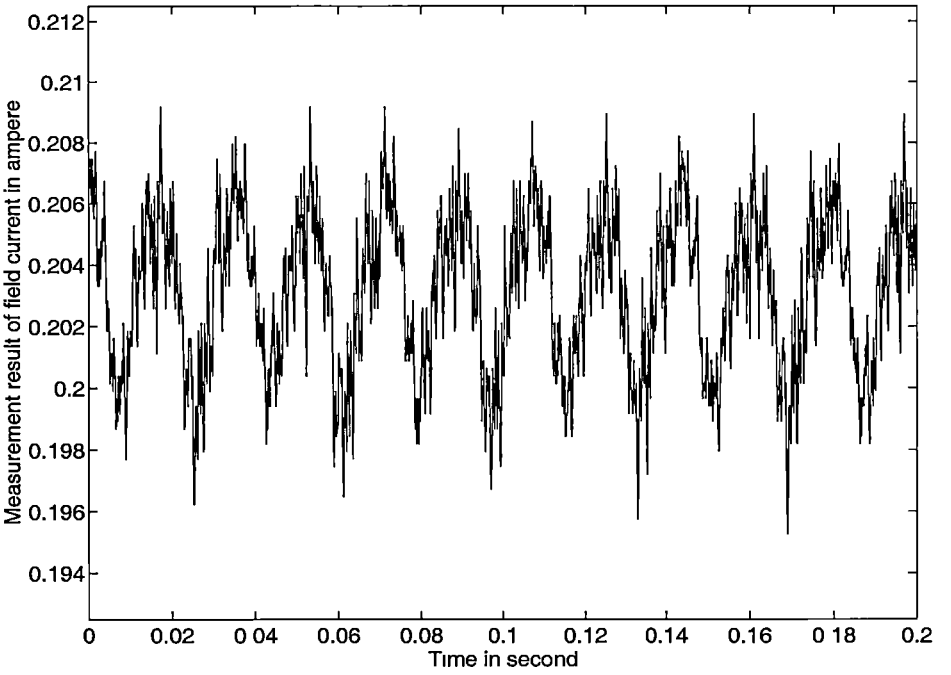

Figure 6.24: Field current waveform of Davey machine with a good armature at steady state (measurement result)

Figure 6.23 and 6.24 show the armature and field current, measured by means of the voltage across a nonconductive resistor so that the DC level can be shown. The armature and field current were sampled at 10kHz and 65536 samples were recorded for each measurement, ie frequency resolution of FFT is 0.15Hz. Significant double speed frequency components can be found in armature and field current waveforms.

Current measurements were also obtained from a clip-on Rogowski coil to avoid the electrical noise, particularly when the motor had a defective armature coil. This type of air-core coil generates a voltage proportional to the coil's mutual inductance and the rate of change of current. The operation of this coil was discussed in section 5.4.1.

Hence, for the simulation results, instead of performing spectrum analysis directly on the waveforms, spectrum analysis was carried out for the time derivative. 32768 samples were used for the spectrum analysis, ie frequency resolution is 0.57Hz, which is lower than the measurement spectrum, 0.15Hz. As a result the peaks in the simulation are wider, compared to measurement.

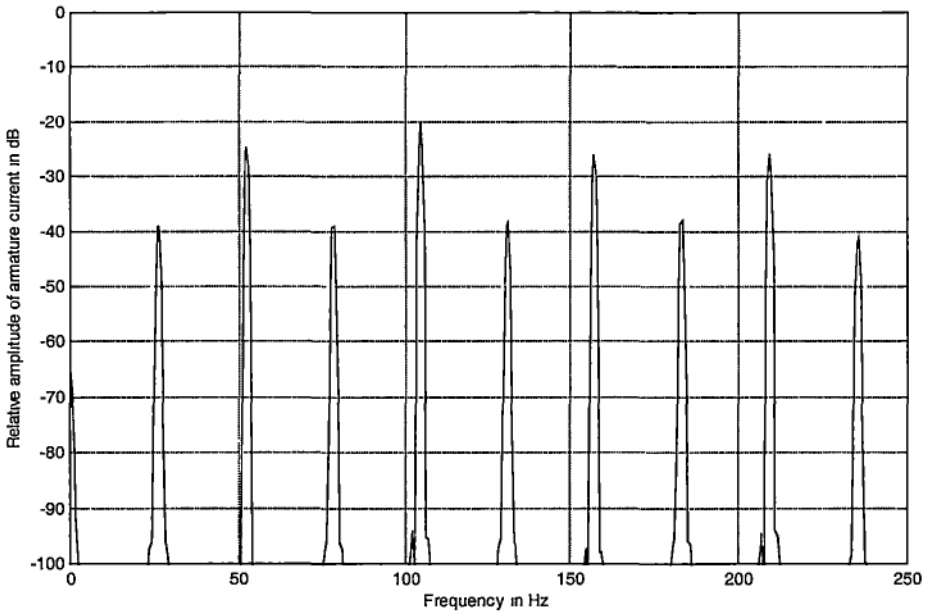

Figure 6.25: Spectrum of the derivative of the armature current of Davey machine in healthy condition (simulation result)

Figure 6.25 shows the simulation spectrum of the armature current from 0 to 250Hz. The zero dB frequency of the simulation results was the slot harmonic (16 times the speed frequency). As the results do not contain the DC level and time harmonics, speed frequency and its multiples become dominant. The even speed harmonics in the simulation result are relatively higher than the rest and are due to the $2\omega_r$ variation of armature coil self-inductance (section 6.62) caused by saliency of the machine. The speed frequency appearing in the simulation result is due to the difference of the resistance value of positive and negative brushes. As in general, the contact drops at positive and negative brushes are different [130].

Figure 6.26 shows measured derivative of the armature current spectrum. The zero dB frequency was the slot frequency. The amplitude of $2f_r$ and $4f_r$ components are significantly higher than the rest. The odd speed frequency components have lower relative amplitude than in the simulation.

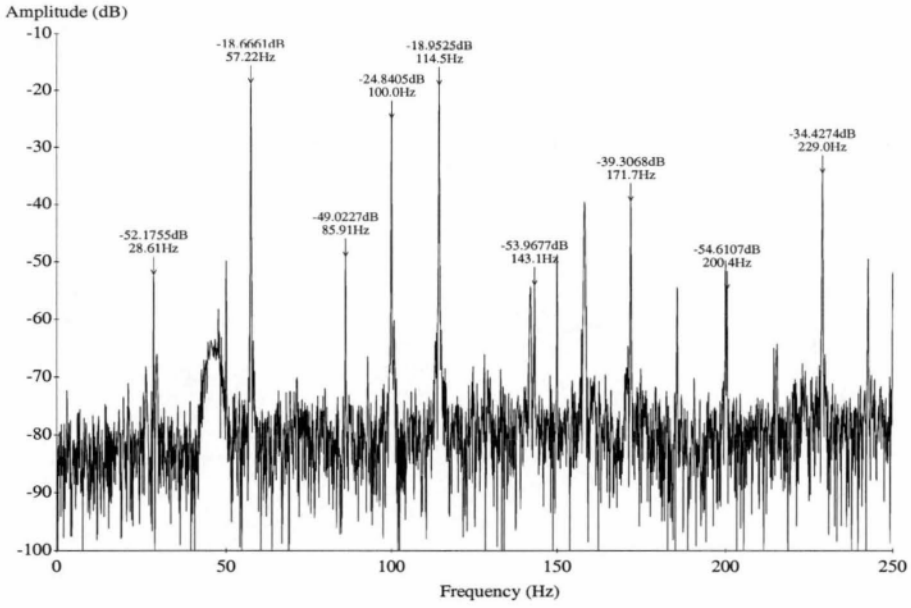

Figure 6.26: Spectrum of the derivative of the armature current of Davey machine in healthy condition (obtained by Rogowski coil)

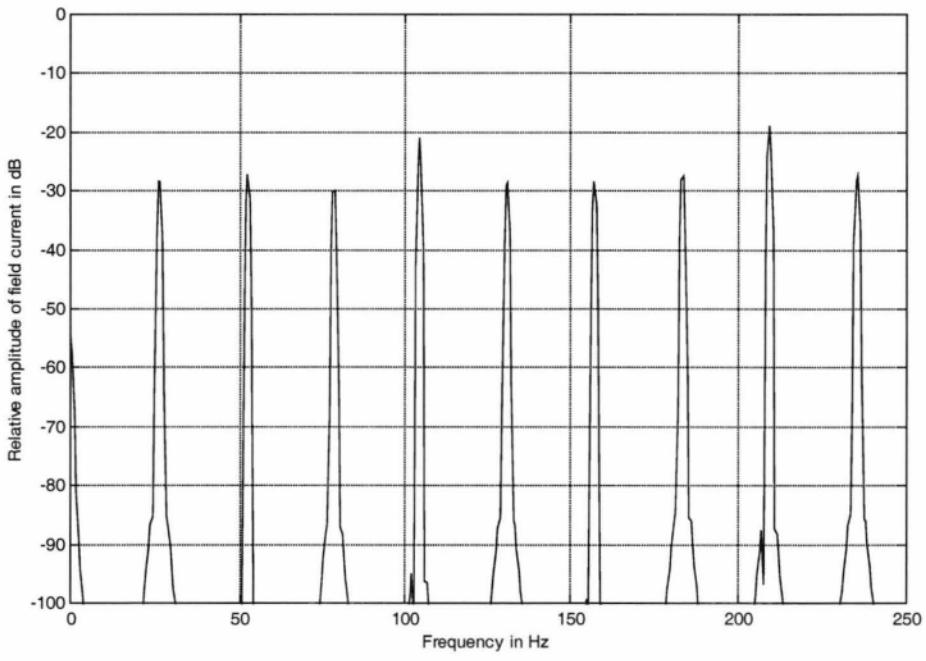

Figure 6.27: Spectrum of the derivative of field current of Davey machine in healthy condition (simulation result)

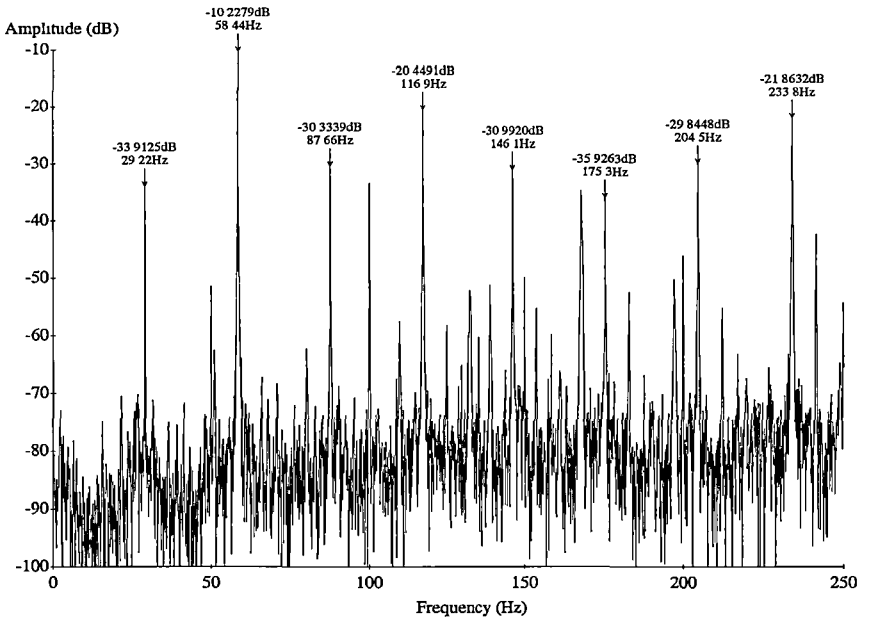

Figure 6.28: Spectrum of the derivative of the field current of Davey machine in healthy condition (obtained by Rogowski coil)

Figures 6.27 shows the corresponding simulated field current spectrum. The relative amplitude of the speed frequency and its multiples are about 25dB down from the $48f_r$ component. Figure 6.28 shows the field current spectrum obtained from measurement. There is a similar pattern dominant frequencies as the corresponding armature current spectrum.

	Average i_a = 1.9A		Average i_a = 1.6A		Average i_a = 1.1A		Average i_a = 0.7A	
	Hz	dB	Hz	dB	Hz	dB	Hz	dB
f_r	26.2	-39.3	26.6	-41.0	26.8	-46.9	27.1	-52.1
$2f_r$	52.8	-24.8	53.3	-26.3	53.6	-32.4	54.2	-38.3
$3f_r$	78.8	-39.2	79.9	-37.5	80.5	-43.5	81.3	-45.5
$4f_r$	104.5	-20.0	106.3	-22.2	107.3	-28.2	108.5	-33.4
$5f_r$	131.0	-38.5	133.1	-40.3	134.2	-46.9	135.4	-52.1
$6f_r$	157.0	-26.1	160.0	-28.3	170.0	-34.5	162.8	-40.0
$7f_r$	183.2	-38.1	186.0	-40.0	188.0	-46.1	190.0	-51.1
$8f_r$	209.2	-25.8	212.9	-28.0	214.1	-33.8	216.5	-38.2
$9f_r$	235.6	-41.2	239.2	-43.0	241.5	-50.0	244.0	-54.8
$16f_r$	418.3	0	426.0	0	430.0	0	433.5	0
$48f_r$	1255	-10.7	1277	-12.9	1286	-19.0	1301	-24.4

Table 6.3 Simulation results of the derivative armature current spectrum of Davey machine in healthy condition

The effect of different load conditions on the relative amplitude of the speed related frequency components was also investigated. Another three simulations were computed for different armature currents. Measurements were also carried out for comparison. The relative amplitude of the harmonics up to 250Hz is summarised in tables 6.3, 6.4, 6.5 and 6.6.

	Average i_a = 2.0A		Average i_a = 1.5A		Average i_a = 1.0A		Average i_a = 0.5A	
	Hz	dB	Hz	dB	Hz	dB	Hz	dB
f_r	28.6	-52.2	29.2	-58.1	29.8	-54.7	30.2	-53.7
$2f_r$	57.2	-18.8	58.4	-20.5	59.6	-17.9	60.4	-16.5
$3f_r$	85.9	-49.0	87.6	-54.5	89.5	-55.0	90.6	-51.8
$4f_r$	114.5	-19.0	117.0	-20.4	119.2	-18.8	120.8	-17.6
$5f_r$	143.1	-54.0	146.1	-55.8	149.1	-40.6	151.1	-60.7
$6f_r$	171.7	-39.3	175.5	-44.8	180.0	-43.6	181.5	-43.7
$7f_r$	200.4	-54.6	204.5	-50.4	208.5	-57.3	211.5	-56.8
$8f_r$	229.0	-34.2	233.8	-36.5	238.3	-38.0	241.7	-39.3
$9f_r$	257.6	-40.9	262.5	-43.0	268.0	-50.0	271.9	-55.2
$16f_r$	458.1	0	467.0	0	476.8	0	483.5	0
$48f_r$	1373	-29.6	1402	-28.0	1430	-30.4	1450	-28.9
300Hz	300	-0.5	300	-2.63	300	-0.7	300	-0.2

Table 6.4: Measurement results of armature current spectrum of Davey machine in healthy condition

	Average i_a = 1.9A		Average i_a = 1.6A		Average i_a = 1.1A		Average i_a = 0.7A	
	Hz	dB	Hz	dB	Hz	dB	Hz	dB
f_r	26.2	-28.4	26.6	-30.5	26.8	-36.7	27.1	-41.9
$2f_r$	52.8	-27.1	53.3	-29.4	53.6	-35.2	54.2	-40.0
$3f_r$	78.8	-30.0	79.9	-31.8	80.5	-38.0	81.3	-43.3
$4f_r$	104.5	-21.0	106.3	-23.1	107.3	-29.3	108.5	-34.2
$5f_r$	131.0	-28.5	133.1	-30.7	134.2	-36.8	135.4	-42.0
$6f_r$	157.0	-28.3	160.0	-30.8	170.0	-36.9	162.8	-41.8
$7f_r$	183.2	-27.5	186.0	-29.2	188.0	-35.1	190.0	-40.1
$8f_r$	209.2	-19.0	212.9	-21.2	214.1	-27.8	216.5	-34.0
$9f_r$	235.6	-27.4	239.2	-29.9	241.5	-36.2	244.0	-41.2
$16f_r$	418.3	-0.9	426.0	-3.1	430.0	-9.6	433.5	-15.1
$48f_r$	1255	0	1277	0	1286	0	1301	0

Table 6.5 Simulation results the derivative of field current spectrum of Davey machine in healthy condition

	Average i_a = 1.9A Neutral-plane shift=8 degrees		Average i_a = 1.6A Neutral-plane shift=6 degrees		Average i_a = 1.1A Neutral-plane shift=4 degrees		Average i_a = 0.7A Neutral-plane shift=0 degrees	
	Hz	dB	Hz	dB	Hz	dB	Hz	dB
f_r	28.6	-33.9	29.2	-44.0	29.8	-46.7	30.2	-43.7
$2f_r$	57.2	-10.2	58.4	-8.5	59.6	-5.1	60.4	-4.5
$3f_r$	85.9	-30.3	87.6	-31.5	89.5	-36.0	90.6	-35.8
$4f_r$	114.5	-20.4	117.0	-16.4	119.2	-15.8	120.8	-17.6
$5f_r$	143.1	-31.0	146.1	-22.8	149.1	-28.6	151.1	-29.7
$6f_r$	171.7	-35.9	175.5	-20.8	180.0	-26.6	181.5	-26.7
$7f_r$	200.4	-29.8	204.5	-23.4	208.5	-29.3	211.5	-29.8
$8f_r$	229.0	-21.9	233.8	-21.5	238.3	-20.0	241.7	-20.3
$9f_r$	257.6	-30.9	262.5	-33.0	268.0	-30.0	271.9	-30.2
$16f_r$	458.1	-9.5	467.0	-1.6	476.8	-3.8	483.5	-4.5
$48f_r$	1373	-8.5	1402	-11.4	1430	-13.4	1450	-15.5
300Hz	300	0	300	0	300	0	300	0

Table 6.6: Measurement results of field current spectrum of Davey machine in healthy condition

It is expected that the amplitude of the harmonics in armature and field current from simulation should vary linearly with the load, since the magnetic circuits of the models are assumed to be linear. However, results in tables 6.3 and 6.5 show the relative amplitude of the harmonics vary with load. This is because the slot frequency $16f_r$ or the commutator segment frequency $48f_r$ is the zero dB components, and their amplitude is a result of the non linear brush resistance.

From measurement results, only the f_r component in armature and field current has significant change in its amplitude at full load condition.

6.7.2 Simulation of an Open-circuit Armature Coil

An open-circuit of one armature coil can be modelled by simply assigning a very large resistance to coil 1; $R_1 = 500\Omega$. Figures 6.29 and 6.31 show the spectrum of the simulated of derivative of armature and field current for the Davey machine with an open-circuit armature coil. The speed was assigned as the case with a good rotor. The steady state value of the armature current dropped about one third of the normal value. In figure 6.29, the zero dB frequency is the slot harmonic. The amplitude of the speed frequency and its multiples increase significantly, particularly for the even speed harmonics (10 to 15dB increase). However, for the measurement results shown in figure 6.30, no significant change was found for the double speed frequency.

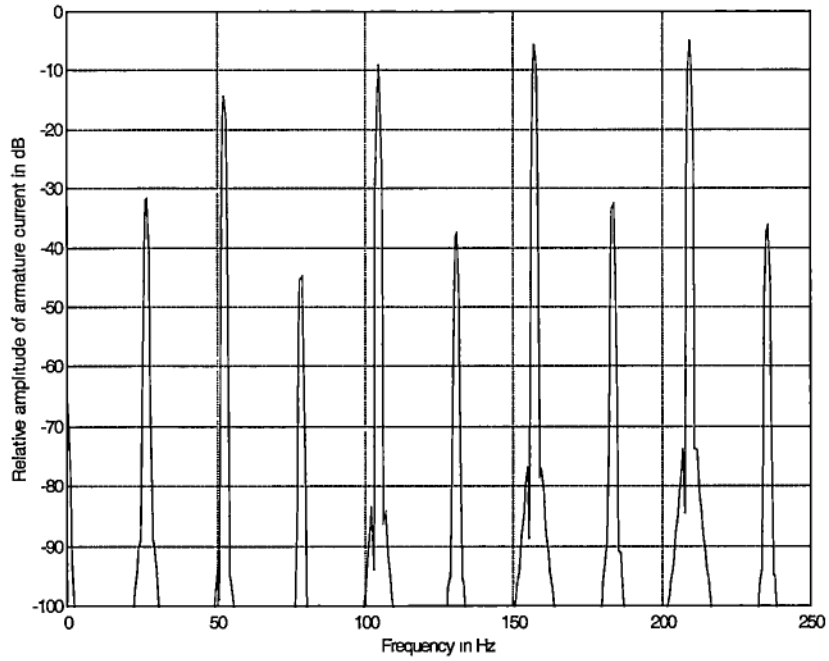

Figure 6.29: Spectrum of the derivative of armature current of Davey machine with open-circuit armature coil (simulation result)

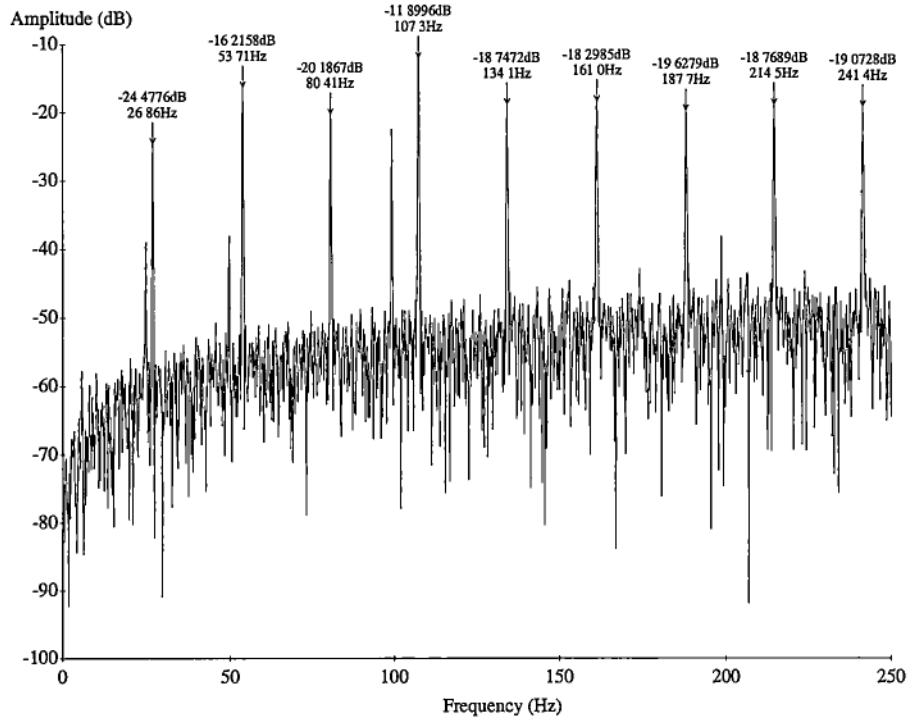

Figure 6.30: Spectrum of the derivative of armature current of Davey machine with open-circuit armature coil (measurement result)

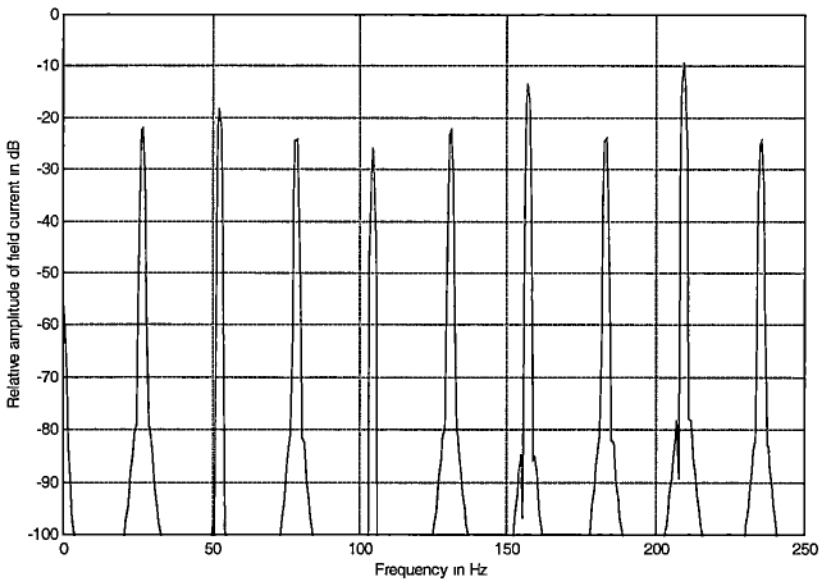

Figure 6.31: Spectrum of the derivative of field current of Davey machine with open-circuit armature coil (simulation result)

	Average i_a = 2.0A Measurement (healthy condition)		Average i_a = 1.5A Measurement (open-circuit coil)		Average i_a = 1.9A Simulation (healthy condition)		Average i_a = 1.6A Simulation (open-circuit coil)	
	Hz	dB	Hz	dB	Hz	dB	Hz	dB
f_r	28.6	-52.2	26.8	-24.5	26.2	-39.3	26.2	-31.0
$2f_r$	57.2	-18.8	53.7	-16.2	52.8	-24.8	52.8	-14.3
$3f_r$	85.9	-49.0	80.4	-20.2	78.8	-39.2	78.8	-45.0
$4f_r$	114.5	-19.0	107.3	-11.9	104.5	-20.0	104.5	-9.0
$5f_r$	143.1	-54.0	134.1	-18.7	131.0	-38.5	131.0	-37.8
$6f_r$	171.7	-39.3	161.0	-18.3	157.0	-26.1	157.0	-5.6
$7f_r$	200.4	-54.6	187.7	-19.6	183.2	-38.1	183.2	-32.8
$8f_r$	229.0	-34.2	214.5	-18.8	209.2	-25.8	209.2	-4.8
$9f_r$	257.6	-40.9	241.4	-19.1	235.6	-41.2	235.6	-36.5
$16f_r$	458.1	0	467.0	0	418.3	0	418.3	0
$48f_r$	1373	-29.6	1402	-18.0	1255	-10.7	1255	-10.5
300Hz	300	-0.5	300	-1.1	-	-	-	-

Table 6.7: Measurement and simulation results of armature current spectrum of Davey machine with and without a open-circuit armature coil

For the simulated field current spectrum, the amplitude change of the speed frequency related components is relatively lower compared to the corresponding armature current spectrum (less than 10dB), shown in figure 6.31. Noticeable amplitude change of the even speed frequency components can be found. The measurement result is shown in figure 6.32. No significant amplitude change of the speed frequency and its multiples can be found, probably due to the low magnetic

coupling factor between the armature and field circuit. The results are in tables 6.7, and 6.8.

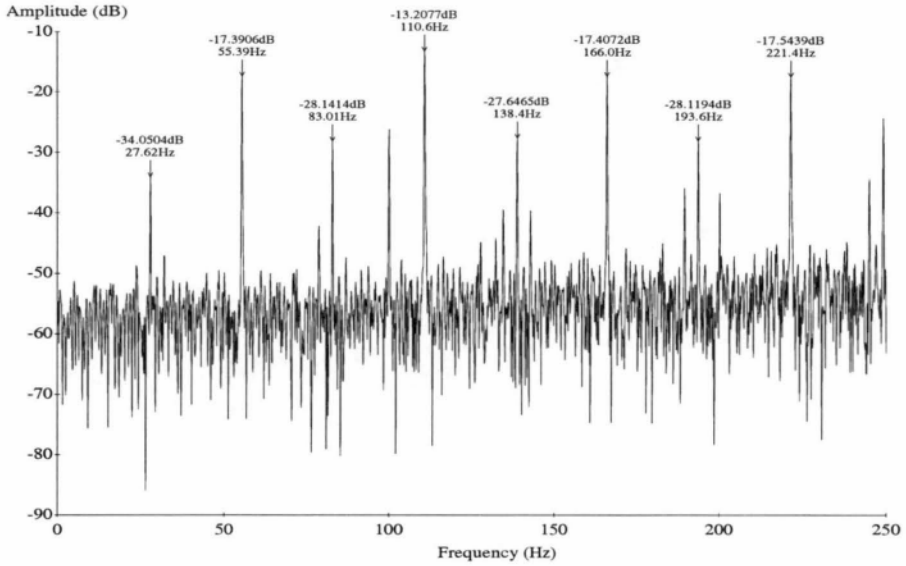

Figure 6.32: Spectrum of the derivative of field current of Davey machine with open-circuit armature coil (measurement result)

	Average i_a = 2.0A Measurement (healthy condition)		Average i_a = 1.5A Measurement (open-circuit coil)		Average i_a = 1.9A Simulation (healthy condition)		Average i_a = 1.6A Simulation (open-circuit coil)	
	Hz	dB	Hz	dB	Hz	dB	Hz	dB
f_r	29.2	-33.9	27.6	-34.1	26.2	-28.4	26.2	-22.8
$2f_r$	58.4	-10.2	55.4	-17.4	52.8	-27.1	52.8	-18.8
$3f_r$	87.7	-30.3	83.0	-28.1	78.8	-30.0	78.8	-24.2
$4f_r$	116.9	-20.4	110.6	-13.2	104.5	-21.0	104.5	-25.8
$5f_r$	146.1	-31.0	138.4	-27.6	131.0	-28.5	131.0	-22.7
$6f_r$	151.3	-35.9	166.0	-17.4	157.0	-28.3	157.0	-13.8
$7f_r$	204.5	-29.8	193.6	-28.1	183.2	-27.5	183.2	-24.1
$8f_r$	233.8	-21.9	221.4	-17.54	209.2	-19.0	209.2	-9.8
$9f_r$	262.8	-30.9	248.4	-28.5	235.6	-27.4	235.6	-25.4
$16f_r$	467.2	-6.5	442.0	-4.5	418.3	-0.9	418.3	-0.9
$48f_r$	1402	0	1325	0	1255	0	1255	0
300Hz	300	-5.4	300	-4.0	-	-	-	-

Table 6.8: Measurement and simulation results of field current spectrum of Davey machine with and without a open-circuit armature coil

The larger amplitude of the even speed harmonics in the simulated armature current spectrum compared to measurement results can be explained as follows. The model of the brush-commutator set uses linear behaviour of the carbon-copper (brush-commutator) resistance. With an open-circuit coil existing, rapid current change occurs in the parallel paths when the faulty coil passes under the brushes. For a two-pole motor (two brushes), the rapid current change occurs two times per revolution. This is reflected in the simulated armature current spectrum at the twice speed frequency and its multiples.

However, in practice, the resistance of the brush-commutator contact film is non-linear and is a function of current density, current direction, temperature, and brush material. When there is an open-circuit coil, excessive arcing, metal transfer, and associated burning occur every time the faulty coil passes under the cathode (negative) brush [28]. During sparking, because the temperature is high enough, thermionic emission is the main source of electrons. With a negative brush, the cathode spot will tend to remain fixed, being a copious source of electrons and cathode vapour compared with other areas. An unduly high current density in this spot results in bar burning. For the positive brush, the thermionic emission can be very small, and movement of the cathode spot is much more likely [132-133]. It causes less sparking. This effect is reflected the amplitude change of the speed frequency of a two pole motor when a fault occurs on the armature (once per revolution). Hence, for the Davey motor, when open-circuit armature coil occurs, the amplitude of the speed frequency in armature current increases rather than the twice speed frequency component.

6.7.3 Simulation of a short-circuit Armature Coil

Figures 6.33 and 6.34 show the spectrum of the simulated armature and field current for the Davey machine with a short-circuit armature coil. The speed was the same as with a good armature. The amplitude of even multiples of speed frequency components increase rapidly. The double speed frequency is the largest component and is the zero dB frequency of the spectra. The speed frequency and its odd multiples show about 10 to 15dB increase in their amplitude. The amplitudes of the

field and armature current, with and without the shorted armature coil, are in table 6.9.

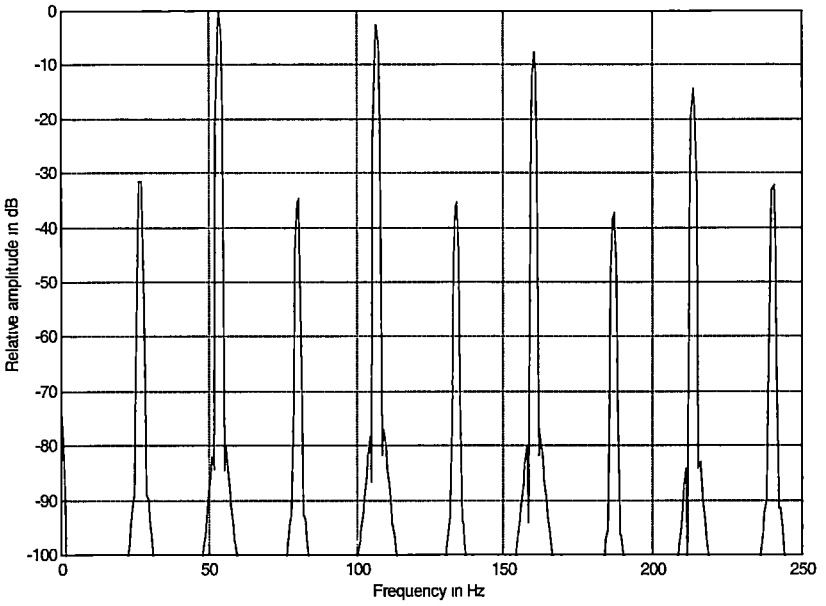

Figure 6.33: Spectrum of the derivative of armature current of Davey machine with short-circuit armature coil (simulation result)

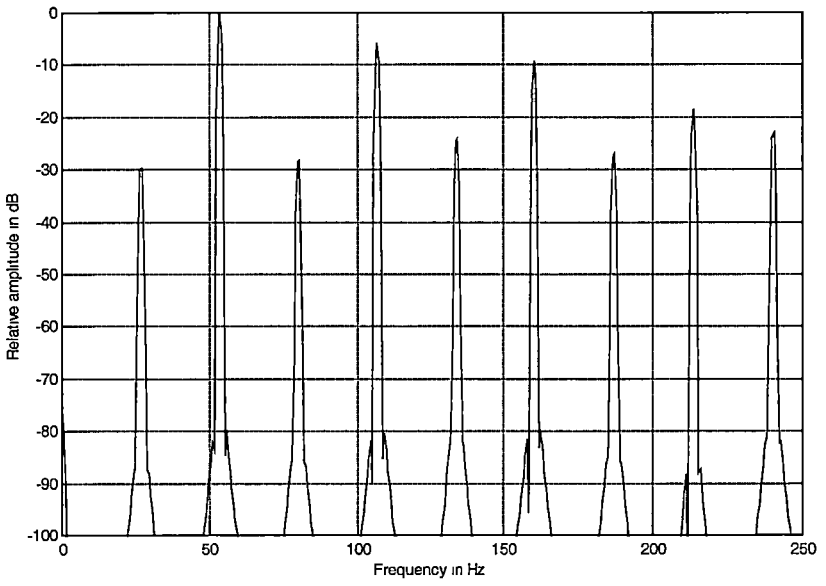

Figure 6.34: Spectrum of the derivative of field current of Davey machine with short-circuit armature coil (simulation result)

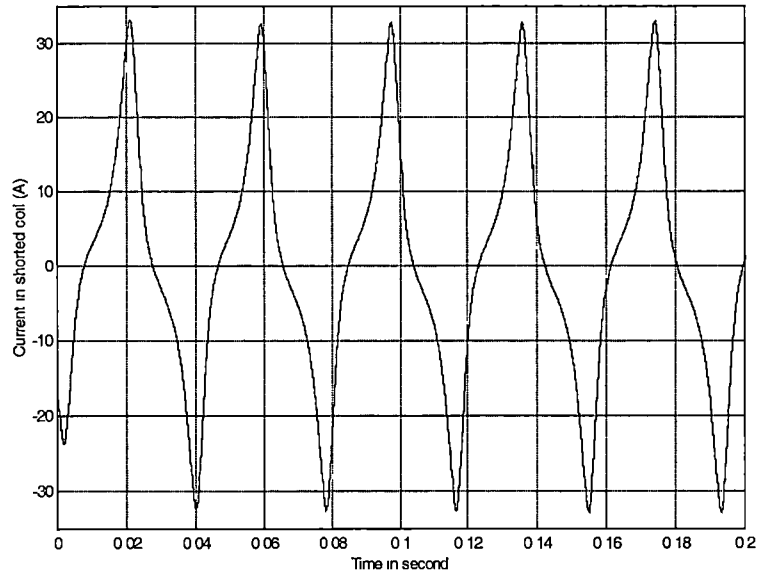

Figure 6.35: Simulated current waveform in the shorted armature coil.

It is expected that a very large alternative current flow in the shorted coil. Figure 6.35 shows that the simulated current is 34A peak to peak and the fundamental component is the speed frequency. Its amplitude is dependent on the rotor speed only, not on the value of the load current.

	Armature current (good armature)		Armature current (with shorted armature coil)		Field current (good armature)		Field current (with shorted armature coil)	
	Hz	dB	Hz	dB	Hz	dB	Hz	dB
f_r	26.2	-39.3	26.2	-14.3	26.2	-28.4	26.2	-15.5
$2f_r$	52.8	-24.8	52.8	17.3	52.8	-27.1	52.8	14.3
$3f_r$	78.8	-39.2	78.8	-14.3	78.8	-30.0	78.8	-13.9
$4f_r$	104.5	-20.0	104.5	14.8	104.5	-21.0	104.5	8.4
$5f_r$	131.0	-38.5	131.0	-18.5	131.0	-28.5	131.0	-9.9
$6f_r$	157.0	-26.1	157.0	9.6	157.0	-28.3	157.0	5.0
$7f_r$	183.2	-38.1	183.2	-20.6	183.2	-27.5	183.2	-13.0
$8f_r$	209.2	-25.8	209.2	3.0	209.2	-19.0	209.2	-4.2
$9f_r$	235.6	-41.2	235.6	-15.2	235.6	-27.4	235.6	-8.8
$16f_r$	418.3	0	418.3	0	418.3	-0.9	418.3	7.2
$48f_r$	1255	-10.7	1255	6.8	1255	0	1255	0

Table 6.9: Simulation results of armature and field current spectrum of Davey machine

As the only measurement result of the Davey machine with a shorted armature coil is when the motor was run at 485rpm, another simulation was run with the same assigned motor speed. A step size of 0.25 mechanical degree (1440 samples per revolution, 11664Hz) was used to satisfactory simulate operation of the machine.

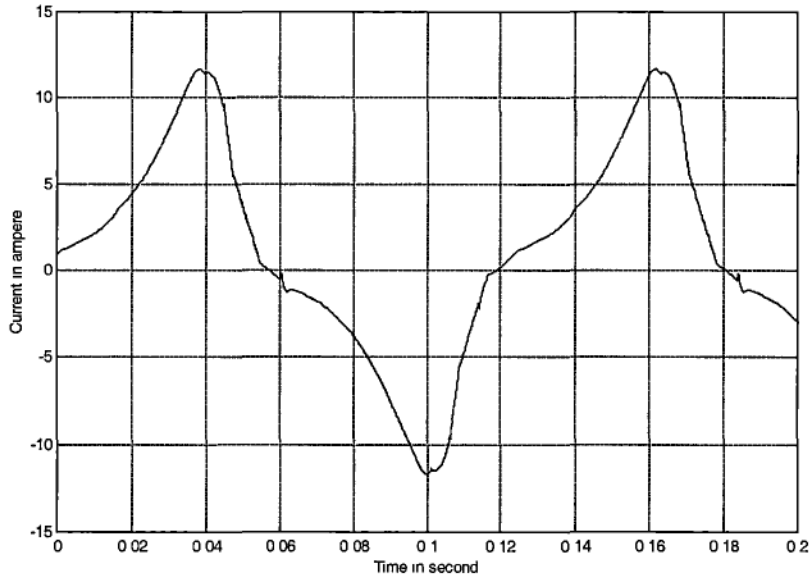

Figure 6.36: Simulated current waveform in the shorted armature coil of the Davey machine running at 485rpm

Figure 6.36 shows the simulated current waveform in the shorted armature coil. The peak to peak value of this waveform is about one third of the full speed case as only one third of the speed was assigned in this simulation. No corresponding measurement result is available for comparison because there was no way of getting at the shorted coil. A Hall plate was used to get an estimate of the shorted coil current.

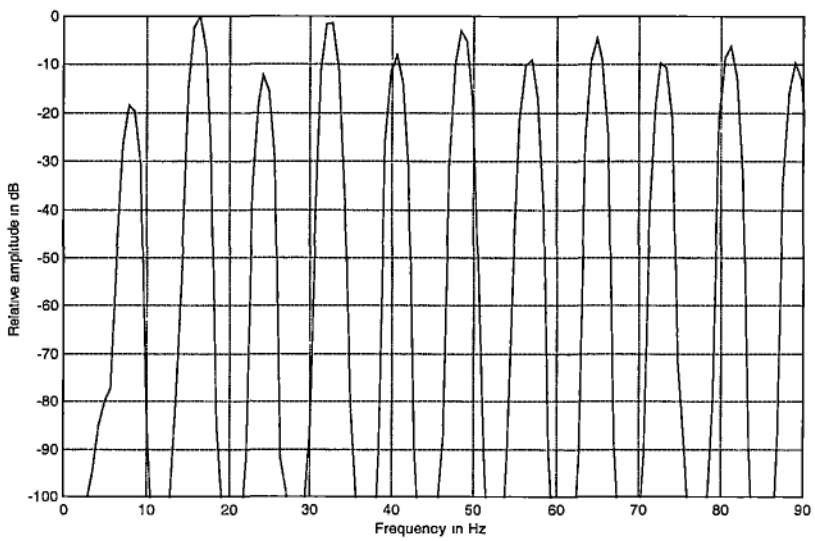

Figure 6.37: Spectrum of the derivative of armature current of Davey machine with short-circuit armature coil running at 485 rpm (simulation result)

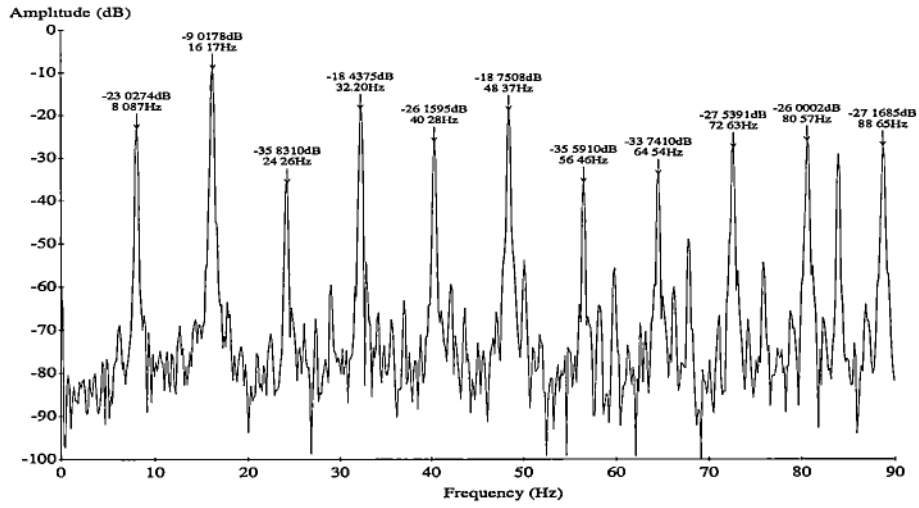

Figure 6.38: Spectrum of the derivative of armature current of Davey machine with short-circuit armature coil running at 485 rpm (measurement result)

Figure 3.37 shows the simulated armature current spectrum at 485rpm. 16384 samples were used for the spectrum analysis, ie the resolution is 0.7Hz, which is a lot worse than the resolution from measurement, 0.15Hz. Thus the peaks of the simulation are a lot wider that those from measurement.

Figures 6.39 and 6.40 show the corresponding field current spectra, from simulation and measurement. The zero dB frequency components of the spectra obtained from measurement is the 300Hz rectifier ripple.

In order to make a comparison between the simulation and measurement results, the $16f_r$ component is used as zero dB frequency of the components in the measured and simulated armature and field current spectrum. The relative amplitude of the components up to 90Hz is shown in table 6.10.

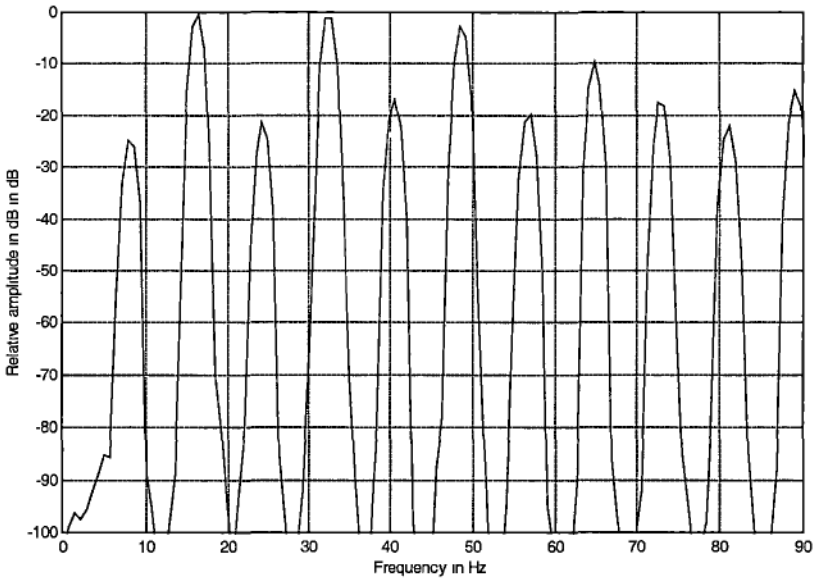

Figure 6.39: Spectrum of the derivative of field current of Davey machine with short-circuit armature coil running at 485 rpm (simulation result)

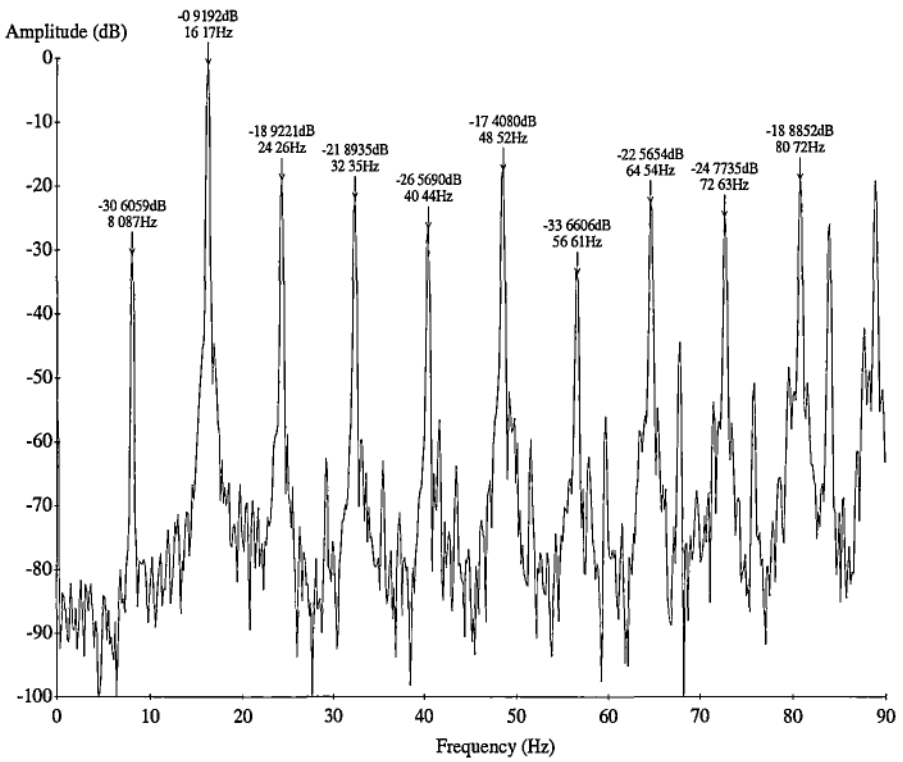

Figure 6.40: Spectrum of the derivative of field current of Davey machine with short-circuit armature coil running at 485 rpm (measurement result)

Simulation result of the armature spectrum shows that the f_r and $2f_r$ components have the same amplitude level as the corresponding components in measurement. The rest of the components have rather higher relative amplitude than those from measurement. Similar pattern can be noticed in the field current spectra, but has a relatively lower relative amplitude in the simulation.

The discrepancy of f_r and $2f_r$ harmonics amplitude between simulation and measurement armature spectrum may be due to the slot opening effect and the sparking occurred at the trailing brush tip. The accuracy of the self-inductance variation of armature coil and the assumption of different voltage drop across the positive and negative brush is also important as the f_r and $2f_r$ harmonics are caused by these variations.

	Armature current (measurements)		Armature current (simulation)		Field current (measurement)		Field current (simulation)	
	Hz	dB	Hz	dB	Hz	dB	Hz	dB
f_r	8.08	-17.0	8.1	-15.5	8.08	-18.4	8.1	25.1
$2f_r$	16.2	-3.0	16.2	3.0	16.2	11.3	16.2	-0.5
$3f_r$	24.3	-29.8	24.3	-9.3	24.3	-6.7	24.3	-21.5
$4f_r$	32.4	-26.2	32.4	1.5	32.4	-9.7	32.4	-1.0
$5f_r$	40.4	-20.2	40.5	-5.2	40.4	-14.4	40.5	-17.0
$6f_r$	48.5	-12.8	48.6	0.1	48.5	-5.2	48.6	-2.8
$7f_r$	56.6	-29.6	56.7	-5.9	56.6	-21.5	56.7	-20.0
$8f_r$	64.5	-27.4	64.8	-1.6	64.5	-10.4	64.8	-9.7
$9f_r$	72.6	-21.5	72.9	-6.8	72.6	-12.6	72.9	-17.5
$10f_r$	80.72	-20.0	81	-3.1	80.72	-6.7	81	-22.2
$16f_r$	128.9	0	129.6	0	128.9	0	129.6	0
$48f_r$	387.0	-25.2	388.8	0.6	387.0	6.0	388.8	-4.6
300Hz	300	6.0	-	-	300	12.2	-	-

Table 6.10: Simulation and measurement results of armature and field current spectrum of Davey machine with a shorted coil in armature running at 485rpm

6.8 Summary

This chapter has outlined the development of the models of the DC machine at steady state operation, which takes into account the physical arrangement of the field and armature coil windings. The model is based on the theory of magnetically coupled coils, and models the interaction of the field and armature magnetic fields that are formed by different coil combination, as the rotor rotates. The model was then modified so that the effects of open-circuit and short-circuit armature coils could be incorporated.

A computer implementation of the model was used to simulate a laboratory machine, both with and without an open-circuit armature and short-circuit coil. Since the measurement of the machine currents was obtained with Rogowski coil, only the derivative of the measurement results was available. The derivative of the simulated current waveforms was used to perform spectrum analysis. Since a pure DC was used for the field voltage, the resultant armature and field waveform contain multiples of speed frequency only.

An open-circuit armature coil was simulated by making one of the coil resistances very large. The amplitude of multiples of speed frequency of armature current increased when the fault occurred. The amplitude change of the even speed harmonics was higher than those measured from the test machine. The same pattern can be found in the field current spectrum but with lower amplitude change.

This was probably due to the non-linear behaviour of the positive and negative brush-commutator contact resistance that causes bar burning every time the faulty coil passes under the negative brush. This is reflected the armature current waveform with the significant amplitude change only on the number of brush pairs times speed frequency. For the field current, the effect of the defect on the armature circuit is low because of the nature of the design of the DC machine that is a low coupling factor between the field and armature circuit.

When the armature contains a shorted coil, an alternating emf is induced in the local closed circuit, so that current is limited solely by the impedance of the shorted coil. The heavy local current very often results in the burnout of the coil.

Regarding the effect of the shorted armature coil on armature and field current spectrum, the relative amplitude of speed frequency and its multiples in armature current increases significantly. Similar results can be obtained from field current, but with relatively lower increase in amplitude. Hence, it can be concluded that for the detection of open-circuit or short-circuit armature coil, the armature current can provide more useful information of the armature condition than can the field current.

Chapter 7

Summary and Future Work

This thesis has examined a variety of topics concerning the detection of defects in squirrel-cage induction motors and DC motors.

Firstly, induction motors. The thesis concentrates on rotor defects of squirrel-cage induction motors, which often occur in the form of cracking at the end-ring. Such defects can be detected by monitoring the double slip-frequency sideband of the stator current when the motor is under load. There has been significant research world-wide on the detection of broken rotor bars in mains-supplied squirrel-cage induction motors. As the use of variable speed AC drives in industrial applications becomes more widespread, further exploration of this aspect is necessary. This thesis summarised the previous approach of using frequency spectrum analysis of stator current to detect broken rotor bars in a squirrel-cage induction motor controlled by a variable frequency drive.

This thesis also describes an alternative non-invasive technique that computes the instantaneous value of the input power, and looks for distinctive frequencies in the waveform of the power. Shorted turns in the stator winding and broken rotor bar were introduced in a laboratory motor and an attempt was made to identify these faults through monitoring electrical power in PWM drives. In order to investigate the

effects of change in drive output frequency and different load conditions on the relative amplitude of frequency components in power, an experimental approach was taken. The AEI motor was run at different frequencies and different load supplied by the Renold drive and Zener drive (Appendix A).

Secondly, DC motors. The second half of this thesis concentrates on a current monitoring technique for DC motors. An attempt was made to detect poor commutation, and rotor defects such as open-circuit and short-circuit armature coils of laboratory DC motors. In addition, two mathematical models were developed to allow the numerical simulation of DC motors with open-circuit and short-circuit armature coils under steady state conditions.

The remainder of this chapter is a summary of the main points achieved in this study. Conclusions, possible extensions and areas of improvement that could be further investigated are also outlined.

7.1 Summary of Work

7.1.1 Stator Current Monitoring of Induction Motors

Chapter 2 is a literature survey of the possible faults and various condition monitoring techniques for induction motors. Particular interest was shown in an attempt to detect rolling-element bearing fault of induction motors by using spectrum analysis of stator current and comparing it to vibration analysis.

Chapter 3 gives the theory of the magnetic field harmonics in the air gap of an induction motor by Cameron [48]. It takes into account the effects of slotting, saturation, and rotor eccentricities, and predicts extra frequencies that could appear in the stator current as a result. The effect of a broken rotor bar on the frequency components caused by rotor slotting and eccentricity is discussed. The predictions by Thomson [16,18] and Kliman [76] of the number of broken rotor bars are applied to experimental results from a laboratory motor with deliberately cut rotor bars, with both mains and variable frequency supply. The difficulties of fault-related frequency identification for induction motors with variable supply frequency are also addressed.

Problems associated with previous attempts to detect broken rotor bars with varying supply frequency are discussed and summarised.

These are the conclusions for stator current monitoring of induction motors (fixed supply frequency):

- On-site monitoring tests showed that it is not possible to detect the early stage of a fault in a rolling-element bearing in induction motors using current monitoring, due to the very low amplitude of the mechanical displacement caused by the bearing faults.

- The main fault frequencies that appear in the stator current spectrum due to broken rotor bars are the double slip-frequency sidebands, resulting from the modulation of the supply frequency. The layout of the stator winding, (distribution factors and coil span factors), will have a very significant effect on which frequencies will actually appear in the current.

- Another distinct feature of the spectrum of a damaged rotor is the appearance of double slip-frequency sidebands centred on the $f_s \pm f_r$ components, the time harmonics, and the slot harmonics (f_s is the supply frequency and f_r is the speed frequency).

- The prediction of the number of broken rotor bar from both Thomson [16-18] and Kliman [76] shows moderate agreement with test results.

7.1.2 Monitoring of Instantaneous Input Power of Induction Motors

Chapter 4 describes a method to detect both shorted coils in the stator winding, and broken rotor bars, from instantaneous input power of the motor, which is computed from measurement of two line-to-line voltages and two line currents. Spectrum analysis identifies the fault-related components. Such a method will still work when the supply changes, and is therefore very useful for VSD, especially as there are no other satisfactory techniques. It was first tried out on a motor with a deliberately damaged rotor, supplied at 50Hz, and gave good results. Later experimental results showed that the frequency spectrum of the power provides almost the same clarity of information of rotor condition at variable frequency operation as at fixed frequency.

The laboratory studies examined two PWM variable frequency drives and one motor. The effect of different frequency and load conditions on fault-related frequency of power was studied. As experimental results were only based on one motor and two drives, general conclusions must be tentative. However, the following features were discovered from laboratory tests:

For a shorted coil in the stator winding:

- There is a very high current induced in the shorted coil, which is independent of the motor load.

- It produces $(5+s)f_s/3$ and $(7-s)f_s/3$ components and increase the amplitude of the twice supply frequency component in the power, where s is the per unit slip. However, the sensitivity of using $2f_s$ component to detect such fault is dependent on the harmonic content of the supply. The $2f_s$ component caused by the fault can not be distinguished when it is less than the $2f_s$ caused by the harmonics from the supply.

For broken rotor bars:

- The main fault frequencies that appear in the power are the double slip-frequency and its multiples. It has the largest change in relative amplitude when the rotor is damaged.

- The trend of $\pm 2nf_s$ (where n is an integer) sidebands of f_r, $2f_r$, $2nf_s$ and time harmonics are also indicated rotor faults.

- These components are all more than 60dB down from the DC power and are either too low in amplitude or too close together when the load decreases.

7.1.3 Current Monitoring of DC Motors

Chapter 5 outlines the problems caused by poor commutation of DC motors and methods for measurement of the sparking level and fault identification. At present, on-line visual observation of sparking is most widely used in industry to assess the condition of DC motors. For suspected winding defects, off-line tests must be used.

This chapter describes experimental studies of the effect of incorrect interpole strength and armature defects, such as open- and short-circuit armature coils, on armature and field current of DC motors. In order to monitor the DC motor currents, an air-cored "Rogowski" coil was developed.

For incorrect interpole strength, significant change in amplitude of the commutator segment frequency and its multiples of speed frequency sidebands in the armature and field current can indicate this defect.

For rotor defects, such as open-circuit or short-circuit armature coil, significant increase in amplitude of the speed frequency (and its multiples) in armature current indicates the defects. The largest amplitude component is the (number of pole-pair) times (speed frequency).

Chapter 6 describes a mathematical model of the DC motor based on magnetically coupled coils. A computer solution of the model equations predicted the steady speed field and armature current waveforms of a particular ½ HP DC motor, both with and without armature defects. As the measurements were obtained by using the Rogowski coil, the derivative of the computed current waveforms was used for spectrum analysis in order to compare them with measurements.

The measurement and simulation results showed that the average value of the armature current dropped to two third of the normal value due to an open-circuit coil in armature. The amplitude change of the even speed harmonics of the simulated armature current was higher than the measurement results. This is due to the non-linear behaviour of the positive and negative brush-commutator contact resistance.

The steady state model was modified to incorporate a shorted-circuit armature coil. Simulation results show that a large current is induced in the shorted coil. The relative amplitude level of the components in simulation is in general higher than measurement. It may due to unfortunate choice in the simulation of zero dB for the slot frequency (or its multiples). These components resulted from the non-linear resistance between the brush and commutator segment. It also showed that frequency spectrum analysis of armature current can provide more useful information of armature circuit condition than field current.

7.2 Future Extensions

7.2.1 Broken Rotor Bar Detection of Induction Motors with Varying Supply Frequency

This thesis has provided some theoretical and experimental studies on the detection of broken rotor bars in an induction motor with varying supply frequency. This information could be used as the basis for implementing a condition monitoring system.

The idea of input power analysis is to detect the double slip-frequency component in the input power, which results from modulation of current waveform by the voltage. It means that the double slip-frequency component in power is the envelope component in the stator current waveform. Hence, envelope analysis on the stator current waveform may give useful information of rotor condition when the motor frequency varies. It only requires one current measurement, instead of the two currents and two voltages needed for power.

7.2.2 Power Monitoring of Induction Motors

A new method of measurement of the frequency spectrum of power was introduced but, the experimental results were limited to only one laboratory motor and two VSDs. In order to get a better understanding of the phenomena, measurement results are needed from a large range of variable speed induction motor drives, to develop a data base. Statistical methods may be applied to divide the motors into sub groups based on the standard measurement results of the current spectrum. This research work certainly needs support from industry.

7.2.3 Current Monitoring of DC Motors

This thesis covers the first stage of applying modern condition monitoring techniques to DC motors. Experiment together with mathematical modelling of the DC motor, have demonstrated the practicability of current monitoring of DC motors. Frequency spectrum analysis of armature and field current should be applied to assess how well a DC motor is commutating by comparison with the conventional 'black-band' test.

Major extensions to the numerical modelling, could be:

- to model the inter-pole windings (where fitted) in order to give a better understanding of the effect of over- or under-commutation on the current spectrum.

- to model inter-turn shorts in field winding.

- the influence of load conditions on different defects.

As the fault-related frequency in the armature and field current spectrum is speed-related, improved signal analysis techniques will be required for DC drives that change speed rapidly. A transient model of the DC motor will be needed to study the implications that such drives have for detection of the defects.

7.2.3 Artificial Intelligence

Although thermal and vibration monitoring have been utilised for decades, most recent research has been directed towards monitoring of motor current. All of the present techniques require the user to have some degree of expertise in order to distinguish a normal operating condition from a potential failure mode. For example, the frequency spectrum of the stator current of an induction motor with a broken rotor bar contains a very large range of frequency components, especially when it is supplied by a variable frequency drive. This is due to both the construction and design of the motor, the drive and the variation in the driven load. In general, a maintenance expert is necessary to analyse the on-line measurements. The trend of condition monitoring, in widely varying applications, is to automate the analysis of the data collected by incorporating expert systems [133-137] or neural networks [138-139] into the on-line measurement systems. The future of condition monitoring systems certainly lies in this direction.

Appendix A

Laboratory Equipment

A1 Induction Motors

A1.1 The Pope Motor

The main induction motor used for laboratory experiments was manufactured by Pope Electric Motors Australia Pty. Ltd. This motor had three different rotors available for it: the original, one was damaged by milling through the junction between one rotor bar and an end-ring, and one had two adjacent damaged rotor bars. The specifications of the motor is as follows:

- 415V, 50Hz, 3 phase, 4 pole
- Rated output 7.5kW
- Rated current 14.1A.
- Rated speed 1455 rpm
- Rated power factor 0.86
- Moment of inertia 0.040 kgm^2

Design details:

- 36-slot stator, delta-connected concentric winding, three coils per group, 75 turns per coil.
- 32 slot rotor, cast aluminium cage.

A1.2 The AEI Motor

The other two identical induction motors used for laboratory experiments were manufactured by Australian Electric Industry Ltd. One of them had a rotor that damaged by milling through the junction between one rotor bar and an end-ring. The specifications of the motors is as follows:

- 415V, 50Hz, 3 phase, 6 pole
- Rated output 4.5kW
- Rated current 7.5A.
- Rated speed 955 rpm
- Rated power factor 0.86

Design details:

- 48-slot stator, delta connected winding. Two and two thirds coils per coil.
- 57-slot rotor, cast aluminium cage.

A2 DC Motors

Three motors were used for laboratory experiments.

A2.1 Motor 45 (M45)

This motor was manufactured by Crompton Parkinson Ltd. It has separate terminals for the interpole winding. The motor has the following specifications:

- Rated output 2.9HP

- Rated current 25A
- Rated armature voltage 110V
- Rated field current 2A
- Rated field voltage 110V
- Rated speed 1400 rpm

Design details:

- 4-pole with 28 slots and 83 segments lap-winding armature.

A2.2 Motor 87 (M87)

The motor has the following specifications:

- Rated output 5kW
- Rated current 10A
- Rated armature voltage 500V
- Rated field current 1.5A
- Rated field voltage 250V
- Rated speed 1500 rpm

Design details:

- 4-pole with 39 slots and 117 segments wave-winding armature.

A2.3 Davey DC Motor

This motor was manufactured by F.W. Davey & Co. Pty Ltd, Melbourne, Australia. The motor has the following specifications:

- Rated output 0.5HP
- Rated current 2A

- Rated armature voltage 180V
- Rated field current 0.2A
- Rated field voltage 220V
- Rated speed 1500 rpm

Design details:

- 2-pole with 16 slots and 48 segments simplex-lap winding armature,
- three subcoils per slot, 17 turns per sub coil, 7 slots pole pitch,
- brush surface area 14.15×6.95 mm, commutator diameter 51.62mm

Measurement values:

- Self inductance of the field 284H
- Field resistance 1100Ω
- Mutual inductance of armature 3.75H
- Self inductance of a sub coil 5.7mH(min), 15.6mH(max)
- Sub coil resistance 0.34Ω

A3 Variable Speed Drives

A3.1 VSC 2000 Zener Drive

The main variable speed AC drive that was used in the experiments was VSC 2000 Zener Drive.

- Model VSC-2G27
- Output voltage: 346/480 Vac, three-phase, 50/60Hz.
- Output current: 27A cont., 29.7A int.

A3.2 Renold VFD Drive

This drive was manufactured by Renold Australia PTY. LTD.

- Output voltage: 380/415 V, 50/60Hz.
- Rated output: 5.5kVA, 80/(160/320) Hz, 8A.
- AC motor 3.7kW (max)

A3.3 ABB Drive

This drive was a SAMI GS drive manufactured by ABB StrömbergDrives Oy, Finland.

- Model Acs501-020-3
- Rated output 20kVA

A4 Current Clamps

Four types of current clamp were used to sample the motor current waveform of induction motors and DC motors.

A4.1 Fluke Current Clamp

This is a Hall-effect type, clip-on multimeter, made by Fluke Inc. It has an amplifier located in the handles, and it is all enclosed in a plastic case without any shielding.

- Model 80I-1010
- Current Range 1-1000A DC, or 1-700A AC
- Frequency range DC to 440Hz
- Output 1mV per ampere
- Uncertainty 2-5% depending on current

A4.2 FCC Current Clamp

This is a RF, fully shielded, wound transformer, manufactured by Fischer Custom Communication Inc.

- Model F-14-1
- Frequency response :flat from 10Hz to 400kHz with 50Ω terminator
- Phase error 25 degrees at 50Hz

A4.3 Split-core Current Transformers

These were designed by Mr. R. A. Langman and manufactured by the technical support group in the Electrical Engineering Department of the University of Tasmania. One model covered the current range 16 to 80 amp; the other the range 80 to 400 amp.

The design philosophy differed somewhat from a conventional current transformer, which has a low as possible secondary resistance in order that the ratio and phase errors are minimised. In fact, this was the guideline followed for initial designs of split core CT. However, the variable frequency drives caused massive interference spikes of voltage into the data acquisition system, which were at least an order amplitude greater than the voltage we really wanted. Many techniques of shielding against this interference were tried (the interference was from a combination of electrostatic and electromagnetic causes) but in the end, the most effective technique was to increase the secondary load resistance of the CT in order to get several volts ($\leq$ 10 volt peak to peak) rather than a few hundred milli volts into the data acquisition card.

The CT for 16 to 80A is described here in more detail. It consists of lines U-cores of silicon iron laminations, of core cross section 17mm×43mm. The central hole was 20mm×58mm. One of the cores carried two windings, one on each leg of the U, each of 200 turns of 0.5mm diameter enamelled copper wire. The other U core had no winding on it, leaving plenty of room for the primary cable.

Secondary winding resistance was about 4.2Ω. Load resistance was 27Ω, which gave 5.4V RMS for a primary current of 80amp. The "calibration" of the CT was then adjusted to 3V RMS (8.5V peak to peak) by a voltage divider of two resistors in parallel with the 27Ω (the data acquisition system accepted a maximum of ±5V). Use of the low power resistance divider meant that the output voltage could be conveniently adjusted without altering the main secondary resistor, which was a fairly bully 5-watt rating.

The CT was completed with a BVC socket attached to a plate that was glued onto one side of the U core. The cores were held together by a clip and spring arrangement.

The frequency response, defined as output voltage divided by primary current, was constant (to within 1 %), from 10Hz to 2kHz. However, the phase error was large, 3.6 degrees for 80A at 50Hz. This was an unavoidable result of the split core (that gave an effective permeability of only about 4000).

- Current range 16 - 80A
- Frequency response flat from 10Hz to 2kHz
- Output 3V for 80A
- Phase error 3.6 degrees for 80A at 50Hz, increasing to 15 degrees at 10Hz

A4.4 Split-core Rogowski Coil

It was designed by Mr. R. A. Langman and manufactured by the technical support group in the Electrical Engineering Department of the University of Tasmania. It consists of about 16,000 turns, of mean diameter 15 mm wound on 8 separate bobbins assembled in a ring pattern of about 80mm diameter. The bobbin assembly was encapsulated inside an aluminium housing that was then cut across a diameter. The two halves were electrically connected by a short piece of coaxial cable, and clipped together by a toggle. The inside diameter was 40mm, which allowed it to be put over the largest cable encountered in DC motors in industry.

- Current range: unlimited

- Frequency response greater than 10kHz
- Output: 0.11mV / ampere / Hz

A5 Data Acquisition System

The data acquisition system consisted of a 486 PC, with a Boston Technology PC 30D data acquisition card. A separate instrument contained instrumentation amplifiers, low-pass filters and sample-and-hold amplifiers. The current transducers described in section B4 were used to measure the motor current. A three-phase opto-isolator unit was used to measure two line-to-line voltages and provide complete isolation at the same time. It was designed by Glenn Mayhew of technical support unit and has the input / output relationship $V_{in} = \pm 600V \Rightarrow V_{out} = \pm 5V$, DC to 100kHz.

The four-channel instrumentation amplifier has five different gain settings, 1, 3, 10, 30 and 100, to suit different signal level. Two four-channel six-pole low-pass filters are available with corner frequency at 2000Hz. The fast-four-channel sample-and-hold amplifier is triggered externally by the A/D strobes generated from the PC 30D data acquisition card. All four circuits are contained in one box, and the inputs and outputs of all circuits are connected to RCA sockets mounted at the front panel. This design provides high flexibility in the use of the circuits, low-pass-filter and sample-and-hold circuit.

Appendix B

Voltage Equations of the Davey Machine Equivalent Circuits

B1 Voltage Equations of 7-coil Equivalent Circuit

From figure B1, the current equations of the 7-coil equivalent circuit are

$$i_{p1} = i_{cp1} - i_{s1} \tag{B1}$$

$$i_{p2} = i_{cp2} - i_{cp1} \tag{B2}$$

$$i_{p3} = i_{s2} - i_{cp2} \tag{B3}$$

$$i_{n1} = i_{s2} - i_{cn1} \tag{B4}$$

$$i_{n2} = i_{cn1} - i_{cn2} \tag{B5}$$

$$i_{n3} = i_{cn2} - i_{s1} \tag{B6}$$

$$i_a = i_{p1} + i_{p2} + i_{p3} = i_{n1} + i_{n2} + i_{n3} = i_{s2} - i_{s1} \tag{B7}$$

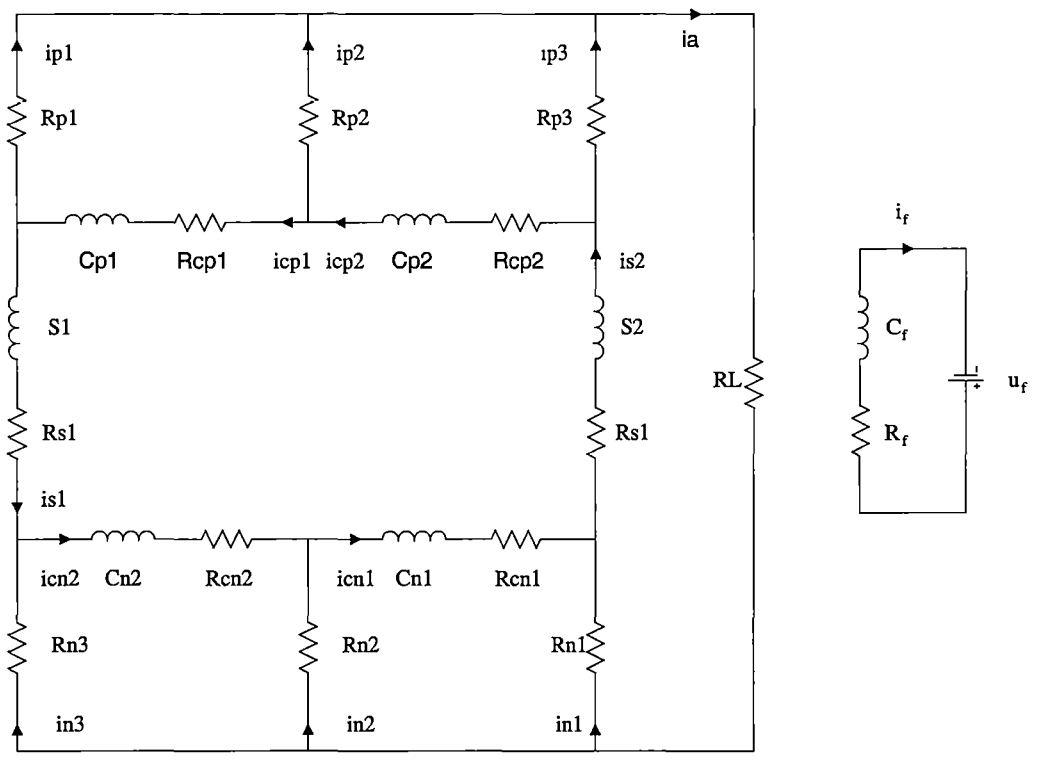

Figure B1: The 7-coil equivalent circuit of the Davey machine

The voltage equations are

$$\text{For coil } C_{p1}: U_{cp1} = i_{cp1} \cdot R_{cp1} + \dot{\lambda}_{cp1} = i_{p2} \cdot R_{p2} - i_{p1} \cdot R_{p1} \quad \text{(B8)}$$

$$\text{For coil } C_{p2}: U_{cp2} = i_{cp2} \cdot R_{cp2} + \dot{\lambda}_{cp2} = i_{p3} \cdot R_{p3} - i_{p2} \cdot R_{p2} \quad \text{(B9)}$$

$$\text{For coil } C_{s2}: i_{s2} \cdot R_{s2} + \dot{\lambda}_{s2} + i_{p3} \cdot R_{p3} + i_{n1} \cdot R_{n1} + i_a R_L = 0 \quad \text{(B10)}$$

$$\text{For coil } C_{n1}: U_{cn1} = i_{cn1} \cdot R_{cn1} + \dot{\lambda}_{cn1} = i_{n1} \cdot R_{n1} - i_{n2} \cdot R_{n2} \quad \text{(B11)}$$

$$\text{For coil } C_{n2}: U_{cn2} = i_{cn2} \cdot R_{cn2} + \dot{\lambda}_{cn2} = i_{n2} \cdot R_{n2} - i_{n3} \cdot R_{n3} \quad \text{(B12)}$$

$$\text{For coil } C_{s1}: i_{s1} \cdot R_{s1} + \dot{\lambda}_{s2} - i_{p1} \cdot R_{p1} - i_{p3} \cdot R_{p3} - i_a R_L = 0 \quad \text{(B13)}$$

Substitute equations (B1) to (B7) into (B8) to (B13) gives

$$\left(R_{cp1}+R_{p1}+R_{p2}\right)i_{cp1}-R_{p2}\cdot i_{cp2}-R_{p1}\cdot i_{s1}+\dot{\lambda}_{cp1}=0 \tag{B14}$$

$$-R_{p2}i_{cp1}+\left(R_{cp2}+R_{p2}+R_{p3}\right)i_{cp2}-R_{p3}\cdot i_{s2}+\dot{\lambda}_{cp2}=0 \tag{B15}$$

$$-R_{p3}i_{cp2}+\left(R_{s2}+R_{p3}+R_{n1}+R_{L}\right)i_{s2}-R_{n1}\cdot i_{cn1}-R_{L}\cdot i_{s1}+\dot{\lambda}_{s2}=0 \tag{B16}$$

$$-R_{n1}i_{s2}+\left(R_{cn1}+R_{n1}+R_{n2}\right)i_{cn1}-R_{n2}\cdot i_{cn2}+\dot{\lambda}_{cn1}=0 \tag{B17}$$

$$-R_{n3}i_{s1}-R_{n2}i_{cn1}+\left(R_{cn2}+R_{n2}+R_{n3}\right)i_{cn2}+\dot{\lambda}_{cn2}=0 \tag{B18}$$

$$-R_{p1}i_{cp1}+\left(R_{s1}+R_{p1}+R_{n3}+R_{L}\right)i_{s1}-R_{n3}\cdot i_{cn2}-R_{L}\cdot i_{s2}+\dot{\lambda}_{s2}=0 \tag{B19}$$

$$R_f i_f+\dot{\lambda}_f=U_f \tag{B20}$$

Seven differential equations (B14) to (B20) can be rewritten in matrix form as $\mathbf{v}=\mathbf{Ri}+\mathbf{i}\frac{d\mathbf{L}}{dt}+\mathbf{L}\frac{d\mathbf{i}}{dt}$, where $\lambda=\mathbf{Li}$, $\dot{\lambda}=\mathbf{i}\frac{d\mathbf{L}}{dt}+\mathbf{L}\frac{d\mathbf{i}}{dt}$,

$$\mathbf{v}=\left[U_f\ 0\ 0\ 0\ 0\ 0\ 0\right]^T; \tag{B21}$$

$$\mathbf{i}=\left[i_f\ i_{cp1}\ i_{cp2}\ i_{s2}\ i_{cn1}\ i_{cn2}\ i_{s1}\right]^T \tag{b22}$$

$\mathbf{R}=$

$$\begin{bmatrix}
R_f & 0 & 0 & 0 & 0 & 0 & 0 \\
0 & R_{cp1}+R_{p1}+R_{p2} & -R_{p2} & 0 & 0 & 0 & -R_{p1} \\
0 & -R_{p2} & R_{cp2}+R_{p2}+R_{p3} & -R_{p3} & 0 & 0 & 0 \\
0 & 0 & -R_{p3} & R_{s2}+R_{p3}+R_{n1}+R_L & -R_{n1} & 0 & -R_L \\
0 & 0 & 0 & -R_{n1} & R_{cn1}+R_{n1}+R_{n2} & -R_{n2} & 0 \\
0 & 0 & 0 & 0 & -R_{n2} & R_{cn2}+R_{n2}+R_{n3} & -R_{n3} \\
0 & -R_{p1} & 0 & -R_L & 0 & -R_{n3} & R_{s1}+R_{p1}+R_{n3}+R_L
\end{bmatrix} \tag{B23}$$

$$\mathbf{L} = \begin{bmatrix} L_{ff} & M_{f\_cp1} & M_{f\_cp2} & M_{f\_s2} & M_{f\_cn1} & M_{f\_cn2} & M_{f\_s1} \\ M_{cp1\_f} & L_{cp1} & m_{cp1\_cp2} & m_{cp1\_s2} & m_{cp1\_cn1} & m_{cp1\_cn2} & m_{cp1\_s1} \\ M_{cp2\_f} & m_{cp2\_cp1} & L_{cp2} & m_{cp2\_s2} & m_{cp2\_cn1} & m_{cp2\_cn2} & m_{cp2\_s1} \\ M_{s2\_f} & m_{s2\_cp1} & m_{s2\_cp2} & L_{s2} & m_{s2\_cn1} & m_{s2\_cn2} & m_{s2\_s1} \\ M_{cn1\_f} & m_{cn1\_cp1} & m_{cn1\_cp2} & m_{cn1\_s2} & L_{cn1} & m_{cn1\_cn2} & m_{cp1\_s1} \\ M_{cn2\_f} & m_{cn2\_cp1} & m_{cn2\_cp2} & m_{cn2\_s2} & m_{cn2\_cn1} & L_{cn2} & m_{cn2\_s1} \\ M_{s1\_f} & m_{s1\_cp1} & m_{s1\_cp2} & m_{s1\_s2} & m_{s1\_cn1} & m_{s1\_cn2} & L_{s1} \end{bmatrix} \quad \text{(B24)}$$

B2 Voltage Equations of 5-coil Equivalent Circuit

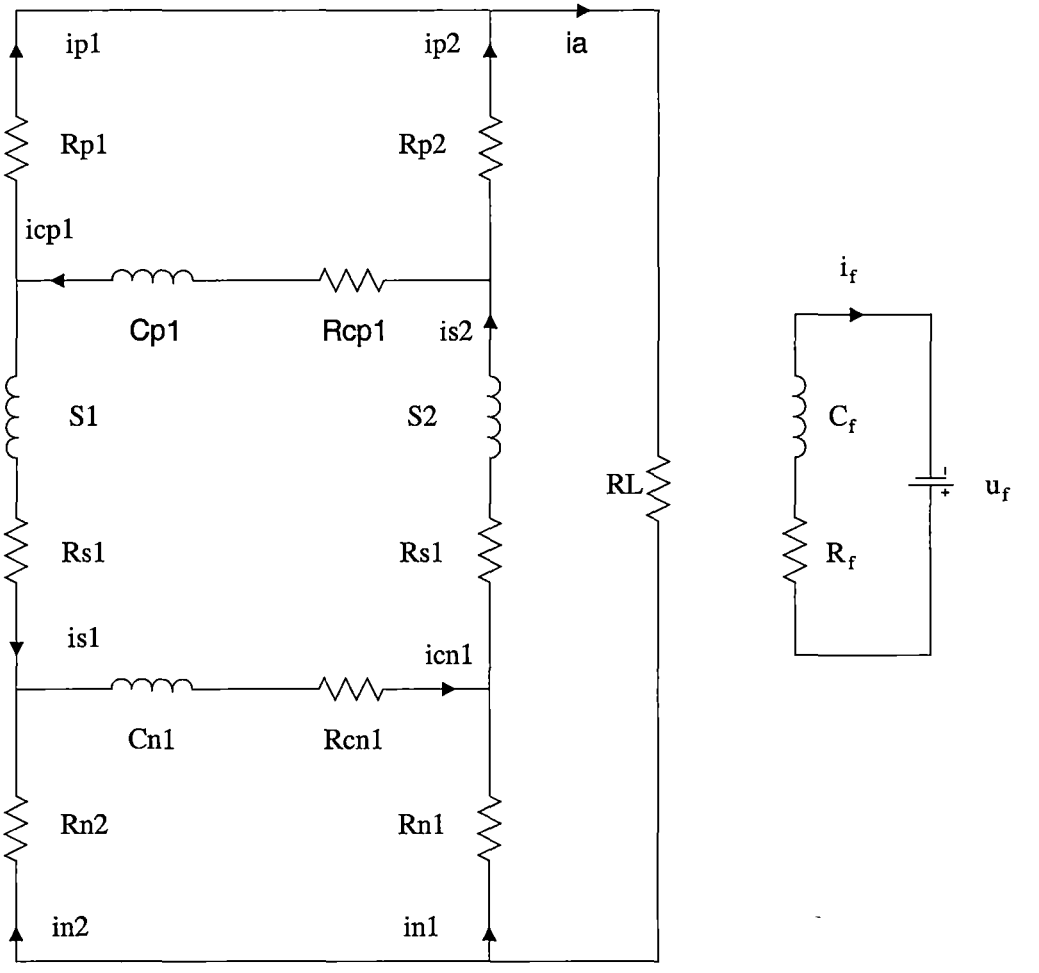

Figure B2: The 5-coil equivalent circuit of the Davey machine

The current equations are

$$i_{p1} = i_{cp1} - i_{s1} \tag{B25}$$

$$i_{p2} = i_{s2} - i_{cp1} \tag{B26}$$

$$i_{n1} = i_{s2} - i_{cn1} \tag{B27}$$

$$i_{n2} = i_{cn1} - i_{s1} \tag{B28}$$

$$i_a = i_{p1} + i_{p2} = i_{n1} + i_{n2} = i_{s2} - i_{s1} \tag{B29}$$

The voltage equations are

$$\text{For coil } C_{p1} : U_{cp1} = i_{cp1} \cdot R_{cp1} + \dot{\lambda}_{cp1} = i_{p2} \cdot R_{p2} - i_{p1} \cdot R_{p1} \tag{B30}$$

$$\text{For coil } C_{s2} : i_{s2} \cdot R_{s2} + \dot{\lambda}_{s2} + i_{p2} \cdot R_{p2} + i_{n1} \cdot R_{n1} + i_a R_L = 0 \tag{B31}$$

$$\text{For coil } C_{n1} : U_{cn1} = i_{cn1} \cdot R_{cn1} + \dot{\lambda}_{cn1} = i_{n1} \cdot R_{n1} - i_{n2} \cdot R_{n2} \tag{B32}$$

$$\text{For coil } C_{s1} : i_{s1} \cdot R_{s1} + \dot{\lambda}_{s2} - i_{p1} \cdot R_{p1} - i_{n2} \cdot R_{n2} - i_a R_L = 0 \tag{B33}$$

Substitute equations (B25) to (B29) into (B30) to (B33) gives

$$\left(R_{cp1} + R_{p1} + R_{p2}\right) i_{cp1} - R_{p2} \cdot i_{cp2} - R_{p1} \cdot i_{s1} + \dot{\lambda}_{cp1} = 0 \tag{B34}$$

$$-R_{p2} i_{cp1} + \left(R_{s2} + R_{p2} + R_{n1} + R_L\right) i_{s2} - R_{n1} \cdot i_{cn1} - R_L \cdot i_{s1} + \dot{\lambda}_{s2} = 0 \tag{B35}$$

$$-R_{n1} i_{s2} + \left(R_{cn1} + R_{n1} + R_{n2}\right) i_{cn1} - R_{n2} \cdot i_{s1} + \dot{\lambda}_{cn1} = 0 \tag{B36}$$

$$-R_{p1} i_{cp1} + \left(R_{s1} + R_{p1} + R_{n2} + R_L\right) i_{s1} - R_{n2} \cdot i_{cn1} - R_L \cdot i_{s2} + \dot{\lambda}_{s2} = 0 \tag{B37}$$

$$R_f i_f + \dot{\lambda}_f = U_f \tag{B38}$$

Five differential equations (B34) to (B38) can be rewritten in matrix form as $\mathbf{v} = \mathbf{R}\mathbf{i} + \mathbf{i}\frac{d\mathbf{L}}{dt} + \mathbf{L}\frac{d\mathbf{i}}{dt}$, where $\lambda = \mathbf{L}\mathbf{i}$, $\dot{\lambda} = \mathbf{i}\frac{d\mathbf{L}}{dt} + \mathbf{L}\frac{d\mathbf{i}}{dt}$,

$$\mathbf{v} = \left[U_f \;\; 0 \;\; 0 \;\; 0 \;\; 0\right]^T; \tag{B39}$$

$$\mathbf{i} = \left[i_f \;\; i_{cp1} \;\; i_{s2} \;\; i_{cn1} \;\; i_{s1}\right]^T \tag{B40}$$

$$\mathbf{R} = \begin{bmatrix} R_f & 0 & 0 & 0 & 0 \\ 0 & R_{cp1}+R_{p1}+R_{p2} & -R_{p2} & 0 & -R_{p1} \\ 0 & -R_{p2} & R_{s2}+R_{p2}+R_{n1}+R_L & -R_{n1} & -R_L \\ 0 & 0 & -R_{n1} & R_{cn1}+R_{n1}+R_{n2} & -R_{n2} \\ 0 & -R_{p1} & -R_L & -R_{n2} & R_{s1}+R_{p1}+R_{n2}+R_L \end{bmatrix} \tag{B41}$$

$$\mathbf{L} = \begin{bmatrix} L_{ff} & M_{f\_cp1} & M_{f\_s2} & M_{f\_cn1} & M_{f\_s1} \\ M_{cp1\_f} & L_{cp1} & m_{cp1\_s2} & m_{cp1\_cn1} & m_{cp1\_s1} \\ M_{s2\_f} & m_{s2\_cp1} & L_{s2} & m_{s2\_cn1} & m_{s2\_s1} \\ M_{cn1\_f} & m_{cn1\_cp1} & m_{cn1\_s2} & L_{cn1} & m_{cn1\_s1} \\ M_{s1\_f} & m_{s1\_cp1} & m_{s1\_s2} & m_{s1\_cn1} & L_{s1} \end{bmatrix} \tag{B42}$$

References

[1] Tavner P. J. and Penman J., " Condition monitoring of electrical machines", Research Studies Press Ltd., 1987

[2] Michael Neil and Associates, "A Guide to the Condition Monitoring of Machinery", Her Majesty's Stationery Office, London, 1979.

[3] Ray Beebe, "Machine Condition Monitoring", Engineering Publications, Australia, 1988.

[4] Thomson W. T., "Condition monitoring of induction motors for availability assessment in offshore installations", 4th Euredata Conference, March 1983.

[5] Werninck E. H., "Electric Motor Handbook.", McGraw-Hill, Great Britain, 1978.

[6] Stone G. C., Gupta B. K., and Kurtz M., "Investigation of turn insulation failure mechanisms in large AC motors", IEEE Transactions on Power Apparatus and System, Vol. PAS-103, No. 9, Sept., 1984, pp2588-2593.

[7] Leonard R. A., and Thomson W. T., "Vibration and stray flux monitoring for unbalanced supply and interturn diagnosis in induction motors", 1st UK International Conference, Condition Monitoring 84.

[8] Thomson W. T., and Leonard R. A., "Vibration and stray flux monitoring for electrical fault diagnosis in electrical machines", 1984 Advanced Maintenance Tech. and Diagnostic Tech. Conference, Inst. of Diagnostic Eng., London, Sept., 1984.

[9] Penman J., Dey M. N., Tait A. J. and Bryan W. E., "Condition monitoring of electrical drives", IEE Proceedings, Vol. 133, pt. B, No. 3, May, 1986, pp142-148.

[10] Sottile J. and Kohler J. L., "An on-line method to detect incipient failure of turn insulation in random wound motors", IEEE Transactions on Energy Conversion, Vol. 8, N0. 4 pp762-768, December 1993.

[11] Natarajan R., "Failure identification of induction motors by sensing unbalanced stator currents", IEEE Transactions on Energy Conversion, Vol. 4, No. 4, pp585-590, December 1989.

[12] Mbaye A., Bellomo J. P., Lebey T., Oraison J. M., and Peltier F., "Electrical stresses applied to stator insulation in low-voltage induction motors fed by PWM drives", IEE Proc. -Electrical. Power Application., Vol. 144, No. 3, May 1997, pp191-198.

[13] Thomson W. T., and Leonard R. A., "Monitoring strategy for discriminating between different types of rotor defects in induction motors", 18th UPEC Proc., University of Surrey, Guildford, UK, 1983, pp241-246.

[14] Thomson W. T., Leonard R. A., Milne A. J., and Penman J., "Failure identification of offshore induction motor systems using on-line condition monitoring", Proc. of 4th National Reliability Conference, Birmingham, UK, 1983, pp2c/3/1-2c/3/11.

[15] Thomson W. T., "Diagnosing faults in induction motors", Eng. Ideas, Elect. Rev., Vol. 215, No. 17, Nov. 1984.

[16] Thomson W. T., and Rankin D., "Case histories of rotor winding fault diagnosis in induction motors", 2nd Inter. Condition Monitoring Conference CM 87, University Coll Swansea, March 1987.

[17] Thomson W. T., "On-line diagnostics of large induction motors", NATO RAW, Catholic University of Leuven, 1986, Pub. in NATO Asi Series, Pub. "Martinus Hijhoff", 1988.

[18] Thomson W. T., "On-line current monitoring fault diagnosis in HV induction motors-case histories and coat saving in offshore installations", Offshore Europe 87 Conference, Sept. 1987, Aberdeen, Scotland.

[19] Thomson W. T., "An on-line computer based current monitoring system for rotor fault diagnosis in 3-phase induction motors", 3rd Inter. Turbomaching Conf., Oct. 1987, London.

[20] Thomson W. T., "On-line current monitoring and analysis to quantify the level of airgap eccentricity in induction motors", ICEM. 1988, Italy.

[21] Thomson W. T., and Chalmers S. J., "A new on-line computer based current monitoring system for expert system fault diagnosis of induction motors", 23rd Universities Power Eng. Conf., Trent Polytechnic, Sept 1988

[22] Innes A. G., "Condition Monitoring of Induction Motors: The Detection of Broken Rotor Bars in Variable Speed Induction Motor Drivers", PhD Thesis, University of Tasmania, Australia, 1996.

[23] IEEE Committee Report, "Report on reliability survey of industrial plants, part I: Reliability of electrical equipment", IEEE Transactions on Industry Applications, Vol. 10, No. 2, pp213-235, March/April 1974.

[24] Motor Reliability Working Group, "Report of large motor reliability survey of industrial and commercial installations, part I.", IEEE Transactions on Industry Applications, Vol. 21, No. 4, pp853-862, July/August 1985.

[25] Albrecht P. F., Owen E. L. and Sharma D. K., "Discussion on Report of large motor reliability survey of industrial and commercial installations, part I", IEEE Transactions on Industry Applications, Vol. 21, No. 4, pp862-864, July/August 1985.

[26] Thomson O. V. and Dalva M., "A survey of faults on induction motors in offshore oil industry, petrochemical industry, gas terminals, and oil refineries", IEEE Transactions on Industry Applications, Vol. 31, No. 5, pp1186-1196, September/October 1995.

[27] Bonnett A. H. and Soukup G. S., "Cause and analysis of stator and rotor failures in three-phase squirrel-cage induction motors.", Transactions on Industry Applications, Vol. 28, No. 4, pp921-937, July/August, 1992.

[28] Engelmann R. H., and Middendorf W. H., "Handbook of Electric Motors", Marcel Dekker, Inc, USA, 1995.

[29] Harker R. G., and Sandy J. L., "Rolling element bearing monitoring and diagnostics techniques", Transactions of the American Society of Mechanical Engineers, Journal of Engineering for Gas Turbines and Power, Vol. 111, April 1989, pp251-256.

[30] Herraty A. G., "Bearing vibration-failures and diagnosis", Mining Technology, February 1993, pp51-53.

[31] Sachs N. W., "Logical failure analysis in rolling element bearings", Power Transmission Design, October 1992, pp22-25.

[32] Stewart R. M., "Application of signal processing techniques to machinery health monitoring", Noise and Vibration, Halsted Press, 1983, Chapter 23, pp607-632.

[33] Filbert D., "Technical diagnosis and testing of electric motors in quality assurance", 8th International IMEKO Symposium on Technical Diagnostics, Sept. 23-25, 1992.

[34] Schoen R. R. and Kamram F., "Motor bearing damage detection using stator current monitoring", IEEE Transaction on Industry Applications, Vol. 31, No. 6, November/December, 1995, pp1274-1279.

[35] Smith R. L., "Rolling element bearing diagnostics with lasers, microphones, and accelerometers", Proceedings of 46th Meeting of the Mechanical Failures Prevention Group, San Diego, California, April 1992, pp43-52.

[36] Smith J. D., "Vibration monitoring of bearings at low speeds", Tribology International, June 1982, pp139-144.

[37] McFadden P. D. and Smith J. D., "Model of vibration produced by a single point defect in a rolling element bearing", Journal of Sound and Vibration, Vol. 96, No. 1, 1984, pp69-82.

[38] Bowdler G. B., "Measurements in high-voltage test circuits", Pergamon Press, 1973.

[39] McDermid W., "Insulation systems and monitoring for stator windings of large rotating machines", IEEE Electrical Insulation Magazine, July/August 1993, Vol. 9, No. 4 pp7-15.

[40] Lonseth P., and Mulhall V. R., "High intensity slot spark discharge-its cause and cure", 1976 International Symposium on Electrical Insulation, paper C-4, Montreal, June 1976.

[41] Wilson A., "Slot discharges in air-cooled stator windings", Proceeding of the 18th Electrical/Electronics Insulation Conference, pp125-129, Chicago, 1987.

[42] Sedding H. G., Campbell S. R., Stone G. C., and klempner G. S., "A new sensor for detecting partial discharges in operating turbine generators", IEEE Transactions on Energy Conversion, Vol. 6, No. 4, December 1991, pp700-706.

[42] Mbaye A., Grogorescu F., Lebey T. and Ai B., "Existence of partial discharges in low-voltage induction machines supplied by PWM drives", IEEE Transactions on Dielectrics and Electrical Insulation, Vol. 3, No. 4, August 1996, pp 554-560.

[43] Persson E., "Transient effects in application of PWM inverters to induction motors", IEEE Transactions on Industry Applications, Vol. 28, No. 5, Sept/Oct, 1992, pp1095-1100.

[44] Zhu H. and Kemp I. J., "Pulse propagation in rotating machines and its relationship to partial discharge measurement", Conf. Record of the IEEE Int. Symp. Electrical Insulation, Baltimore, MD, USA, 7-10 June 1992, pp411-414.

[45] Berth M., Eberhardt M., and Speck J., "Potential grading, and wave parameters of winding phases of induction motors", Proceeding of 9th Int. Symp. on High Voltage Engineering, Aug/Sept, 1995, pp7857-7864.

[46] Bonnett A. H., "Analysis of the impact of pulse-width modulated inverter voltage waveforms on AC induction motors", IEEE Transactions on Industry Applications, Vol. 32, No. 2, March/April 1996, pp386-392

[47] Bonnett A. H., "Available insulation systems for PWM inverter-fed motors", IEEE Industry Applications Magazine, Vol. 4, No. 1, pp14-26, January/February, 1998.

[48] Cameron J. R., Thomson W. T., and Dow A. B., "Vibration and current monitoring for detecting airgap eccentricity in large induction motors.", IEE Proceedings part B, Vol. 133, No. 3, pp155-163, May 1986.

[49] Cameron J. R., and Thomson W. T., "On-line current monitoring of induction motors-a method of calculating the level of eccentricity", Proceeding of IEE EMD 87 Conference, London.

[50] Thomson W. T., "On-line current monitoring to diagnose shaft misalignment in three-phase induction motor drive systems", Proceeding of ICEM 94, D9 pp238-243, 1994.

[51] Dorrel D. G., Thomson W. T., and Roach S., "Analysis of airgap flux, current and vibration signals as a function of the combination of static and dynamic airgap eccentricity in 3-phase induction motors", IEEE IAS meeting, Oct. 95, pp563-570.

[52] Dorrel D. G., Thomson W. T., and Roach S., "Combined effects of static and dynamic eccentricity on airgap flux waves and the application of current monitoring to detect dynamic eccentricity in 3-phase induction motors", IEE Conference Publication No. 412, Electrical Machine and Drives, 11-13 Sept. 1995, pp151-155.

[53] Dorrel D. G., "The influence of rotor skew on unbalanced magnetic pull in cage induction motors with eccentric rotors", IEE Conference Publication No. 412, Electrical Machine and Drives, 11-13 Sept. 1995, pp67-71.

[54] Dorrel D. G., "The effect of dynamic rotor eccentricity in cage induction motors", Proceeding of UPEC 94, pp402-405.

[55] Dorrel D. G., and Smith A. C. "Calculation of U.M.P. in induction motors with series or parallel winding connections", IEEE Transaction of Energy Conversion, Vol. 9, No. 2, June 1994, pp304-310.

[56] Boyle C., Thomson W. T., Sutherland D. N., and Lumsden K. J., "On-line current monitoring to detect misalignment and dynamic eccentricity in three-phase induction motor drivers", Proceeding of UPEC 94, pp5-8.

[57] Ellison A. J. and Yang S. J., "Effects of rotor eccentricity on acoustic noise from induction machines", ibid, 1982, pp61-64.

[58] Verma S. P. and Natarajan R., "Effects of eccentricity in induction motors.", Proceedings of International Conference on Electrical Machines, 3, Budapest, Hungary, Sept., 1982, pp930-933.

[59] Binns K. J. and Barnard W. T., "Some aspects of the use of flux and vibration spectra in electrical machines ", Proceedings of Conference on Applications on Time-series Analysis, University of Southampton, Southampton, UK, 1977, pp17.1-17.12.

[60] Marques C. A. J. and Saraiva S. E. S., "Computer-aided detection of airgap eccentricity in operating three-phase induction motors by Park's vector approach", IEEE Transactions on Industry Applications, Vol. 29, No. 5, Sept., 1993, pp897-901.

[61] Ellison D. H., Exon J. L. T., and Ward D. A., "Protection of slip ring induction motors", IEE Conference Publications 185, pp49-53, 1980.

[62] Kamerbeek E. M. H., "Torque measurements on induction motors using Hall generators or measuring windings", Philips Tech. Rev., 1974, 34, (7), pp152-162.

[63] Sarma M. S., "Electrical machines steady state theory and dynamic performance", Wm. C. Brown publisher 1985, pp248-249.

[64] Gaydon B. G., "An instrument to detect induction motor rotor circuit defects by speed fluctuation measurements.", IEE Conference publish 174, 1979, pp5-8.

[65] Ho Sam Y. S., and Langman R. A., " Accurate speed and slip measurement of induction motors.", Journal of Electrical and Electronics Engineering, Australia, Vol. 16, No.1, March 1996.

[66] Janda Z., Petrovic D., and Lazarevic Z., "New approach for broken rotor bars detection in induction motors", Proceeding of ICEM 94, Vol. 4, pp6-10.

[67] Hsu J. S., "Monitoring of defects in induction motors through air-gap torque observation", IEEE Transactions on Industry Applications, Vol. 31, No. 5, Sept./Oct., 1995, pp1016-1021.

[68] Penman J., and Stavrou A., "The effects of broken rotor bars on the transient run up of induction machines", IEE Conference Publication No. 412, Electrical Machines and Drives, 11-13 Sept., 1995, pp47-51.

[69] Tilak Siyambalapitiya D. J., McLaren P. G., Acarnley P. P., "A rotor condition monitoring for squirrel-cage induction machines", IEEE transactions on Industry Applications, Vol. IA-23, No. 2, March/April, 1987.

[70] Cho K.R., Lang J.H. and Umans S.D., "Detection of broken rotor bars in induction motors using state and parameter estimation.", IEEE Transactions on Industry Applications, Vol. 28 N0. 3, pp702-709, May/June 1992.

[71] Firoozian R. and Lee C.C., "Condition monitoring of automatic control systems using parameter and systems identification: a numerical investigation", Transactions of the Institute of Measurement and Control, Vol. 16, No. 2, pp86-98, 1994.

[72] Du B., Capolino G. A. and Dessoude M., "A fast algorithm for a PC-based motor surveillance system", Proceedings of the International Conference on Electrical Machines, Vol. 2, pp273-277, Paris, France, 5-8 September 1994.

[73] Hargis C., Gaydon B. G., and Kamash K., "The detection of rotor defects in induction motors", International Conference on Electrical Machines - Design and Applications, IEE Conference Publication No. 213, pp213-220, London, 13-15 July 1982.

[74] Elkasabgy N. M., Eastham A. R., and Dawson G. E., "The detection of broken bars in the cage rotor of an induction machine", Conference Record of the IEEE Industry Applications Society Annual Meeting, Vol. 1, pp181-187, 1988.

[75] Tavner P. J., Armin K. K. and Hargis C., "An electrical technique for monitoring induction motor cages", Proceedings of the Third International Conference on Electrical Machines and Drives, IEE Publication No. 282, pp43-46, 16-18 November 1987.

[76] Kliman G. B. and Koegl R. A., "Noninvasive detection of broken rotor bars in operating induction motors", IEEE Transactions on Energy Conversion, Vol. 3, No 4, pp873-879, December 1988.

[77] Deleroi W., "Der stabbruch im Käfigläufer eines asynchronmotors, Teil 1: beschreibung mittels überlagerung eines störfeldes", Archiv für Elektrotechnik, Vol. 67, pp91-99, 1984.

[78] Kliman G. B., "Spectral analysis of induction motor current to detect rotor faults with reduced false alarms", US Patent Number 5,049,815, 17 September 1991.

[79] Elder S., Watson J.F. and Thomson W.T., "Fault detection in induction motors as a result of transient analysis", IEE Publication No. 310, pp182-186, 1989.

[80] Keuck J. D., Criscoe J. C. and Burstein N. M., "Assessment of valve actuator motor rotor degradation by Fourier analysis of current waveform", IEEE Transactions on Energy Conversion, Vol. 7, No. 3, pp460-469, September 1992.

[81] Thomson W. T. and Chalmers S. J., "On-line condition monitoring of electrical machines - research to applications", Proceedings of the Vibration Analysis for Condition Monitoring - Techniques and User Experience Seminar, British Institute of Non-Destructive Testing, pp73-87, 1989

[82] Hirvonen R., "On-line condition monitoring of defects in squirrel cage motors", Proceedings of the International Conference on Electrical Machines, Vol. 2, pp267-272, Paris, France, 5-8 September 1994.

[83] Gaydon B. G. and Hopgood D. J., "Faltering pulse can reveal an ailing motor", Electrical Review Vol, 205, No. 14, pp37-38, 12 October 1979.

[84] Steele M. E., Ashen R. A., and Knight L. G., "An electrical method for condition monitoring of motors", International Conference on Electrical Machines - Design and Applications, IEE Conference Publication No. 213, pp231-235, London, 13-15 July 1982.

[85] Kliman G. B. and Stein J., "Methods of motor current signature analysis", Electric Machines and Power Systems, Vol. 20, pp463-474, 1992.

[86] Watt P. A. and Langman R. A., "Condition monitoring of large induction motors", IE Aust. Conference on Industrial Drives, pp213-219, Rockhampton, Australia, 18-20 September1991

[87] Innes A. G., Watt P. A., and Langman R. A., "Condition monitoring of large induction motors", Proceedings of the Australasian Instrumentation and Measurement Conference, pp265-271, Auckland, New Zealand, 24-27 November 1992.

[88] Kryter R. C. and Haynes H. D., "Condition monitoring of machinery using motor current signature analysis", Sound and Vibration, pp14-21, September 1989.

[89] Vas P., Filippetti F, Franceschini G., and Tassoni C., "Transient modelling oriented to diagnostics of induction machines with rotor asymmetries", Proceeding of ICEM 94, Vol. 2, pp62-67.

[90] Paterson N. C., Watson J. F., and Dorrell D. G., "The application of finite element methods to aid and improve techniques for on-line condition monitoring of electrical machines", Proceeding of ICEM 96, Vol. 2, pp482-487.

[91] Fiser R., Ferkolj S., and Solinc H., "Steady state analysis of induction motor with broken rotor bars", IEE Conferences Publication No. 412, Electrical Machines and Drivers, 11-13 Sept., 1995, pp42-46.

[92] Manloas S. T., Tegopoulos J., and Papdopoulos M., "Anaylsis of squirrel cage induction motors with broken rotor bars", Proceeding of ICEM 96, Vol. 3, pp19-23.

[93] Thomson W. T. and Stewart I. D., "On-line current monitoring for fault diagnosis in inverter fed induction motors", Proceedings of the Third International Conference on Power Electronics and Variable-Speed Drives, IEE Conference Publication 291, pp432-435, 1988.

[94] Marques C. A.J. and Saraiva E. S., "Condition monitoring of current source inverter-fed induction machines", Proceedings of the 6th Conference on Power Electronics and Motion Control, Vol. 3, pp744-748, Budapest, Hungary, 1990.

[95] Sethuraman S. K. and Saravanan M. G., "Pulse width modulated embedded control and on-line condition monitoring of induction motors.", Proceedings of the 29th Universities Power Engineering Conference, Vol. 2, pp645-647, Galway, Ireland, 14-16 September 1994.

[96] Thian B.M., "Methods for Monitoring the Condition of Electrical Machines Fed from Variable Speed Drives", PhD Thesis, University of Aberdeen, UK, 1991.

[97] Yang S. J., "Low noise electrical motors", Clarendon Press, Oxford, 1981

[98] Freise W. and Jordan H., "Unilateral magnetic pulls in 3-phase machines", ETZ-A, Vol. 83, No. 9, 23 April 1962, C: E Trans. 7836.

[99] Dubey G. K., "Power semiconductor controller drivers", Prentice-Hall International Editions.

[100] Holtz J., "Pulsewidth modulation for electronic power conversion", Proceedings of the IEEE, Vol. 82, No. 8, pp1194-1214, August 1994.

[101] Rioul O. and Vetterli M., "Wavelets and signal processing", IEEE Spectrum magazine, Oct., 1991, pp14-38.

[102] Gabor D., "Theory of communication.", J. IEEE, 93, 1946, pp429-457.

[103] Legowski S. F. and Trzynadlowski A. M., "Instantaneous stator power as a media for the signature analysis of induction motors", Conference Record of the 1995 IEEE, Industry Applications Society, 30th IAS Annual Meeting Vol. 1, pp619-624.

[103] Johnson S., "Commutation adjustments of DC machines", Electrical Times, 21 Sept., 1961, pp418-420.

[104] "How right are your brushes? Factors affecting life and efficiency of carbon brushes", Electrical Times, 18 May 1961, pp797.

[105] Clayton A. E. & Hancock N. N., "The performance and design of direct current machines", Pitman, 1959.

[106] Smith H. G., "Commutator temperature of traction motors", IEE Conference Publication No. 11, Commutation in Rotating Machines, pp239-244, 1964.

[107] Kennedy D. A. and Gates D., "The measurement of commutator profiles", IEE Conference Publication No. 11, Commutation in Rotating Machines, pp245-247, 1964.

[108] Roumanis S. J., "The null point method of commutation adjustment", AIEE Trans., 56-38, April 1956.

[109] Johnson J. L., "Multiplier phototube commutation indicator", IEE paper, Jan., 1963.

[110] Iqbal M. Z. and Hindmarsh J., "Detectors for commutation measurement and control", Electrical Machines in the Seventies, University of Dundee, 1970.

[111] Destefan D. E., "Calibration and testing facility for resistance welding current monitors", IEEE Transactions on Instrumentation and Measurement, Vol. 45, No. 2, April 1996, pp453-456.

[112] Ramboz J. D., "Machinable Rogowski coil, design, and calibration", IEEE Transactions on Instrumentation and Measurement, Vol. 45, No. 2, April 1996, pp511-515.

[113] Guhmann C. and Filbert D. "Fault diagnosis of electrical low-power motors by analysis the motor current", IFAC/IMACS-Symposium on Fault Detection, Supervision and Safety for Technical Processes, vol. 1 pp67-72.

[114] Chari M.V.K., and Silvester P.P., "Finite Element Problems in Electrical and Magnetic Field Problems", John Wiley and Sons, New York, 1980.

[115] Filbert D., "Fault diagnosis in nonlinear electromechanical system by continuous time parameter estimation", ISA Trans., 24(3), 1985.

[116] Filbert D., "A contribution to the test of electric motors by parameter estimation method", 25th UPEC Conference Proceeding Vol. 1, 1990, pp687-690.

[117] Filbert D., "Technical diagnosis of electric drive systems", Measurement Vol. 8, No. 3, July-Sept., 1990, pp121-127.

[118] Filbert D., Spannhake S. and Schneider C., "Model equation and fault detection of electric motors", IFAC/IMACS Symposium on Fault Detection, Supervision on Technical Diagnosis, Dresden, ISA Trans., 24(3), 1985, pp66-67.

[119] Filbert D., "Technical diagnosis and testing of electric motors in quality assurance", 8th IMECO, Symposium on Technical Diagnostic, Dresden, 1992, pp66-67

[120] Nold S., Isermann R., "Identifiability of process coefficients for technical failure diagnosis", 25th IEEE Conference on Decision and Control, Athens, 1986.

[121] Schneider C., Filbert D., "Parameter estimation and residual analysis – a comparison", IFAC/IMACS-Symposium on Fault Detection, Supervision and Safety for Technical Process, Safe Process 1994.

[122] Krisch E., Smikal F., "Investigation of commutation of DC machines with wave winding", International Conference of Electrical Machines Proceeding, Vol. 2, pp488-491, Sept., Budapest, Hungary, 1982

[123] Glowacz Z., "Analysis of failure states of D.C. machine", the Proceedings of International Conference on Electrical Machines, ICEM'96, September 10-12, 1996, Vigo, Spain, Vol 2., pp. 464-469.

[124] Schröder R. and Oberretl K., "Neues Verfahren zur Berechnung der Kommutierung von Gleichstrom-maschinen unter Berübergangswiderstände", Archiv für Elektrotechnik, Vol. 73, No.2, 1990, 69-79.

[125] Jones C. V., "An analysis of commutation for the unified-machine theory", The Institution of Electrical Engineers Monograph No. 302U, April 1958, pp476-488.

[126] Barton T. H. and Jones C. V., "A practical commutator primitive for generalised machine theory", Transactions of AIEE, 79, Part III, 1960, pp277.

[127] Johnson L.W. and Riess R.D., "Numerical Analysis", 2nd edition, Addison Wesley, Reading Massachusetts, 1982.

[128] Press W.H., Teukolsky S.A., Vetterling W.T. and Flannery B.P., "Numerical Recipes in C: The Art of Scientific Computing", 2nd edition, Cambridge University Press, Cambridge UK, 1992.

[129] Langman R. A., "The manual of the Direct Current Inductance Bridge", Electrical Engineering Department, University of Tasmania.

[130] Say M. G. and Taylor E. O., "Direct Current Machines", Pitman, Great Britain, 1980.

[131] Deng X. and Ritchie E., "Detection of broken rotor bars in induction motor rotors by investigating the flux linkages of the stator windings", Proceeding of the international Conference on Electrical Machines in Australia, Vol. 1, pp164-169, Adelaide, Australia, Sept., 1993.

[132] Turner M. J. B. and Swinnerton B. R. G., "Sparking and arcing in electrical machines", Proceeding of IEE, Vol. 113, No. 8, August, 1966, pp1376-1386.

[133] Cobine J. D., "Gaseous conductors, theory and engineering applications.", Dover Publications Inc. New York, 1958.

[134] Filippetti F., Franceschini G., and Tassoni C., "Neural networks aided on-line diagnostics of induction motor rotor faults", IEEE Transactions on Industry Applications, Vol. 31, No. 4, pp892-899, July/August 1995.

[135] Penman J. and Yin C. M., "Feasability of using unsupervised learning, artificial neural networks for the condition monitoring of electrical machines", IEE Proceedings - Electric Power Applications, Vol. 141, No. 6, pp317-322, November 1994.

[136] Filippetti F., Franceschini G., Tassoni C., Meo S., and Ometto A., "Neural network aided on-line diagnostics of induction machine stator faults", Proceedings of the 30th Universities Power Engineering Conference, Vol. 1, pp148-151, London, UK, 5-7 September 1995.

[137] Penman J., Stavrou A., Yin C.M., Jiang H., and Hatzipantelis E., "Machine diagnostics with ANNs: possibilities and problems.", Proceedings of the International Conference on Electrical Machines, Vol. 2, pp363-368, Paris, France, 5-8 September 1994.

[138] Protopapas C.A., Kaminaris S.D., Machias A.V., and Papadias B.C., "An expert system for fault repairing and maintenance of electric machines", IEEE Transactions on Energy Conversion, Vol. 5, No. 1, pp79-83. March 1990.

[139] Gentile G., Rotondale N., Tursini M., Franceschini G., and Tassoni C., "An approach to knowledge-base representation in electric drive fault diagnosis", Proceedings of the International Conference on Electrical Machines, Vol. 2, pp358-362, Paris, France, 5-8 September 1994.

[140] Cash M. A., Habetler T. G., and Kliman G. B., "Insulation failure prediction in ac machines using line-neutral voltages", IEEE Transactions on industry Applications, Vol. 34, No. 4, Nov., 1998, pp1234-1239.